

UNIVERSITÉ DU QUÉBEC À CHICOUTIMI

**THESIS SUBMITTED TO THE
UNIVERSITY OF QUEBEC AT CHICOUTIMI
IN PARTIAL FULFILLMENT OF THE
REQUIREMENTS FOR THE DEGREE OF
DOCTOR OF PHILOSOPHY**

BY

AHMED MOHAMMED NABAWY

**INFLUENCE OF ZIRCONIUM AND SCANDIUM ON THE
MICROSTRUCTURE, TENSILE PROPERTIES, AND HOT-TEARING
SUSCEPTIBILITY OF AL-2WT%CU-BASED ALLOYS**

MAY 2010

UNIVERSITÉ DU QUÉBEC À CHICOUTIMI

THÈSE PRÉSENTÉ À

L'UNIVERSITÉ DU QUÉBEC À CHICOUTIMI

COMME EXIGENCE PARTIELLE

DU DOCTORAT EN INGÉNIERIE

PAR

AHMED MOHAMMED NABAWY

**EFFET DU ZIRCONIUM ET DU SCANDIUM SUR LA
MICROSTRUCTURE, LES PROPRIÉTÉS DE TRACTION ET LA
SUSCEPTIBILITÉ À LA DÉCHIRURE À CHAUD POUR LES
ALLIAGES DE BASE AL-2%CU**

MAI 2010

RÉSUMÉ

Le développement de nouveaux alliages, caractérisés par un rapport résistance-poids élevé et par un faible coût de production est un des objectifs majeurs de l'industrie de l'automobile afin de réduire les émissions de CO₂ en réduisant le poids des pièces tout en conservant les propriétés mécaniques à haute température. L'alliage Al-2%Cu contenant 2%Cu, 1%Si, 0.4%Mg, 0.42%Fe, 0.7%Mn et 0.02%Ti est l'un de ces alliages. Sa faible teneur en Cu et Si associé à un niveau acceptable de la résistance à la traction, permet à ce dernier de remplacer un certain nombre d'alliages comme le 319 pour des applications similaires telles que la coulée de culasses et de bases de moteur. En tant que nouvel alliage, il nécessite une enquête approfondie afin d'optimiser différentes caractéristiques telle la coulabilité, la microstructure et les propriétés mécaniques. Cette étude a été entreprise afin d'étudier les effets des additifs chimiques comme le zirconium et le scandium sur la microstructure, les propriétés de traction et la susceptibilité à la déchirure à chaud. Cette enquête a été réalisée à partir de 31 compositions d'alliage (Al-2%Cu) qui ont été divisés en trois catégories d'alliages principaux liés à la microstructure, les propriétés de traction et les enquêtes sur la déchirure à chaud. À titre comparatif, sept compositions de l'alliage 206 (Al-4%Cu) ont également été employées.

Dans la première catégorie, dix alliages ont été coulés utilisent comme principaux additifs le Zr et le Sc en combinaison avec le Ti-B, le Sr et l'Ag sous des conditions de refroidissement lent d'environ 0,3°C/s et à des concentrations relativement élevées de 0,5%Zr et 0,5%Sc. Un certain nombre d'intermétalliques primaires de Zr, Sc et Zr-Sc ont été observés dans les alliages étudiés, à savoir la phase étoilée Al₃(Sc_{1-x}Zr_x), les phases Al₃Sc, V-AlSc₂Si₂, Al₃Zr, en plus de deux autres composés intermétalliques de Zr. Il a été observé que les cristaux Al₃Zr servent de noyaux pour les phases étoilées qui croient par la précipitation des couches d'Al₃Sc, avec la substitution progressive des atomes Sc par les atomes Zr. Également, la phase en étoile continue de croître à l'état solide par l'absorption de Sc pour ainsi former la phase Al₃Sc, observée sous la forme de spirale sur les bords de la particule. Des composés intermétalliques inconnus ternaires AlZrSi et quaternaires AlZrTiSi ont également été détectés. Il a été constaté que les additions combinées de Zr et Sc ont grandement modifiées la taille et la morphologie des grains de l'alliage de base. La taille des grains diminue proportionnellement avec l'augmentation de la fraction volumique des intermétalliques résultants de l'ajout combiné de Zr et de Sc qui, à son tour, conduit à la formation à profusion de la phase étoilée. Les effets bénéfiques des éléments de transition Zr, Sc, Ti à affiner la taille des grains α-Al et à transformer la morphologie d'un précipité dendritique à un non-dendritique mène, indirectement, à une réduction sensible de la taille des composés intermétalliques tels que les phases α - Fe et Al₂Cu.

Dans la seconde catégorie, dix-sept alliages différents ont été préparés en utilisant différentes additions de Zr, Sc, Ti-B, Sr, Ag et Si. Ces alliages ont été divisés en quatre

sous-groupes, comme suit: Zr-Ti, Zr-Sr, Zr-Sc et les alliages de silicium. Les barreaux pour les essais de traction (Vitesse de refroidissement 7°C/s) coulés de ces alliages ont été mis en solution pour une période de 8 heures à 490°C, puis durci par vieillissement à des temps de 2, 4, 6, 10, 16, 24 et 48h à 180°C et 0.5, 1, 1.5, 2, 4, 6, 10, 16, 24 et 48h à 220°C. Il a été signalé que les additions combinées de Zr-Ti, Zr-Sr, Zr-Sc réduit considérablement la taille des grains de l'alliage de base de 219 microns à 104-46 µm étant donné que ces éléments forment des intermétalliques trialuminide primaire y compris $Al_3(Sc_{1-x}Zr_x)$, $Al_3(Sc_{1-x-y}Zr_xTi_y)$, et Al_3Zr qui agissent comme sites de nucléation pour les grains α -Al, produisant ainsi une structure fine non dendritique. La morphologie raffinée non-dendritique produite par les additions combinées de Zr-Ti, Zr-Sr, Zr-Sc a entraîné une réduction d'environ 65% dans la fraction de surface de la phase Al-2%Cu dans l'alliage de base, et à une réduction de la porosité d'environ 50%. Une augmentation de 2%Si a également produit les mêmes résultats, provoquée par l'augmentation de la teneur en Al-Si eutectique. Le durcissement maximal est atteint après des vieillissements de 10h et 24h à 180°C et de 1h et 2h à 220°C. Les groupes d'alliage Zr-Sr et Zr-Ti ont fournis la meilleure amélioration des propriétés de mécaniques de l'alliage de base Al-2%Cu alors que les groupes Zr-Sc et Si occupent le troisième et quatrième niveau, respectivement. L'alliage contenant 0.02%Sr-0.7%Zr a fourni la plus grande limite à la rupture et des valeurs de résistance de 383 MPa et 326 MPa, respectivement, après 4h de vieillissement à 180°C. La résistance de l'alliage augmente dans le groupe d'alliage Zr-Ti en raison de l'augmentation de la teneur en Zr de 0,15% à 0,7% après un vieillissement de 10h à 180°C. Cette augmentation peut être attribuée aux dispersoïdes Al_3Zr et $Al_3(Zr_{1-x}Ti_x)$ agissant en tant que sites de nucléation hétérogène pour les phases durcies par vieillissement, à l'action modifiante du Zr sur la phase Al_2CuMg et à l'action du Zr-Ti à produire une structure de grains raffinés non-dendritiques. Les additions combinées de Zr-Sr et Sr-Ti produisent les meilleurs niveaux d'allongement de tous les alliages étudiés, comme en témoignent les alliages contenant 0.02%Sr-0.15%Ti et 0.02%Sr-0.7%Zr. Ces niveaux améliorés sont le résultat des effets de la modification du Sr sur les particules α -Fe, ainsi que le rôle du Zr et du Ti à produire une structure non dendritique α -Al. L'alliage contenant 0.02%Sr-0.15%Ti a montré le plus haut niveau de résistance au ramollissement au cours du vieillissement à 220°C en raison des effets respectifs de la modification et du raffinage du Sr et du Ti sur la microstructure.

La troisième catégorie d'alliage comprend six alliages sélectionnés dans la seconde catégorie afin d'étudier les effets de la composition chimique et des paramètres du moule sur la susceptibilité à la déchirure à chaud (HTS) du nouvel alliage Al-2%Cu. Les résultats HTS ont été comparés avec l'alliage 206. Généralement l'alliage de base Al-2%Cu a donné une plus grande résistance à la déchirure à chaud que l'alliage 206. Une température du moule élevée est bénéfique dans la réduction de la susceptibilité à la déchirure à chaud des alliages Al-2%Cu et 206 par une baisse de la valeur HTS de 21 à 3 et 9, respectivement. La température du moule est passée de 250°C à 450°C. Le raffinement de la structure des grains obtenus avec les additions de Zr-Ti ou Ti a diminué la gravité de la déchirure à chaud suite à l'augmentation du nombre de film inter granulaire liquide par unité de volume et a retardé l'atteinte du point de cohérence. L'augmentation de la teneur en silicium

réduit considérablement la vulnérabilité à la déchirure à chaud de l'alliage Al-2%Cu; cette réduction est attribuable à une augmentation de la fraction volumique de l'eutectique, et une diminution du point de fusion de l'alliage. L'ajout du Sr a détérioré la résistance à la déchirure à chaud en raison de la formation d'oxydes de Sr et à l'extension de l'échelle de congélation de l'alliage. Il a été signalé que les particules α -Fe peuvent gêner la propagation de la fissure lors de la déchirure à chaud.

ABSTRACT

The development of new alloys characterized by a high strength-to-weight ratio and low production costs is one of the major objectives of the modern automotive industry with a view to lowering CO₂ emissions and obtaining automotive castings that are both lightweight and capable of maintaining their performance under elevated temperature service conditions. The Al-2wt%Cu alloy is one such alloy; it contains 2wt% Cu, 1wt% Si, 0.4wt% Mg, 0.42wt% Fe, 0.7wt% Mn, and 0.02wt% Ti. The low Cu and Si content of the alloy, associated with an acceptable level of tensile strength, make this alloy suitable as a replacement for a number of other alloys such as the 319-type alloys used in engine blocks and cylinder heads. As a new alloy under development, the Al-2wt%Cu alloy has necessitated an in-depth investigation of its castability, microstructure, mechanical properties and other characteristics, and the metallurgical parameters controlling them. A study was therefore undertaken to investigate the effects of chemical additives, mainly zirconium (Zr) and scandium (Sc), on the microstructure, tensile properties, and hot-tearing susceptibility of Al-2wt%Cu-based alloys, Zr and Sc additions being known to improve the high temperature performance of aluminum alloys. As Al-Cu alloys are invariably prone to hot-tearing, it was deemed important to also investigate the effects such alloying additions on minimizing the hot-tearing sensitivity of these alloys. The investigation was carried out using thirty-one Al-2wt%Cu based alloy compositions, as well as seven alloy compositions using the 206 (Al-4wt%Cu) alloy for comparison purposes. These alloys were subsequently divided into three main alloy categories designated, respectively, for the investigation of the microstructure, tensile properties, and hot-tearing behavior of these alloys.

In the first alloy category, ten alloys were cast using Zr and Sc as the main additives in combination with Ti-B, Sr, and Ag under slow cooling rate conditions of ~0.3 °C/s and at relatively high concentrations of 0.5 wt% each of Zr and Sc. A number of primary Zr-, Sc-, and Zr-Sc-containing intermetallics were detected in the alloys investigated, namely, the star-like Al₃(Sc_{1-x}Zr_x) phase, the Al₃Sc phase, the V-AlSc₂Si₂ phase, the Al₃Zr phase, and two other Zr-intermetallic compounds. It was observed that the Al₃Zr crystals act as nuclei for the star-like phase which grows through the precipitation of layers of Al₃Sc on these nuclei, with the successive substitution of Sc by Zr atoms. It was also reported that the star-like phase continues to grow in the solid state by absorbing Sc to form the Al₃Sc phase, observed in the form of a rim along the edges of the particle. Ternary AlZrSi and quaternary AlZrTiSi intermetallic compounds were also detected in this study. It was found that combined additions of Zr-Sc alter the α-Al grain size and morphology of the base alloy to a great extent. The grain size decreases linearly with the increase in the volume fraction of intermetallics, attributed to the profuse formation of the star-like phase, resulting from the combined Zr-Sc additions. The beneficial effects of the transition elements Zr, Sc, and Ti in refining the α-Al grain size and in transforming the morphology from dendritic to a non-dendritic type lead, indirectly, to a noticeable reduction in the size of intermetallic compounds such as the Al₂Cu and α-Fe phases.

In the second alloy category, seventeen alloy compositions were prepared, using different additions of Zr, Sc, Ti-B, Sr, Ag, and Si. These alloys were further divided into four groups, namely, the Zr-Ti, Zr-Sr, Zr-Sc, and Si alloy groups. Tensile test bars (cooling rate 7°C/s) prepared from these alloys were solutionized for 8h at 490°C then age-hardened at temperatures of 180°C and 220°C for aging times of 2, 4, 6, 10, 16, 24, and 48h, and 0.5, 1, 1.5, 2, 4, 6, 10, 16, 24, and 48h, respectively. It was observed that combined additions of Zr-Ti, Zr-Sr, or Zr-Sc refined the grain size of the base alloy considerably, from 219 μm to 104-46 μm , since these elements form primary trialuminide intermetallics including $\text{Al}_3(\text{Sc}_{1-x}\text{Zr}_x)$, $\text{Al}_3(\text{Sc}_{1-x-y}\text{Zr}_x\text{Ti}_y)$, and Al_3Zr which act as nucleation sites for α -Al grains, thereby producing fine non-dendritic structures. The refined non-dendritic morphology produced by the combined additions of Zr-Ti, Zr-Sr, or Zr-Sc caused a reduction of about 65% in the amount of the Al_2Cu phase in the base alloy, and a reduction in porosity of about 50%. The addition of 2 wt% Si also produced the same reduction levels in the amount of Al_2Cu and porosity, brought about by the increase in the Al-Si eutectic content. Age-hardening peaks were observed after aging for 10h and 24h at 180°C, and after aging for 1h and 2h at 220°C. The Zr-Sr and Zr-Ti alloy groups displayed the highest level of improvement in the tensile properties of the Al-2wt%Cu base alloy followed by the Zr-Sc and Si alloy groups, in that order. The 0.02wt%Sr-0.7wt%Zr containing alloy produced the highest ultimate tensile and yield strength values of 383 MPa and 326 MPa, respectively, after 4h of aging at 180°C. The strength of the base alloy increased in the Zr-Ti alloy group with an increase in Zr content from 0.15wt% to 0.7wt% after aging at 180°C for 10h. This increase may be variously attributed to Al_3Zr and $\text{Al}_3(\text{Zr}_{1-x}\text{Ti}_x)$ dispersoids acting as heterogeneous nucleation sites for age-hardening phases; to the modifying action of Zr on the S' (Al_2CuMg) phase; and to the action of Zr-Ti in producing a refined non-dendritic grain structure. Combined additions of Zr-Sr and Sr-Ti displayed the best elongation levels of all the alloys investigated, as witnessed by the 0.02wt%Sr-0.15wt%Ti-containing alloy and, 0.02wt%Sr-0.7wt%Zr-containing alloy. These improved levels may be the result of the modifying effects of Sr on α -Fe particles, as well as of the roles of Zr and Ti in producing a fine non-dendritic α -Al structure. The 0.02wt%Sr-0.15wt%Ti-containing alloy displayed the highest resistance to softening during aging at 220°C because of the respective modifying and refining effects of Sr and Ti on the microstructure.

The third alloy category comprised six alloys selected from the second category in order to investigate the effects of chemical composition and mold variables on the hot-tearing susceptibility (HTS) of the new Al-2wt%Cu alloy. The HTS results were then compared with 206 alloys containing the same chemical additions. Generally, the Al-2wt%Cu-based alloys exhibited higher resistance to hot-tearing than 206-based alloys did. It was found that an elevated mold temperature is beneficial in reducing the hot-tearing susceptibility of the Al-2wt%Cu and 206 alloys in that the HTS value decreased from 21 for the two alloys to 3 and 9, respectively, as the mold temperature was increased from 250°C to 450°C. The refinement of the grain structure obtained with the Zr-Ti or Ti additions decreased the hot-tearing severity as result of an increase in the number of intergranular liquid films per unit volume and a delay in reaching the coherency point. Increasing the Si content reduced the

hot-tearing susceptibility of the Al-2wt%Cu alloy considerably; this reduction is attributed to an increase in the volume fraction of eutectic in the structure, and a decrease in the freezing range of the alloy. The addition of Sr caused a deterioration in the hot-tearing resistance of the base alloy as a result of the formation of Sr-oxides and an extension of the freezing range of the alloy. It was also observed that α -Fe particles may obstruct the propagation of hot-tearing cracks. The 1%wtSi-containing Al-2wt%Cu alloy was judged to be the best composition in view of its low hot-tearing susceptibility.

ACKNOWLEDGMENT

It has been an honor to be able to work under the supervision of Professor Dr. Fawzy Samuel and Professor Dr. Agnes Samuel. I am grateful for having the chance to work with them and I deeply appreciate all of their help, and guidance.

Financial support received from the Natural Sciences and Engineering Research Council of Canada (NSERC) and from General Motors Powertrain Group is hereby gratefully acknowledged.

I would like to thank Alain Bérubé and Mathieu Paradis for helping me so consistently at various stages of the experimental work; I would also like to acknowledge M. Sinclair for help in proofreading the manuscript.

Lastly, I would like to make special mention of my parents and my wife, El-Shimaa, for their unfailing support and encouragement during the preparation of the thesis.

TABLE OF CONTENTS

ABSTRACT	IV
ACKNOWLEDGMENT.....	VII
TABLE OF CONTENTS.....	VIII
LIST OF FIGURES	XI
LIST OF TABLES.....	XX
CHAPTER 1 INTRODUCTION.....	2
1.1 Definition of the Problem	2
1.2 Objectives.....	4
CHAPTER 2 THEORETICAL BACKGROUND	8
2.1 General Aspect of Al-Cu Alloys	8
2.1.1 Microstructure.....	8
2.1.2 Heat Treatment.....	12
2.1.2.1 Solution Heat Treatment.....	13
2.1.2.2 Quenching	18
2.1.2.3 Aging	20
2.1.3 Precipitation in Al-Cu Systems	22
2.1.3.1 Al-Cu System.....	22
2.1.3.2 Al-Cu-Mg-Si System.....	24
2.1.4 Tensile Properties as Affected by Different Parameters	28
2.2 Transition Elements (Zr, Sc).....	34
2.2.1 Zirconium (Zr).....	34
2.2.2 Scandium	39
2.3 Hot Tearing.....	44
2.3.1 Introduction	45
2.3.2 Factors Controlling Hot Tearing	46
2.3.2.1 Metallurgical Factors.....	46
a. Chemical Composition.....	46
b. Grain Size and Grain Morphology.....	49
c. Superheat	52
d. Mold Temperature	54
e. Gas Content.....	56
2.3.2.2 Mechanical Factors.....	56

<i>a.</i>	<i>Casting Design</i>	56
<i>b.</i>	<i>Mold Variables</i>	58
<i>c.</i>	<i>Mold Friction</i>	59
2.3.3	Hot Tearing Theories	59
2.3.3.1	Strain Theory.....	59
2.3.3.2	Shrinkage-Brittleness Theory.....	60
2.3.3.3	Liquid Metal Embrittlement Theory	62
2.3.4	Hot-Tearing Testing Methods	64
CHAPTER 3 EXPERIMENTAL PROCEDURES		68
3.1	Preparation of Materials and Melting Procedures	69
3.2	Casting Procedures	70
3.2.1	Graphite Mold Castings and Thermal Analysis	70
3.2.2	Tensile Test Bar Casting	73
3.2.3	Hot Tearing Test.....	75
3.3	Heat Treatment Procedures	79
3.4	Tensile Testing	79
3.5	Metallography	80
CHAPTER 4 PHASE IDENTIFICATION AND QUANTIFICATION		86
4.1	Base Alloy Intermetallic Phases	87
4.2	Zr and Sc Intermetallic Phases	90
4.2.1	Scandium Intermetallics	92
4.2.1.1	Al ₃ (Sc _{1-x} Zr _x)-Star Intermetallic Phase	92
4.2.1.2	Al ₃ Sc Intermetallic Phase	99
4.2.1.3	V-Phase (AlSc ₂ Si ₂)	100
4.2.2	Zirconium Intermetallics	104
4.2.2.1	Al ₃ Zr Intermetallic Phase.....	104
4.2.2.2	Other Zirconium Intermetallic Phases	107
4.3	Grain Structure	110
4.4	Conclusions	124
CHAPTER 5 TENSILE PROPERTIES		128
5.1	Microstructure	129
5.2	Tensile Properties	144
5.2.1	As-Cast and As-Solutionized Conditions	144
5.2.2	Age-Hardening Conditions	149
5.2.2.1	Zr-Ti Alloy Group	149
5.2.2.2	Zr-Sr Alloy Group	158

5.2.2.3	Zr-Sc Alloy Group.....	166
5.2.2.4	Si Alloy Group.....	171
5.3	Fracture Mechanism.....	177
5.4	Conclusions	182
CHAPTER 6 HOT-TEARING SUSCEPTIBILITY		187
6.1	Hot-Tearing Susceptibility (HTS).....	188
6.2	Effects of Mold Temperature	196
6.3	Effects of Grain Structure	200
6.4	Effects of Silicon Content	208
6.5	Effects of Strontium Addition	213
6.6	Effects of α -Iron Intermetallic Phase.....	217
6.7	Proposed Hot-Tearing Criteria.....	220
6.8	Conclusions	224
RECOMMENDATIONS FOR FUTURE WORK		228
REFERENCES		229

LIST OF FIGURES

Figure 2.1	The microstructure of Al-4Cu alloy; (a) The optical dendritic morphology of α -Al at cooling rate of 0.3°C/s^5 , and (b) Backscattered image of eutectic- Al_2Cu phase. ⁶	9
Figure 2.2	SEM micrographs of a region adjacent to the fracture surface of tensile specimens showing cracking of (a) θ - Al_2Cu intermetallics and (b) α - $(\text{Al}_{15}(\text{Mn},\text{Fe})_3\text{Si}_2)$ intermetallics. (A319 alloy). ⁸	9
Figure 2.3	Microstructure of B319.1 alloy at cooling rate of 0.3°C/s , showing the $\text{Al}_5\text{Mg}_3\text{Si}_6\text{Cu}_2$ phase grown out from Al_2Cu particles. ⁵	10
Figure 2.4	Microstructure of as-cast Al-4.5wt%Cu-2wt%Si alloy. ⁶	11
Figure 2.5	Variation of DAS of 319 alloys containing different levels of Cu and poured in different molds which provide different cooling rates. ¹³	12
Figure 2.6	The temperature ranges of heat treatment in Al-Cu system alloys.....	13
Figure 2.7	Effect of solution heat treatment on the amount of dissolved Al_2Cu in 319 alloy. ²²	14
Figure 2.8	Effect of Cu concentration on (a) strength, and (b) elongation. ²²	15
Figure 2.9	Melting process of Al_2Cu Phase in solution heat-treated samples at 540°C : (a) initiation of melting (arrowed) in a sample heated up to 540°C and quenched immediately; (b) after 2h, (c) after 8h, (d) after 24h, showing the presence of cavities and structureless phase particles. ²²	16
Figure 2.10	Effects of solution treatment time on tensile properties of alloy 204.0. ¹⁹ ..	19
Figure 2.11	Partial equilibrium diagram of Al-Cu alloys representing the solvus lines of the metastable and equilibrium phases. ³⁸	21
Figure 2.12	Hardness-time curves of the Al-4wt%Cu-0.3wt%Mg alloy aged at 150, 200, 250°C . ⁴²	22
Figure 2.13	Transmission electron micrographs of metastable phases and equilibrium Al_2Cu phase. ⁴³	23
Figure 2.14	HRTEM image of lath-shaped Q precipitate in Al-7wt%Si-0.5wt%Mg-1wt%Cu alloy after 12h of aging at 175°C . ⁵⁷	25
Figure 2.15	Experimentally observed phase compositions after decomposition of supersaturated solid solutions for alloys with (a) 0–0.25wt% Cu; (b) 0.5–0.8wt% Cu; (c) 0.9–2.5wt% Cu; and (d) 2.5–4.5wt% Cu. ⁵⁸	27
Figure 2.16	Tensile properties of B206 alloy at: (a) T7 <i>i.e.</i> SHT @ $480^{\circ}\text{C}/1\text{h}$ - $495^{\circ}\text{C}/2\text{h}$ - $528^{\circ}\text{C}/10\text{h}$ -WQ @ 65°C -aging @ $200^{\circ}\text{C}/4\text{hr}$, and (b) T4 same as T7 but after WQ @ 65°C , keeps for 7 days. ⁵⁹	29

- Figure 2.17** Effects of aging time in the temperature range 155-220°C on tensile properties of Al-6wt%Si-4wt%Cu-0.46wt%Fe-0.14wt%Mn alloy: (a) YS, (b) UTS, and (c) Elongation (%).⁶⁰ 30
- Figure 2.18** The tensile properties of Al-7wt%Si-0.44wt%Mg-0.36wt%Fe with respect to the Cu content and cooling rate: (a) as cast condition, and (b) after heat treatment (SHT@490°C-12h/WQ@60°C/Ag@180°C-5h).¹³ 33
- Figure 2.19** The effects of Ag addition on the tensile properties of A201-T7 alloy (T7:SHT@529°C-16h/WQ/24h@RT/Aging@188°C-5 h).⁶³ 33
- Figure 2.20** Al₃Zr precipitates observed in 2014 aluminum alloy. 34
- Figure 2.21** Effects of 0.15wt% Zr addition on hardness of 319 alloy type after solution heat treatment at 503°C for different times.⁷² 35
- Figure 2.22** Optical image of grain showing the non-uniform distribution of Al³Zr dispersoids appearing as white dots at the grain center) after isothermal homogenisation for 20 h at 500°C.⁷³ 36
- Figure 2.23** Predicted variation of the Al₃Zr dispersoid nucleation and growth rates with temperature.⁷⁶ 36
- Figure 2.24** Partial equilibrium phase diagram for Al-Zr system. Adapted from⁶⁷ 37
- Figure 2.25** Microstructure of an Al-2.2wt%Zr alloy solidified at 102 K/s, SEM.⁷⁵ 37
- Figure 2.26** Microstructure-Section map for the Al-Zr alloy system pertaining to cooling rate and Zr content..... 38
- Figure 2.27** Precipitation of Sc-rich phase onto primary Zr-rich particles during solidification. The arrow points to the Sc-rich layer.⁷⁵ 39
- Figure 2.28** Images of Al-0.3wt% Sc alloy aged at 350°C for 120h; (a) weak-beam dark-field image, and (b) bright field image.⁸³ 40
- Figure 2.29** Equilibrium phase diagram for Al-Sc system.⁸⁵ 41
- Figure 2.30** (a) Grain size of pure aluminum DC ingots vs. Sc addition, and (b) an example of as cast microstructure of Al- 0.7wt%Sc alloy under cooling rate of 100 k/s, N.B. GZ=75 μm.⁷⁸ 41
- Figure 2.31** Effects of 0.18 wt% Zr on grain refining efficiency of Sc content in commercial aluminum alloys.⁸⁴ 42
- Figure 2.32** Isothermal section of the Al-corner of the Al-Sc-Zr phase diagram at 600°C..... 43
- Figure 2.33** Backscattered electron image of an Al₃(Sc,Zr) particle..... 43
- Figure 2.34** Isothermal section at 500°C of (a) Al-Sc-Si phase diagram, and (b) Al-Sc-Cu phase diagram.⁷⁵ 44
- Figure 2.35** Different hot tearing features:(a) External hot tear; and (b) SEM image of hot tear surface..... 45

Figure 2.36	Schematic illustration of possible hot crack initiators and some crack propagation mechanisms	46
Figure 2.37	The lambda curve showing hot-tearing susceptibility vs. copper content (X _{cr} is defined as the ratio of the reduction in cross-sectional area resulting from cracking as a proportion of the original cross-sectional area). ¹⁰³	48
Figure 2.38	Ternary diagram of hot cracking for Al-Cu-Si alloys. ¹⁰⁵	50
Figure 2.39	Effects of grain size on strain distribution at grain boundary liquid films. ¹⁰⁷	51
Figure 2.40	Effects of grain structure on the behavior of materials during solidification. ¹¹³	52
Figure 2.41	Effects of superheat on: (a) grain size, and (b) surface crack length. ¹⁰⁷	53
Figure 2.42	Displacement vs. time curves for the 206 alloy at three pouring temperatures. ¹¹⁶	54
Figure 2.43	Load vs. time curves for the 206 alloy at mold temperatures of 200 and 380°C. ¹¹⁶	55
Figure 2.44	Displacement vs. time curves for the 206 alloy at mold temperatures of 200°C and 380°C. ¹¹⁶	55
Figure 2.45	Two bars joined by flanges. ⁹³	57
Figure 2.46	Time-contraction characteristics of bars of different sizes, not joined together. ⁹³	57
Figure 2.47	Contraction of three different steel shapes cast in green sand. ⁹²	58
Figure 2.48	Bar with flanges. ⁹³	59
Figure 2.49 Illustration of basic concepts of Strain Theory ¹²¹	61
Figure 2.50	Brittleness range based on shrinkage-brittleness theory for hot tearing. ¹²⁴	62
Figure 2.51	Tensile strength of Al-Si alloys at temperatures in the vicinity of solidus ¹²⁸	63
Figure 2.52	Equilibrium distribution of liquid at grain boundaries in semi-solid metals. ¹⁰⁷	64
Figure 2.53	Number of hot tearing test molds (a) ring mold used for hot tearing assessment, ¹²³ (b) cold finger mold used for testing hot cracking susceptibility, ¹¹² (c) backbone mold for assessment of hot tearing, ¹²³ (d) Combination of several backbone molds for evaluation of hot tearing susceptibility with variation of <i>a</i> cast length, and <i>b</i> diameter ¹²³ and (e) CRC mold.....	66
Figure 3.1	The thermal analysis set-up.....	71
Figure 3.2	Schematic sketch of the positions of the inserted thermocouples.	72

Figure 3.3	(a) ASTM B-108 type permanent mold; and (b) corresponding casting. Each casting provided two test bars for tensile testing.	74
Figure 3.4	CRC hot-tearing test mold and casting.	76
Figure 3.5	The dimensions of the CRC hot-tearing test mold.	77
Figure 3.6	Categorization of crack severity level.	78
Figure 3.7	The dimensions (in mm) of a standard ASTM-B108 tensile test bar.	80
Figure 3.8	(a) Clemex image analyzer system, and (b) Electron probe microanalyzer-JEOL JXA-8900L.	81
Figure 3.9	Locations of metallography samples sectioned from (a) graphite mold castings, (b) tensile-tested bars, and (c) CRC mold castings. The shaded or circled areas represent the surfaces which were examined.	82
Figure 4.1	Cooling curve and first derivative of Al-2wt%Cu base alloy.	88
Figure 4.2	Optical microstructure of Al-2wt%Cu base alloy.	88
Figure 4.3	Backscattered Image of (a) eutectic- θ phase (Al_2Cu) in combination with Q-phase ($\text{Al}_3\text{Mg}_8\text{Cu}_2\text{Si}$), and (b) α -Fe phase ($\text{Al}_{15}(\text{CuFeMn})_3\text{Si}_2$).	90
Figure 4.4	Line scan results showing the distribution of various elements across α -Al grains in the matrix of the GSZA-alloy (0.2wt%Ti-0.5wt%Sc-0.5wt%Zr-0.5wt%Ag) samples: (a) as cast condition; (b) solutionized condition.	91
Figure 4.5	(a) Backscattered image taken from the SZ alloy (0.5wt%Sc-0.5wt%Zr) sample, showing a particle of the star-like intermetallic $\text{Al}_3(\text{Sc}_{1-x}\text{Zr}_x)$ phase; (b) corresponding WDS analysis of (a). Pink and blue line scans across the particle in (a) show the concentrations of Zr and Sc across the particle.	94
Figure 4.6	(a) Backscattered image showing a $\text{Al}_3(\text{Sc}_{1-x-y}\text{Zr}_x\text{Ti}_y)$ phase particle in the GSZ-alloy (0.2wt%Ti-0.5wt%Sc-0.5wt%Zr), and corresponding X-ray images of Sc, Ti and Zr; (b) corresponding WDS analysis of (a).	95
Figure 4.7	Schematic diagram showing the formation and growth sequence of the $\text{Al}_3(\text{Sc}_{1-x}\text{Zr}_x)$ -star-like phase particle.	97
Figure 4.8	(a) Backscattered image showing an $\text{Al}_3(\text{Sc}_{1-x-y}\text{Zr}_x\text{Ti}_y)$ phase particle in the GSZA-alloy (0.2wt%Ti-0.5wt%Zr-0.5wt%Sc-0.5wt%Ag) in the solution heat-treated condition (490°C/8 h), and corresponding X-ray images of Sc, Zr and Ti; (b) corresponding WDS analysis of (a).	98
Figure 4.9	(a) Backscattered image taken from S-alloy (0.5wt%Sc) showing clusters of primary Al_3Sc intermetallic particles; (b) corresponding EDX spectrum; and (c) WDS analysis (c).	100
Figure 4.10	(a) Backscattered image taken from SG-alloy (0.2wt%Ti-0.5wt%Sc) sample, showing the occurrence of the V-phase intermetallic particle together with the Al_2Cu phase, and (b) the corresponding WDS analysis.	101

- Figure 4.11** Backscattered image showing the V-phase in combination with the Q-phase and the corresponding X-ray mapping images of Si, Mg, Sc, and Cu..... 102
- Figure 4.12** (a) Backscattered image taken from the GS-alloy (0.2wt%Ti-0.5wt%Sc) showing the presence of V-phase and $Al_3(Sc,Ti)$ intermetallic phase particles, and (b), (c), (d) corresponding X-ray images of (b) Sc, (c) Si, (d) Ti; (e) WDS analysis of the two phases shown in (a)..... 103
- Figure 4.13** (a) Backscattered image taken of the GSZ-alloy (0.2wt%Ti-0.5wt%Sc-0.5wt%Zr) showing the presence of different $Al_3(Zr_{1-x-y}Sc_xTi_y)$ and Al_3Zr intermetallic particles with varying compositions and (b,c,d) corresponding X-ray images of (b) Zr, (c) Sc, (d) Ti; (e) WDS analysis of (a)..... 105
- Figure 4.14** (a) Backscattered image taken of the GMZ-alloy (0.2wt%Ti-0.02wt%Sr-0.5wt%Zr) showing a Al_3Zr phase particle; (b, c) EDX spectra taken from the central (b) and outer (c) regions of the particle; and (d) corresponding WDS analysis of the two regions of the particle. 107
- Figure 4.15** (a) Backscattered image taken of the Z-alloy (0.5wt%Zr), showing the presence of the $AlZrSi$ ternary phase particles; (b) corresponding EDX spectrum; (c) and (d) corresponding X-ray images of Zr and Si, respectively; and (e) WDS analysis. 108
- Figure 4.16** (a) Backscattered image taken of the GZ-alloy (0.2wt%Ti-0.5wt%Zr), showing an $AlZrTiSi$ quaternary intermetallic phase particle; (b) corresponding EDX spectrum; (c), (d), and (e),..... 109
- Figure 4.17** Average grain sizes displayed by the alloys investigated. 111
- Figure 4.18** Morphology of the primary α -Al phase; (a) in the base Al-2wt%Cu alloy, (b) in the Z-alloy (0.5wt%Zr), (c) in the GZ-alloy (0.2wt%Ti-0.5wt%Zr), (d) in the SZ-alloy (0.5wt%Sc-0.5wt%Zr), (e) GSZ-alloy(0.2wt%Ti-0.5wt%Sc), (f) GMZS-alloy (0.2wt%Ti -0.5wt%Sc-0.5wt%Zr-0.02wt%Sr), (g) GSZA-alloy (0.2wt%Ti-0.5wt%Sc-0.5wt%Zr-0.5wt%Ag), and S-alloy (0.5wt%Sc). 113
- Figure 4.19** Volume fraction of intermetallics (%) observed in the investigated alloys. 114
- Figure 4.20** Relationship of Grain Size vs. Vol. Fraction of Intermetallics in Al-Cu base alloy containing various additives. 114
- Figure 4.21** Microstructure of a number of alloys investigated;(a) base alloy, (b) Z-alloy (0.5Zr), (c) SZ-alloy (0.5wt%Sc-0.5wt%Zr), (d) GSZ-alloy (0.2wtTi-0.5wtSc-0.5wt%Zr), (e) GSZA-alloy (0.2wt%Ti-0.5wt%Sc-0.5wt%Zr-0.5wt%Ag), and (f) S-alloy (0.5wt%Sc)..... 118
- Figure 4.22** Average surface area of Al_2Cu particles vs. grain size in several of the alloys investigated..... 120

Figure 4.23	Average surface area of $Al_{15}(Mn,Fe,Cu)_3Si_2$ particles vs. grain size in several alloys investigated.....	120
Figure 4.24	Backscattered images of microstructure of number of Zr-alloys: a) Z-alloy (0.5wt%Zr), b) GZ-alloy (0.2wt%Ti-0.5wt%Zr), and c) GMZ-alloy (0.2wt%Ti-0.02wt%Sr-0.5wt%Zr).....	122
Figure 4.25	Backscattered images of the microstructure of a number of Sc-Zr alloys: a) SZ-alloy (0.5wt%Sc-0.5wt%Zr), (b) GSZ-alloy (0.2wt%Ti-0.5wt%Sc-0.5wt%Zr), and c) GMSZ-alloy (0.2wt%Ti-0.02wt%Sr-0.5wt%Sc-0.5wt%Zr).....	123
Figure 5.1	Average grain size of the alloys investigated.....	130
Figure 5.2	Morphology of primary α -Al observed in Al-2wt%Cu alloy containing various additions: (a) base alloy, (b) B2Si-alloy, (c) M-alloy, (d) G-alloy, (e) GM-alloy, (f) MZ-alloy, (g) GM7Z-alloy, (h) AGM7Z, (i) G1Z-alloy, (j) G3Z-alloy, (k) G5Z-alloy, (l) G7Z-alloy, (m) 7Z-alloy, (n) GS-alloy, (o) GS1Z-alloy, and (p) AGS1Z-alloy.	135
Figure 5.3	Surface fraction of Al_2Cu (%) in various alloys investigated in the as-cast and as-solutionized conditions.	137
Figure 5.4	Surface fraction of porosity (%) in a number of alloys investigated.....	139
Figure 5.5	Porosity (%) and surface fraction of Al_2Cu versus grain size in Al-2wt%Cu alloys containing various additions of transition elements	141
Figure 5.6	Morphology of α -Fe intermetallic particles in as-solutionized condition for (a) the base alloy, (b) the M-alloy, and (c) the GM-alloy.....	143
Figure 5.7	(a) Backscattered image of β -iron particles; (b) corresponding X-ray image of Sr; (c) backscattered image of α -Fe; and (d) corresponding X-ray image of Sr. ¹⁸¹	144
Figure 5.8	Ultimate tensile strength for as-cast and as-solutionized conditions.....	145
Figure 5.9	Yield strength for as-cast and as-solutionized conditions.....	147
Figure 5.10	Elongation (%) for as-cast and as-solutionized conditions	148
Figure 5.11	Effects of aging time on the ultimate tensile strength of the Zr-Ti alloy group at 180°C.....	150
Figure 5.12	Effects of aging time on the yield strength of the Zr-Ti alloy group at 180°C	151
Figure 5.13	Effects of aging time on the elongation (%) of the Zr-Ti alloy group at 180°C.....	152
Figure 5.14	Effects of aging time on the ultimate tensile strength of the Zr-Ti alloy group at 220°C.....	154
Figure 5.15	Effects of aging time on the yield strength of the Zr-Ti alloy group at 220°C	155

Figure 5.16 Effects of aging time on the elongation (%) of the Zr-Ti alloy group at 220°C.....	156
Figure 5.17 Effects of aging time on the ultimate tensile strength of the Zr-Sr alloy group at 180°C.....	158
Figure 5.18 Effects of aging time on the yield strength of the Zr-Sr alloy group at 180°C.....	159
Figure 5.19 Effects of aging time on the elongation (%) of the Zr-Sr alloy group at 180°C.....	160
Figure 5.20 Effects of aging time on the ultimate tensile strength of the Zr-Sr alloy group at 220°C.....	162
Figure 5.21 Effects of aging time on the yield strength of the Zr-Sr alloy group at 220°C.....	163
Figure 5.22 Effects of aging time on the elongation (%) of the Zr-Sr alloy group at 220°C.....	164
Figure 5.23 Effects of aging time on the ultimate tensile strength of the Zr-Sc alloy group at 180°C.....	166
Figure 5.24 Effects of aging time on the yield strength of the Zr-Sc alloy group at 180°C.....	167
Figure 5.25 Effects of aging time on the elongation (%) of the Zr-Sc alloy group at 180°C.....	168
Figure 5.26 Effects of aging time on the ultimate tensile strength of the Zr-Sc alloy group at 220°C.....	169
Figure 5.27 Effects of aging time on the yield strength of the Zr-Sc alloy group at 220°C.....	170
Figure 5.28 Effects of aging time on the elongation (%) of the Zr-Sc alloy group at 220°C.....	170
Figure 5.29 Effects of aging time on the ultimate tensile strength of the Si alloy group at 180°C.....	172
Figure 5.30 Effects of aging time on the yield strength of the Si alloy group at 180°C.....	172
Figure 5.31 Effects of aging time on the elongation (%) of the Si alloy group at 180°C.....	173
Figure 5.32 Effects of aging time on the ultimate tensile strength of the Si alloy group at 220°C.....	175
Figure 5.33 Effects of aging time on the yield strength of the Si alloy group at 220°C.....	175

Figure 5.34	Effects of aging time on the elongation (%) of the Si alloy group at 220°C.....	176
Figure 5.35	Optical microstructure near tensile fracture surface in a longitudinal section: (a), (b) base alloy, (c) B2Si-alloy, (d) M7Z-alloy, (e) G7Z-alloy, and (f) GS1Z-alloy.....	179
Figure 6.1	Effects of dwell time on the hot-tearing susceptibility of G3Z-alloy at 0° mold slope angle.	189
Figure 6.2	Effects of dwell time on the hot-tearing susceptibility of G3Z-alloy at 17° mold slope angle.	189
Figure 6.3	HTS vs. composition of Al-2wt%Cu base alloy at different mold temperatures.	191
Figure 6.4	HTS vs. composition of 206 alloy at different mold temperatures.....	192
Figure 6.5	The linear relationship between HTS values and mold temperature for Al-2wt%Cu base alloys.....	194
Figure 6.6	The linear relationship between HTS values and mold temperature for 206 alloys.	194
Figure 6.7	Microstructure of base alloy at two mold temperatures; (a) 250°C, and (b) 350°C.....	198
Figure 6.8	Measurement of porosity (%) in Al-2wt%Cu base alloys	199
Figure 6.9	Average grain size of alloys investigated using hot-tearing test at 250°C mold temperature.	200
Figure 6.10	Grain structure obtained for the different Al-2wt%Cu alloy compositions: (a) base alloy, (b) M-alloy, (c) G-alloy, (d) G1Z-alloy, (e) G3Z-alloy, and (f) B1Si-alloy.....	202
Figure 6.11	HTS vs. average grain size of the alloys investigated at 250°C mold temperature.....	203
Figure 6.12	Average grain size vs. porosity (%) of alloys investigated at 250°C mold temperature.....	205
Figure 6.13	Cooling curves and first derivatives of Al-2wt%Cu base alloy (a), and G3Z-alloy (b) obtained at the center and the boundary of 200°C preheated mold	206
Figure 6.14	Cooling curves and first derivatives of Al-2wt%Cu base alloy (a), and G3Z-alloy (b) obtained at the center and the boundary of 600°C preheated mold	207
Figure 6.15	(a) Crack-path healed with eutectic Si, (b) higher magnification of region, blue-framed rectangle	210
Figure 6.16	Effect of Si content on the cooling curve of the Al-2wt%Cu base alloy. .	212

Figure 6.17	The liquidus temperature against Si content	212
Figure 6.18	Sr-oxide particles detected in M-alloy: (a) backscattered image of Sr-oxide particle trapped between dendrites; (b) backscattered image of Sr-oxide particle on the crack surface, (c) corresponding oxygen X-ray image for (b); and (d) corresponding Sr X-ray image for (b).	214
Figure 6.19	(a) Backscattered image taken from 206-M alloy showing the presence of Sr-oxide particle on crack surface, and (b) and (c) corresponding X-ray images of Oxygen and Sr, respectively.....	216
Figure 6.20	Effects of Sr addition (200 ppm) on the cooling curve of the Al-2wt%Cu base alloy.....	216
Figure 6.21	Optical micrographs demonstrating the role of α -Fe particles in preventing the propagation of hot-tear cracks in: (a) base alloy, (b) M-alloy, (c) G-alloy, (d) G1Z-alloy, (e) G3Z-alloy, and (f) B1Si-alloy.	219
Figure 6.22	Schematic sketch showing how the α -Fe particles obstruct crack propagation in the alloy.....	220
Figure 6.23	Flow chart of the suggested factors and corresponding parameters controlling hot-tearing.....	222

LIST OF TABLES

Table 2.1	Common Practice for the Heat treatment of Alloys 201.0 and 206.0.....	13
Table 2.2	Tensile properties and heat treatment of alloy 204.0 (4.6Cu0.25Mg0.17Fe0.17Ti). ¹⁹	28
Table 2.3	Effects of Cu content on the tensile properties of Al-0.54wt%Si-0.98wt%Mg-0.33wt%Fe. ⁶¹	31
Table 3.1	Chemical Composition of As-Received Al-2wt%Cu Base Alloy Ingots ...	69
Table 3.2	Master Alloys Used for Alloying Additions.	69
Table 3.3	Chemical Composition of the Alloys Prepared for Phase Identification Purposes.	71
Table 3.4	Chemical Composition of the Alloy Group Prepared for Tensile Properties Investigation	74
Table 3.5	Chemical Composition of the Alloys Prepared for Hot Tearing Tests.....	75
Table 3.6	Numerical Values C_i Representing Crack Severity	78
Table 3.7	Numerical Values L_i Representing Bars of Different Lengths	78
Table 3.8	Mounting and Polishing Procedures	83
Table 4.1	Dimension Characteristics of Al_2Cu Particles.....	117
Table 4.2	Dimension Characteristics of $Al_{15}(Mn,Fe,Cu)_3Si_2$ Particles, α -Fe.	117
Table 6.1	The linear representative Equation between HTS Values and MT in Al-2wt%Cu Base Alloys	195
Table 6.2	The linear representative Equation between HTS Values and MT in 206 Alloys	195

CHAPTER 1
INTRODUCTION

CHAPTER 1

INTRODUCTION

1.1 Definition of the Problem

Aluminum-copper (Al-Cu) casting alloys are characterized by their superior strength and excellent ductility thus making them suitable for automotive, marine, and aerospace applications. These alloys require a high degree of purity for casting which makes them difficult to recycle. The designated purity levels make it necessary to take specific casting precautions which, in turn, add to the production costs. The copper content of Al-Cu casting alloys is usually 4wt% to 8wt% which equates them with expensive alloys. As a result of the elevated density of Cu, 8.92 g/cm^3 , the high Cu content of Al-Cu alloys increases the weight of the cast parts manufactured from these same alloys, thereby leading to increased fuel consumption and higher levels of gas emissions. Based on these facts, the necessity for producing new low-cost, lightweight Al-Cu casting alloys which possess acceptable levels of tensile properties and are easy to recycle becomes an important priority for the end-user industries. One of these new alloys is Al-2wt%Cu alloy, being

currently developed by General Motors for use in the manufacture of engine blocks and cylinder heads.

The new Al-2wt%Cu base alloy contains 2wt% Cu, 1wt% Si, 0.4wt% Mg, 0.42wt% Fe, 0.7wt% Mn, and 0.02wt %Ti. This chemical composition causes the Al-2wt%Cu alloy microstructure to reveal some similarity to that of 319-type alloys, however, with a minor difference. This difference arises as a result of the fact that the 319-type alloys contain 5.5-6.5wt% Si and ~ 4wt% Cu, while the new alloy contains only 1wt% Si and 2wt% Cu. The difference in chemical composition also makes the new Al-2wt%Cu alloy lighter and cheaper to produce than 319-type alloys. Accordingly, this new alloy can also replace 319 alloys in similar applications since it provides higher yield and tensile strengths than does the 319 alloy.

The new Al-2wt%Cu alloy suffers from a major drawback in that it exhibits a high susceptibility to hot-tearing. The main reasons for this are (i) the long freezing range of the alloy, and (ii) the low amount of eutectic formed which may be attributed to the low Cu and Si contents of the alloy. This susceptibility to hot-tearing decreases castability and lowers the casting quality of the alloy, leading to a deterioration in the tensile properties.

Transition elements are usually added to aluminum wrought alloys and a number of aluminum casting alloys in order to alter their microstructure and thus improve their mechanical properties.^{1,2} The transition elements Zr and Sc form trialuminide particles (Al_3Zr , Al_3Sc) which occur either during solidification as primary particles or else during solution heat treatment as tiny coherent and semi-coherent precipitates.^{3,4} The primary trialuminides Al_3Zr and Al_3Sc act as potent heterogeneous nucleation sites for the α -Al

phase during solidification, thereby producing a refined α -Al grain structure. The coherent and semi-coherent Al_3Zr and Al_3Sc precipitates or dispersoids tend to harden the alloy and improve the tensile properties. These two elements Zr and Sc were therefore selected in the current study as the main additives for the new Al-2wt%Cu base alloy, and added individually, or in combination with other alloying elements with the aim of improving the hot-tearing resistance, microstructure, and tensile properties.

An extensive study was carried out to investigate the effects of Zr and Sc additions individually or in combination with other additives, on the microstructure, tensile properties, and hot-tearing susceptibility of the Al-2wt%Cu base alloy. Thirty one different alloy compositions were prepared using the base alloy to cover all aspects of these investigations, as listed and elaborated upon in the following section.

1.2 Objectives

This study will investigate the effects of the transition elements Zr and Sc on the microstructure, tensile properties, and hot-tearing susceptibility of a new Al-2wt%Cu base alloy. The latter feature is considered to be the main drawback of this alloy. This study will be accomplished by fulfilling the following objectives.

1. Undertaking an extensive investigation using thermal analysis and metallographic techniques such as optical microscopy and electron probe microanalysis (including electron dispersive x-ray and wavelength dispersive spectroscopic analyses) to (a) identify and quantify the phases formed by the interactions between the different alloying elements Zr, Sc, Ti-B, Sr, and Ag in samples obtained under slow cooling

rate conditions (0.3°C/s), and (b) to study the effects of these intermetallic phases on the grain structure. Both as-cast and heat-treated alloy samples will be examined.

2. Determining the optimum age-hardening heat treatment required to maximize the tensile properties (UTS, YS, % El) through the application of various aging heat treatments to the alloys studied.
3. Improving the hot-tearing susceptibility of the Al-2wt%Cu base alloy by understanding how it is affected in the presence of the additions of Zr, Ti-B, Sr, and Si, and by the mold variables.

In order to implement the abovementioned objectives, forty melts were prepared from the thirty-one Al-2wt%Cu based alloy compositions used in this study, as well as seven alloy compositions using 206 alloy type as the base alloy. These 38 alloys were divided into three categories corresponding to the three objectives. Accordingly, Category I comprised ten alloy melts including the base Al-2wt%Cu alloy and other alloy compositions containing the various additives. These melts were poured into a preheated graphite mold to obtain castings at very slow cooling rates (~0.3°C/s). A thermocouple inserted through the bottom of the mold also served to provide cooling curves for certain melts/castings. Samples sectioned from the central part of these castings near the thermocouple tip were used to examine the microstructures and identify the intermetallic phases obtained in each case.

Category II involved seventeen alloy melts corresponding to the base Al-2wt%Cu alloy and several other compositions. These melts were poured into a preheated ASTM B-

108 permanent mold to prepare test bars for tensile testing, in keeping with objective 2. The test bars were subjected to various aging treatments before the testing was carried out.

Finally, Category III involved thirteen alloy compositions, corresponding to the base Al-2wt%Cu and six other compositions from Category II, as well as seven compositions based on 206 Al-4wt%Cu alloy. These alloy melts were poured into a constrained rod casting (CRC) mold for conducting hot tearing tests, in keeping with objective 3. The Zr, Ti, Si and Sr additions for both sets of alloys (Al-2wt%Cu and 206 based compositions) kept the same for comparing the hot-tearing susceptibility of the new Al-2wt%Cu alloy with an established alloy such as 206 alloy.

CHAPTER 2
THEORETICAL BACKGROUND

CHAPTER 2

THEORETICAL BACKGROUND

2.1 General Aspect of Al-Cu Alloys

2.1.1 Microstructure

The microstructure of Al-Cu alloys is controlled by chemical composition and cooling rate. Bäckerud *et al.*⁵ found that Al-Cu alloys start to solidify through the development of a dendritic network followed by a eutectic reaction in the interdendritic regions by means of which the eutectic Al_2Cu is formed in combination with the remaining aluminum. Accordingly, the microstructure of Al-Cu alloys consists mainly of α -Al and the primary Al_2Cu phase, as displayed in Figure 2.1. A number of alloying elements such as Mg, Si, Fe, and Mn may be added to Al-Cu alloys in order to enhance their properties so as to satisfy the requirements of rapidly developing commercial applications. The addition of these elements is associated with the formation of much more complex intermetallic compounds part of which are insoluble. The insoluble intermetallics such as π ($\text{Al}_8\text{Mg}_3\text{FeSi}_6$), β ($\text{Al}_5\text{Fe}_2\text{Si}$), and α -iron ($\text{Al}_{15}(\text{Mn,Fe,Cu})_3\text{Si}_2$) are introduced by iron addition. Iron-intermetallics are extremely brittle as well as being harmful to mechanical properties. Molinar and Cisneros^{7,8} reported that when plastic deformation is applied

stresses are imposed by the matrix on such primary intermetallic particles as β , α -iron and Al_2Cu . As these stresses reach the critical level of particle strength, the particle undergoes cracking, upon which an intraparticle microcrack, or void, is formed and continues to grow, as may be seen in Figure 2.2. Also, a number of investigators,^{9, 10, 11} mentioned that the presence of Fe-intermetallic compounds such as β -iron (Al_5FeSi) prevents the liquid metal-feeding by blocking the interdendritic liquid-metal channels resulting in the formation of porosity.

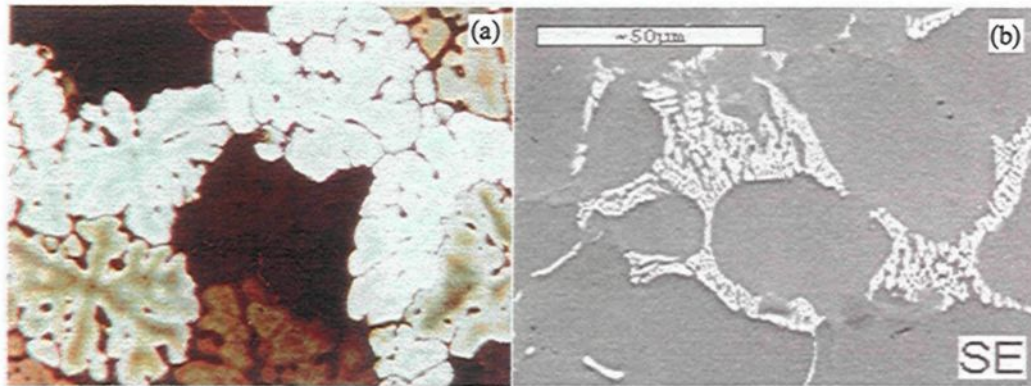


Figure 2.1 The microstructure of Al-4Cu alloy; (a) The optical dendritic morphology of α -Al at cooling rate of $0.3^\circ\text{C}/\text{s}^5$, and (b) Backscattered image of eutectic- Al_2Cu phase.⁶

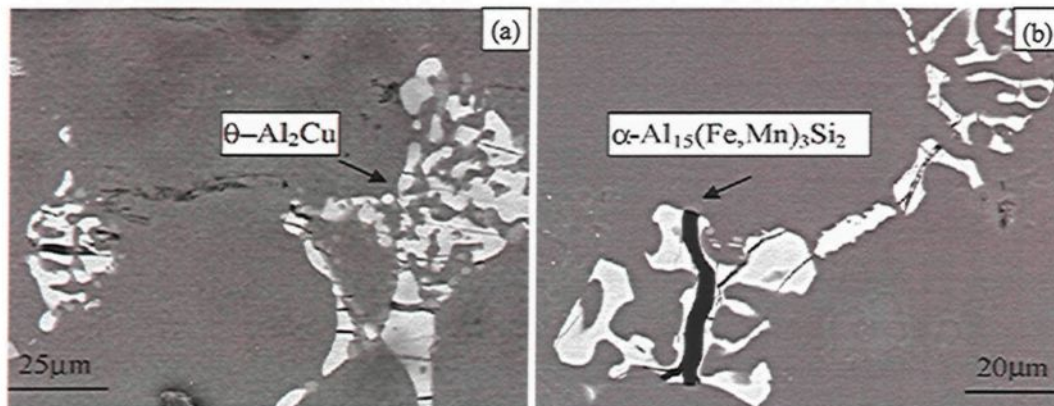


Figure 2.2 SEM micrographs of a region adjacent to the fracture surface of tensile specimens showing cracking of (a) θ - Al_2Cu intermetallics and (b) α - $(\text{Al}_{15}(\text{Mn},\text{Fe})_3\text{Si}_2)$ intermetallics. (A319 alloy).⁸

Porosity not only provides stress concentration sites but also easy paths for crack propagation and hence the high density of porosity will cause a deterioration of the mechanical properties. Hwang *et al.*¹² who has studied the effects of Mn addition on Al-Si-Cu casting alloys concluded that the Mn is added mainly to enhance the mechanical properties by transforming the elongated β -iron into compacted α -iron which is less harmful in degree. The addition of Mg in a proportion greater than 0.2% with Si leads to the formation of Mg_2Si and the quaternary phase, or Q-phase, ($Al_5Mg_8Cu_2Si_6$), which is formed in the last reaction of solidification in combination with the Al_2Cu phase, as appears in Figure 2.3.⁵ If the level of silicon addition exceeds its solubility, eutectic silicon particles will be formed, as shown in Figure 2.4. In their study, Hwang *et al.* also concluded that primary silicon particles may be harmful on to mechanical properties since they act as crack initiators when under load application.¹²

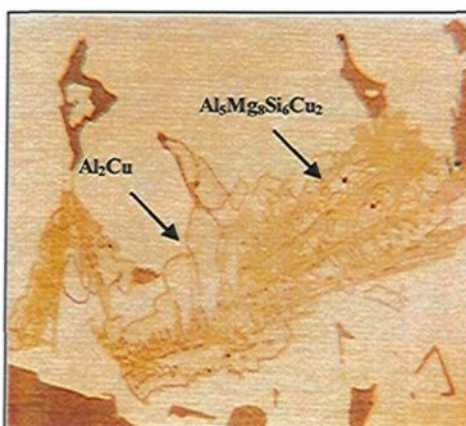


Figure 2.3 Microstructure of B319.1 alloy at cooling rate of 0.3°C/s , showing the $Al_5Mg_8Si_6Cu_2$ phase grown out from Al_2Cu particles.⁵

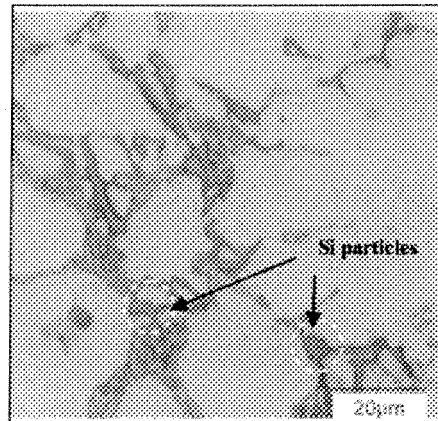


Figure 2.4 Microstructure of as-cast Al-4.5wt%Cu-2wt%Si alloy.⁶

The cooling rate is another parameter which affects the microstructure of Al-Cu alloys. The main features of the microstructure which are affected by cooling rate are the dendrite arm spacing, size and distribution of the intermetallics, porosity, grain size, and morphology. During their investigations, Several authors,^{13,14,15} drew attention to the fact that dendrite arm spacing (DAS) decreases as the cooling rate increases, as may be seen in Figure 2.5. In industrial practice, the effects of the cooling rate on DAS may be determined by applying the equation $DAS = AV_c^{-n}$ where A is an alloy-dependent parameter, n is the parameter equal to 0.33 for aluminum alloys, and V_c is the cooling rate.¹⁵ The reduction in the DAS leads to refining, and to the homogeneous distribution of intermetallic compounds.^{12,14} Both the refining and the homogeneous distribution of intermetallics reduces diffusion distances, thereby making the dissolution of the latter easier during solution heat treatment, reducing composition gradients and producing a higher degree of supersaturated solid solution and ,consequently, a greater age-hardening response.¹⁶ Argo and Gruzleski¹⁷, and Emadi and Gruzleski¹⁸ reported that shrinkage porosity is reduced by diminishing interdendritic feeding distances, whereby this type of porosity will become less

as the DAS gets smaller. Accordingly, the small dendrite arm spacing will improve the mechanical properties.

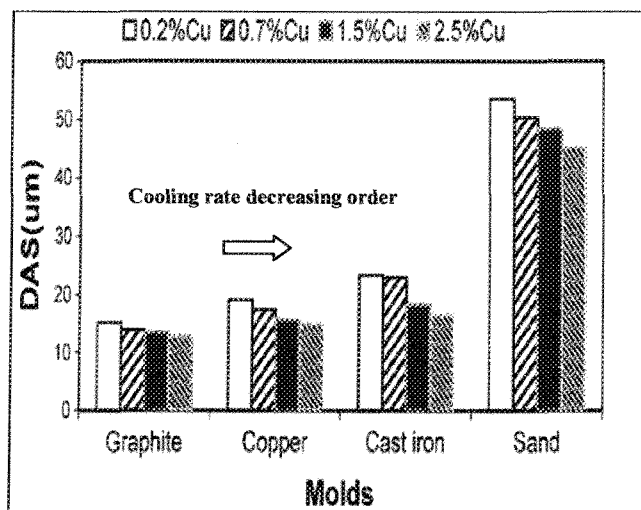


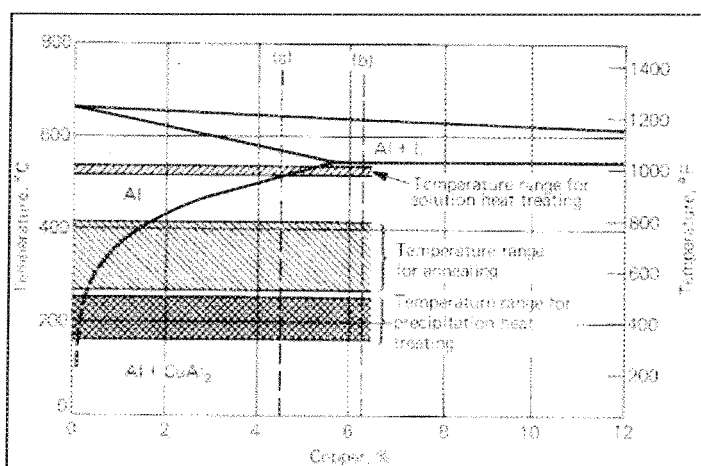
Figure 2.5 Variation of DAS of 319 alloys containing different levels of Cu and poured in different molds which provide different cooling rates.¹³

2.1.2 Heat Treatment

Aluminum-copper cast alloys are considered to be heat-treatable alloys. Figure 2.6 displays the temperature ranges of the heat treatment applied to Al-Cu alloys.¹⁹ For example, the solution heat treatment range of Al-4.5Cu alloy is 515 to 550°C in which the Cu completely dissolves thereby producing a complete solid solution. This solid solution will become supersaturated as the temperature decreases to below 515°C. In order to produce the age-hardening of an Al-4.5Cu alloy, it should be maintained within a temperature range of 150°C to 220°C for a pre-determined aging period. From Table 2.1, it may be observed that such Al-Cu alloys as 201.0 and 206.0 can be heat-treated under three different kinds of temper regimens, namely, T4, T6, T7.²⁰

Table 2.1 Common Practice for the Heat treatment of Alloys 201.0 and 206.0.¹⁹

<i>Temper Designation</i>	<i>Solution Treatment</i>	<i>Aging Treatment</i>
T4	(a) 2h at 510-515°C followed by (b) 14-20 h at 525-530°C, and (c) a water quench (c)	None
T6	Same as T4	Room temperature for 12-24 h, then 150-155°C for 20 h
T7	Same as T4	Room temperature for 12-24 h, then 185-190°C for 5 h

**Figure 2.6** The temperature ranges of heat treatment in Al-Cu system alloys.²⁰

Generally speaking, in order to age harden Al-Cu alloys, it is necessary to apply heat treatment involving three stages, as follows: (i) solution heat treatment, then (ii) quenching, and finally (iii) aging.

2.1.2.1 Solution Heat Treatment

The main function of solution heat treatment is to maximize the solubility of elements in the matrix such as Cu and Mg, to dissolve and alter the intermetallics which are formed during solidification, and to increase the homogeneity of the microstructure. Solution heat treatment is controlled by temperature and time. The temperature of solution

treatment is a critical parameter in Cu-containing alloys due to the occurrence of incipient melting. Samuel *et al.*^{21,22} investigated the dissolution and melting of Al_2Cu in Al-Si alloys and found that the amount of dissolved Al_2Cu particles in 319-type alloys, is enhanced as the solution temperature and time span are increased, as shown in Figure 2.7. Upon increasing the amount of dissolved Al_2Cu , an enrichment of the supersaturated solid solution structure in Cu may be observed; this leads to an enhancement of the driving force of Al_2Cu precipitation during aging treatment, thereby multiplying the tensile properties. Figure 2.8 represents this increment in strength and elongation which may be attributed to the increase in the amount of dissolved Cu.

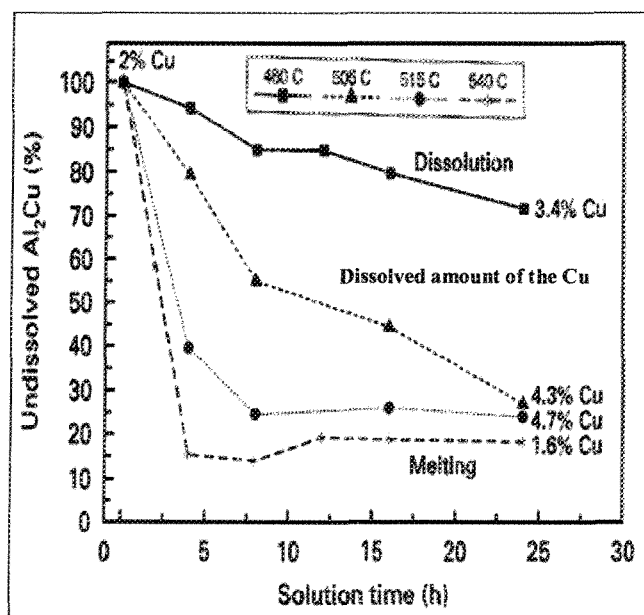


Figure 2.7 Effect of solution heat treatment on the amount of dissolved Al_2Cu in 319 alloy.²²

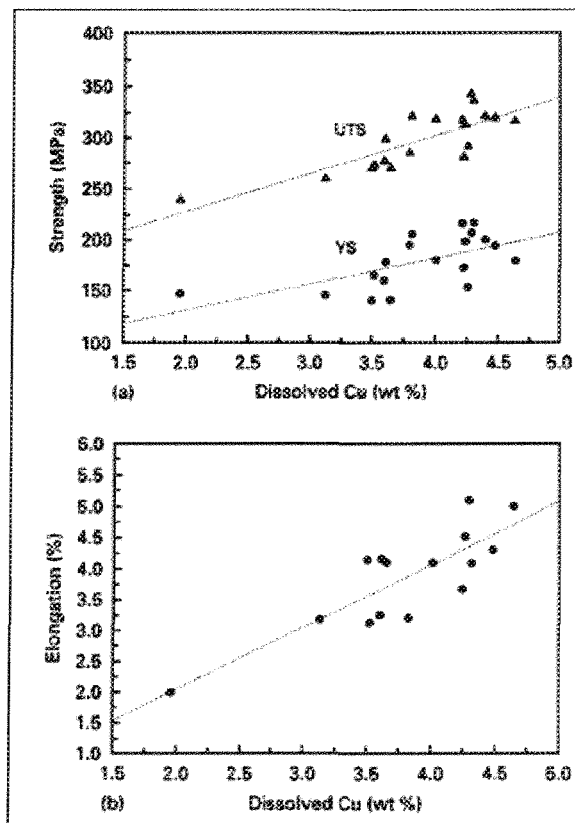


Figure 2.8 Effect of Cu concentration on (a) strength, and (b) elongation.²²

Samuel,²² summarized the topic of incipient melting of $\text{Al}_5\text{Mg}_8\text{Si}_6\text{Cu}_2$ and Al_2Cu intermetallics in 319-type alloys and concluded that, although the high solution temperature enriches the Cu concentration in the supersaturated solid solution structure, there is a critical temperature for Cu-containing aluminum alloys such as 319 alloy which cannot be exceeded due to the occurrence of incipient melting. This critical temperature is determined based on the lowest eutectic-melting point of the intermetallic constitution or, in other words, of the melting point of latest solidified intermetallics. Copper-rich intermetallics, such as Al_2Cu (θ) and $\text{Al}_5\text{Mg}_8\text{Cu}_2\text{Si}_6$ (Q), are the main intermetallics facing the possibility of melting during solution heat treatment because of their low melting points of 507°C and

525°C, respectively.⁵ The incipient melting takes place at and above the corresponding eutectic temperature as a result of the reduction in the Gibbs free energies as postulated by Reiso and *et al.*²³

The detrimental effect of incipient melting on the mechanical properties arises from the void formation which may be attributed to the difference in density between the particles (θ , Q , β), and the matrix, and the insufficient available time for the aluminum atoms to diffuse back into the volume occupied by the particles in order to accumulate this same volume. Figure 2.9 provides an example of incipient melting in the 319 alloy type after solution heat treatment at 540°C for different time periods. It will also be observed that the severity of incipient melting at 540°C increases as the solution time increases.

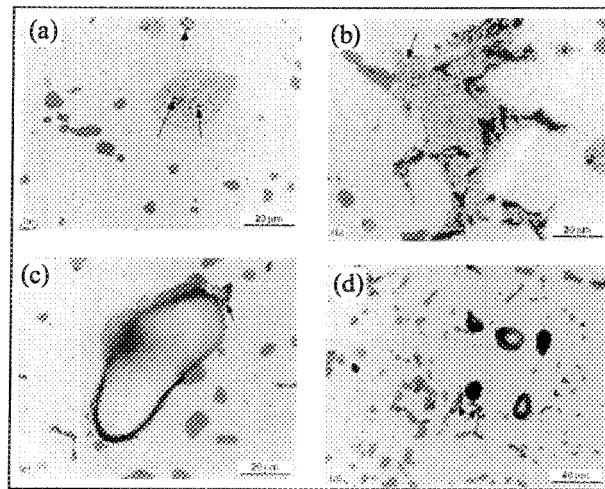


Figure 2.9 Melting process of Al_2Cu Phase in solution heat-treated samples at 540°C: (a) initiation of melting (arrowed) in a sample heated up to 540°C and quenched immediately; (b) after 2h, (c) after 8h, (d) after 24h, showing the presence of cavities and structureless phase particles.²²

A number of investigators^{24, 25, 26} made an attempt to solve the problem of incipient melting during solution heat treatment and they concluded that this type of melting can be avoided by applying three techniques. The first of these involves maintaining the solution

temperature at 495°C or below, while the second technique requires applying a two-stage solution heat treatment. The first of the two solution stages is usually applied in the form of a conventional solution heat treatment such as 495°C/8hr which was applied in order to dissolve the considerable amount of Al₂Cu already present, then the second stage may proceed at higher temperatures so as to maximize the amount of Al₂Cu particles dissolved in the absence of incipient melting. The third technique is implemented through the addition of Be since it has been found that Be raises the eutectic temperature of the Al₂Cu phase, thus the solution temperature can also be raised without any melting of the Al₂Cu.

Silicon particle morphology is a vital aspect of characterizing mechanical properties. Under normal cooling rates, the silicon particles appear as coarse acicular needles which act as crack initiators and reduce the mechanical properties to an observable degree. This type of deleterious silicon morphology is responsive to treatment by means of chemical or thermal modification. When applying thermal modification, the casting is subjected to a high temperature solution heat treatment for the required lengths of time. A number of studies by Apelian *et al.*,²⁷ Tillova and Panuskova,²⁸ and Li *et al.*²⁹ investigated the effects of thermal modification on silicon particles. In these studies, it was found that the silicon particles became modified through a special sequence triggered by the breaking down of silicon particles into small fragments followed by the gradual spheroidization of these fragments. Prolonged solution heat treatment causes the undesired coarsening of silicon particles. The high solution temperature leads to high rates of spheroidization and coarsening. The main driving force for the spheroidization and coarsening of silicon particles is the reduction of surface energy.

Also, solution heat treatment can be used to dissolve and alter the harmful β -iron displaying platelet morphology which leads to a deterioration in the mechanical properties and an increase in the shrinkage porosity. It was concluded from a number of articles written by Crepeau,¹⁰ Samuel and coworkers,^{30,31} and Mbuya and Odera³² that, in order to investigate the effects of solution heat treatment on iron intermetallics, the solution temperatures below 500°C (*i.e.* equilibrium heat treatment) cannot dissolve the β -iron. The dissolution of β -iron is accelerated as the solution temperature increases. The process of the dissolution of β -iron platelets starts with necking, then segmentation, and finally spheroidization.

The cooling rate during casting is an important factor which must be taken into consideration during the solution heat treatment stage. The castings cooled at lower cooling rates during casting need to undergo longer solution heat treatment time spans than the ones required for higher cooling rates to achieve good strength and ductility; this may be observed in Figure 2.10 which represent the solutionizing time vs. the mechanical properties of alloy 204.0 under two different cooling rates.¹⁹

2.1.2.2 Quenching

The purpose of this stage is to maintain a high degree of supersaturated solid solution as well as to provide excess vacancies, all of which may be obtained by applying a high cooling rate. Quenching is a critical heat treatment stage in which the subsequent

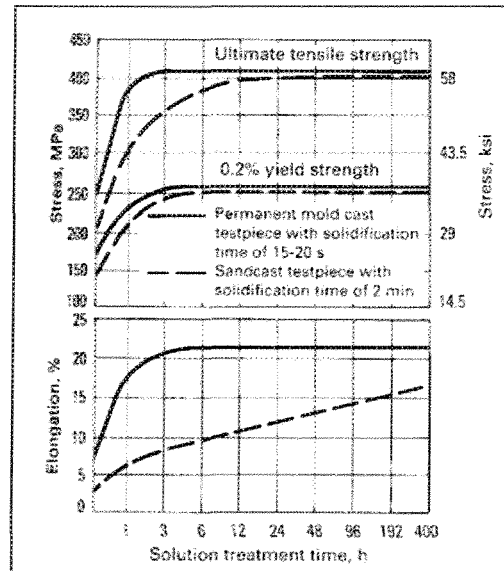


Figure 2.10 Effects of solution treatment time on tensile properties of alloy 204.0.¹⁹

precipitation behaviour is determined. Heterogeneous precipitation occurs intensively at intermediate temperatures under low cooling rates because of relatively high supersaturation and high diffusion rates. Accordingly, the resulting heterogeneous precipitation at low quenching rates will consume the solutes from the matrix and, consequently, will also reduce the subsequent age-hardening response. This outcome leads to lower ultimate tensile and yield strength, as well as lower ductility values and fracture toughness.^{33,34,35} The high quenching rate in Al-Cu alloys or Cu-containing alloys tends to enhance strength values.

It should be noted that the quenching medium is the factor which determines the quenching rate and heat extraction rate. The quenching medium for wrought alloys is usually cold water, whereas the castings and complex shape parts are immersed or quenched in warm water between 65°C and 80°C or in solutions such as polyalkylene

glycol. Molten salt and low-melting eutectic baths have also been used as quenching mediums.^{36,37}

2.1.2.3 Aging

The age-hardening of aluminum-copper alloys has been the subject of intensive scientific investigation for a number of decades now by numerous researchers.^{38,39,40} Throughout the aging process, the supersaturated solid solution is decomposed by heating it to a point below the equilibrium solvus line as well as to below the GP solvus line to produce artificial aging, or otherwise by keeping it at room temperature for an extended length of time in order to produce natural aging. Figure 2.11 illustrates the solvus lines of the different metastable and stable phases of the Al-Cu binary system. At the beginning of the precipitation process, the solute atoms segregate in special crystallographic planes of the matrix forming zones (GPZ_I and GPZ_{II}). These zones are fully coherent with the matrix and measure 1-5 nm. Depending on the aging temperature and aging time, these zones can be developed to subsequent semi-coherent metastable and equilibrium phases.

The fully coherent precipitates usually form and remain more stable at lower aging temperatures than the semi-coherent and non coherent precipitates because of their lower solvus lines, as may be seen in Figure 2.11. The presence of fully coherent zones and the semi-coherent metastable phase strengthens the matrix by inhibiting and/or hindering the dislocation movement.⁴¹

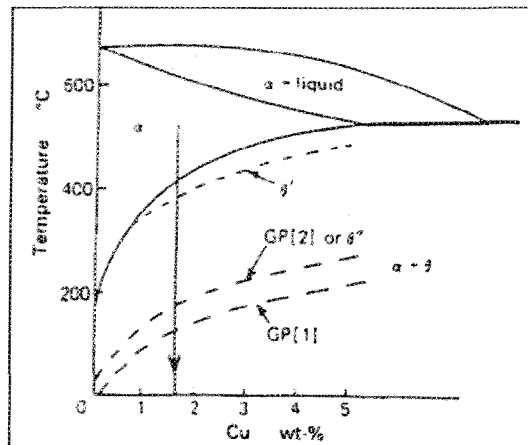


Figure 2.11 Partial equilibrium diagram of Al-Cu alloys representing the solvus lines of the metastable and equilibrium phases.³⁸

During the aging process, it will be observed that the age-hardening curve usually goes through three stages, namely, the under-aged stage displaying moderate strength and good ductility; the peak-aged stage displaying high strength and moderate ductility; and the over-aged stage displaying low strength and high ductility. These stages are related mainly to the precipitation sequences and the development of coherency through these sequences. These same stages will be observed in the age-hardening curve of the AlCuMg system shown in Figure 2.12; the effects of aging temperatures may also be noted. As the aging temperature is increased, the age-hardening stages occur in rapid succession and the maximum alloy strength will decrease; this may be attributed to an increase in precipitation kinetics and the reduction of the precipitation driving force as the aging temperature increases.⁴² Precipitation hardening in Al-Cu alloys will be discussed in the next subsection; two different systems are involved in this process, one is a simple Al-Cu system, while the other is a more complex one, namely, an Al-Cu-Mg-Si system.

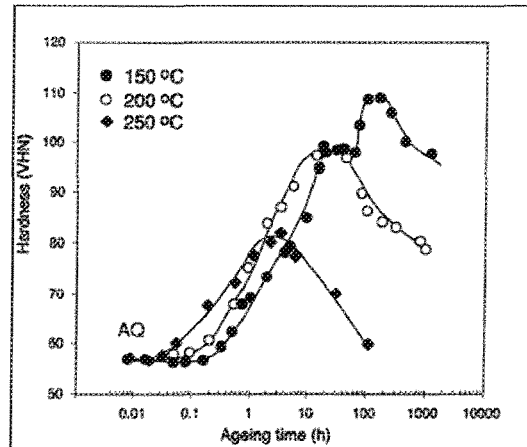
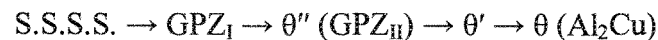


Figure 2.12 Hardness-time curves of the Al-4wt%Cu-0.3wt%Mg alloy aged at 150, 200, 250 °C⁴²

2.1.3 Precipitation in Al-Cu Systems

2.1.3.1 Al-Cu System

The precipitation-hardening behavior of an aluminum-copper system was investigated intensively in numerous studies.^{20,39,43,44,45} In the Al-Cu system precipitation hardening is implemented by means of the formation of metastable phases through the decomposition of a supersaturated Al-Cu solid solution during the aging process in a special sequence as follows:



Here, the precipitation sequence in the Al-Cu system starts with the formation of fully coherent Guinier-Preston zones (GPZ) which are clusters of copper atoms which have acquired a disc-like shape and which lie along the {100} planes. The GPZ phases are ultimately replaced by the coherent θ'' phases as aging progresses. The coherent θ'' phases still lie along the {100} planes of the matrix and are tetragonal in structure. As the aging

process develops further, the final metastable θ' phase is formed. This phase is a semi-coherent one displaying a tetragonal structure and a Al_2Cu composition. The θ' phase precipitates on dislocations and on low-angle grain boundaries at an angle of less than nine degrees.

As the aging time extends in the overaging condition, the θ' phase begins to lose coherency while the dislocation accommodates the interface misfit between the precipitates and the matrix; consequently, the formation of the equilibrium precipitate, θ , will proceed. Figure 2.13 shows the transmission electron micrographs of the metastable phases and the equilibrium Al_2Cu phase in Al-Cu alloys. It is also worth mentioning that the nucleation of any of the metastable phases can occur individually and independently because each phase has a special solvus forming below it. Thus, if the aging temperature is higher than the metastable solvus of the GP zone or the θ'' phase, for example, then these phases will never be formed.^{43,44}

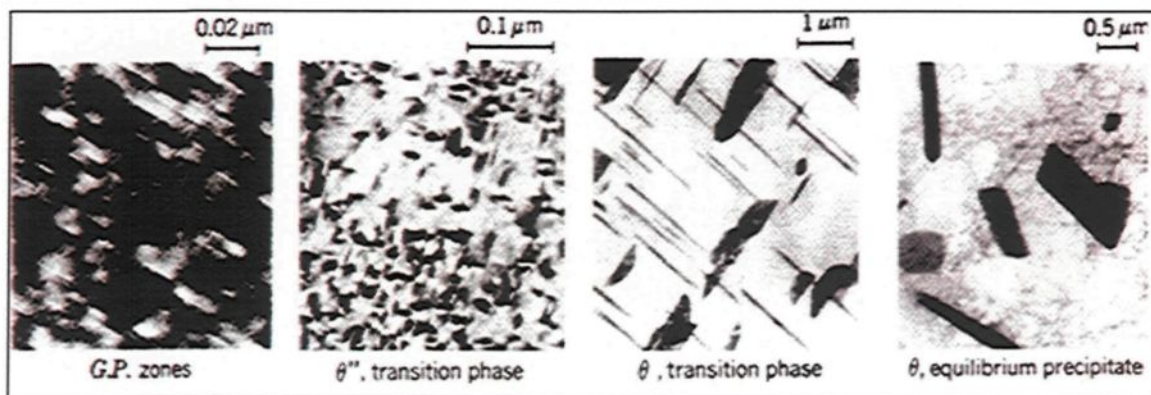


Figure 2.13 Transmission electron micrographs of metastable phases and equilibrium Al_2Cu phase.⁴³

2.1.3.2 Al-Cu-Mg-Si System

In this particular system, the precipitation sequence is more complex and hard to predict using the equilibrium phase diagram. This characteristic may be ascribed to the fact that the phase composition of the Al-Cu-Mg-Si system is relatively complex, and that the decomposition of the supersaturated solid solution is a kinetic and non-equilibrium process. It should also be noted that the gradual change in the composition of the supersaturated solid solution and the co-precipitation of the various precipitates make it fairly difficult to follow the precipitation sequence.

The Al-Cu-Mg-Si system has been investigated carefully by a number of research teams in order to study the relevant precipitation behavior.^{46,47,48,49} In order to understand the precipitation behavior of this system, it should first be approached in the absence of Si; based on this, the major phase to be detected is Al_2Cu (θ) in addition to its metastable phases, namely, GPZ, θ'' , and θ' . As the Mg is added in excess amounts, a new ternary phase of Al_2CuMg is formed through the following precipitation sequence: GPB zones \rightarrow $S'' \rightarrow S' \rightarrow S$ (Al_2CuMg) besides the Al_2Cu phase and its metastable phases.^{42,50,51} If the silicon is added to the Al-Cu-Mg system, the precipitation sequences will be more complicated due to the fact that the Si interacts with Al-Cu-Mg system and forms a new generation of intermetallic compounds. Silicon forms a binary intermetallic compound with Mg (Mg_2Si) through a precipitation sequence starting with the formation of needle-like zones, then coherent needle-like β'' precipitates which transform into semi-coherent rod β' precipitates and finally the formation of the equilibrium Mg_2Si (β).

Moreover, there is another phase containing Si which may form in the Al-Cu-Mg-Si system; this is called the Q phase⁵² or quaternary phase $\text{Al}_4\text{CuMg}_5\text{Si}_4$ which forms upon solidification or aging.^{53,54,55,56} This Q phase can form upon solidification under conditions of $\text{Mg/Si} < 1.73 \text{ wt\%}$, $\text{Mg} > 2 \text{ Cu}$, and $\text{Cu} > 1 \text{ wt\%}$; it can also coexist with Al_2Cu , Mg_2Si , and Si depending on the ratio between Cu, Mg, and Si. The Q phase is known to have either a cubic structure where $a = 1.263 \text{ nm}$, or a hexagonal structure where $a = 1.04 \text{ nm}$ and $c = 0.405 \text{ nm}$; it precipitates in the form of laths in the Al-Cu-Mg-Si system, as may be seen in Figure 2.14.⁵⁷ One of the suggested mechanisms for the formation of the Q phase is that the Cu atoms dissolve in the β'' which then evolves either to β or to Q based on the chemical composition of the alloy and precipitation status.^{48,49} Although it was once believed that the Q phase and its precursors have no hardening ability, Hwzng *et al.*⁵⁵ recently recorded an age-hardening effect for Q' in 319 alloys upon Mg addition. The appearance of the Q' phase precipitates was either faceted or lath-like.

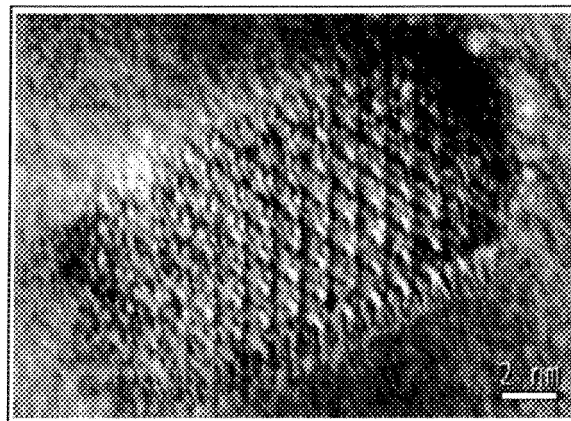


Figure 2.14 HRTEM image of lath-shaped Q precipitate in Al-7wt%Si-0.5wt%Mg-1wt%Cu alloy after 12h of aging at 175°C.⁵⁷

The Mg/Si ratio and the Cu/Mg ratio, as well as the Cu content and the Si content, are all principal controlling factors which determine the main precipitation-hardening phases in Al-Cu-Mg-Si alloys. For example, it was found that the θ' -Al₂Cu phase can precipitate in Al-1.5Cu-0.75Mg during aging at 175°C only when the Si content is greater than 0.3wt%, whereas there was no precipitation of θ' -Al₂Cu to be found in the Al-2Cu-0.9Mg-0.25Si alloy after aging.⁵² Also the addition of Si to Al-Cu-Mg alloys reduces the density of the dislocation loops and hence also decreases the preferential sites of S' metastable phase.⁵⁸ The addition of Cu increases the number and density of the needle-shaped β'' precipitates while also inducing the precipitation of precursors to Q phase artificial aging in Al7Si0.5Mg alloys.⁵⁷

Eskin⁵⁸ analyzed and summarized the age-hardening phases detected in the different studies carried out earlier with regard to the Cu content and Mg/Si ratio, as shown in Figure 2.15. For alloys containing up to 0.25%Cu, reflecting the 6xxx series, the β phase with its metastable modifications is the main hardening phase at a Mg/Si ratio >1, as shown in Figure 2.15 (a). The β'_C and Si phase are observed to be formed for the alloys with a Mg-to-Cu ratio of less than 1.2 and the same Cu content. As Cu concentrations increase to 0.5-0.8%, the β phase in its metastable modification becomes the main precipitation phase in addition to Q', as shown in Figure 2.15 (b). As shown in Figure 2.15 (c), at a Cu content of 0.9-2.5%, the Mg/Si ratio determines the main hardening phases as follows: S' or GPB for a Mg/Si ratio of >3, and θ' or β'' for a Mg/Si ratio located between the values of 0.5 and 2.0. In this regard, it should be remembered that silicon forms its particles at Mg/Si<1.

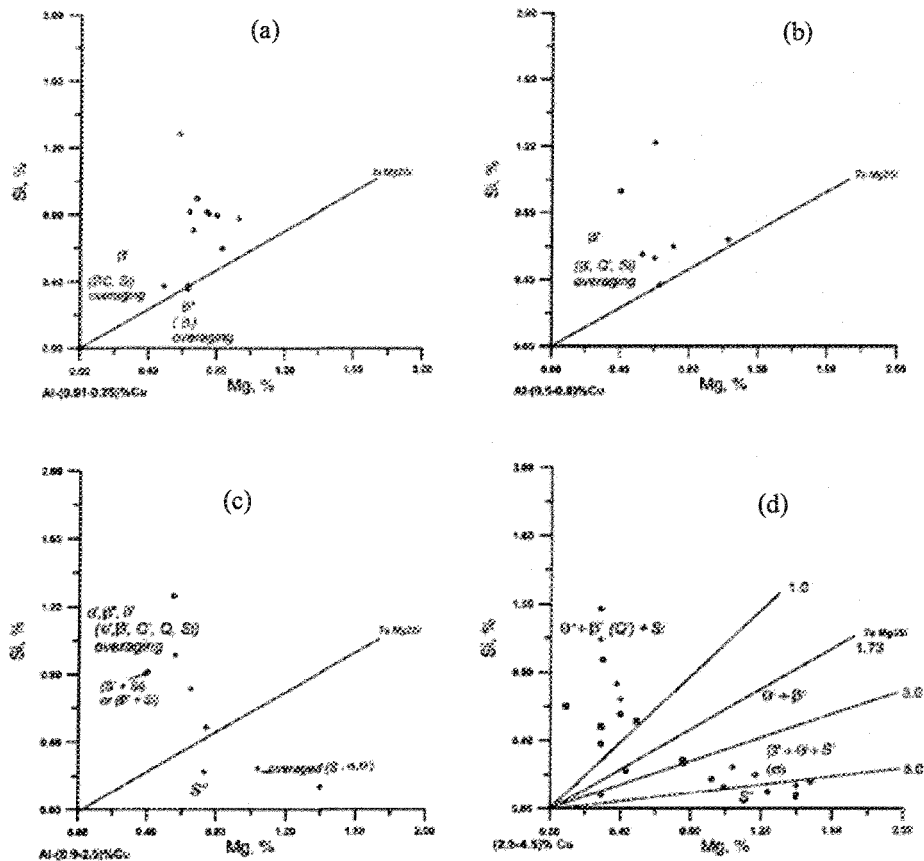


Figure 2.15 Experimentally observed phase compositions after decomposition of supersaturated solid solutions for alloys with (a) 0–0.25wt% Cu; (b) 0.5–0.8wt% Cu; (c) 0.9–2.5wt% Cu; and (d) 2.5–4.5wt% Cu.⁵⁸

For 2.5–4.5% Cu content, as shown in Figure 2.15 (d), the θ' phase may be detected in the alloys containing $Mg/Si < 8$, the S' phase is present at $Mg/Si < 8$, and the β'' (β') is formed at $1 < Mg/Si < 8$. Moreover, it will be observed from a later Figure that, at $Mg/Si < 1$, almost all of the phase types (θ' , $\beta'(Q')$, Si) may be detected except the S phase. The author,⁵⁸ also suggested the following precipitation sequences in Al-Cu-Mg-Si systems based on the Cu content:

Low Cu: $Al_{ss} \rightarrow GP \text{ zones} \rightarrow \beta'' \rightarrow \theta' \rightarrow Si \rightarrow \beta', \beta'_C \rightarrow Mg_2Si, Al_2Cu, Si$

High Cu: $Al_{SSS} \rightarrow GP \text{ zones} \rightarrow \beta'' \rightarrow \theta' \rightarrow Si \rightarrow \beta', \beta'_C (Q') \rightarrow Q (AlMgSiCu), Al_2Cu, Si$

At intermediate Cu concentrations, the combination of the above sequences can occur in conditions of natural aging prior to artificial aging over 200°C.

2.1.4 Tensile Properties as Affected by Different Parameters

Aluminum-Copper alloys are characterized by their superior tensile properties. The tensile properties of these alloys are controlled by different parameters such as heat treatment, Cu content, dendrite arm spacing (DAS), and chemical additions. Generally speaking, Al-Cu alloys such as 201.0, 204.0, 206.0 are able to achieve ultimate tensile strength, yield strength, and elongation (%) within the ranges of 360 to 450 MPa, 215 to 280 MPa, and 3 to 20%, respectively, after heat treatment.¹⁹ This treatment plays a vital role in determining the level of tensile properties.

Table 2.2 represents the effects of the aging temperature on the tensile properties of 204.0 type Al-Cu alloys; it will be observed that the peak-aged condition is reached at an aging temperature of 180°C.

Table 2.2 Tensile properties and heat treatment of alloy 204.0 (4.6Cu0.25Mg0.17Fe0.17Ti).¹⁹

Alloy	Condition	UTS (MPa)	0.2 Y.S (MPa)	Elong. in 50mm, %
Permanent molds	12 h at 140°C	395±10	230	20±2
	12 h at 160°C	405±20	290	16±1
	12 h at 180°C	420±20	380	8±1
Sand castings	12 h at 140°C	395±10	250	13.5±1
	12 h at 160°C	400±20	300	9±1
	12 h at 180°C	420±20	395	3±0.5

Sigworth and Major⁵⁹ studied a variety of different heat treatment types including T7, T4 tempers in relation to the tensile properties of the B206.0 alloy; in so doing he found that applying the T7 treatment contributes to enhancing alloy strength at the expense of alloy ductility, as can be seen in Figure 2.16 (a) where the T7 produces ultimate tensile strength, yield strength and elongation values of 420-490 MPa, 365-450 MPa, and 3.5-10%, respectively. At the same time, T4 enhances the ductility of the alloy at the expense of strength as follows: 390-450 MPa (UTS), 230-280MPa (YS), and 15-23% (Elongation) as can be observed in Figure 2.16 (b). Sigworth also added that the quality index is significantly less for the T7 temper (725MPa) when compared to 800-825 MPa for the T4 temper.

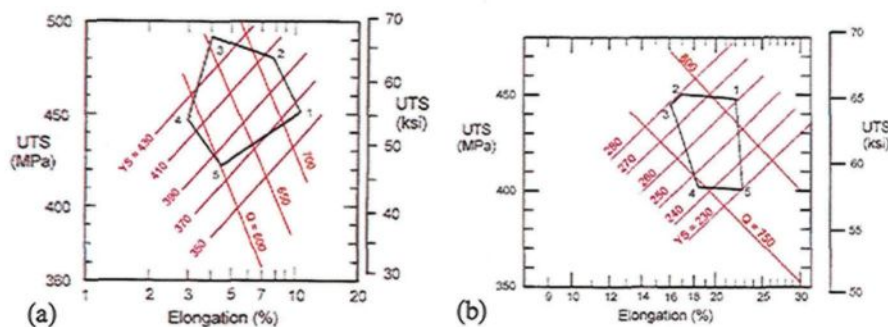


Figure 2.16 Tensile properties of B206 alloy at: (a) T7 i.e. SHT @ 480°C/1h -495°C/2h -528°C/10h -WQ @ 65°C-aging @200°C/4hr, and (b) T4 same as T7 but after WQ @ 65°C, keeps for 7 days.⁵⁹

The effects of the aging temperature range of 155-220°C for periods up to 24 h. on the tensile properties of the Al6Si4Cu0.46Fe0.14Mn alloy were investigated by Gauthier, *et al.*⁶⁰ Generally, the highest level of tensile properties is reached at an aging temperature of 150°C, as shown in Figure 2.17. Figure 2.17 also shows that the YS increases with aging time at 155°C and attains a maximum of 350MPa after 24h or a maximum of 330 MPa after

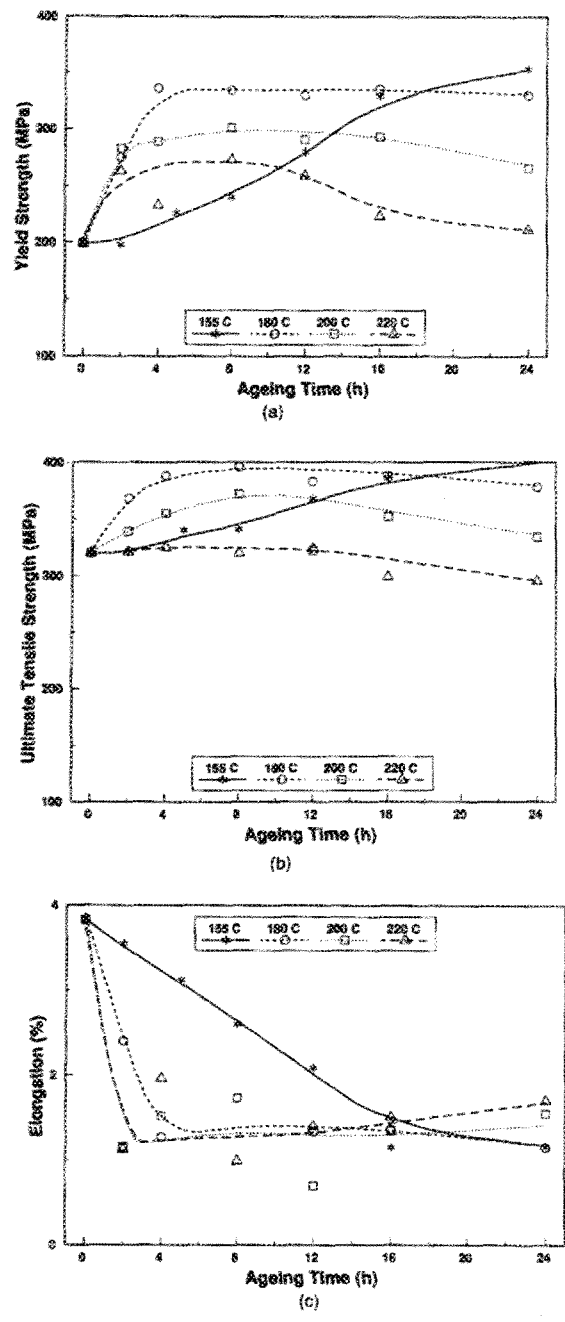


Figure 2.17 Effects of aging time in the temperature range 155-220°C on tensile properties of Al-6wt%Si-4wt%Cu-0.46wt%Fe-0.14wt%Mn alloy: (a) YS, (b) UTS, and (c) Elongation (%).⁶⁰

4h at 180°C. As the aging temperature reaches 200°C, the softening starts after 2 h of exposure and the ultimate and yield strength drop to a minimum after 24 h at 220°C. The UTS reveals a similar trend to that of the YS where peak aging is achieved after 24 h at 155°C (400MPa) which is a higher value than the one produced when aging at 180°C for 8 h (380MPa). The elongation decreases suddenly from 4% to 2% after 2 h of aging at 220°C and does not improve subsequently.

A number of studies^{54,61,62} have been directed towards investigating the effects of Cu content on tensile properties; there appears to be some agreement on the fact that alloy strength and hardness values are improved by an increase in the Cu content, as may be observed in Table 2. This improvement is attributed to the increment in the density of the number of Al₂Cu precipitates associated with the increase in the Cu content. It is worth mentioning that although the increase in Cu increases the tensile strength and hardness, it also reduces the percentage elongation, as shown in Table 2.3, where the increase in copper leads to the formation of a high density of Al₂Cu precipitates thereby lowering dislocation motion and reducing the ductility and hence the elongation.

Table 2.3 Effects of Cu content on the tensile properties of Al-0.54wt%Si-0.98wt%Mg-0.33wt%Fe.⁶¹

Alloy	Tensile Strength (MPa)	Hardness (HB)	Elongation (%)
1%Cu	152	45	12.7
3%Cu	290	85	7.5
4.5%Cu	360	105	5.4
6%Cu	402	118	2.5

Shabestari and Momeni¹³ investigated the tensile properties of Al-7wt%Si-0.35wt%Mg with regard to the effects of cooling rate and Cu content. He concluded that tensile properties may be improved by applying high cooling rates as shown in Figure 2.18; the improvements to be observed may be attributed to the fact that the high cooling rates refine the DAS which in turn refines the Fe-bearing intermetallic platelets. Additionally, the high cooling rate leads to fragmentation of the silicon particles and refining of the secondary phases. It may also be seen from Figure 2.18 that the UTS and YS increase with Cu content of up to 1.5wt% due to an increase in the density of Cu-bearing precipitates in the interdendritic spaces. As Cu content increases beyond 1.5 wt%, the strength decreases; this is related to the negative effect of fine porosity which arises as Cu content exceeds 1.5wt%.

Chemical addition is a further parameter which is known to affect the tensile properties of Al-Cu alloys. Silver is considered to be one of the most important additions used in Al-Cu alloys. Usually, Ag is added in the range of 0.1 to 0.6 wt%; it is added to Al-Cu alloys such as the A201 alloy, where it improves the strength values, as shown in Figure 2.19. It is assumed that Ag strengthens the A201 alloy through a mechanism of solid solution⁶³ in view of the fact that there is no evidence of Ag-bearing precipitates in Al-Cu-Mg alloys; Ag forms co-clusters with Mg which then act as heterogeneous nucleation sites for the Ω -phase displaying a composition of Al_2Cu .^{64,65,66} The Cu atoms aggregate to the co-clusters and start to grow along the $\{111\}$ planes.

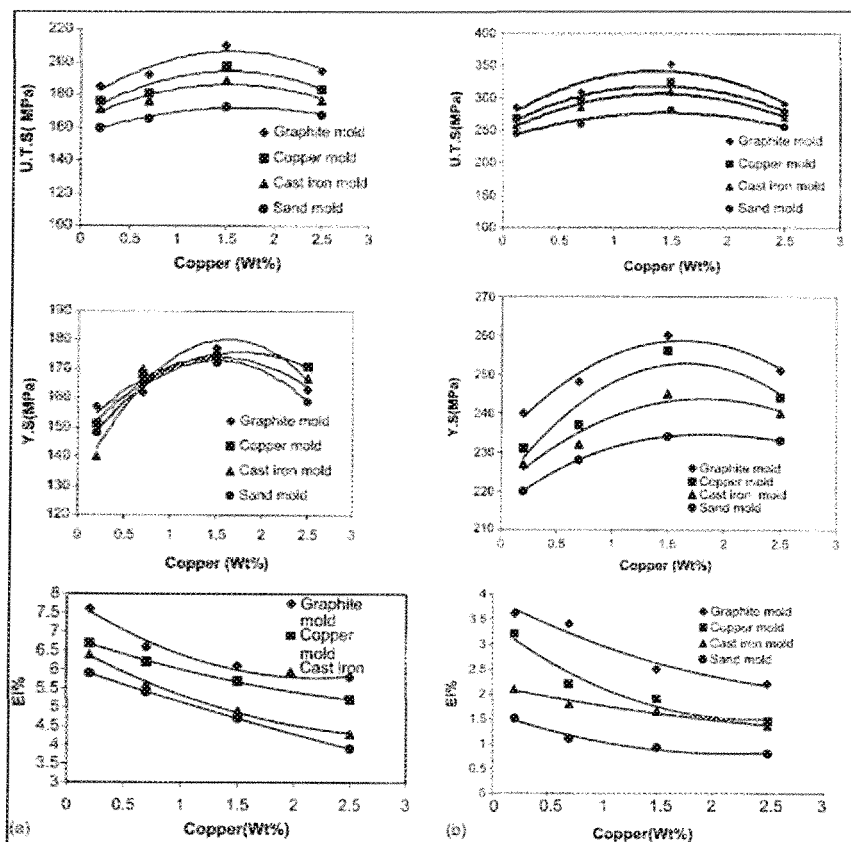


Figure 2.18 The tensile properties of Al-7wt%Si-0.44wt%Mg-0.36wt%Fe with respect to the Cu content and cooling rate: (a) as cast condition, and (b) after heat treatment (SHT@490°C-12h/WQ@60°C/Ag@180°C-5h).¹³

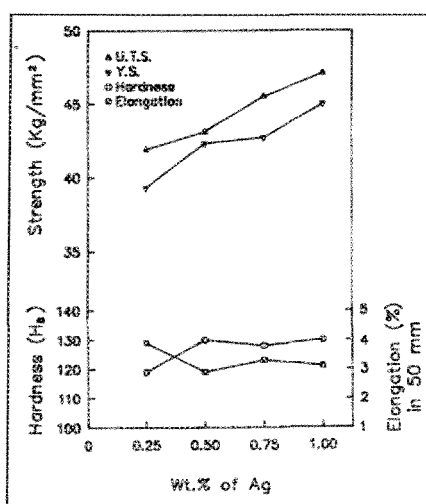


Figure 2.19 The effects of Ag addition on the tensile properties of A201-T7 alloy (T7:SHT@529°C-16h/WQ/24h@RT/Aging@188°C-5 h).⁶³

2.2 Transition Elements (Zr, Sc)

2.2.1 Zirconium (Zr)

Zirconium is one of the transition elements which is used in a wide selection of aluminum alloys in order to control the microstructure and mechanical properties. When zirconium is added in small quantities, it forms tiny coherent precipitates of L1₂-ordered trialuminide (Al₃Zr) through the decomposition of a supersaturated solid solution of aluminum,^{67,68} as is shown in Figure 2.20.⁶⁹

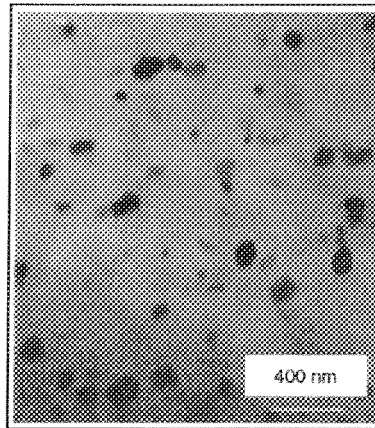


Figure 2.20 Al₃Zr precipitates observed in 2014 aluminum alloy.⁶⁹

Forbord *et al.*⁷⁰ and Jia and Hu.⁷¹ reported that these tiny precipitates of Al₃Zr, or dispersoids, strengthen the matrix through a process of pinning and the prevention of dislocation motion, additionally these precipitates succeeded in pinning the grain boundary and slowing the recrystallization kinetics. Also, due to the low solubility and diffusion coefficient of zirconium trialuminide (Al₃Zr), this phase stabilises the alloy microstructure at high temperatures.

Sepehrband *et al.*⁷² studied the effects of the addition of 0.15% Zr on the aging behaviour of A319 alloy; they found that Al_3Zr precipitates are formed through the decomposition of an Al(Zr) supersaturated solid solution during solution heat treatment at 503°C. These precipitates strengthen the matrix and provide the stable hardening response under solution heat treatment for an extended length of time, as may be observed in Figure 2.21.

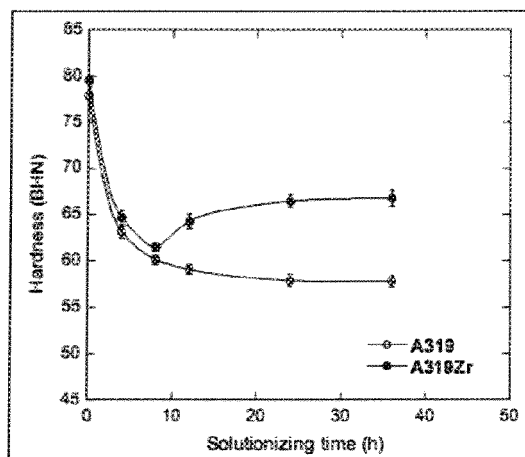


Figure 2.21 Effects of 0.15wt% Zr addition on hardness of 319 alloy type after solution heat treatment at 503°C for different times.⁷²

Robson and Prangnell,⁷³ in their study of dispersoid precipitation in Zr-containing aluminum alloys, concluded that zirconium becomes strongly segregated toward the dendrite centers during the casting of 7050 aluminum alloys, as illustrated in Figure 2.22. Consequently in the low zirconium regions the solubility limit is not exceeded and no Al_3Zr dispersoids precipitate. Thus the dispersoid precipitation will only be thermodynamically possible if the Zr concentration is greater than about 0.01 wt% at 350°C which increases to over 0.08 wt% at 500°C. These researchers also predicted that the most rapid precipitation kinetics for dispersoids would be found at 495°C at in the high Zr region. Robson,⁷⁴ in

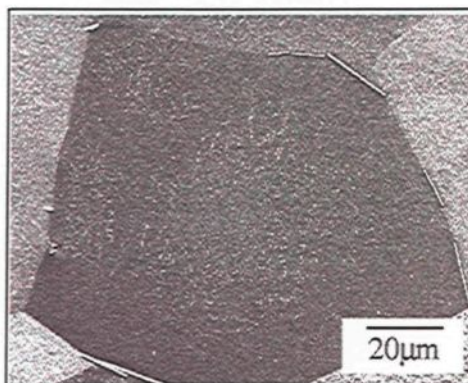


Figure 2.22 Optical image of grain showing the non-uniform distribution of Al_3Zr dispersoids appearing as white dots at the grain center) after isothermal homogenisation for 20 h at 500°C .⁷³

another study, suggested that zirconium content is the main controlling factor in nucleation and growth rate where the Zr concentration increases the magnitude of both these parameters, as shown in Figure 2.23. Moreover, as the zirconium level is reduced, the temperatures at which the maximum growth and nucleation rates occur also decrease.

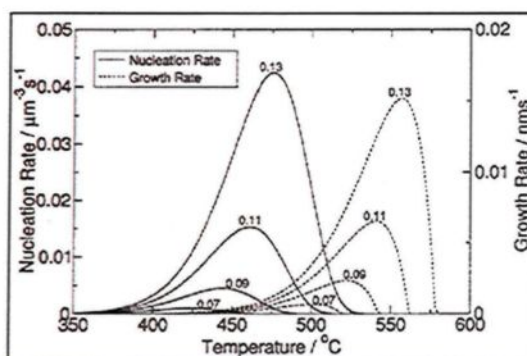


Figure 2.23 Predicted variation of the Al_3Zr dispersoid nucleation and growth rates with temperature.⁷⁶

Eskin and a number of coworkers^{75,76} reported a variety of significant facts regarding the effects of adding Zr to aluminum alloys. As zirconium content exceeds 0.11%, Al_3Zr particles form as primary phase particles in a peritectic reaction, as

represented in the Al-Zr phase diagram shown in Figure 2.24. The primary Al_3Zr particles act as potent nuclei for $\alpha\text{-Al}$ during solidification through the following reaction: $\text{L (Al)} + \text{Al}_3\text{Zr} \rightarrow \alpha\text{-Al (refined)}$. With regard to the cooling rate the primary particles of Al_3Zr which are in equilibrium with aluminum solid solution, appear as needle-shaped particles or as fine star-like particles, as may be seen in Figure 2.25.

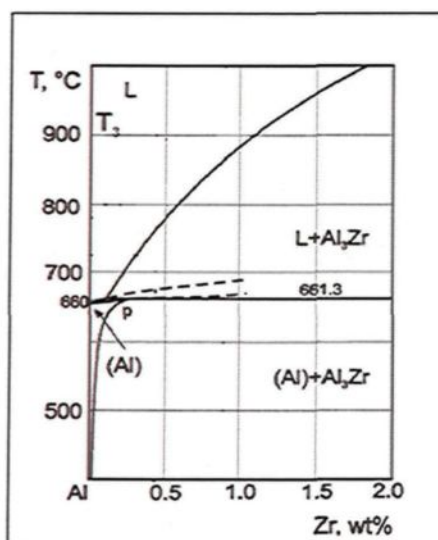


Figure 2.24 Partial equilibrium phase diagram for Al-Zr system. Adapted from⁶⁷

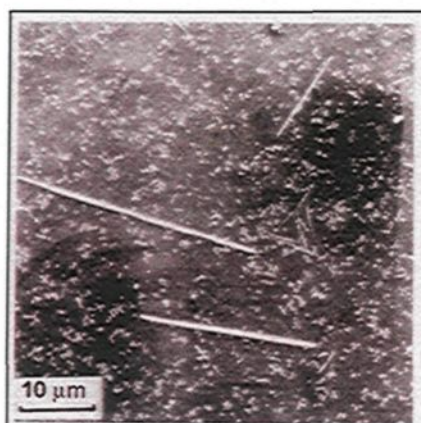


Figure 2.25 Microstructure of an Al-2.2wt%Zr alloy solidified at 102 K/s, SEM.⁷⁵

The Al_3Zr phase is distinguished by two different crystallographic structures: the first is the stable tetragonal DO_{23} structure which is body-centered with eight atoms per unit cell, while the second is the coherent metastable Al_3Zr phase with an L1_2 -type structure which is simple cubic with four atoms per unit cell and having a slight lattice mismatch with $\alpha\text{-Al}$ ^{75,76} The structure of the Al_3Zr intermetallic phase is dependent on the level of Zr added to the alloy as well as on the cooling rate, as shown in Figure 2.26. Also Al_3Zr can dissolve up to 5 wt% Sc and form a $\text{Al}_3(\text{Zr}_{1-x}\text{Sc}_x)$ phase particle; when the Al_3Zr phase dissolves the Sc, the lattice parameter of this phase is observed to decrease.⁷⁷

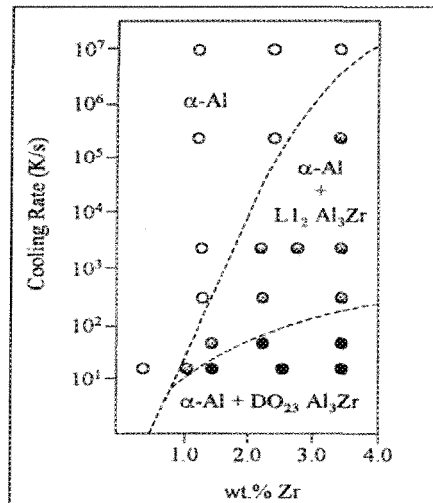


Figure 2.26 Microstructure-Section map for the Al-Zr alloy system pertaining to cooling rate and Zr content.⁷⁸

The $\text{Al}_3(\text{Zr}_{1-x}\text{Sc}_x)$ may form upon the decomposition of the solid solution or as a primary phase during solidification. The primary $\text{Al}_3(\text{Zr}_{1-x}\text{Sc}_x)$ type phase has a greater efficiency as a grain refiner than the primary Al_3Zr phase. Moreover, the primary Al_3Zr phase particles may act as nucleation sites for Al_3Sc as shown in Figure 2.27.⁷⁵ As the Al_3Sc phase nucleates on the surface of Al_3Zr phase particles, the grain refining capacity of

the primary Al_3Zr phase particles for $\alpha\text{-Al}$ shows improvement because of the small lattice misfit between the Al_3Sc phase and $\alpha\text{-Al}$.^{75,77}

Rao and *et al.*⁷⁹ investigated the fading effect which Zr may ultimately have on the Al-5Ti-1B grain refiner. It was found that zirconium tends to poison the Al-5Ti-1B grain refiner by impairing its potency through the formation of such complex aluminides as the Zr aluminides containing Ti and Fe, the Ti aluminides containing Zr and Fe, and the Fe aluminides containing Zr and Ti, which are all considered to be weak nucleates for $\alpha\text{-Al}$.

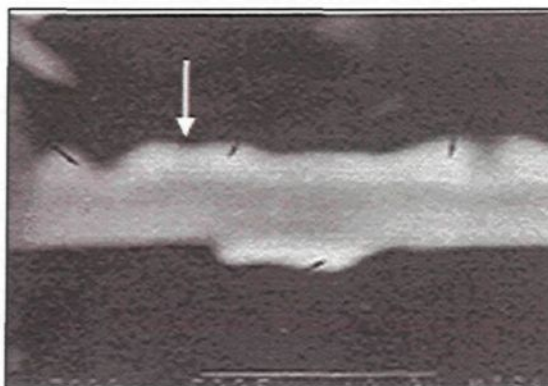


Figure 2.27 Precipitation of Sc-rich phase onto primary Zr-rich particles during solidification. The arrow points to the Sc-rich layer.⁷⁵

2.2.2 Scandium (Sc)

Scandium is a transition element added to aluminum alloys to alter their microstructure and mechanical properties. The decomposition of a supersaturated solid solution of $\text{Al}(\text{Sc})$ produces elastically hard and coherent Al_3Sc precipitates at a high number density.^{80,81,82} The Al_3Sc precipitates are characterized by their observable stability at a high temperature ($1320^\circ \pm 7^\circ\text{C}$).⁸³

Seidman⁸³ and Zakharov⁸⁴ investigated scandium in aluminum alloys and they observed that, in the Al-0.5 wt% Sc alloy, Al₃Sc precipitates may form below 350°C although they lose their coherency and undergo rapid coarsening above 400°C. These Al₃Sc precipitates strengthen the aluminum matrix by pinning the dislocation lines and resisting their motion, as shown in Figure 2.28. In addition to this, these precipitates play another important role in which they prevent recrystallization almost to the solidus by Zener pinning of grain boundaries.^{76,83}

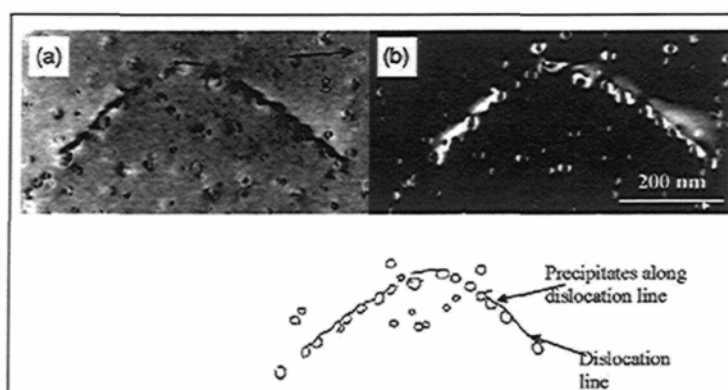


Figure 2.28 Images of Al-0.3wt% Sc alloy aged at 350°C for 120h; (a) weak-beam dark-field image, and (b) bright field image.⁸³

Eskin and coworkers^{75,76} reported that the effect of the addition of scandium on the grain size of α -Al is to refine the α -Al to a great degree through a eutectic reaction. Based on the Al-Sc phase diagram displayed in Figure 2.29, when the scandium content reaches the eutectic composition of 0.55 wt% Sc, primary particles of L1₂-Al₃Sc are formed in a eutectic reaction of $L + Al_3Sc \rightarrow (Al)$ (refined) at 665°C, and they in turn act as nucleation sites for α -Al in the molten metal during solidification.^{75,76,85} Similarly, Hyde *et al.*⁸⁵ observed that the addition of Sc below the eutectic composition of 0.55 wt % has no effect

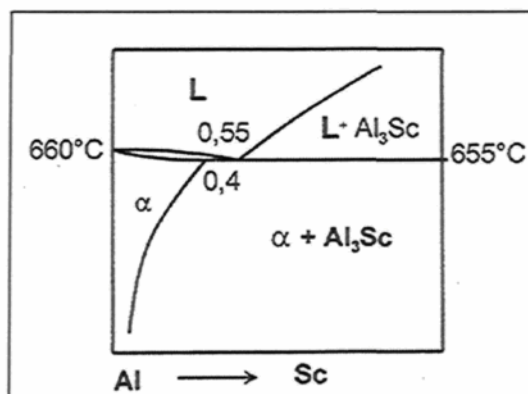


Figure 2.29 Equilibrium phase diagram for Al-Sc system.⁸⁵

on the grain size of α -aluminum although, as the Sc content continues to exceed eutectic composition and reaches 0.7%, the grain size of α -Al is refined perfectly, as shown in Figure 2.30. The potent grain refining efficiency of $L1_2$ - Al_3Sc for α -Al may be attributed to the near identical crystal structures between Al_3Sc and α -Al as well as to the very low lattice misfit between the two phases ($\approx 1.5\%$).⁷⁸

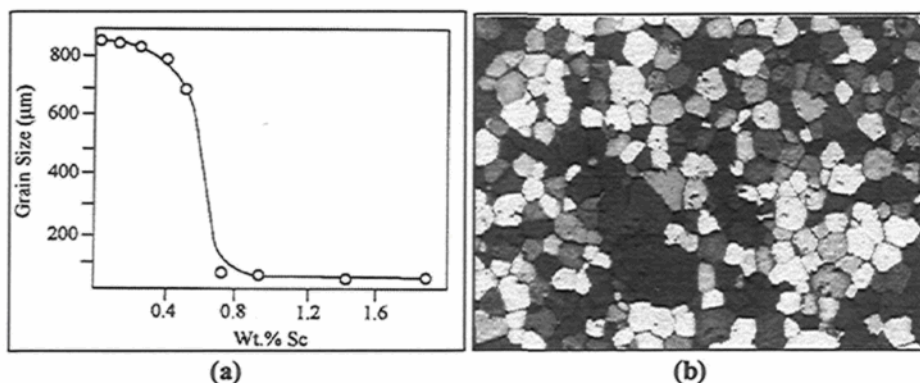


Figure 2.30 (a) Grain size of pure aluminum DC ingots vs. Sc addition, and (b) an example of as cast microstructure of Al- 0.7wt%Sc alloy under cooling rate of 100 k/s, N.B. GZ=75 μm .⁷⁸

Hyde *et al.*⁸⁵ also mentioned that the minimum level of Sc required for the refinement of α -Al can be significantly reduced by the addition of Zr and Ti; such a potential capacity may be deduced from Figure 2.31 where it is suggested that Zr and Ti

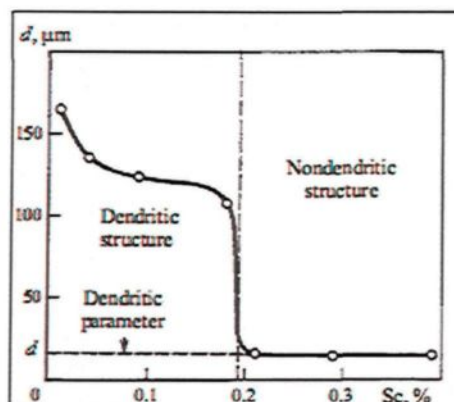


Figure 2.31 Effects of 0.18 wt% Zr on grain refining efficiency of Sc content in commercial aluminum alloys.⁸⁴

additions may shift the eutectic composition of Sc to lower values.⁸⁴ The Al_3Sc dissolves up to 35%Zr and forms $\text{Al}_3(\text{Sc}_x\text{Zr}_{1-x})$ intermetallics whether during solidification as primary particles with a lower misfit ($\sim 0.5\%$) with the matrix compared to the Al_3Sc phase, or through the decomposition of the solid solution into tiny dispersoid precipitates.^{86,87,88}

Forbord *et al.*⁸⁹ studied the formation of $\text{Al}_3(\text{Sc,Zr})$ dispersoids and reported that this type of dispersoid has a duplex morphology consisting of a 5 nm diameter core surrounded by an 8 nm thick shell. The core is of an average Al_3Sc composition, while the shell is composed of the Zr atoms of the dispersoids. The high Zr content in the outer layers of the $\text{Al}_3(\text{Sc,Zr})$ lowers the coarsening rate of these dispersoids compared to Al_3Sc . This lowering of the coarsening rate is attributed to the fact that Zr acts as a barrier to the diffusion of Sc across the interface.

Based on the isothermal section of the Al-Sc-Zr system shown in Figure 2.32, the Al_3Zr and Al_3Sc phases are presented individually; the $\text{Al}_3(\text{Zr}_{1-x}\text{Sc}_x)$ and $\text{Al}_3(\text{Sc}_{1-x}\text{Zr}_x)$ phases would not be considered as new compounds, but simply as phases resulting from the substitution of Zr atoms in the Al_3Sc compound and *vice versa* for the Al_3Zr compound.

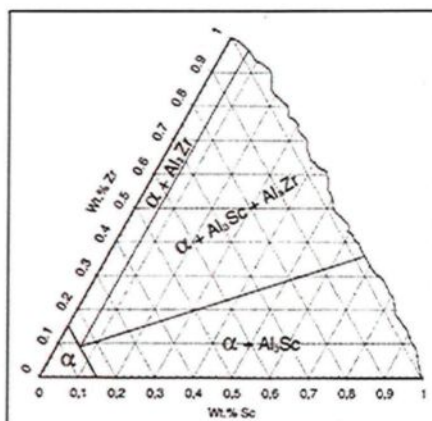


Figure 2.32 Isothermal section of the Al-corner of the Al-Sc-Zr phase diagram at 600°C.⁷⁶

The primary particles of $\text{Al}_3(\text{Sc}_x\text{Zr}_{1-x})$ have greater refining efficiency than the primary particles of Al_3Sc or Al_3Zr .⁷⁶ The Al_3Sc phase can also dissolve up to 5% of the titanium to produce $\text{Al}_3(\text{Sc}_{1-x}\text{Ti}_x)$, so that, in the presence of titanium combined with zirconium, $\text{Al}_3(\text{Sc}_{1-x-y}\text{Zr}_x\text{Ti}_y)$ may be formed.^{76,90} The primary phase particles of $\text{Al}_3(\text{Sc}_x\text{Zr}_{1-x})$ normally appear in two dimensions in the form of a star-like shape, as shown in Figure 2.33.

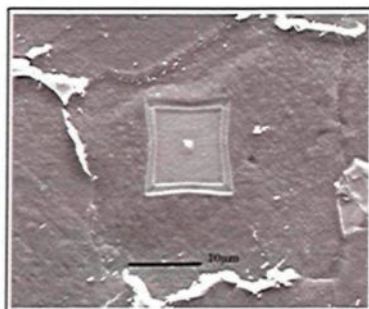


Figure 2.33 Backscattered electron image of an $\text{Al}_3(\text{Sc,Zr})$ particle.⁹¹

Scandium interacts with silicon and copper to form two different ternary intermetallic phases as follows: (i) AlScSi which is called the V-phase, with a stoichiometric composition of AlSc_2Si_2 , and (ii) AlCuSc called the W phase, having a

chemical formula of $\text{Al}_{5.8}\text{Cu}_{7.4}\text{Sc}$ with an average composition of 31.8% Al, 58.9% Cu, and 9.3% Sc. The two isothermal sections of the Al-Sc-Si phase diagram and the Al-Sc-Cu phase diagram, each at 500°C, respectively, as may be observed in Figure 2.34, provide an indication of the compositional range in which the V phase and the W phase may form.^{75,76} It should not be forgotten here that the scandium tends to diminish the solubility of copper and silicon in the aluminum matrix.

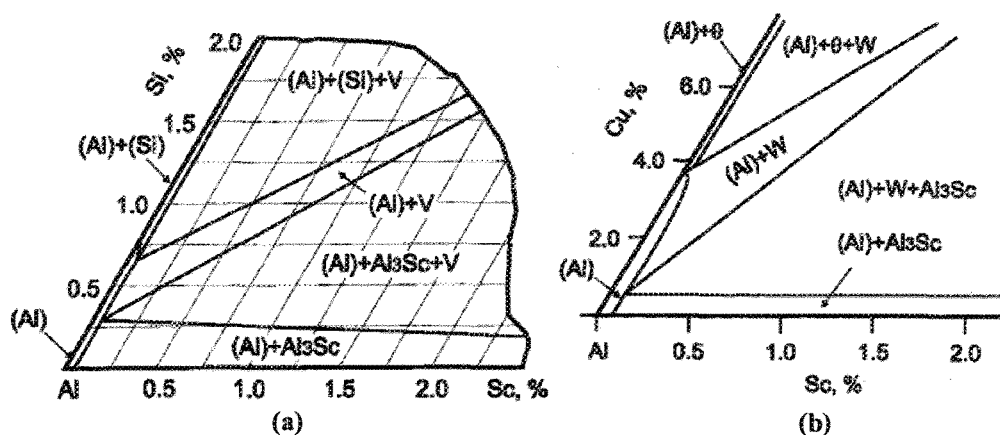


Figure 2.34 Isothermal section at 500°C of (a) Al-Sc-Si phase diagram, and (b) Al-Sc-Cu phase diagram.⁷⁵

2.3 Hot Tearing

Hot tearing is considered to be one of the more serious casting defects which may occur during solidification. This section will cover the different aspects of hot tearing including (i) the metallurgical and mechanical factors giving rise to hot-tearing susceptibility; (ii) the theories of hot tearing; and (iii) the methods of testing hot tearing in a casting.

2.3.1 Introduction

A hot tear, hot shortness, and hot cracking are different names for the hot-tearing phenomenon. Hot tearing occurs because of the uniaxial failure of a weak or stress-sensitive material. Hot tears are a result of solidification shrinkage and the linear contraction of a casting which cause localized stress and strain concentrations in the weak regions of the casting. Hot tearing may be recognized by the presence of one or more of the following characteristics:⁹² (i) it appears in the form of a ragged, branching crack [see Figure 2.35 (a)]; (ii) the tear will usually follow intergranular paths; (iii) dendrite morphology can be detected from the cracked surface [see Figure 2.35 (b)]; and (iv) the tear surface is heavily oxidized due to any subsequent thermal treatment.

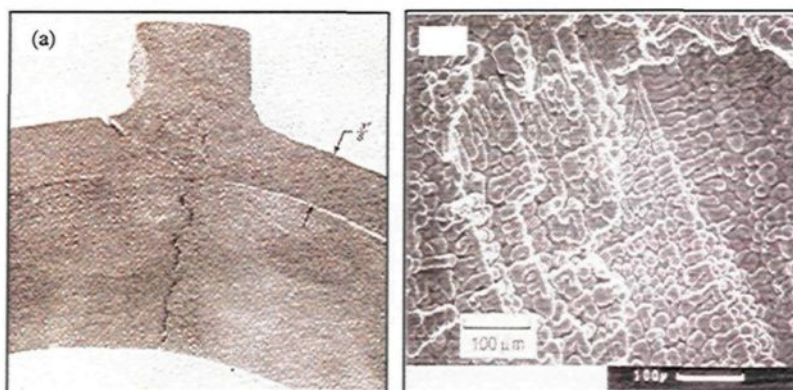


Figure 2.35 Different hot tearing features:(a) External hot tear;⁹³ and (b) SEM image of hot tear surface.⁹²

Hot tearing occurs through the following two sequential stages known as crack nucleation and crack propagation. The hot tear usually initiates from one of the following crack nuclei (i) liquid film or liquid pool; (ii) pore or series of pores; (iii) grain boundary; and (iv) non-wetted inclusions such as oxides or bifilms, intermetallic particles or oxide

films.⁹⁴ The hot tear propagates through the liquid film in more highly alloyed materials and through solid bridges in the less alloyed materials.⁹⁵ Figure 2.36 displays examples of hot crack initiators and a number of crack propagation mechanisms.

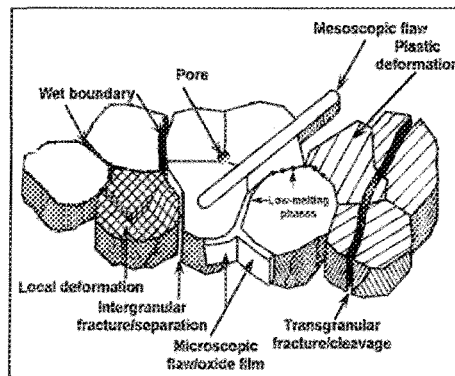


Figure 2.36 Schematic illustration of possible hot crack initiators and some crack propagation mechanisms⁹⁴

2.3.2 Factors Controlling Hot Tearing

The factors which play a significant role in hot-tearing susceptibility may be classified as two types, metallurgical factors and mechanical factors. Metallurgical factors include alloy composition, mold temperature, superheating, grain size and morphology, and gas content; mechanical factors, on the other hand, are related to such aspects as casting design, mold variables, and mold friction.

2.3.2.1 Metallurgical Factors

a. Chemical Composition

The effects of chemical composition on hot-tearing behaviour was investigated previously in numerous studies.^{96,97,98,99,100,101} The chemical composition of the alloy controls its hot-tearing behaviour by controlling the freezing range, the eutectic content,

and the grain size. The effects of grain size will be discussed in a separate section. The alloys which solidify under long freezing range conditions are more susceptible to the occurrence of hot tearing than the alloys under short freezing range conditions; this may be attributed to the fact that a long freezing range extends the liquid film stage (*i.e.* the hot tearing critical range during solidification) in which the hot tearing is initiated. Also, solidification shrinkage increases with the long freezing range and hence high stress levels will occur in the alloy during solidification.¹⁰²

The relationship between the eutectic content and hot tearing can be monitored at three different stages. For example, the Al-Cu binary system displaying a low eutectic content of $< 1\% \text{Cu}$ reacts as pure metal distinguished by high hot tearing resistance. As eutectic content increases to intermediate levels of $1\text{-}2\% \text{Cu}$, hot tearing susceptibility reaches a peak then it decreases as the eutectic content continues to increase to $> 2 \text{ wt}\% \text{Cu}$. Spittle and Cushway¹⁰³ explained this behaviour with respect to the copper content which in turn controls the mode of growth and the interface morphology of the solid-solution grains during solidification. In Al-Cu systems, although the growth mode remains columnar, the interface morphology of the solid-solution grains will change with an increase in Cu content, going from planar to cellular to dendritic. At a low Cu content of $< 0.5 \text{ wt}\% \text{Cu}$, the interface morphology is planar, hence the development of a sufficiently strong and continuous solid network to resist the formation and growth of cracks will now depend on the ability of the system to form solid bridges between the grains. This ability diminishes gradually as the Cu content increases because of the development of dendritic interface morphology; as an intermediate Cu content is reached, namely $1\text{-}2 \text{ wt}\% \text{Cu}$, the bridging

ability disappears completely between the primary grains in hot spot regions thus causing low hot-tearing resistance.

As the Cu content continues to increase, the volume fraction of the eutectic increases and hence the interdendritic flow becomes easier and better able to heal the incipient tears. Spittle and Cushway¹⁰⁴ represented the effects of Cu content on the hot-tearing susceptibility of the Al-Cu binary alloy on a lambda curve, as shown in Figure 2.37. The lambda curve is used in binary alloy systems to clarify the degree of severity of the hot tearing vs. the solute content.

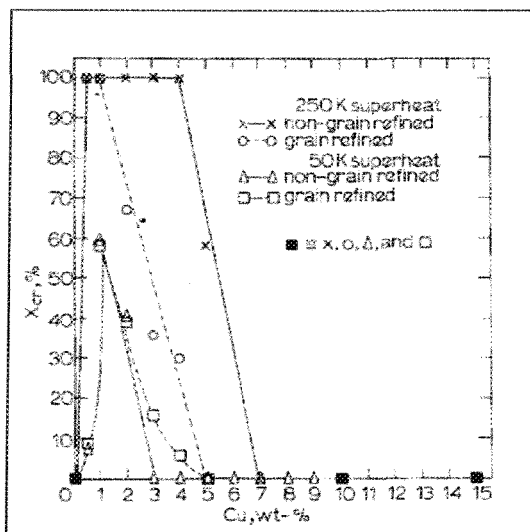


Figure 2.37 The lambda curve showing hot-tearing susceptibility vs. copper content (X_{cr} is defined as the ratio of the reduction in cross-sectional area resulting from cracking as a proportion of the original cross-sectional area).¹⁰³

Singer and Jennings¹⁰⁴ detected the same behavior in Al-Si binary alloys and introduced an important new conclusion. These researchers concluded that the limit of the solid solubility of Si in aluminum is the most critical limit for the occurrence of hot-tearing; the greatest degree of hot shortness takes place in alloys containing 0.7-0.8% silicon thus

coinciding with the effective solid solubility limit with regard to experimental conditions. An increase in the silicon content beyond the solid solubility limit leads to an improvement in hot-tearing resistance which results from a high eutectic liquid fraction which in turn activates healing of the incipient crack.

Jennings and Singer¹⁰⁵ also investigated the hot-tearing tendency of a ternary Al-Cu-Si alloy system. They found that the first additions of Cu to Al-Si and of Si to Al-Cu cause a rapid decrease in the freezing temperature of about 52°C and 25°C, respectively. As a result of this decrease in the solidus temperature, the hot shortness increases. Further additions of the third element do not have any further effect on the solidus temperature although they reduce the liquidus temperature. This reduction in liquidus temperature makes the freezing range shorter and hence the hot-tearing susceptibility diminishes. Figure 2.38 illustrates the ternary diagram of hot cracking for Al-Cu-Si alloys established by Jennings and Singer.¹⁰⁶ From this figure it may be deduced that silicon additions are more efficient than copper additions in improving the resistance to hot-tearing. The beneficial effect of silicon additions may be attributed to the fact that the silicon enhances fluidity and feedability while reducing the freezing range.¹⁰⁶

b. Grain Size and Grain Morphology

Both grain size and morphology are known to be factors which influence the susceptibility to hot tearing. In the case of A356 aluminum alloys, Kim and Loper¹⁰⁷ reported that a fine grain structure increases the number of grain boundary films in one unit volume leading to a dispersal of the contraction stress and hence to a reduction of this susceptibility. On the other hand, the contraction stresses may be found concentrated on a

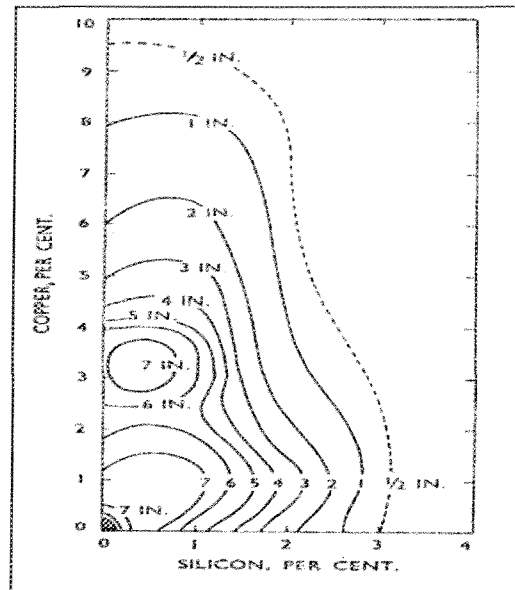


Figure 2.38 Ternary diagram of hot cracking for Al-Cu-Si alloys.¹⁰⁵

small number of grain boundary films for coarse grain structures in one unit volume, as represented in Figure 2.39. Metz and Flemings¹⁰⁸ tested the effects of coarse and fine grain structures on the hot-tearing resistance of Al-4%Cu alloys. They concluded that, in fine grain castings, the grains remain essentially isolated from each other for a much longer time than occurs in coarse grain castings; the alloy can, thus, accommodate the contraction stress for longer times without the unsought for appearance of crack formation. As solidification progresses further, the resulting flow stress occurring with a coarse grain structure is higher than it is with a small grain structure because of the existence of less dendrite branching in this case than in the case of the latter.

Lin *et al.*¹⁰⁹ mentioned that the beneficial effects of a refined grain structure in lowering the hot-tearing tendency of AA3104 and AA1050 alloys may be attributed to the fact that refined grain structures tend to delay the coherency point to lower

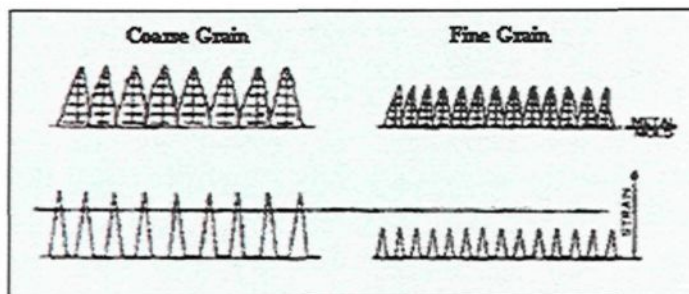


Figure 2.39 Effects of grain size on strain distribution at grain boundary liquid films.¹⁰⁷

temperatures, thereby enhancing the liquid interdendritic feeding and healing the cracks. Also, Lu *et al.*¹¹⁰ mentioned that, during solidification, grain refining enhances the resistance sources, the capillary forces, and the solid bridges, in action against the tensile strain initiated at the interface between two grains. Lees¹¹¹ described the influence of grain size on the tendency to hot-tearing as relating to the fact that a coarse grain structure with well-developed branches will establish a more solid and coherent network in the earlier stages of freezing than would occur in the presence of a fine grain structure. In parallel, the amount of contraction will multiply and reach a critical level in the case of coarse grain structures faster than in the case of fine grain structures leading to a heightened susceptibility to hot tearing. Lees¹¹¹ also observed that, in the case of a fine grain structure, when the stresses are set up by preventing free contraction, they may be partially relieved by tiny movements of any of the small crystals; where coarse grain structure is concerned, however, stress relief is difficult to obtain.

In the context of grain refining, grain shape also affects the degree of susceptibility of the alloy to hot tearing. As Warrington and McCartney¹¹² observed, the hot-tearing susceptibility of an alloy increases with equiaxed cellular grain morphologies. Also,

columnar grains increase the hot-tearing susceptibility by providing favorable orientations for tear initiation and propagation although equiaxed dendritic grain morphologies provide high resistance to hot cracking. In their investigation of the shear behaviour of partially solidified Al-Si-Cu alloys, Sumitomo *et al.*¹¹³ established the effects of grain size and morphology on the dendrite coherency point, packing fraction, and rates of strength gain with regard to the solid fraction, as shown in Figure 2.40. From the latter figure it would appear that small globular grain structures delay the coherency point and maximum packing fraction point to a higher solid fraction than they do in large dendritic grain structures. Accordingly, it may be concluded that a small globular grain structure is capable of lowering hot-tearing susceptibility by improving the stress and strain accommodation and feeding mechanism; at the same time, the coarse dendritic grain structure has an opposite effect.

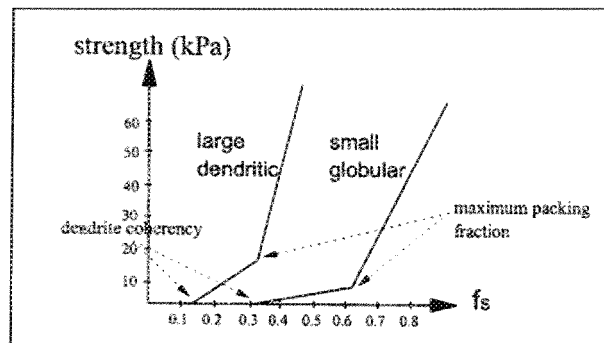


Figure 2.40 Effects of grain structure on the behavior of materials during solidification.¹¹³

c. Superheat

The effect of superheat on the susceptibility to hot tearing is a much-disputed subject. Kim and Loper¹⁰⁷ explained that the increase in superheat results in coarse

equiaxed grains and a higher volume fraction of columnar grains. Consequently, this coarse grain structure reduces the number of grain boundary films in a unit volume causing a high stress and strain concentration in the hot spot and hence heightened hot tearing susceptibility. Kim and Loper¹⁰⁷ illustrated the relationships existing between superheat vs. grain size and superheat vs. crack length, as shown in Figure 2.41(a) and (b). Clyne and Davies¹¹⁴ evaluated the hot-tearing tendency of Al-Mg alloys using the electrical resistance measurement technique. They found that the susceptibility to hot tearing increases at high superheat then decreases at low Mg content.

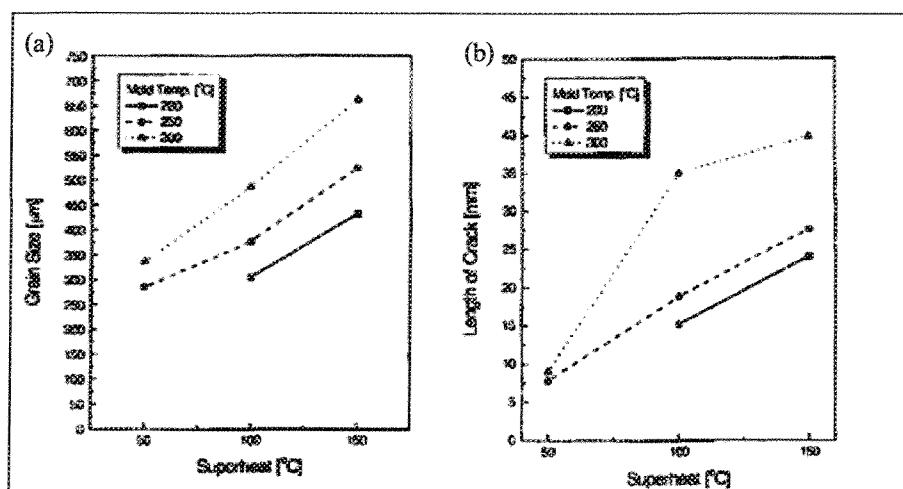


Figure 2.41 Effects of superheat on: (a) grain size, and (b) surface crack length.¹⁰⁷

In their study on the hot-tearing susceptibility of Al-Cu casting alloys, Spittle and Cushway¹⁰³ recorded that high superheat reduces the number of intergranular films causing high cracking susceptibility because of high contraction stress concentrations. They also proposed that superheat might improve hot tearing susceptibility by controlling solidification direction. Eskin *et al.*¹¹⁵ pointed out that the susceptibility to hot tearing is diminished by an increased melt superheat. Other investigators¹¹⁶ observed that the

superheat has a significant effect on the strain rate of the 206-alloy (Al-4.7Cu), which is measured by displacement per time-mm/s, where the castings poured at lower superheat contracted earlier than the ones poured at higher superheat as shown in Figure 2.42. It should be remembered that other variables such as grain size, grain morphology and solidification direction must also be considered during the study of the effects of superheat on hot tearing.

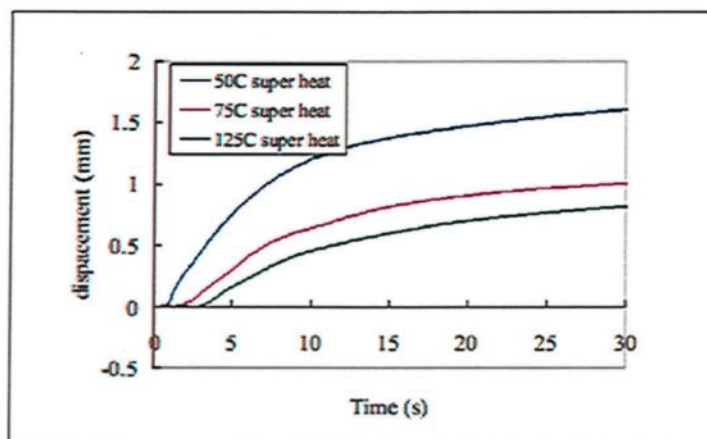


Figure 2.42 Displacement vs. time curves for the 206 alloy at three pouring temperatures.¹¹⁶

d. Mold Temperature

Mold temperature is one of metallurgical factors affecting hot-tearing susceptibility. It is believed that higher mold temperatures will reduce the tendency towards hot tearing.¹¹⁷ Although high mold temperatures cause low cooling rates which in turn produce coarsened grain, the resistance to hot tearing is heightened.

Li and Apelian¹¹⁶ have reported that the development of the load/load rate decreases from 185N/s at a mold temperature of 200°C to 70N/s for a higher mold temperature of 380°C, as shown in Figure 2.43. It was also found that the contraction of castings starts

earlier at the low mold temperature of 200°C than it does at the higher mold temperature of 380°, as shown in Figure 2.44. In contrast, Kim and Loper¹⁰⁷ mentioned that the increment in the mold temperature increases the length of both surface and inner cracks because of the formation of coarser equiaxed and columnar grains which in turn reduces the number of grain boundary liquid films in one unit volume.

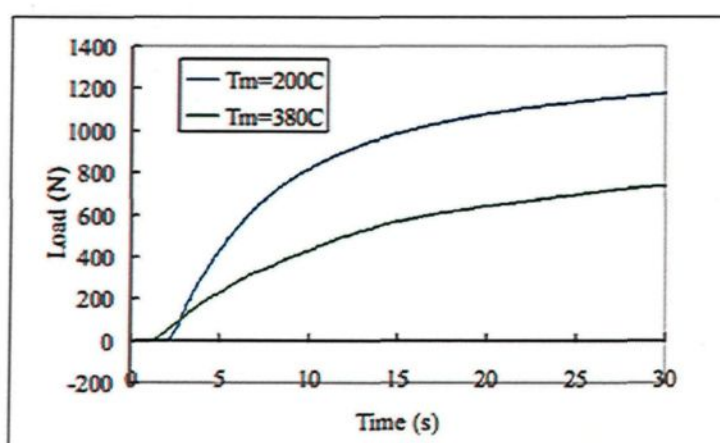


Figure 2.43 Load vs. time curves for the 206 alloy at mold temperatures of 200 and 380°C.¹¹⁶

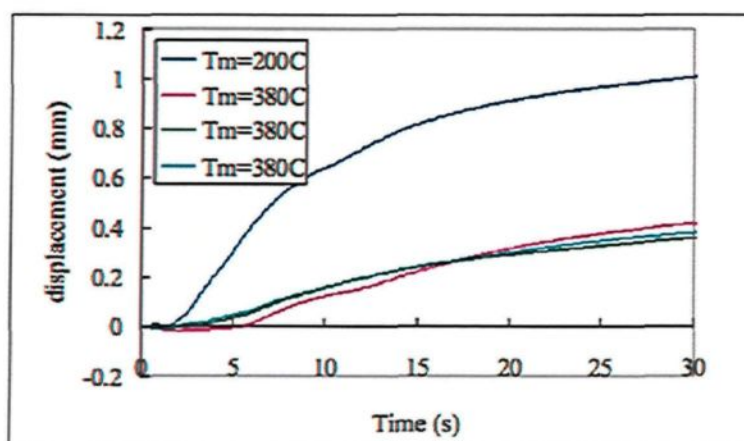


Figure 2.44 Displacement vs. time curves for the 206 alloy at mold temperatures of 200°C and 380°C.¹¹⁶

e. Gas Content

Lees¹¹⁸ investigated the effects of dissolved gas on the hot-tearing tendency of Al-Cu and Al-Cu-Si alloys, and reported that although the dissolved gas enhances the hot tearing slightly, its effects are still small when compared to that of the eutectic content. This researcher also suggested that the gas effect is more efficient in alloys with a relatively high eutectic content as a result of two actions. Firstly, if gas is rejected from the solution at the primary stage of the formation of a coherent network, then the internal gas pressure which is generated relieves the contraction stresses in the network itself. Secondly, upon reaching the solidification stage, the gas pressure may force residual liquid into the small tears and hence activate the crack healing mechanism.

2.3.2.2 Mechanical Factors

a. Casting Design

The casting design controls hot tearing by controlling the cooling rate, thermal distribution, and contraction variation. Figure 2.45 shows the design of two bars having different cross-sectional areas which are joined together at each end by two flanges. Upon measuring the contraction rate of the two bars with the different cross sectional areas shown in Figure 2.46, it was found that the bar with the small cross section, A_2 , starts to contract earlier with higher contraction rates than the bar A1 with the large cross section.⁹³

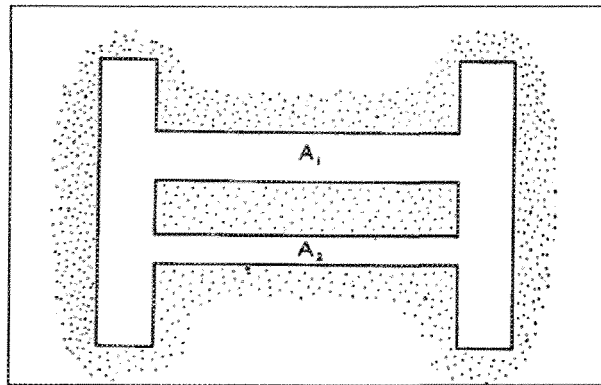


Figure 2.45 Two bars joined by flanges.⁹³

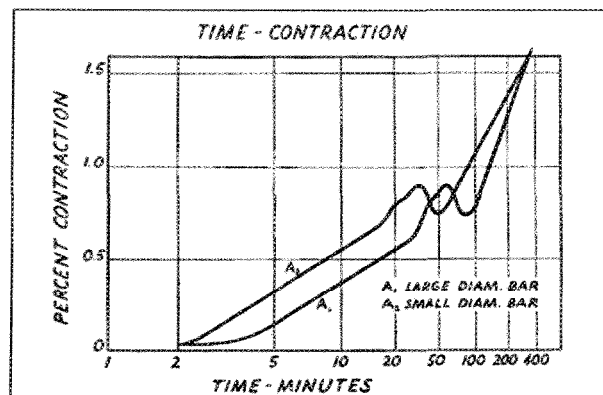


Figure 2.46 Time-contraction characteristics of bars of different sizes, not joined together.⁹³

As the two bars are joined together the small A_2 bar will be under tensile stress whereas A_1 will be under compression stress. Thus, if the resultant tensile stress acting on the casting is greater than the casting strength, the casting will lose its capacity for hot-tearing resistance; in this case, the tears will probably be located at the junction area between the small bar and the flange. In Figure 2.47, it will be observed that the casting shape type restricts the degree of free contraction. The casting of the straight parallel-sided bar contracted by about 2.4%, whereas the flanged bar contracted by only about 0.92%, and the spherical ended bar produced an intermediate value of 1.64%.⁹² Based on these

contraction rates, it is possible to deduce that the hot-tearing susceptibility of a casting can be reduced by modifying the casting shape.

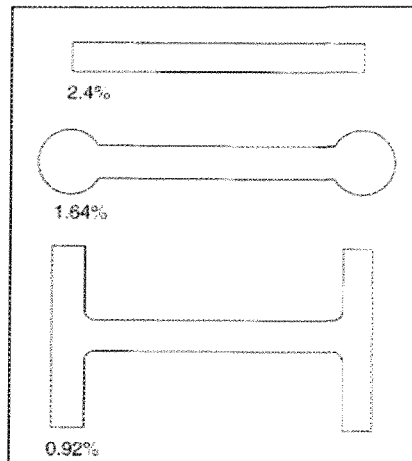


Figure 2.47 Contraction of three different steel shapes cast in green sand.⁹²

b. Mold Variables

A high percentage of hot tears originate in the unsuitable choice of sand mold, cores, feeding, and gating systems which all contribute to obstructing the contraction of a casting. Figure 2.48 is a good example of the hindering effect of a mold with regard to the free contraction of a bar ending in two flanges. The restricting effect of the mold creates high tensile stresses along the bar length, which then transfer along the bar as solidification develops till they reach the last location in the bar to solidify such as the hot spot region, which may be found at the junction of the bar and the flanges. The hot spot region is considered to be the weakest location in the bar where hot tearing will occur if the resultant tensile stresses exceed the strength of the metal.

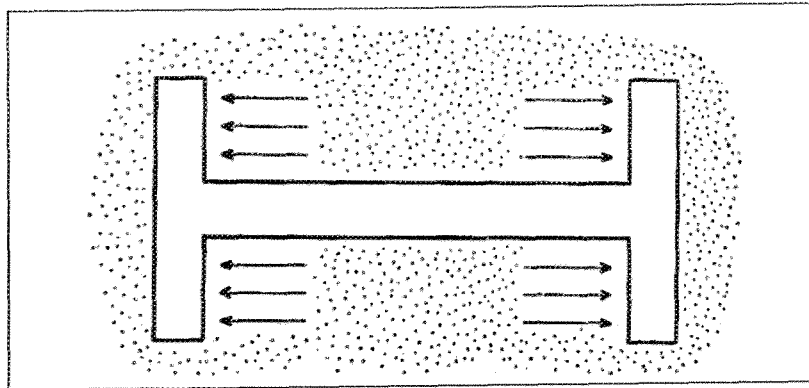


Figure 2.48 Bar with flanges.⁹³

c. *Mold Friction*

Based on a study carried out by Andrew and Protheroe¹¹⁹ on the effects of mold friction using different degrees of sand coarseness, it may be deduced that mold friction does not have any observable influence on the tendency towards hot tearing. In contrast, Parkins and Cowan¹²⁰ found that residual stresses can be controlled by adjusting the smoothness or the degree of friction in the sand mold by using coatings of certain grain size distributions which implies that under such circumstances mold friction may exert the necessary restraint to cause tearing.

2.3.3 Hot Tearing Theories

2.3.3.1 Strain Theory

The Strain Theory was formulated by Pellini^{121,122} in order to generate an explanation of the hot tearing mechanism. This theory suggests that the occurrence of the hot tearing of metal depends on the amount and rate of strain developed in the liquid film regions. According to this theory, the length of the liquid film stage under constraining conditions is the main controlling parameter for the occurrence of hot tearing. For example,

in non-segregated conditions, or normal film stage, the metal goes through the liquid film stage in only a few seconds, whereas, in segregated conditions the liquid film stage lasts for several minutes. Consequently, the strain rate, which is not able to cause fracture in only a few seconds, may cause fracture after the passage of several minutes due to the accumulation of a high strain level.

Figure 2.49 illustrates the main concepts of the strain theory of hot tearing. Three main factors control the development of a high strain rate resulting in hot tearing:^{121,122} (i) a longer contracting region, (ii) the high cooling rate in the contracted region, and (iii) narrower hot spot regions undergoing contraction. A longer contracted region at a high cooling rate produces a high degree of contraction for each unit of time; as the hot spot becomes narrower, the extension per unit of time, or strain rate, will multiply in order to compensate for the high contraction level of the colder regions. All of these factors amplify opportunities for the occurrence of hot tearing. The low cooling rate applied to hot spots has the same effect as the wider temperature range developed by segregated films since the low cooling rate of the hot spot provides extended periods of time for accumulating an contraction strain to high levels.

2.3.3.2 Shrinkage-Brittleness Theory

According to this theory, the liquid-solid range of any metal can be divided into two different stages, namely, before the coherence point and after the coherence point.¹²³ During the first stage, before the point of coherence, the liquid metal fraction is high and

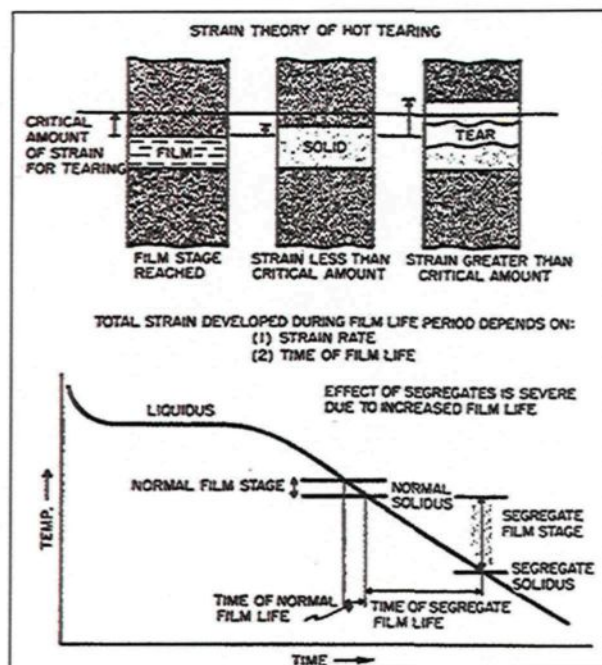


Figure 2.49 Illustration of basic concepts of Strain Theory¹²¹

the continuous solid network is still unformed, consequently, any cracking or defects occurring at this stage can be healed by liquid flow. As the system reaches a coherent temperature, or the coherence point, the primary dendrites which grow at the expense of a drop in the liquid fraction, come into contact and interlock. During this stage, below the coherent temperature, linear shrinkage starts to develop and to impose stresses on the solid network; according to the shrinkage-brittleness theory, hot tearing takes place when the shrinkage stress exceeds the rupture stress.

The shrinkage-brittleness theory defines the range of brittleness as the range of temperature between the coherent temperature and the solidus, as shown in Figure 2.50.¹²⁴ Once the alloy passes the range of brittleness, that is to say below solidus, hot tearing is unlikely

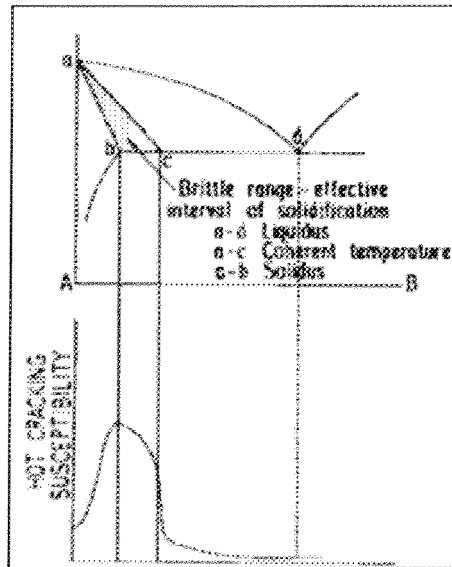


Figure 2.50 Brittleness range based on shrinkage-brittleness theory for hot tearing.¹²⁴

to occur. The degree of hot-tearing susceptibility depends on the accommodation behavior of the alloy to prevent cracking. Also, the freezing range is considered to be a controlling factor based on the shrinkage brittleness theory where, as the freezing range increases, *e.g.* through alloying additives, the susceptibility to hot tearing is expected to increase as well.

2.3.3.3 Liquid Metal Embrittlement Theory

A number of studies have recorded^{125,126,127} the loss of ductility upon application of tensile testing, when the alloy was heated above the solidus line to reach the liquid-solid phase equilibrium region. Singer and Cottrell¹²⁸ studied the high temperature properties of Al-Si alloys; they observed that tensile strength decreases gradually until the solidus temperature is reached. As the solidus temperature is exceeded by between 5°C and 30°C, the strength decreases rapidly to zero value, as shown in Figure 2.51. This reduction in strength was associated with a complete loss of ductility.

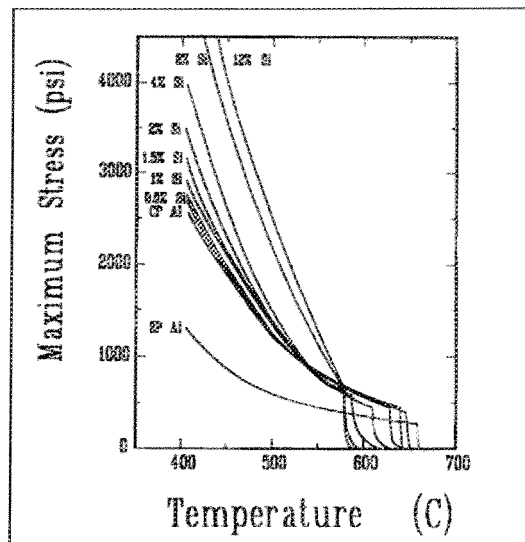


Figure 2.51 Tensile strength of Al-Si alloys at temperatures in the vicinity of solidus¹²⁸

Singer and Cottrell¹²⁹ pointed to the fact that, in fully solid samples at $T < T_{\text{Sol}}$, the fracture surface was of the ductile fracture type and the reduction in the cross-sectional area was 100% although the fracture surface in semi-solid samples (liquid + solid) at $T > T_{\text{Sol}}$, was of the brittle fracture type and the reduction in the cross-sectional area was very small. In parallel studies, Pellini and his coworkers^{121,122} tested aluminum and steel plates during solidification by means of X-ray and they confirmed the Singer-Cottrell results.¹²⁸

Smith¹²⁹ was one of the first to point out the effective role of surface tension forces and the dihedral angle in liquid metal embrittlement; he carried this out through his study of a number of copper materials and a Fe-30% Cu alloy. The dihedral angle (θ), determining the liquid film distribution, depends on the ratio between γ_{ss} , which is the interfacial free energy between two solid grains, and γ_{sl} , which is the interfacial free energy between solid and liquid, as shown in Figure 2.52. Fredriksson and Lehtinen¹³⁰ detected the crack propagation using a SEM equipped with a video camera to conclude that the dihedral angle

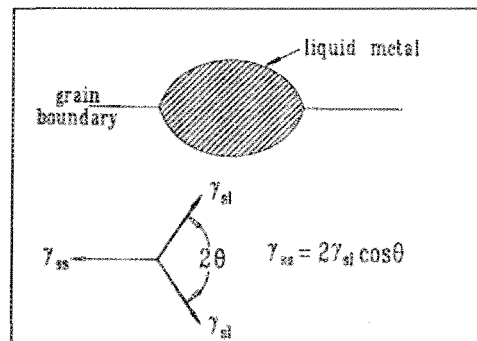


Figure 2.52 Equilibrium distribution of liquid at grain boundaries in semi-solid metals.¹⁰⁷

is a controlling factor in determining the fracture mechanism. When the dihedral angle equals zero the liquid metal completely wets all the grains.

All of the recently introduced studies are considered as important steps toward the formulation of a liquid metal embrittlement theory. The liquid embrittlement concept may be attributed to the fact that the surface energy between liquid and solid is small, thereby making it easy to create liquid cracks from an energy point of view.¹³¹ Moreover, a liquid-filled crack is considered to be a crack initiator, whereas the propagation of a crack is determined by the critical stress which in turn is determined by applying Griffith's modified crack theory.¹³² The degree of embrittlement is affected by the dihedral angle. It has been observed that the smaller the dihedral angle, tending towards zero, the greater the liquid embrittlement.

2.3.4 Hot-Tearing Testing Methods

The susceptibility of metal to hot tearing can be tested by means of a mold testing technique or a mechanical test. The mechanical test involves applying tensile and impact

tests at high temperatures close to T_{Sol} ; this technique is beyond the scope of this study, and hence is not described here. Mold testing can be classified into two groups of mold type based on the orientation of the stresses developed with respect to the direction of solidification which may be either parallel or perpendicular.

Ring molds¹²² and cold finger molds¹¹² are examples of molds in which the developed stresses are perpendicular to the direction of solidification. The ring mold consists of a ring and a core with the same central axis, both resting on a flat plate. In the ring mold test, after the pouring and solidification of the tested metal, the susceptibility to hot tearing is measured by obtaining the sum of crack lengths over the entire surface divided by the perimeter of the radial section of the ring casting. Also, the length of the main crack may be used as the hot-tearing susceptibility index.

In other types of mold testing such as when using a backbone mold, or a constrained rod casting (CRC) mold,¹³³ or a flanged-bar hot-tearing test, the developed stresses are parallel to the direction of solidification. The minimum critical length of the samples in which the hot tearing occurs is considered to be a hot tearing susceptibility index. A number of equations may be used to determine the severity of hot tearing based on the length of the bar and the degree of tearing severity. For example, hot tearing susceptibility (HTS) may be determined by using a CRC mold and applying the following equation: $HTS = \sum (C_i \times L_i)$ where C is a numerical value which is used to represent the degree or “level” of the crack severity of the bar, and L is a numerical value corresponding to the bar length. Figure 2.53 shows schematic diagrams of a ring mold, a cold finger mold, a backbone mold, and a CRC mold used for conducting such tests. Some of these molds are

CHAPTER 3
EXPERIMENTAL PROCEDURES

CHAPTER 3

EXPERIMENTAL PROCEDURES

In order to implement the objectives laid out for this study, the specifically designed alloy compositions were classified into three different categories. The first category served the aim of identifying and quantifying the intermetallic compounds which form during solidification; the high concentration of alloying elements and a slow cooling rate during casting were taken into account in order to achieve this intended aim. The slow cooling rate was induced by pouring the molten metal into a 600°C preheated graphite mold. This first category consisted of ten alloys and was investigated from a metallographic point of view.

The second alloy category was designed mainly to investigate the effects of composition and heat treatment on the tensile properties and microstructure of the Al-2wt%Cu based alloy. This alloy category consists of seventeen alloys which in turn are divided into four sub-groups as follows: Zr-Ti, Zr-Sr, Zr-Sc, and Si alloy groups. These alloys were cast using an ASTM B-108 type permanent mold (tensile bars mold), at a cooling rate of 7°C/s.

The third category was selected from the second category based on compositions which provided maximum applicability, cost effectiveness, and acceptable tensile properties level. These alloys were specifically assigned to investigate the hot-tearing

susceptibility of the Al-2wt%Cu based alloy. A constrained rod casting mold (or CRC mold) was used for these investigations, where the hot-tearing tests were conducted under several casting conditions. Metallographic examinations were also carried out in this case. The procedures for the experimental work which were applied to these various alloys will be discussed collectively under the following headings.

3.1 Preparation of Materials and Melting Procedures

The Al-2wt%Cu base alloy was received in the form of small ingots of 8 Kg each, having the composition shown in Table 3.1. The ingots were cut into small pieces and melted in a 40-kg capacity or 1-Kg capacity SiC crucible using an electrical resistance furnace equipped with a rotary degassing impeller. The melting temperature was maintained at $750^{\circ}\text{C} \pm 5^{\circ}\text{C}$. For each alloy composition, the specified alloying elements were added using calculated amounts of the corresponding master alloys to obtain the desired addition levels. Table 3.2 shows the master alloys used for these additions.

Table 3.1 Chemical Composition of As-Received Al-2wt%Cu Base Alloy Ingots

Element	Cu	Si	Fe	Mn	Mg	Ti	Al
wt%	2	1.05	0.42	0.6	0.4	0.02	Bal.

Table 3.2 Master Alloys Used for Alloying Additions.

Addition	Master Alloy
Zr	Al - 15%Zr
Sc	Al - 2%Sc
Ti	Al - 5%Ti - 1%B
Sr	Al - 10%Sr
Ag	Al - 50% Ag
Si	Added in pure form

The additions were made using a perforated graphite bell which was plunged deep into the melt. The melt was degassed by injecting pure, dry argon gas into it for about 15 min to ensure the homogeneous mixing of the additions and to minimize the hydrogen absorbed into the melt. The melt surface was carefully skimmed to remove oxides and other inclusions before pouring. Chemical analysis sampling was carried out simultaneously for each alloy melt in order to obtain the actual chemical composition. The melts were poured into three different preheated molds based on the type of test involved, as described in the next section.

3.2 Casting Procedures

As mentioned previously, three different molds were used for casting based on the three alloy categories: (i) a preheated graphite mold was used for phase identification and thermal analysis purposes; (ii) an ASTM B-108 permanent mold was used for preparing test bars for tensile testing; and (iii) a constrained rod casting or CRC mold was used to test for hot-tearing susceptibility. All molds were preheated before use.

3.2.1 Graphite Mold Castings and Thermal Analysis

The alloys belonging to category i were melted in a 1-Kg capacity SiC crucible using an electrical resistance furnace and then poured into a cylindrical graphite mold preheated to 600°C, as shown in Figure 3.1. The alloy codes and compositions for the ten alloys are given in Table 3.3. With regard to the codes, the letters Z, S, G, M, represent additions of 0.5wt% Zr, 0.5wt% Sc, 0.2wt% Ti, 200 ppm Sr, and 0.5wt% Ag, respectively.

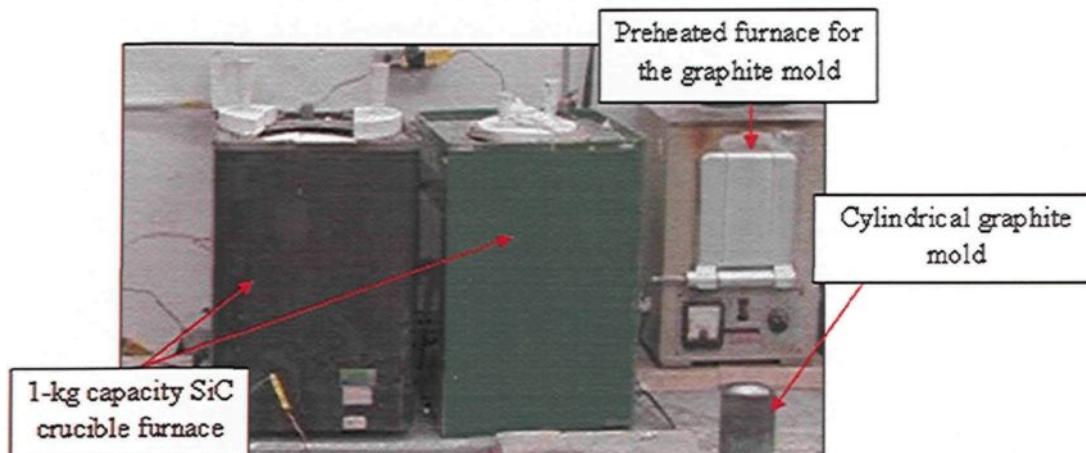


Figure 3.1 The thermal analysis set-up

Table 3.3 Chemical Composition of the Alloys Prepared for Phase Identification Purposes.

Alloy Code	Element (wt %)										
	Cu	Si	Fe	Mn	Mg	Ti	Zr	Sc	Sr	Ag	Al
Base Alloy	1.91	1.03	0.57	0.58	0.34	0.02	-	-		-	Bal.
Z	1.87	1.31	0.48	0.51	0.33	0.02	0.49	-		-	Bal.
GZ	1.8	1.3	0.44	0.47	0.32	0.19	0.51	-		-	Bal.
GMZ	1.86	1.32	0.47	0.47	0.31	0.18	0.5		0.02	-	Bal.
GMSZ	1.38	1.02	0.38	0.40	0.25	0.13	0.52	0.47	0.020	-	Bal.
S	1.95	1.84	0.44	0.47	0.34	0.02	-	0.47		-	Bal.
SZ	1.65	1.1	0.50	0.51	0.54	0.03	0.52	0.49		-	Bal.
GS	2.24	1.10	0.45	0.59	0.37	0.24	-	0.5		-	Bal.
GSZ	1.46	0.98	0.44	0.46	0.47	0.21	0.49	0.48		-	Bal.
GZSA	1.53	1	0.42	0.46	0.48	0.20	0.47	0.46		0.51	Bal.

Thermal analysis experiments were also carried out using the same set-up, and a thermocouple inserted through the bottom of the mold into the mold cavity, reaching up to one-third of the mold height along the mold center-line. The preheated graphite mold (600°C) provided close-to-equilibrium cooling conditions. A data acquisition system

attached to the thermocouple provided temperature-time data at a rate of 10 readings per sec. from which the cooling curve and first derivative curve could be plotted to determine the various reactions taking place during solidification.

The thermal analysis technique was also used to determine the time to reach the dendrite coherency point for the base alloy and the G3Z-alloy in order to investigate the influence of the grain refinement effect of Zr on the hot-tearing tendency. For this purpose, a second thermocouple was inserted at a distance of 5 mm from the inner boundary of the graphite mold in addition to the first thermocouple which was inserted along the mold center-line as shown in Figure 3.2. The dendrite coherency point was determined by measuring the difference in time between the two primary α -Al dendritic reactions detected by the two thermocouples.

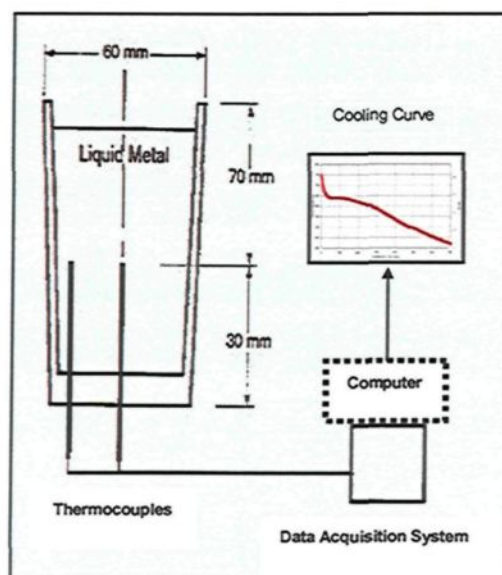


Figure 3.2 Schematic sketch of the positions of the inserted thermocouples.

3.2.2 Tensile Test Bar Casting

The Al-2wt%Cu base alloy was used to pour seventeen different alloys into an ASTM B-108 type permanent mold preheated to 455°C (cooling rate 7°C/s) to obtain castings for tensile tests, each casting providing two test bars, as shown in Figure 3.3. The seventeen alloys were prepared using different addition levels of Zr, Sc, Ti-B, Sr, Ag, and Si, individually or in combination, using the same master alloys as mentioned before. In order to facilitate recognizing the chemical composition of any alloy, the alloy codes were composed of letters and numbers referring to the element(s) added and the wt% of each element. In the alloy codes shown in Table 3.4 and Table 3.5, the letters S, G, M, and A represent 0.15wt% Sc, 0.15wt% Ti, 0.02wt% Sr, and 0.5wt% Ag additions, respectively, while 'Z' and 'Si' represent Zr and Si additions. As the latter two addition levels varied, numbers were used before the 'Z' and 'Si' to indicate the corresponding additions. Thus, in the case of Zr addition, the numbers 7, 5, 3, 1 before 'Z' in alloy code indicate 0.7, 0.5, 0.3, and 0.15wt% Zr, respectively, while the numbers 1 and 2 before 'Si' indicate 1 and 2wt% Si additions, respectively, in the alloys coded B1Si and B2Si in the two tables. B refers to the base alloy. Accordingly, the B1Si and G7Z alloys represent base alloy with 1wt%Si, and the base alloy with 0.15wt%Ti-0.7wt%Zr, respectively. The seventeen alloys were categorized into four sub-groups: Zr-Ti, Zr-Sr, Zr-Sc, and Si alloy groups. The alloy codes and compositions of the 17 alloys investigated are shown in Table 3.4. For each alloy composition, 50 castings or 100 test bars were prepared for tensile testing.

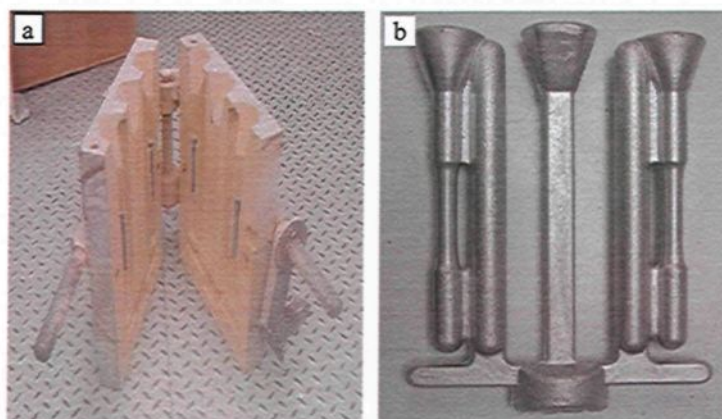


Figure 3.3 (a) ASTM B-108 type permanent mold; and (b) corresponding casting. Each casting provided two test bars for tensile testing.

Table 3.4 Chemical Composition of the Alloy Group Prepared for Tensile Properties Investigation

Alloy Code		Element (wt %)										
		Cu	Si	Fe	Mn	Mg	Ti	Zr	Sc	Sr	Ag	Al
Base Alloy		1.91	1.03	0.57	0.58	0.34	0.02	-	-	-	-	Bal.
Zr-Ti Group	7Z	1.83	0.97	0.54	0.57	0.32	0.02	0.68	-	-	-	Bal.
	G	1.85	0.99	0.55	0.54	0.31	0.18	-	-	-	-	Bal.
	G7Z	1.80	0.90	0.47	0.51	0.30	0.20	0.71	-	-	-	Bal.
	G1Z	2.06	1.15	0.52	0.57	0.35	0.13	0.14	-	-	-	Bal.
	G3Z	2.07	1.11	0.51	0.57	0.34	0.14	0.26	-	-	-	Bal.
	G5Z	2.08	1.10	0.51	0.58	0.34	0.11	0.47	-	-	-	Bal.
Zr-Sr Group	M	1.96	1.03	0.58	0.58	0.34	0.02	-	-	0.02	-	Bal.
	M7Z	1.85	0.98	0.57	0.57	0.32	0.03	0.71	-	0.016	-	Bal.
	GM	1.87	0.98	0.53	0.53	0.23	0.19	-	-	0.017	-	Bal.
	GM7Z	1.91	1.00	0.56	0.56	0.32	0.12	0.65	-	0.015	-	Bal.
	AGM7Z	1.91	1.0	0.54	0.54	0.31	0.18	0.35	-	0.016	0.55	Bal.
Zr-Sc Group	GS	1.45	0.83	0.42	0.41	0.27	0.11	-	0.14	-	-	Bal.
	GS1Z	1.40	0.81	0.41	0.41	0.26	0.11	0.13	0.15	-	-	Bal.
	AGS1Z	1.93	1.10	0.56	0.55	0.35	0.12	0.13	0.14	-	0.51	Bal.
Si Group	B1Si	1.93	1.79	0.59	0.59	0.36	0.03	-	-	-	-	Bal.
	B2Si	1.93	2.66	0.56	0.59	0.35	0.02	-	-	-	-	Bal.

Table 3.5 Chemical Composition of the Alloys Prepared for Hot Tearing Tests

Alloy Code	Al-2wt%Cu Base Alloy								
	Element (wt %)								
	Cu	Si	Fe	Mn	Mg	Ti	Zr	Sr	Al
Base Alloy	2.4	1.2	0.40	0.60	0.38	0.04	-		Bal.
M	2.4	1.2	0.41	0.63	0.37	0.06	-	0.025	Bal.
G	2.42	1.3	0.38	0.57	0.35	0.19	-	-	Bal.
G1Z	2.4	1.2	0.38	0.57	0.35	0.18	0.15	-	Bal.
G3Z	2.42	1.4	0.39	0.57	0.35	0.19	0.27	-	Bal.
B1Si	2.77	2.63	0.5	0.66	0.37	0.06	-	-	Bal.
Alloy Code	206 Alloy Type								
	Element (wt %)								
	Cu	Si	Fe	Mn	Mg	Ti	Zr	Sr	Al
206-Base Alloy	5.18	0.11	0.067	0.40	0.26	0.005	-	-	Bal.
206-M	5.45	0.43	0.078	0.39	0.24	0.015	-	0.018	Bal.
206-G	5.09	0.038	0.05	0.36	0.25	0.18		-	Bal.
206-G1Z	5.05	0.041	0.06	0.36	0.23	0.16	0.14	-	Bal.
206-G3Z	4.88	0.12	0.07	0.35	0.22	0.18	0.29	-	Bal.
206-B1Si	5.79	1.28	0.11	0.42	0.24	0.012	-	-	Bal.
206-B2Si	5.73	2.239	0.07	0.40	0.26	0.005	-	-	Bal.

3.2.3 Hot Tearing Test

Six alloys were selected from the alloys used for tensile testing in order to investigate the effect of chemical composition on the hot-tearing tendency of the Al-2wt%Cu base alloy, using different mold conditions. These alloys are the base alloy, and alloys M, G, G1Z, G3Z, and B1Si. Alloy 206 was used in parallel, as a reference to judge the hot-tearing susceptibility (HTS) results of the Al-2wt%Cu base alloy because the alloy 206 is a known commercial alloy and also contains very low Si content. The two base

alloys contained the same addition levels of alloying elements as those shown in Table 3.5. The sole exception was that 2% Si was added to the 206 alloy in order to bring its Si content to that of the B1Si alloy (B being the Al-2wt%Cu base alloy). The hot-tearing susceptibility (HTS) of these alloys was investigated using a constrained rod casting mold (CRC mold), as shown in Figure 3.4. In order to adjust and select the best hot tearing test specifications, two kinds of coatings (graphite and boron nitride lubricoat-Zv), different dwell times (2, 4, 8 min), and different mold slope angles (0° , 17°) were used. Based on trial tests the Boron Nitride Lubricoat-ZV coating, a dwell time of 4 min, and a mold slope angle of 0° were selected as the mold parameters for carrying out the hot tearing tests. The dwell time denotes the time period between the pouring of the melt and releasing the casting from the mold. The hot tearing tests were carried out at the following mold temperatures: 450°C , 400°C , 350°C , 300°C , and 250°C .

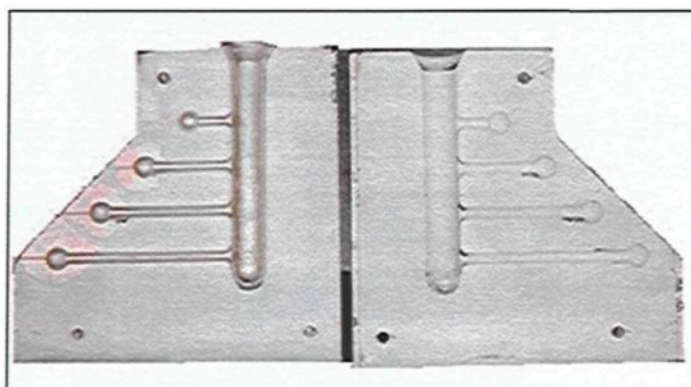


Figure 3.4 CRC hot-tearing test mold and casting.

As shown in Figure 3.5, the CRC mold consists of four bars A, B, C, and D of different lengths, namely 2in /5.1cm, 3.5in /8.9cm, 5in /12.7cm and 6.5in /16.51cm, respectively, all measuring 0.5in in diameter. The bars are constrained at one end by a sprue

and at the other end by a spherical riser (feeder) of 0.75in (1.9cm) diameter. The distance between each bar is 1.5in (3.81cm) from center to center. The metal is poured through the 7-in (17.8cm) sprue. The hot tearing sensitivity or HTS value for a sample was calculated using the following equation:

$$HTS = \sum (C_i \times L_i)$$

where C_i is a numerical value used to represent the degree or “level” of crack severity in the bar (see Table 3.6), and L_i is a numerical value assigned to the corresponding bar length (see Table 3.7).

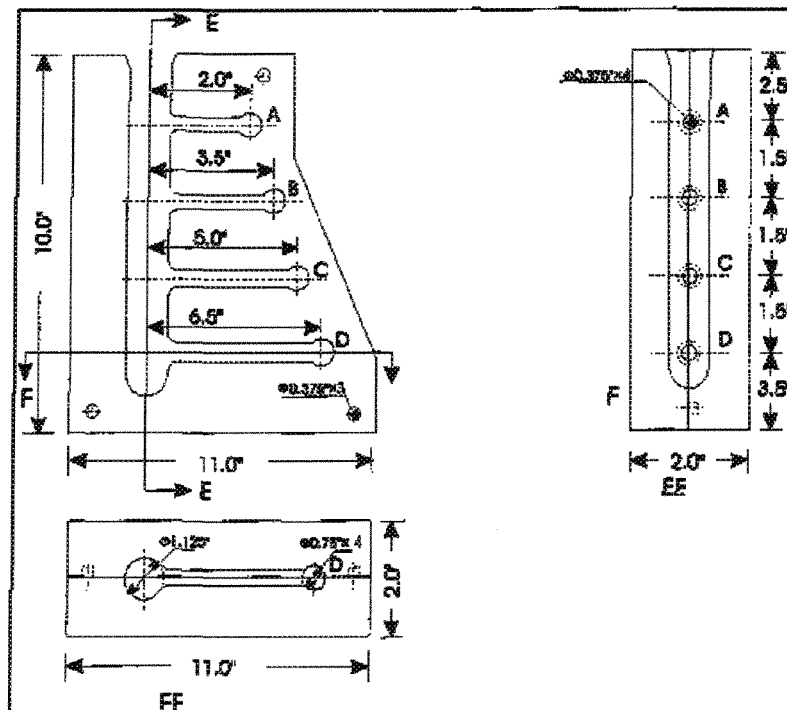


Figure 3.5 The dimensions of the CRC hot-tearing test mold.

Figure 3.6 shows the four levels which were used to classify the crack severity observed in the bars of the CRC mold castings. In fact, it was observed that the longer bars were less resistant to hot tearing than the shorter ones. Each HTS value reported was obtained from an average of five experiments.

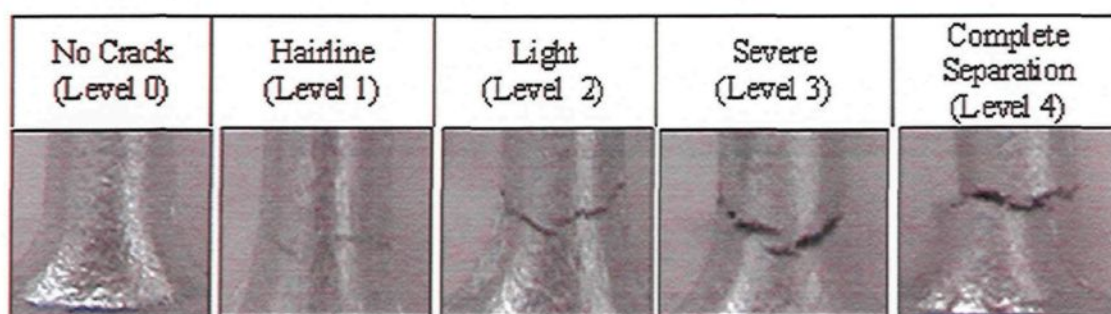


Figure 3.6 Categorization of crack severity level.

Table 3.6 Numerical Values C_i Representing Crack Severity

Category	Numerical Value of Crack Severity Level (C_i)
Complete Separation	4
Severe Crack	3
Light Crack	2
Hairline Crack	1
No Crack	0

Table 3.7 Numerical Values L_i Representing Bars of Different Lengths

Bar Type (Length inch)	Numerical Value (L_i)
A (2.0)	4
B (3.5)	3
C (5)	2
D (6.5)	1

3.3 Heat Treatment Procedures

In order to determine the optimum tensile properties, heat treatments were carried out on the as-cast tensile test bars and comprised three consecutive stages:

- (i) solution heat treatment at 490°C for 8 h;
- (ii) quenching in warm water at 60°C (the quenched samples were stored in a freezer at -20°C until aging was carried out to avoid natural aging.)
- (iii) artificial aging at two different temperatures, either at 180°C for various times (2, 4, 6, 10, 16, 24, and 48 h) or at 220°C for time periods of 0.5, 1, 1.5, 2, 4, 6, 10, 16, 24, and 48 h.

Five test bars were used for each heat treatment condition. The heat treatment was carried out in a fully programmable Blue M forced-air furnace with a temperature control of $\pm 2^\circ\text{C}$.

3.4 Tensile Testing

The standard dimensions of the tensile test bars obtained from the ASTM B-108 permanent mold as described in subsection 3.2.2 are shown in Figure 3.7. Ninety-five test bars (or 19 batches of 5 bars each) were tested per alloy composition as follows:

- (i) five test bars (or one batch) were tested in the as-cast-condition;
- (ii) five test bars tested in the solution heat-treated condition;
- (iii) eighty-five bars (or 17 batches) divided into two sets were tested in the T6-180°C and T6-220°C aged conditions as follows:

- The first set of thirty-five bars (or 7 batches) was aged at 180°C at the seven aging times of 2, 4, 6, 10, 16, 24, and 48 h.
- The second set of fifty bars (or 10 batches) was aged at 220°C at the ten aging times of 0.5, 1, 1.5, 2, 4, 6, 10, 16, 24, and 48 h.

The tensile testing was carried out using a Servohydraulic Mechanical Testing Machine at a strain rate of 1×10^{-4} /s. The average ultimate tensile strength, UTS, yield strength, YS, and elongation percentage, El (%), values were calculated over the five bars tested for each condition.

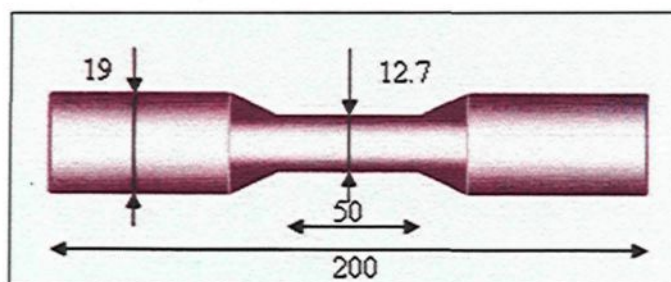


Figure 3.7 The dimensions (in mm) of a standard ASTM-B108 tensile test bar.

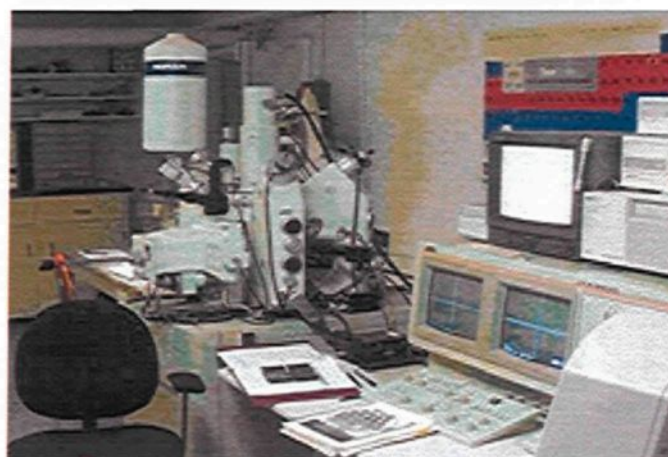
3.5 Metallography

In this study, the microstructure was investigated using optical microscopy and image analysis, and electron probe microanalysis (EPMA) including EDX and WDS analyses. Figure 3.8 shows the optical microscope-image analyzer system and the electron probe microanalyzer employed for these investigations.

Selected samples for metallographic investigations were sectioned, then mounted, ground, and polished to the required finish; Figure 3.9 shows the typical locations in different castings from where these samples were sectioned.



(a)



(b)

Figure 3.8 (a) Clemex image analyzer system, and (b) Electron probe microanalyzer- JEOL JXA-8900L

- (i) for the graphite mold castings, 2.5cm x 2.5cm samples were cut at 10 mm height from the bottom as shown in Figure 3.9(a);
- (ii) in the case of the tensile test bars, samples were taken from the gauge length at two different locations; the first was sectioned parallel to the cross section area of the tensile-tested bar, 10 mm below the fracture surface, as shown in

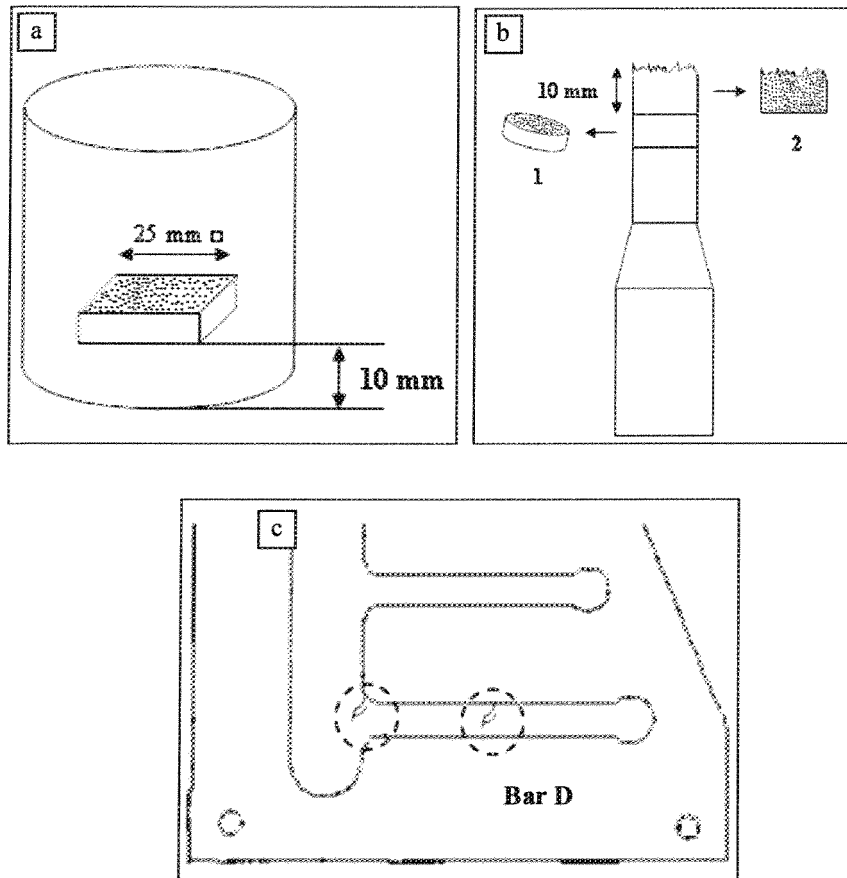


Figure 3.9 Locations of metallography samples sectioned from (a) graphite mold castings, (b) tensile-tested bars, and (c) CRC mold castings. The shaded or circled areas represent the surfaces which were examined.

- (iii) Figure 3.9(b) (sample #1); the second was sectioned longitudinally to examine the sample area below the fracture surface, as shown in Figure 3.9(b) (sample # 2);
- (iv) for the CRC mold castings, samples were sectioned from areas containing cracks in the hot-spot regions, usually located at the conjunction of the sprue with bar D or at the bar mid-section, as shown in Figure 3.9(c). It must be

noted that in this case, the metallography samples were sectioned from castings corresponding to mold temperatures of 250°C and 350°C only.

The preparation details of the metallographic samples are provided in Table 3.8.

Table 3.8 Mounting and Polishing Procedures

(1) Mounting: Sectioned sample was mounted in cold mounting resin (Phenolic resin combined with dially phthalate)
(2) Grinding: Mounted sample was subjected to grinding using consecutively finer grit size waterproof SiC papers (grit sizes 320, 400, 600, 800 and 1200)
(3) Polishing: Sample was polished using polycrystalline diamond suspension (6µm, 3 µm, for 3 min each), followed by colloidal silica suspension (0.06 µm) to obtain a mirror-like finish of the sample surface

Grain size measurements were carried out for all of the alloys investigated. For these measurements, after the final grinding stage, the samples were etched using a solution made up of 12.5g CrO₃, 2.5 ml HF, 30 ml HCl, 40 ml HNO₃, and 42.5 ml water. Measurements were then carried out using the optical microscope- Clemex image analyzer system and applying the line intercept method. Micrographs were obtained from the polished samples using optical microscopy.

The sizes measurements of α -Fe (Al_{1.5}(Mn,Fe,Cu)₃Si₂), θ (Al₂Cu) intermetallic phase particles, and porosity (%) were measured for a number of selected metallography samples, using the image analyzer in conjunction with the optical microscope.

A JEOL JXA-8900L electron probe microanalyzer, with EDX and WDS facilities, was used mainly to detect and analyse the chemical compositions of the various intermetallic phases which formed during solidification. Volume fraction and line-scan measurements were also carried out using the same set-up. X-ray images of various elements constituting the identified phases were also obtained to determine the distribution of these elements in the phases. In these cases the samples were cleaned in high purity ethanol in an ultrasonic agitator before being examined in the electron probe microanalyzer.

CHAPTER 4
PHASE IDENTIFICATION AND QUANTIFICATION

CHAPTER 4

PHASE IDENTIFICATION AND QUANTIFICATION

As mentioned earlier, ten different compositions of the Al-2wt%Cu base alloy were prepared by adding a number of transition elements such as Zr, Sc, and Ti, either individually or in combination with each other; in order to study the precipitation behavior of their intermetallics during solidification and also to determine the effects of these elements and their intermetallics on the microstructural constituents of the Al-2wt%Cu base alloy. The possibility of the interaction between the transition elements and Sr and Ag was investigated by adding 200 ppm Sr and 0.50 wt% Ag. The dominant intermetallic compounds of the base alloy formed during solidification by the interactions between the main constituent elements of the base alloy were also investigated.

A low cooling rate (0.3°C/s) and a high concentration of the transition elements (0.50 wt%) were selected in order to activate the precipitation sequences and also to facilitate their detection and analysis. Again the techniques which were applied to investigate the solidified intermetallic compound phases are as follows: thermal analysis providing information about the main phase reactions in the base alloy, electron probe microanalysis (EMPA) in conjunction with EDX and WDS providing chemical analysis and the morphological features of the phases, and using an optical microscope in

conjunction with a Clemex image analyzer to provide the measurements of grain size and microstructure constituents.

This chapter will be composed of three main subsections with the following headings:

- Base alloy intermetallic phases
- Transition elements intermetallic phases (Zr, Sc)
- Grain Structure

4.1 Base Alloy Intermetallic Phases

The base alloy under investigation contains around 2wt% Cu, 1wt% Si, 0.42wt% Fe, 0.6wt% Mn, 0.40wt% Mg, and 0.02wt% Ti; it can hence be classified as an Al-Cu alloy. Based on the composition mentioned above, the main phases expected for this alloy will be restricted in Cu-rich intermetallic phases as well as iron-rich intermetallic phases. In order to determine the main intermetallic phases and their formation reactions in the base alloy, thermal analysis techniques were applied under low cooling condition $\sim 0.3^\circ\text{C/s}$.

Based on the thermal analysis data obtained, the cooling curve and first derivative are drawn, as shown in Figure 4.1, from which it is possible to follow up the main reactions during the course of the solidification of the base alloy. This alloy starts to solidify at 640°C (Reaction Number One) through the development of the dendritic network followed by the precipitation of α -iron ($\text{Al}_{15}(\text{Mn,Fe,Cu})_3\text{Si}_2$) at 619°C (Reaction Number Two) and then Al_2Cu and $\text{Al}_5\text{Mg}_8\text{Cu}_2\text{Si}_6$ precipitate simultaneously as a last reaction at 495°C (Reaction Number Three). Figure 4.2 shows the possible morphology of the abovementioned intermetallics; thus α -iron ($\text{Al}_{15}(\text{Mn,Fe,Cu})_3\text{Si}_2$) appears as compacted Chinese script which is gray in color, while the Al_2Cu -phase may appear

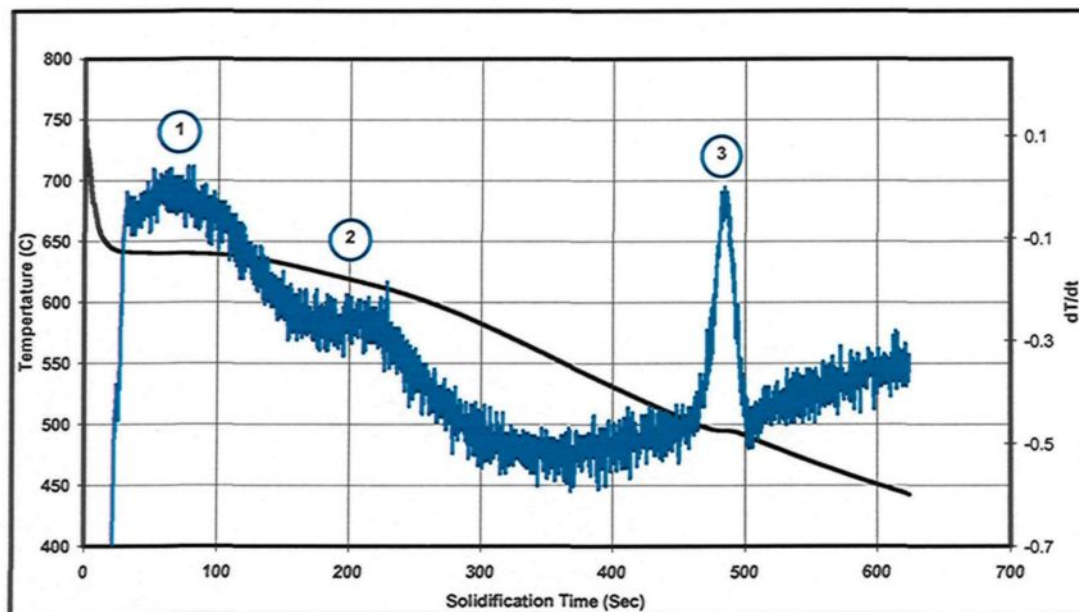


Figure 4.1 Cooling curve and first derivative of Al-2wt%Cu base alloy

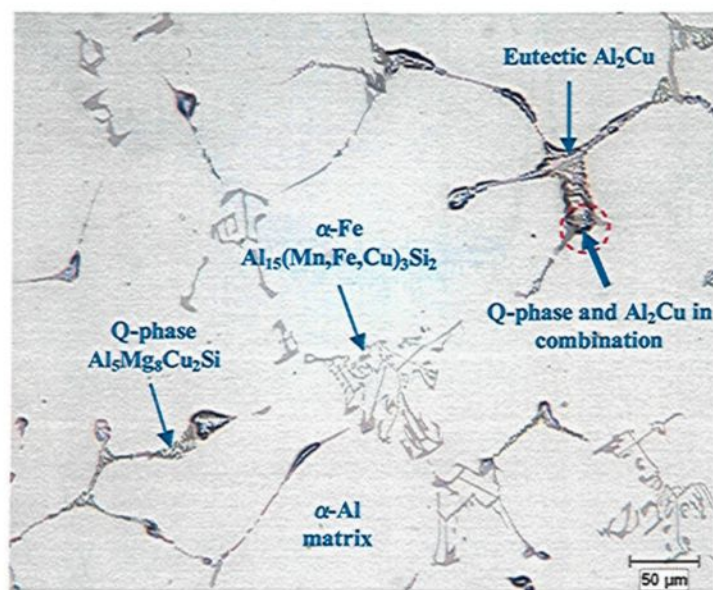


Figure 4.2 Optical microstructure of Al-2wt%Cu base alloy.

either in eutectic form (Al + Al₂Cu) or as blocklike particles which are pink in color. The Q-phase, Al₅Mg₃Cu₂Si₆, may appear in the form of small particles which are dark gray in

color and may be found in combination with the Al_2Cu phase or alone. Based on the preceding, the Al-2wt%Cu base alloy possesses simple microstructural components consisting of three main intermetallics, namely $\text{Al}_{15}(\text{Mn,Fe,Cu})_3\text{Si}_2$, Al_2Cu , and $\text{Al}_5\text{Mg}_8\text{Cu}_2\text{Si}_6$, in addition to the α -Al matrix.

The previous phases were also detected and analyzed using electron probe microanalysis, as shown in Figure 4.3 (a) and (b) which reveal that the same features were obtained using optical microscopy. The coarse morphology of the α -iron, the Al_2Cu and the $\text{Al}_5\text{Mg}_8\text{Cu}_2\text{Si}_6$ phases may be attributed to the low silicon content and to the low cooling rate of 0.3°C/s . The low Si level in the alloy contributes to the production of a larger fraction of the primary α -Al which in turn causes the final Cu- and Fe- enriched liquid to become concentrated in a few large-sized liquid pools. The intermetallic particles will thus precipitate in these regions in the form of long interconnected particle stringers. This effect of low Si-content is found to be in agreement with results obtained by Cáceres *et al.*¹³⁴

At the same time, it was observed that the low cooling rate provides the required period for the significant growth of intermetallic particles through solidification thereby producing coarse size particles; this low cooling effect has also been reported in a number of other studies.^{5,135} In spite of the presence of a high iron content in the base alloy, the β -iron phase did not precipitate, whereas the α -iron phase was detected. This fact may be attributed to the high Mn content in this alloy for which there are previous reports^{12,136,137} that the Mn neutralizes the Fe content by promoting the formation of α -iron displaying Chinese script morphology at the expense of the formation of β -iron displaying platelet morphology.

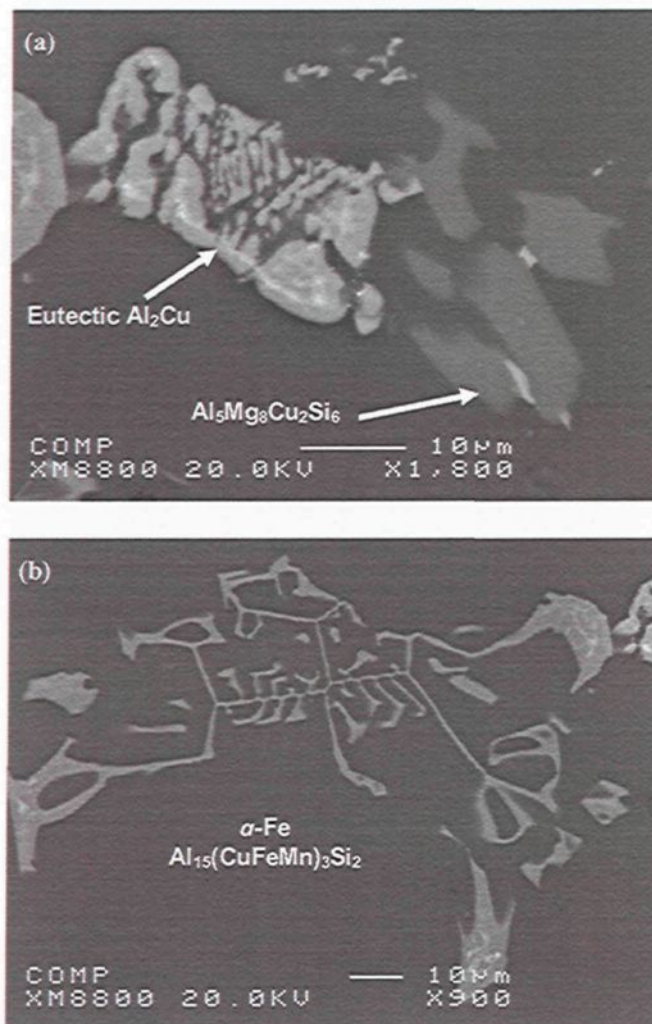
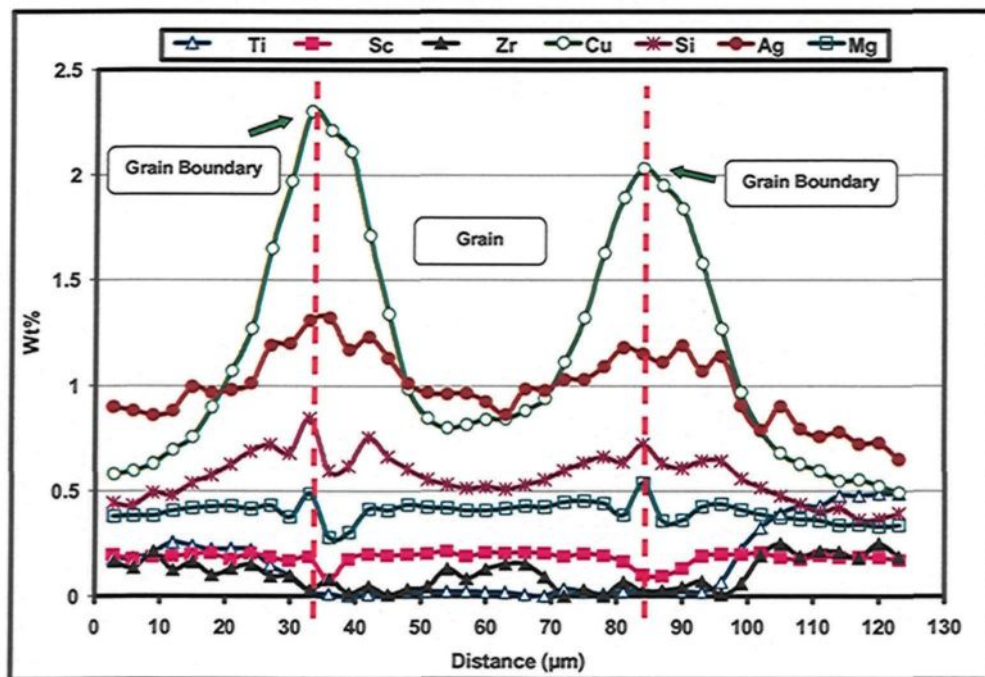


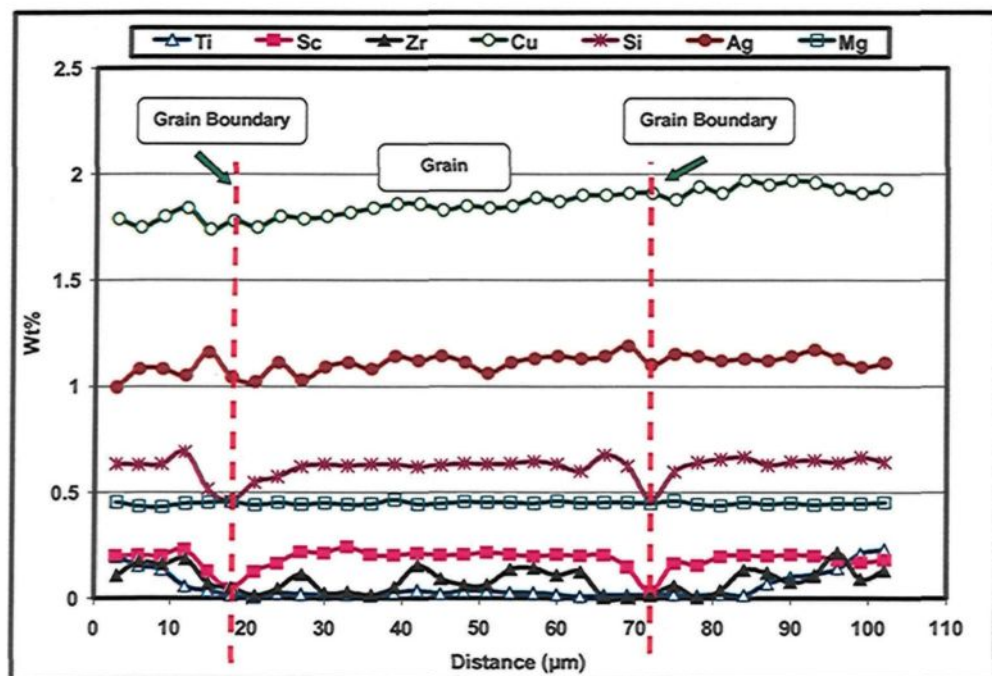
Figure 4.3 Backscattered Image of (a) eutectic- θ phase (Al_2Cu) in combination with Q-phase ($\text{Al}_5\text{Mg}_8\text{Cu}_2\text{Si}_6$), and (b) α -Fe phase ($\text{Al}_{15}(\text{CuFeMn})_3\text{Si}_2$).

4.2 Zr and Sc Intermetallic Phases

In this section, intermetallics containing either Zr or Sc, or both will be investigated in order to understand their formation sequences. It is important to be aware of the distribution of the different alloying elements in the matrix which would then contribute to understanding the manner of the formation of these intermetallics. Accordingly, line scans were carried out between two grain centers in the GSZA-alloy, *i.e.* the one containing a grain refiner, and Sc, Zr, and Ag additions, using as-cast and solution heat-treated samples; an example of this is given in Figure 4.4. Based on the



(a)



(b)

Figure 4.4 Line scan results showing the distribution of various elements across α -Al grains in the matrix of the GSZA-alloy (0.2wt%Ti-0.5wt%Sc-0.5wt%Zr-0.5wt%Ag) samples: (a) as cast condition; (b) solutionized condition.

distribution curves of the different elements, it will be noted that the alloying elements Cu, Si, Mg, and Ag are segregated during solidification and then redistributed uniformly during the solution heat treatment. This behavior is not observed for the transition elements which, showing no such segregation effects in the cast structure, are thereby not affected by the solution heat treatment to the same extent.

This contrast in behavior between the alloying elements (Cu, Si, Mg, Ag) and the transition elements (Zr, Sc, Ti) may be attributed to the differences in their solid solubility in aluminum, since the alloying elements Cu, Si, Mg, and Ag are more highly solid-soluble than the transition elements Zr, Sc, and Ti. For example, the solid solubility of Zr and Sc in aluminum is 0.05 wt% and 0.1 wt% at 500°C which is considered low compared with the solid solubility of Cu (4.05 wt%) at 504°C and the solid solubility of Si (0.8 wt%) at 500°C. Also, it is worth noting that the peaks detected at the grain boundaries indicate the existence of intermetallic phases which form and are localized at the grain boundary during solidification; these include Al_2Cu , $\text{Al}_5\text{Mg}_8\text{Cu}_2\text{Si}_6$ and so forth. As the solution heat treatment is applied, almost all of these intermetallics dissolve and their elements return to the matrix; this, however, is not applicable in the situation of transition element intermetallic phases.

4.2.1 Scandium Intermetallics

4.2.1.1 $\text{Al}_3(\text{Sc}_{1-x}\text{Zr}_x)$ -Star Intermetallic Phase

The star-like phase, $\text{Al}_3(\text{Sc}_{1-x}\text{Zr}_x)$, is considered to be the most important of the Sc-Zr intermetallics because of its heightened efficiency in nucleating α -Al grains. This type of efficiency may be attributed to the L1_2 -crystal structure of the star-like phase

which is characterized by its low mismatch with the α -Al lattice structure.¹³⁸ In addition, as this phase forms within a temperature range of 655-663°C which is higher than that of the α -Al phase, it has the possibility for being used as a potent grain refiner for a wide selection of aluminum alloys^{139,140}

Based on extracts from the existing literature in the field, the nucleation and growth processes of the star phase are not yet clear, and the roles of Zr and Sc in the formation of this phase are as yet unknown and require further clarification. In addition, the effects of alloy composition and heat treatment on the star phase have not yet been investigated in depth, either. The results presented in this section will attempt to shed some light on these points.

Figure 4.5 (a) shows the backscattered image of a star phase particle observed in the SZ-alloy (0.5Sc-0.5Zr). It will be seen that the star phase particle consists of different layers which may be discerned by the variations in brightness across the four arms of the particle. The change in the brightness from layer to layer indicates that the Zr and Sc concentrations are varied within the star phase, since the atomic number of Zr (40) is higher than the atomic number of Sc (21), so that the Zr-rich layer will be brighter than the Sc-rich layer. The layers also indicate that the star phase grows through the accumulation of layers having different compositions as solidification proceeds. The line scan taken across one of the arms of the star phase particle shown in Figure 4.5(a) reveals that the zirconium concentration in the particle center is high. Based on the WDS analysis of the particle shown in Figure 4.5 (b), the average composition of the star phase was determined to be $Al_{3.18}(Sc_{0.5}Zr_{0.5})$. Accordingly, the composition of $Al_{3.18}(Sc_{0.5}Zr_{0.5})$ may

be found in relation to the chemical composition of the SZ-alloy which contains equal amounts of scandium and zirconium with a Zr:Sc ratio equal to unity. This composition

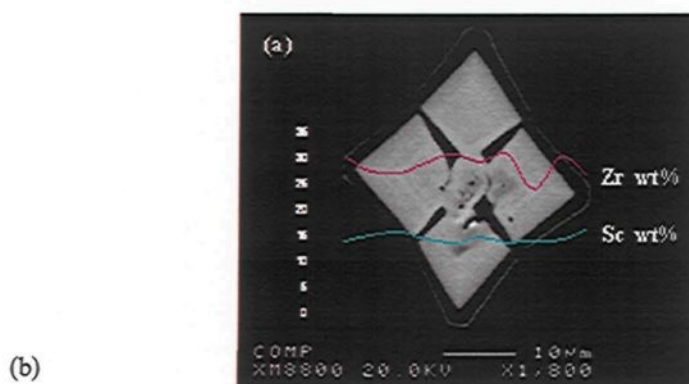


Figure 4.5 (a) Backscattered image taken from the SZ alloy (0.5wt%Sc-0.5wt%Zr) sample, showing a particle of the star-like intermetallic Al₃(Sc_{1-x}Zr_x) phase; (b) corresponding WDS analysis of (a). Pink and blue line scans across the particle in (a) show the concentrations of Zr and Sc across the particle.

corresponds to a Zr:Sc ratio of 1 in keeping with the Zr and Sc levels present in the SZ-alloy.

To investigate the variation in composition further, X-ray mapping was carried out in addition to WDS analysis, an example of which is shown in Figure 4.6 for a star phase particle observed in the GSZ-alloy (0.2Ti-0.5Sc-0.5Zr). The same layers detected in the star phase particle shown in Figure 4.5 are also noted in the backscattered image shown in Figure 4.6 (a), thereby confirming that the star-phase particle grows in different stages during solidification. Careful examination of the X-ray maps of Sc and Zr reveals that the Sc concentration is high in the intermediate regions of the particle (distinguished by pink and red colors), whereas the scattered red points in the center region denote points of high Zr concentration. From the corresponding WDS analysis, composition of

the star phase was determined to be $\text{Al}_{3.05}(\text{Sc}_{0.46}\text{Zr}_{0.41}\text{Ti}_{0.13})$, showing once again the relation between the composition of the star phase and the alloy composition.

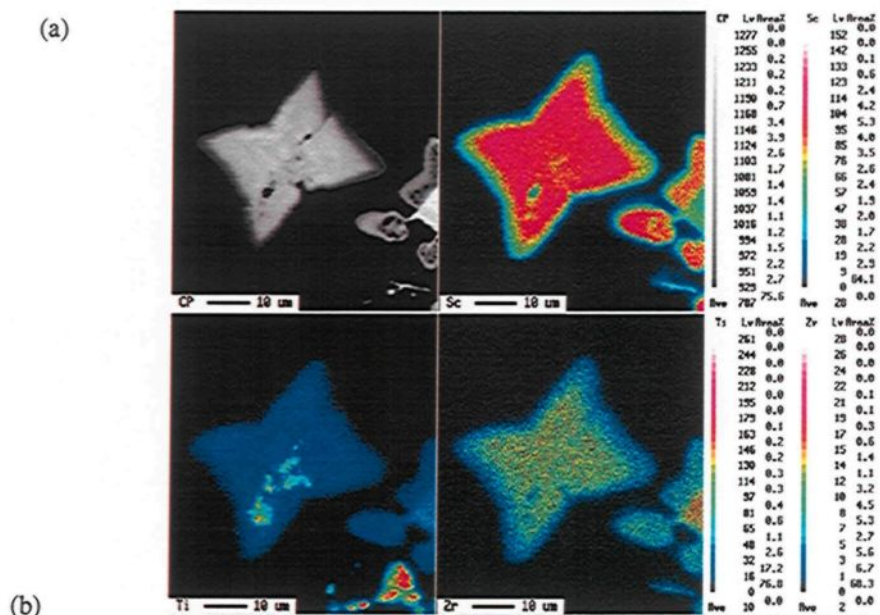


Figure 4.6 (a) Backscattered image showing a $\text{Al}_3(\text{Sc}_{1-x-y}\text{Zr}_x\text{Ti}_y)$ phase particle in the GSZ-alloy (0.2wt%Ti-0.5wt%Sc-0.5wt%Zr), and corresponding X-ray images of Sc, Ti and Zr; (b) corresponding WDS analysis of (a).

When 0.2wt% Ti is added to the SZ-alloy, *i.e.* the GSZ-alloy, the composition of the star phase is changed from $\text{Al}_{3.18}(\text{Sc}_{0.5}\text{Zr}_{0.5})$ to $\text{Al}_{3.05}(\text{Sc}_{0.46}\text{Zr}_{0.41}\text{Ti}_{0.13})$. These findings indicate that the alloy content of the transition elements influences the composition of the star phase. In Figure 4.6 (a), the presence of Ti-rich intermetallic particles, which might be either TiB_2 or TiAl_3 , at the centre of the star-like particle suggests that they may play a role in the nucleation of the star phase.

In the light of the above data and that of the observations noted in Figure 4.5 and Figure 4.6, two mechanisms may be suggested to explain the formation sequence of the

star phase. In the first mechanism, as the alloy melt passes the liquidus line, crystals of Al_3Zr are primarily nucleated; these nuclei then grow by absorbing the zirconium from the surrounding liquid. As the zirconium is depleted from these regions, the nuclei of the star phase, namely Al_3Zr , continue to grow through the precipitation of Al_3Sc on the surface of these nuclei. At this point, the Al_3Zr starts to precipitate on the surface of Al_3Sc as the scandium also begins to become progressively depleted from the surrounding liquid, and so on in sequence. The fluctuations in the precipitation sequences are considered to be the main reason of the layer formation throughout the star phase.¹⁴¹ Also, it was established previously^{142,143,144} that the Al_3Zr phase solidifies as a primary phase through a peritectic reaction and subsequently interacts with the Al-liquid in an invariant reaction to nucleate Al_3Sc as follows: $\text{L} + \text{Al}_3\text{Zr} \rightarrow \text{Al}_3\text{Sc} + \text{Al}$.

From the line scan shown in Figure 4.5 (a) and the X-ray mapping for Zr shown in Figure 4.6 (a) which both show high Zr concentrations in the center of the star phase, it is reasonable to conclude that the Al_3Zr phase acts as a nucleus for the star phase.

In the second mechanism suggested, it is believed that since the Al_3Zr phase nucleates as the primary phase, the star phase grows predominantly through the precipitation of Al_3Sc on the surface of the Al_3Zr in the form of layers displaying different degrees of brightness. The variation in brightness from one layer to another is ascribed to the variation in the amount of Zr atoms replacing Sc atoms in the Al_3Sc phase. Since Al_3Sc is known to dissolve zirconium up to 35 wt%,⁷⁶ this suggestion is in conformity with the WDS results shown in Figures 4.5 and 4.6, where it will be noted that the stoichiometric composition of the star phase is mainly Al_3Sc with 25% to 30% Zr solid solution. The second mechanism may thus be considered more feasible than the

first. A schematic sketch of the formation sequence for the star phase is provided in Figure 4.7, based on the second mechanism.

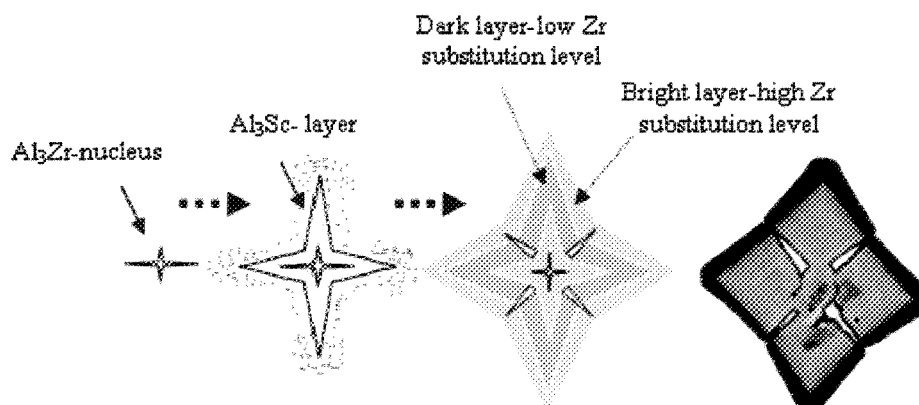


Figure 4.7 Schematic diagram showing the formation and growth sequence of the $\text{Al}_3(\text{Sc}_{1-x}\text{Zr}_x)$ -star-like phase particle.

It is worth mentioning here that, although the Sc content of 0.5 wt% used in the alloys studied is lower than the eutectic composition of 0.55 wt%, the Al_3Sc phase is still formed in Zr-containing alloys. This formation may be attributed to the operation of two effects; the first is that the zirconium may lower the eutectic composition required for the formation of Al_3Sc , which is in agreement with what has already been suggested earlier by other authors.^{145,146} In the second case, it is believed that the formation of Al_3Zr particles provides favored nucleation sites which promote the formation of Al_3Sc through the accumulation of Sc atoms forming clusters which, in turn, continue to grow into Al_3Sc particles.

The question arises here as to whether the growth of the star phase is completed in the liquid state or whether it continues to grow when in the solid state. In order to answer this question, X-ray mapping of the $\text{Al}_3(\text{Sc}_{1-x-y}\text{Zr}_x\text{Ti}_y)$ star phase observed in solution heat-treated GSZA-alloy (490°C/8h) was carried out, as shown in Figure 4.8(a), which presents the backscattered image of a star-like particle taken from the solution heat-

treated GSZA-alloy sample (0.2Ti-0.5Sc-0.5Zr-0.5Ag) and from the corresponding X-ray images of Sc, Zr and Ti. The X-ray mapping for Sc reveals that the edge of the star phase

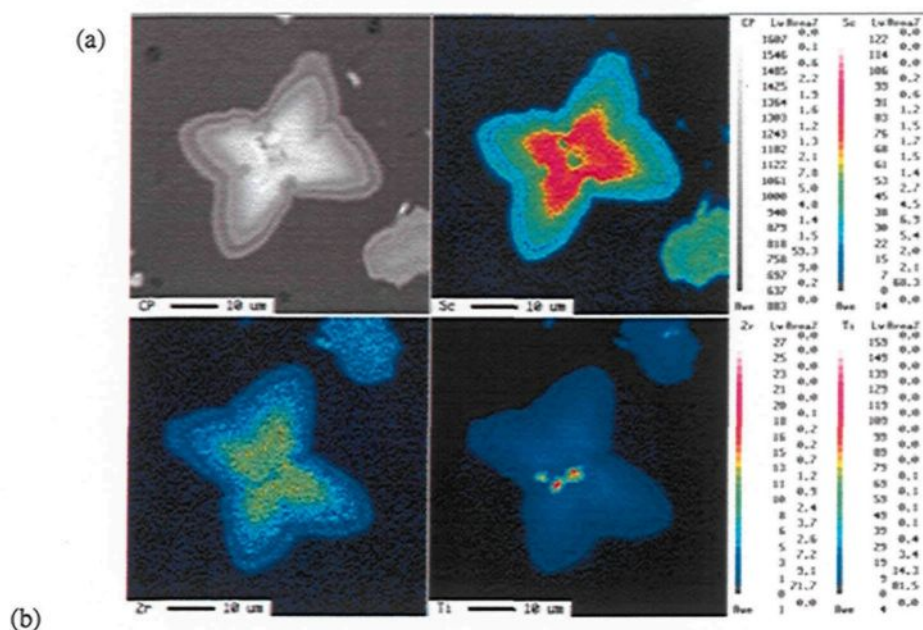


Figure 4.8 (a) Backscattered image showing an $Al_3(Sc_{1-x-y}Zr_xTi_y)$ phase particle in the GSZA-alloy (0.2wt%Ti-0.5wt%Zr-0.5wt%Sc-0.5wt%Ag) in the solution heat-treated condition (490°C/8 h), and corresponding X-ray images of Sc, Zr and Ti; (b) corresponding WDS analysis of (a).

particle displays a region of low Sc concentration (colored royal blue) separated by layers of high Sc concentration (colored turquoise) on either side. The inner turquoise layer represents the end of the growth process of the star phase during solidification, while the outer turquoise layer represents growth during the solution heat treatment through the absorption of Sc to form Al_3Sc (*i.e.* in the solid state).

From Figure 4.8(a), it may also be seen that the length across the star phase particle has increased from 35 μm to 45 μm on going from the innermost layer to the

outermost edges of the particle. This increase in size of the star phase during solution heat treatment will deplete scandium from the matrix, thereby affecting the age-hardening process and consequently, the tensile properties also. The presence of the Ti-intermetallic particles at the center of the star phase, as shown in Figure 4.8(a), reinforces the suggestion that they may act as nucleation sites for the star phase. The WDS analysis of the $\text{Al}_3(\text{Sc}_{1-x-y}\text{Zr}_x\text{Ti}_y)$ star phase particle shown in Figure 4.8(a) reveals that it corresponds to the formula $\text{Al}_{3.05}(\text{Sc}_{0.46}\text{Zr}_{0.41}\text{Ti}_{0.13})$, as shown in Figure 4.8(b).

4.2.1.2 Al_3Sc Intermetallic Phase

Based on the Al-Sc phase diagram, scandium forms the trialuminide Al_3Sc , with the L1_2 crystal structure type, in a eutectic reaction at 0.55 wt% Sc and 655°C .^{76,146} This compound has a great capacity for acting as a nucleant in α -Al due to the similarity of its crystal structure with that of the aluminum.¹⁴⁶ In this study, the Sc content is 0.5 wt%, thus the formation of the primary Al_3Sc intermetallic compound is not expected to take place during solidification. This was confirmed by the fact that primary particles of Al_3Sc phase were difficult to find in the alloys under investigation.

Figure 4.9 (a) shows an example of Al_3Sc phase particles in a backscattered image taken from the S-alloy, containing 0.5 wt% Sc. The corresponding EDX spectrum and WDS analysis are shown in Figure 4.9 (b) and (c), respectively. It will be noted that the Al_3Sc phase appears in the form of aggregated particles lacking regular shape. Based on the WDS analysis, the chemical formula of the phase is found to be $\text{Al}_{3.62}\text{Sc}$; the excess Al atoms which may be noted in this last chemical formula for $\text{Al}_{3.62}\text{Sc}$ is the result of measuring a part of the α -Al matrix during the detection process.

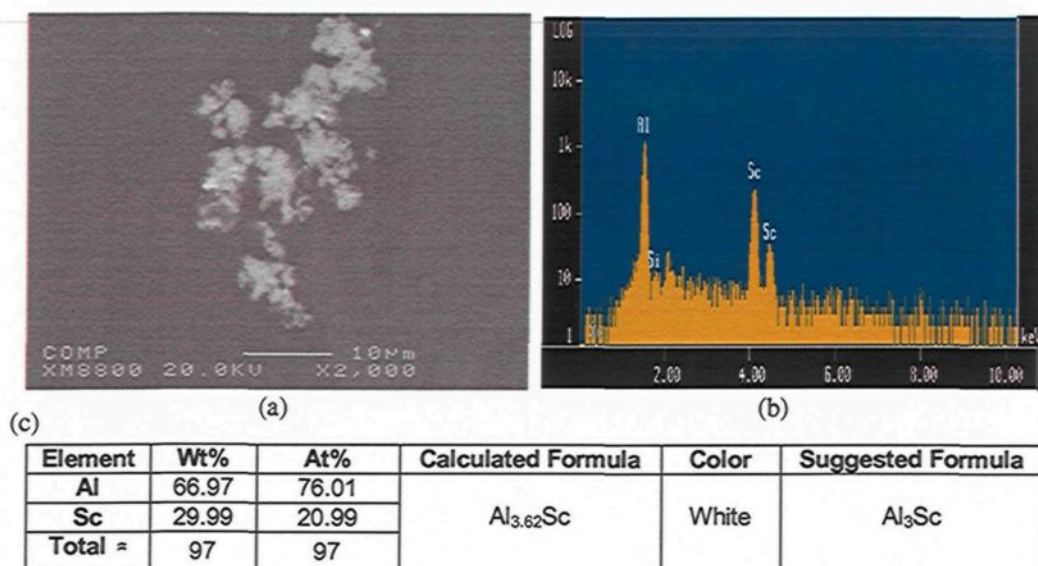


Figure 4.9 (a) Backscattered image taken from S-alloy (0.5wt%Sc) showing clusters of primary Al_3Sc intermetallic particles; (b) corresponding EDX spectrum; and (c) WDS analysis (c).

The formation of Al_3Sc in the S-alloy in the form of irregular aggregated particles may be attributed to the fact that the Sc content of the alloy (0.5 wt%) is lower than the eutectic composition (0.55 wt%). In such a case, it is reasonable to assume that the Sc will behave like Zr and form atom clusters which will in turn interact and grow to form irregular primary phase particles with a stoichiometric composition close to Al_3Sc ; all this is in good agreement with previously reported data.¹⁴⁷

4.2.1.3 V-Phase (AlSc_2Si_2)

The V-phase is a ternary intermetallic compound (AlScSi) formed through invariant reactions,^{148,149,150} and may be distinguished by its dark grey color and a stoichiometric composition of AlSc_2Si_2 .^{147,151} In this study, different forms and sizes of the V-phase particles, whether massive or plate-like, were detected in the Sc-containing alloys.

Figure 4.10 displays the backscattered image obtained from the GS-alloy sample, showing the presence of the V-phase in the form of a grey particle, acting as a nucleating surface for the eutectic- Al_2Cu phase; the composition of the V-phase obtained from WDS analysis is $\text{Al}_{1.1}\text{Sc}_2\text{Si}_{1.9}$. The V-phase, namely $\text{Al}_{1.2}\text{Sc}_2\text{Si}_2$, may also be observed in the S-alloy in combination with the Q-phase, namely $\text{Al}_{3.36}\text{Mg}_8\text{Cu}_{1.8}\text{Si}_{6.16}$, as shown in Figure 4.11.

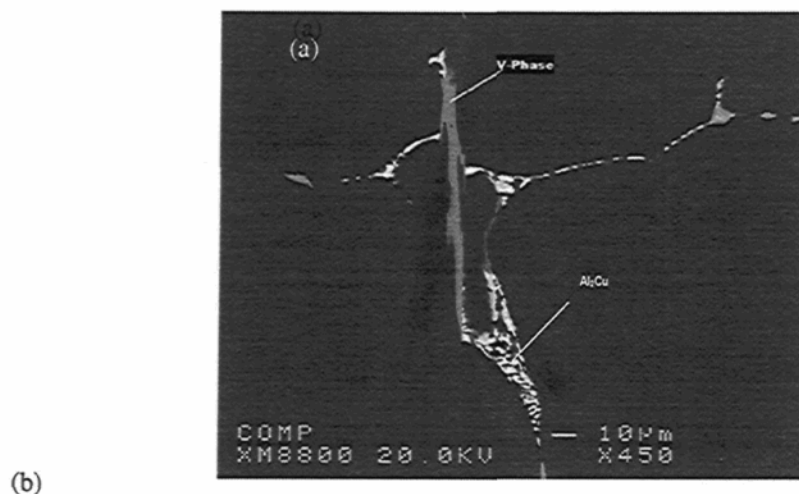


Figure 4.10 (a) Backscattered image taken from SG-alloy (0.2wt%Ti-0.5wt%Sc) sample, showing the occurrence of the V-phase intermetallic particle together with the Al_2Cu phase, and (b) the corresponding WDS analysis.

From the corresponding X-ray mappings of the Si, Mg, Sc, and Cu elements throughout the V-phase and Q-phase shown in Figure 4.12, it is possible to identify the gradual distribution of silicon between the V-phase and the Q-phase, as well as to distinguish the conformity in the surface contour between the V-phase and the Q-phase, indicating the nucleation role played by the V-phase in the Q-phase.

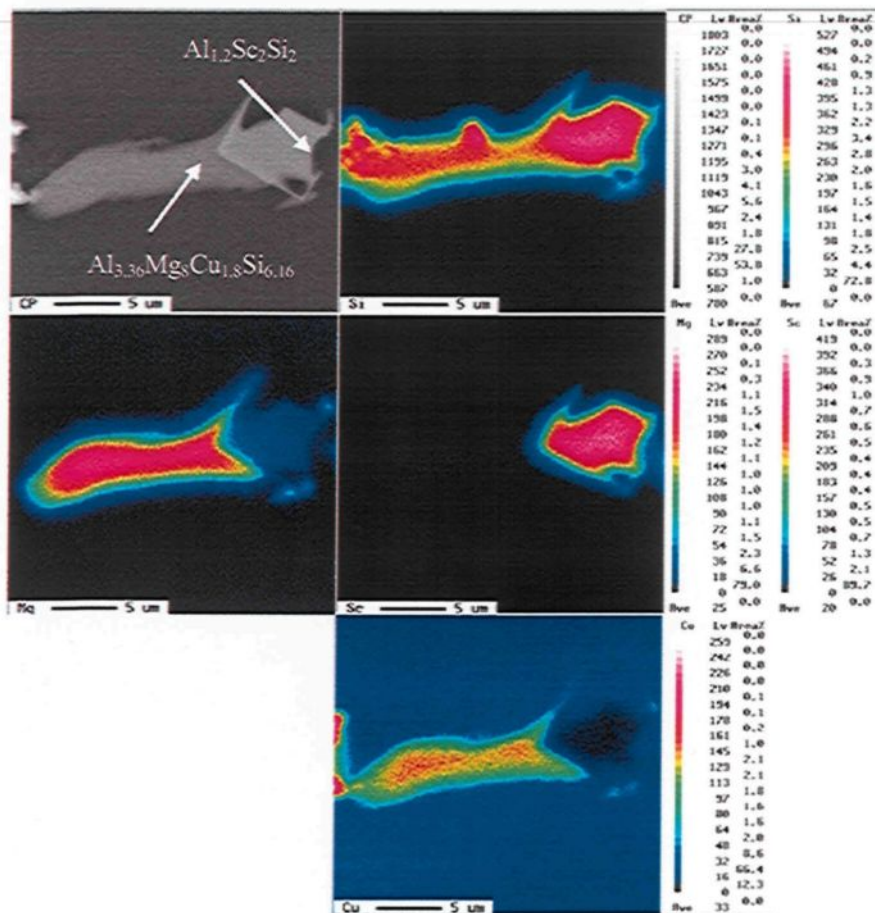
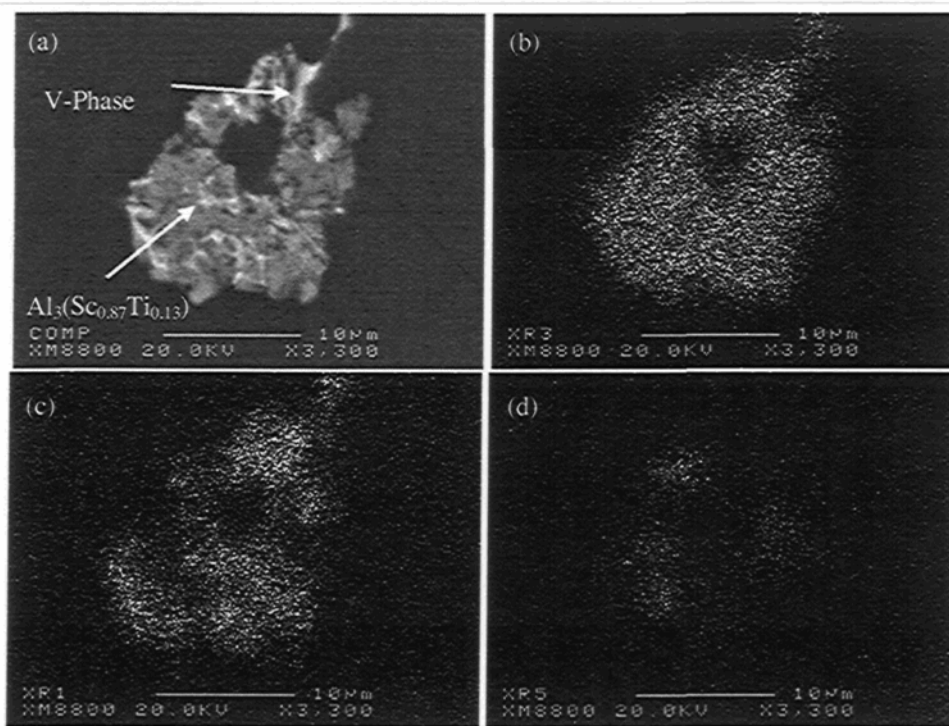


Figure 4.11 Backscattered image showing the V-phase in combination with the Q-phase and the corresponding X-ray mapping images of Si, Mg, Sc, and Cu.

A different morphology for the V-phase was also observed in the SG-alloy sample, as shown in Figure 4.12 (a), where V-phase particles, having a composition of $Al_5Sc_2Si_{1.6}$ appear to envelop the scandium trialuminide particles, whose composition was found to be $Al_{2.73}(Sc_{0.79}Ti_{0.21})$ from the corresponding WDS analysis. The presence of the V-phase on the rim of the $Al_{2.73}(Sc_{0.79}Ti_{0.21})$ phase particle makes its detection difficult and increases the possibility of involving a part of the matrix during detection; this is the reason for the high concentration of Al in the $Al_5Sc_2Si_{1.6}$ phase detected. The X-ray images for Sc, Si, and Ti, shown in Figure 4.12 (b), (c), and (d), reflect these results.



(e)

Element	Wt%	At%	Calculated Formula	Color	Suggested Formula
Al	49.68	57.737	$\text{Al}_5\text{Sc}_2\text{Si}_{1.6}$	Grey	AlSc_2Si_2
Si	16.56	18.483			
Sc	32.4	22.593			
Total ≈	98.64	98.813			
Al	59.27	71.93	$\text{Al}_{2.73}(\text{Sc}_{0.79}\text{Ti}_{0.21})$	Dark Grey	AlSc_2Si_2
Sc	28.54	20.79			
Ti	8.11	5.545			
Total ≈	96	98.26			

Figure 4.12 (a) Backscattered image taken from the GS-alloy (0.2wt%Ti-0.5wt%Sc) showing the presence of V-phase and $\text{Al}_3(\text{Sc,Ti})$ intermetallic phase particles, and (b), (c), (d) corresponding X-ray images of (b) Sc, (c) Si, (d) Ti; (e) WDS analysis of the two phases shown in (a).

As may be seen from Figures 4.10 through 4.12, the V-phase appears in combination with, or enveloping, other phases such as the Q-phase, the Al_2Cu phase, or the $\text{Al}_{2.73}(\text{Sc}_{0.79}\text{Ti}_{0.21})$ phase. These latter phases, whether the $\text{Al}_{2.73}(\text{Sc}_{0.79}\text{Ti}_{0.21})$ phase or the Al_2Cu phase and the Q-phase, form within two different temperature ranges of 655-660°C and 500-520°C, respectively.⁵ These findings imply that the V-phase is formed through two separate invariant reactions, one occurring at a high temperature, as in the case of enveloping scandium trialuminide, and the other at a relatively low temperature as

in the case of nucleating Al_2Cu and Q-phase. These observations are in agreement with what has been reported in other parallel studies,^{77,148} namely, that the V-phase is first formed in a peritectic reaction between the Al_3Sc and L-(Al) as follows:



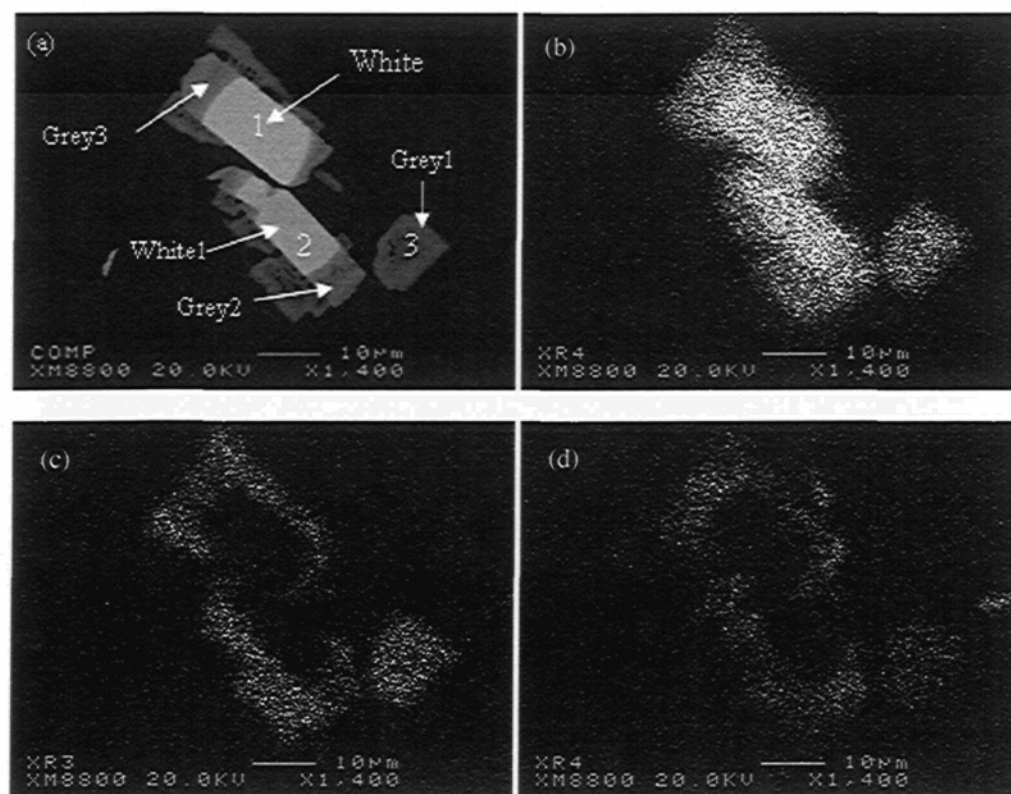
and later in the eutectic reaction as follows:



4.2.2 Zirconium Intermetallics

4.2.2.1 Al_3Zr Intermetallic Phase

In Zr-containing alloys, Al_3Zr primary particles may appear in such different shapes as square, rectangular, and spherical. These primary particles are found to act as nucleation sites for Zr- and Sc-rich intermetallics, as shown in Figure 4.13 (a), representing a backscattered image taken of the GSZ alloy and depicting different particles; two of these are zirconium trialuminide, labelled 1 and 2 in the figure, and are composed of white rectangular centers surrounded by grey regions at the edges. The composition of these central and outer regions was determined using WDS analysis, and was found to correspond to the $\text{Al}_{3.1}\text{Zr}$ phase (white region) and to $\text{Al}_{2.76}(\text{Zr}_{0.46}\text{Sc}_{0.22}\text{Ti}_{0.32})$ and $\text{Al}_{2.97}(\text{Zr}_{0.48}\text{Sc}_{0.27}\text{Ti}_{0.25})$ zirconium trialuminides (grey regions). The third particle, labelled 3 in Figure 4.13 (a), which is a scandium trialuminide particle has a composition corresponding to $\text{Al}_{3.58}(\text{Sc}_{0.48}\text{Zr}_{0.37}\text{Ti}_{0.14})$, as shown in the WDS results presented in Figure 4.13 (e). Also, it should be noted that the X-ray images for Zr, Sc, and Ti, as shown in Figures 4.13 (a), (b), and (d), respectively, reflect the same results.



(e)

Particle Code	Element	Wt%	At%	Calculated Formula	Particle Code	Element	Wt%	At%	Cal. Formula
Grey 1	Al	60.76	77.89	$Al_{3.58}(Sc_{0.48}Zr_{0.37}Ti_{0.14})$	White1	Al	48.09	75.5	$Al_{3.11}Zr$
	Zr	21.27	8.07			Zr	52.28	24.27	
	Sc	13.51	10.39			Total ≈	100	99.77	
	Ti	4.49	2.24		White2	Al	47.89	75.46	$Al_{3.10}Zr$
	Total ≈	100	98.59			Zr	52.17	24.31	
Grey 2	Al	51.09	72.04	$Al_{2.76}(Zr_{0.46}Sc_{0.22}Ti_{0.32})$	Total ≈	100	99.77		
	Zr	28.57	11.91						
	Sc	6.79	5.748						
	Ti	10.55	8.383						
	Total ≈	97	98						
Grey 3	Al	53.24	73.266	$Al_{2.97}(Zr_{0.48}Sc_{0.27}Ti_{0.25})$					
	Zr	29.08	11.836						
	Sc	8	6.60						
	Ti	8.01	6.21						
	Total ≈	98.33	97.9						

Figure 4.13 (a) Backscattered image taken of the GSZ-alloy (0.2wt%Ti-0.5wt%Sc-0.5wt%Zr) showing the presence of different $Al_3(Zr_{1-x-y}Sc_xTi_y)$ and Al_3Zr intermetallic particles with varying compositions and (b,c,d) corresponding X-ray images of (b) Zr, (c) Sc, (d) Ti; (e) WDS analysis of (a).

Figure 4.14 shows an example of the type of Al_3Zr primary particles which were observed in the GMZ-alloy. From the backscattered image shown in Figure 4.14 (a), the particle is seen to consist of a white central region surrounded by a grey rim. Based on the EDX spectra shown in Figures 4.14 (b), and (c), and the WDS analysis, the white central area of the particle corresponds to pure Al_3Zr , whereas the dark rim is a Zr-rich intermetallic having a composition of $\text{Al}_3(\text{Zr}_{0.74}\text{Ti}_{0.26})$ with some traces of Si. Although the EDX spectrum corresponding to the white region, shown in Figure 4.14 (b), reveals the presence of a Sr peak, it was not possible to confirm the presence of Sr in the particle *per se*. The author is of the opinion that the strontium may have been simply located randomly on the particle surface, since no Sr was detected in the WDS analysis, either.

As a result of the low cooling rate ($0.3\text{ }^\circ\text{C/s}$) and the high zirconium content (0.5 wt %), all Zr-containing alloys are located in the $\text{L}+\text{Al}_3\text{Zr}$ region of the Al-Zr phase diagram during the melting stage. This indicates that the coarse Al_3Zr particles are not formed from the melt during solidification but come instead directly from the Al-15%Zr master alloy added to the liquid melt. These particles do not dissolve in the melt, and they provide favored nucleation sites for the growth of the Zr-, Sc-, and Ti-intermetallics from the melt during solidification; (this data is in full agreement with what was reported previously.¹⁵² In Figures 4.13 (a), and 4.14 (a), the white regions of the coarse rectangular particles are those which come from the master alloy, while the grey areas associated with these white regions nucleate on the surfaces of the latter during solidification. If scandium and titanium also exist in the alloy, they will substitute for the zirconium atoms in the Al_3Zr to form $\text{Al}_3(\text{Zr}_{1-x}\text{Sc}_x)$ and $\text{Al}_3(\text{Zr}_{1-x-y}\text{Sc}_x\text{Ti}_y)$ phases, as is demonstrated by the WDS data presented in Figures 4.13 (a), and 4.14 (d).

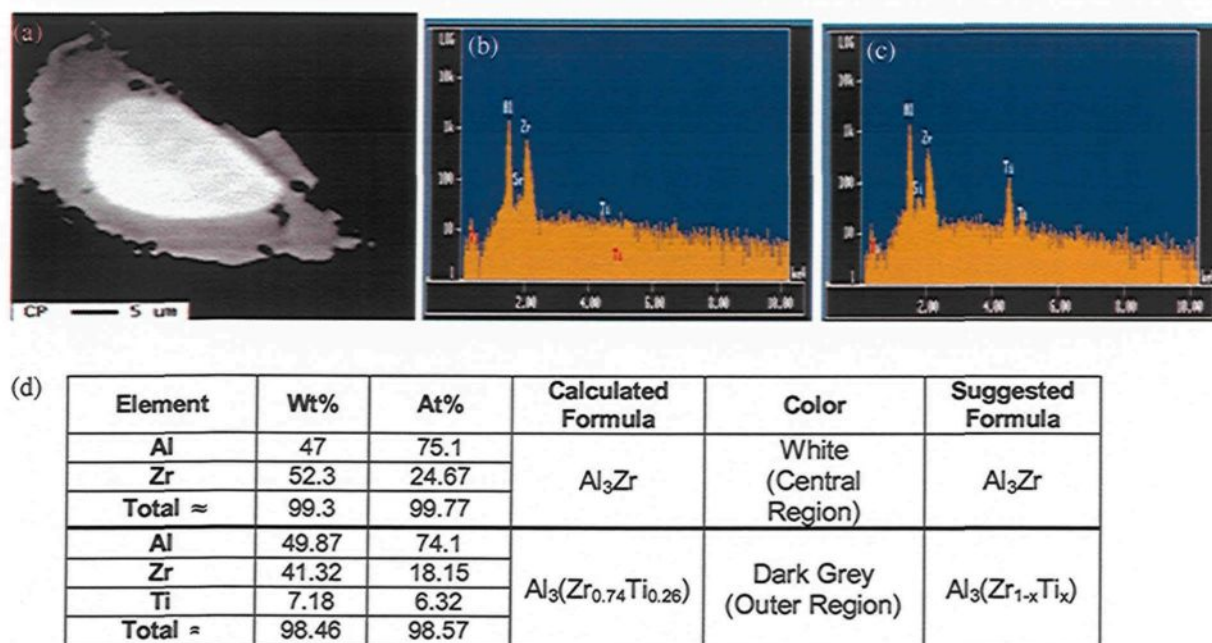


Figure 4.14 (a) Backscattered image taken of the GMZ-alloy (0.2wt%Ti-0.02wt%Sr-0.5wt%Zr) showing a Al₃Zr phase particle; (b, c) EDX spectra taken from the central (b) and outer (c) regions of the particle; and (d) corresponding WDS analysis of the two regions of the particle.

4.2.2.2 Other Zirconium Intermetallic Phases

Two other Zr-containing intermetallic phases were detected in the Z-alloy (0.5wt%Zr) and the GZ-alloy (0.2wt%Ti-0.5wt%Zr), respectively, and are shown in Figures 4.15 and 4.16. To the best of the author's knowledge, these phases have not been reported previously in the literature. The first unknown phase, the β_i -phase, is a ternary intermetallic phase which appears in the form of a grey rose-shaped particle, as shown in Figure 4.15 (a). The corresponding EDX spectrum, Figure 4.15 (b), reveals the presence of Al, Si, and Zr peaks. The WDS analysis of the particle shows that the chemical formula of the β_i -phase may be written as Al_{2.9}ZrSi_{0.32} or as (Al,Si)_{3.2}Zr based on the consideration that the β_i -phase is a special case of the β -phase (Al₃Zr) where it is believed that silicon interacts with Al₃Zr and forms the ternary phase AlZrSi; this

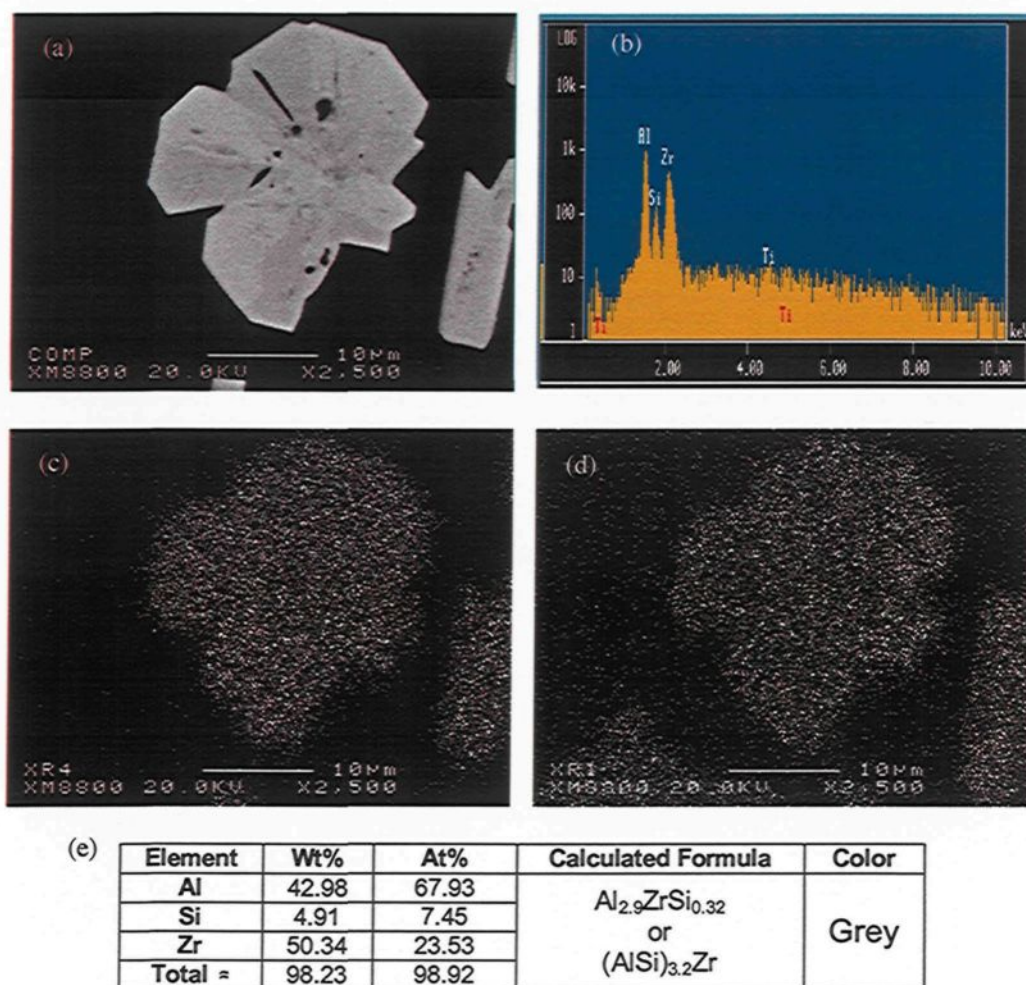
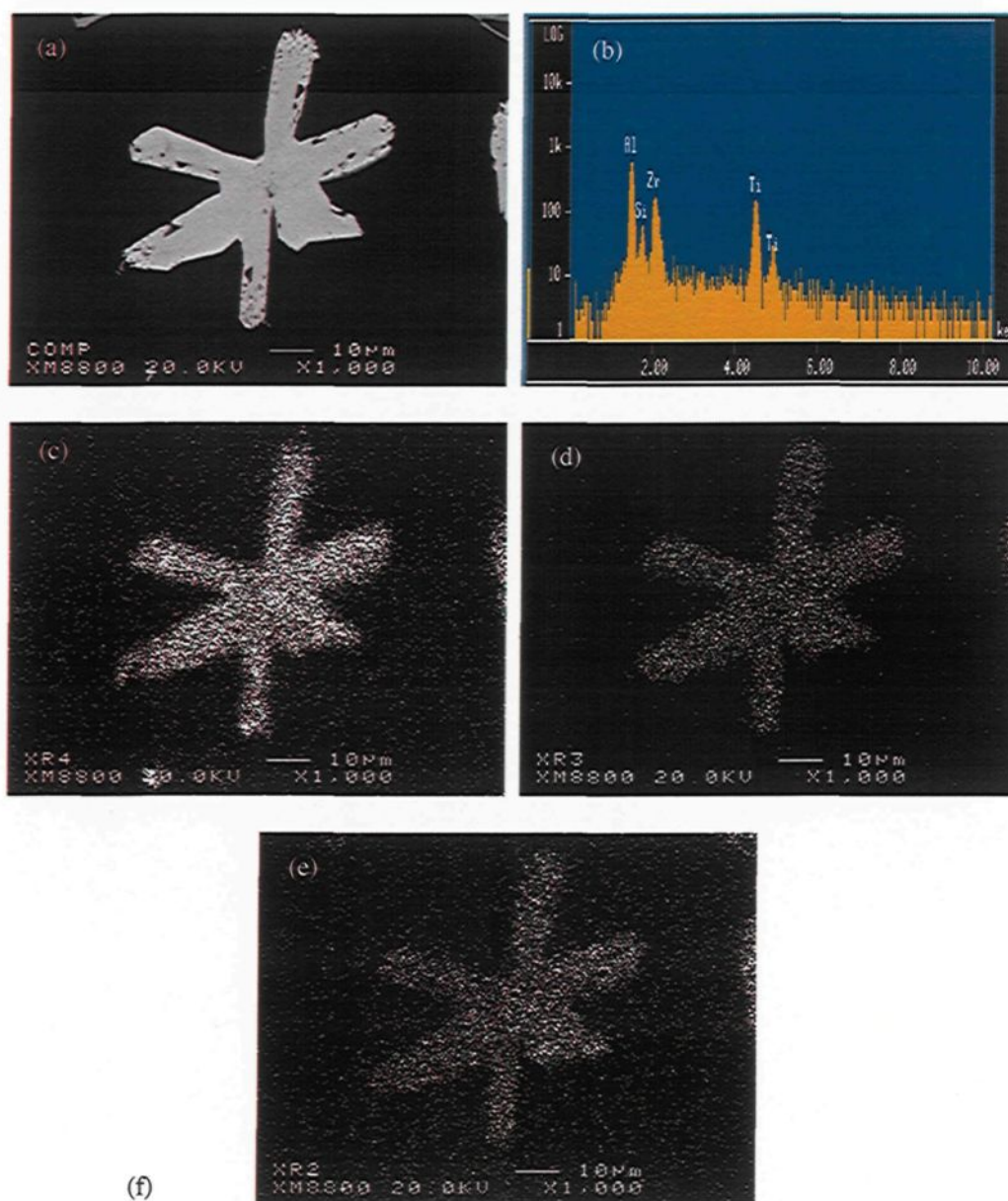


Figure 4.15 (a) Backscattered image taken of the Z-alloy (0.5wt%Zr), showing the presence of the AlZrSi ternary phase particles; (b) corresponding EDX spectrum; (c) and (d) corresponding X-ray images of Zr and Si, respectively; and (e) WDS analysis.

interaction occurs through the substitution of Al atoms with Si atoms where the normal atomic % of Al in Al₃Zr (75 at% Al) is reduced by 7% which is replaced by 7 at% Si, as will be observed from the WDS results shown in Figure 4.15 (e).

The ternary intermetallic phase, AlZrSi, is considered to be an equilibrium phase based on the following aspects, (i) the equiaxed morphology and the large size of the β_1 -phase particle (average diameter $\sim 26 \mu\text{m}$), (ii) the low cooling rate (0.33°C/s) under which the β_1 -phase is formed, (iii) the homogenous distribution of Zr and Si throughout



Element	Wt%	At%	Calculated Formula	Color
Al	48.21	69.4	$\text{Al}_{2.9}(\text{Zr}_{0.59}\text{Ti}_{0.41})\text{Si}_{0.24}$ or $(\text{AlSi})_3(\text{Zr}_{0.59}\text{Ti}_{0.41})$	Grey
Zr	33.66	14.33		
Ti	12.47	10.1		
Si	4.24	5.86		
Total ≈	98.58	99.69		

Figure 4.16 (a) Backscattered image taken of the GZ-alloy (0.2wt%Ti-0.5wt%Zr), showing an AlZrTiSi quaternary intermetallic phase particle; (b) corresponding EDX spectrum; (c), (d), and (e),

the β_1 -phase particle, and (iv) the higher concentration of these two elements in the particle than in the surrounding matrix as evidenced by the corresponding X-ray images for Zr and Si, as shown in Figures 4.15 (c) and (d).

The second unknown phase, the β_{ii} -phase, which was also analyzed using the same techniques, is shown in Figure 4.16 (a), and appears in the form of a grey starfish-like particle with an average diameter of 66 μm . The corresponding EDX spectrum revealed peaks for Al, Zr, Ti, and Si, thereby classifying this phase as a quaternary phase, AlZrTiSi, having the chemical formula of $\text{Al}_{2.9}(\text{Zr}_{0.59}\text{Ti}_{0.41})\text{Si}_{0.24}$ or $(\text{Al,Si})_3(\text{Zr}_{0.59}\text{Ti}_{0.41})$. As in the case of the β_1 -phase, the X-ray images for Zr, Ti, and Si corresponding to the β_{ii} -phase particle, which is shown in Figures 4.16 (c), (d), and (e), confirm the homogeneous distribution of these elements within the phase, as well as their higher concentration within the particle compared to the surrounding matrix. The β_{ii} -phase is also considered as an equilibrium phase for the same reasons as those mentioned for the β_1 -phase. It is believed that in the presence of Ti, the β_1 -phase develops into the β_{ii} -phase. Both phases, whether AlZrSi or AlZrTiSi, are known to form at the same temperature level at which the Al_3Zr phase forms, *i.e.* around 665°C, and are located inside the grains.

4.3 Grain Structure

After discussing Zr- and Sc-containing intermetallics in the previous section, an attempt will be made here to acquire an understanding of the effects that these intermetallics tend to have on alloy microstructure. The effects of the different additives on the average grain size observed in the corresponding alloys are illustrated in Figure 4.17. As the transition elements are added to the base alloy, the average grain size is found to decrease sharply from 593 μm to values ranging from 139 μm to 77 μm . The

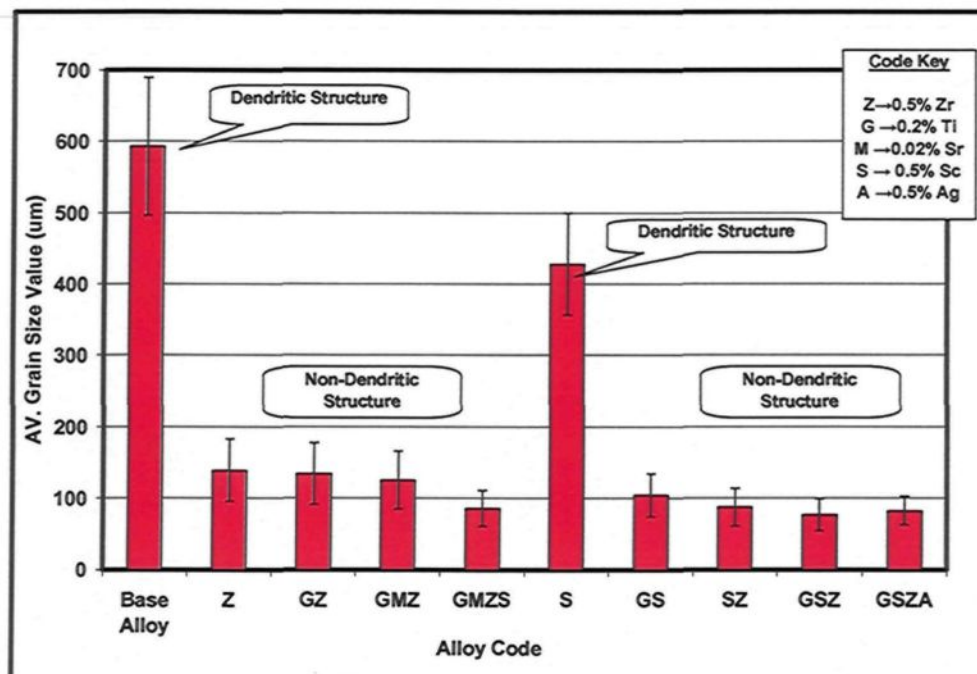
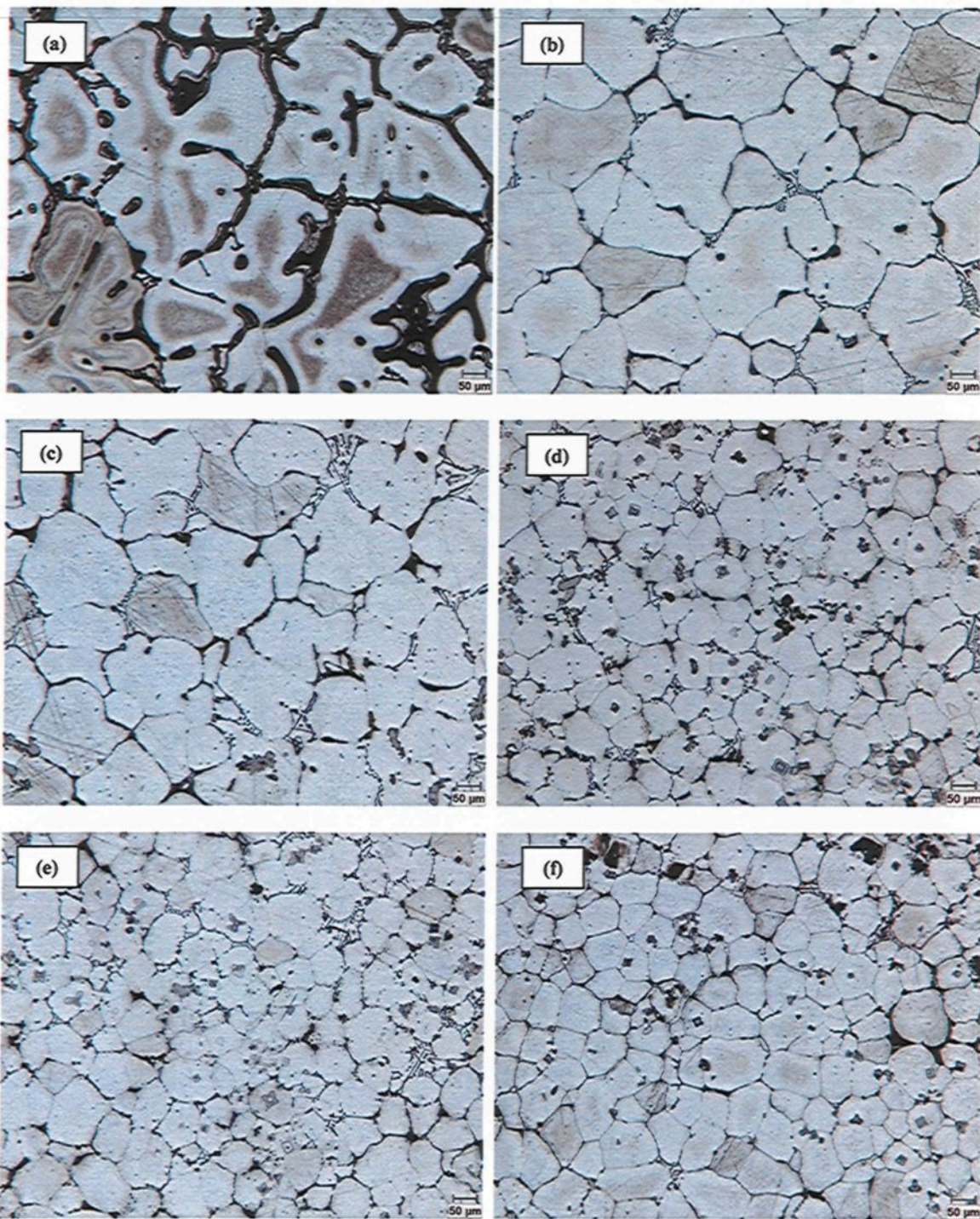


Figure 4.17 Average grain sizes displayed by the alloys investigated.

smallest grain size may be obtained by means of adding a combination of Zr, Sc, and Ti. It should be noted that although zirconium alone reduces the grain size significantly, scandium on its own does not.

In this study, it was also found that the addition of transition elements changes the matrix structure from the dendritic to the non-dendritic type, as shown in Figures 4.18 (a) to (g). It will be seen that the coarse dendritic morphology of the base alloy, as shown in Figure 4.18(a), is transformed into a non-dendritic one in all the alloys containing Zr, and Zr-Sc, as illustrated in Figures 4.18 (b), (c), (d), (e), (f), and (g).

Careful examination of the grains in the alloys containing Zr and Sc also reveals that the star-like phase particles are spread throughout the grains and that they are located at the centre of the dendrite cells. In contrast, the addition of scandium alone, as in the case of the S alloy shown in Figure 4.17 (h), does not transform the dendritic morphology of the base alloy.



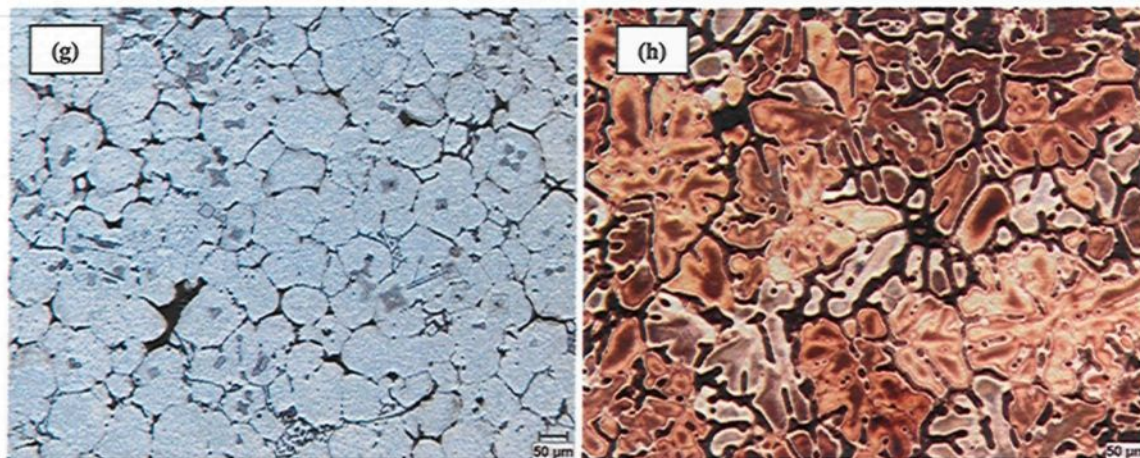


Figure 4.18 Morphology of the primary α -Al phase; (a) in the base Al-2wt%Cu alloy, (b) in the Z-alloy (0.5wt%Zr), (c) in the GZ-alloy (0.2wt%Ti-0.5wt%Zr), (d) in the SZ-alloy (0.5wt%Sc-0.5wt%Zr), (e) GSZ-alloy(0.2wt%Ti-0.5wt%Sc), (f) GMZS-alloy (0.2wt%Ti -0.5wt%Sc-0.5wt%Zr-0.02wt%Sr), (g) GSZA-alloy (0.2wt%Ti-0.5wt%Sc-0.5wt%Zr-0.5wt%Ag), and S-alloy (0.5wt%Sc).

The percentage volume fraction of intermetallics observed in the alloys investigated is displayed in the histogram shown in Figure 4.19. It will be seen that the volume fraction of intermetallics in the base alloy increases with the addition of transition elements; however, addition of Sc alone does not alter the volume fraction of intermetallics by much (*cf.* 6% for S alloy with 5.4% for the base alloy). In order to understand the relationship between the grain size and the volume fraction of the intermetallic compounds, a plotted graph of the grain size *vs.* the volume fraction was drawn, as shown in Figure 4.20, from which it may be deduced that the grain size decreases linearly as the volume fraction of the intermetallics increases.

The beneficial effects of combined Zr-Sc additions in reducing grain size is attributed to the profuse formation of the $Al_3(Sc_{1-x}Zr_x)$ star-like phase as the primary phase during solidification, which in turn acts as a potent nucleant for α -Al. The presence

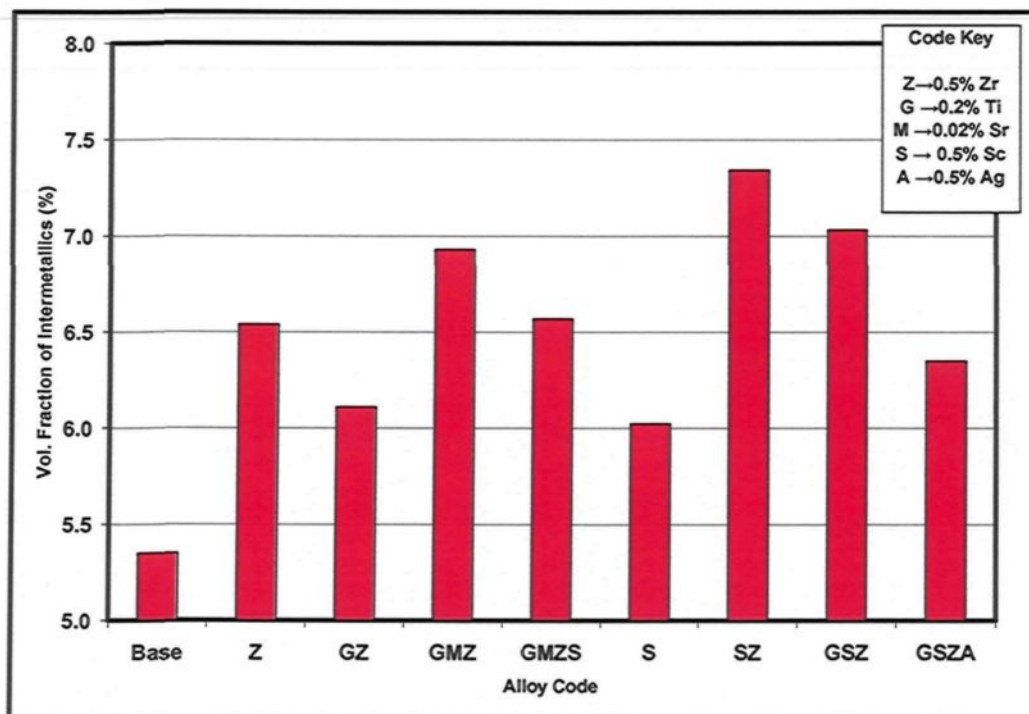


Figure 4.19 Volume fraction of intermetallics (%) observed in the investigated alloys.

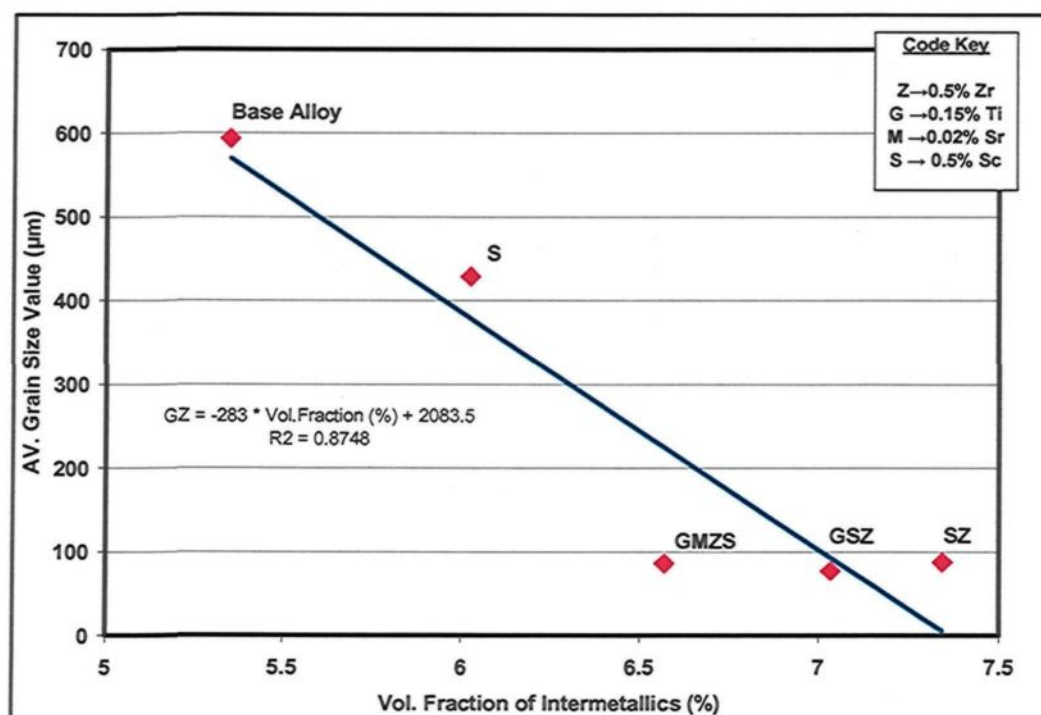


Figure 4.20 Relationship of Grain Size vs. Vol. Fraction of Intermetallics in Al-Cu base alloy containing various additives.

of titanium enhances the efficiency of the star-like phase as an α -Al nucleant in that it reduces the lattice misfit between the $\text{Al}_3(\text{Sc}_{1-x}\text{Zr}_x)$ phase and the α -Al.

There is also another refining mechanism of the transition elements which may exist side by side with that of the formation of potent nucleants in which the solutes play a significant role. It has been reported in a number of studies^{153,154,155} that the segregated elements may act to restrict the growth rate providing more time for nucleation events to occur. It was also found that the constitutionally undercooled zone situated in front of the interface, and which was created by element segregation, tends to activate the nucleants also found in front of the interface, thereby interrupting the growth of the previous grain.

This restricting effect of segregating elements or solutes is called the growth-restriction factor or the GRF; the GRF of any of alloy can be estimated by applying the equation $\Sigma mc_o(k-1)$, where m is the gradient of the liquidus, c_o is the concentration of the solute in the alloy, and k is the partition coefficient between the equilibrium concentrations of the solid and liquid at the growing interface. Zirconium and titanium, each having a partition coefficient greater than one, namely 2.5 and 9, respectively, are considered to be among those elements which may exert a growth-restricting effect. Accordingly, the refining effect observed in the alloys containing Zr and Sc-Zr may be attributed to the segregation effect of Zr and Ti as well as to the presence of potent nucleant particles of Al_3Zr , $\text{Al}_3(\text{Sc}_{1-x}\text{Zr}_x)$, and $\text{Al}_3(\text{Sc}_{1-x-y}\text{Zr}_x\text{Ti}_y)$.

The addition of transition elements alters the matrix structure of the base alloy from dendritic to non-dendritic in the following way: as the number of star phase nuclei and GRF values increase, the number of α -Al grains formed also increases; due to their large numbers, these grains will impinge upon each other early on during growth, before

the dendrite branches can begin to form. By contrast, the addition of 0.5 wt% scandium as a single addition to the base alloy does not alter the grain size or morphology of the base alloy since the Al_3Sc phase does not form at Sc contents of less than 0.55 wt%, and also because Sc does not restrict growth like Zr and Ti do.⁸¹ In a manner of speaking, the linear relationship between the grain size and the volume fraction of intermetallics observed in Figure 4.20 indirectly confirms the above findings where, with combined additions of Zr and Sc, larger volume fractions of the star phase are formed.

Likewise, the low volume fraction of intermetallics in the 0.5wt% Sc-containing S alloy may be used to explain the coarse dendritic morphology of the S alloy matrix where, at a scandium content of less than 0.55 wt%, the primary Al_3Sc phase, *i.e.* α -Al nucleants,^{145,156} will not be able to form. Nor will it consequently be possible for the formation of a large number of α -Al grains to give rise to the non-dendritic morphology of the matrix. Another beneficial effect of the addition of transition elements is found in controlling the size and distribution of intermetallic compounds. As will be observed from Table 4.1 and Table 4.1, the coarse elongated morphology of solidified Al_2Cu and α -Fe phase particles in the base alloy is transformed into a fine form as the transition elements are added to the base alloy.

For example, the average surface area and the average length of Al_2Cu decrease from 983 μm^2 and from 81 μm in the base alloy into a lower range of values of 147-493 μm^2 for the surface area, and 24-55 μm for the length of all the alloys investigated except the S-alloy, as shown in Table 4.1. The same trend is observable with regard to the α -Fe particles where the average surface area and average length decrease sharply from 14593 μm^2 and 261 μm in the base alloy into a lower range of values of 1680-5900

Table 4.1 Dimension Characteristics of Al_2Cu Particles.

Alloy Code	Surface Area (μm^2)		Average Length (μm)	Average Width (μm)
	Range	Average		
Base Alloy	400-1600	983	81	36
Z	100-900	493	55	24
GZ	75-475	212	32	13
GMZ	100-400	218	35	13
GMSZ	80-400	147	27	11.4
S	125-2300	1001	86	38
SZ	20-380	166	24	12
GS	60-510	261	40	16
GSZ	20-400	188	30	13
GZSA	66-400	205	29	15

Table 4.2 Dimension Characteristics of $Al_{15}(Mn,Fe,Cu)_3Si_2$ Particles, α -Fe.

Alloy Code	Surface Area (μm^2)		Average Length (μm)	Average Width (μm)
	Range	Average		
Base Alloy	7600-23000	14593	261	129
Z	3300-12000	5900	142	81
GZ	800-9400	4500	126	77
GMZ	2300-12700	4937	129	77
GMSZ	689-3300	1680	77	43
S	4200-23000	9800	325	110
SZ	1400-4500	2966	102	56
GS	885-5282	2440	97	53
GSZ	815-5600	1864	80	46
GZSA	618-5117	2235	80	52

μm^2 for the surface area and 77-142 μm for the length. These results also appear in Figure 4.21 which illustrates the changes in particle morphology from the extended coarse shape occurring in the base alloy and the S-alloy, as shown in Figures 4.21 (a) to (f), into a refined globular form which may be observed in Z-, SZ-, GSZ-, and GSZA-alloys, as shown in Figures 4.21 (b), (c), (d), and (e).

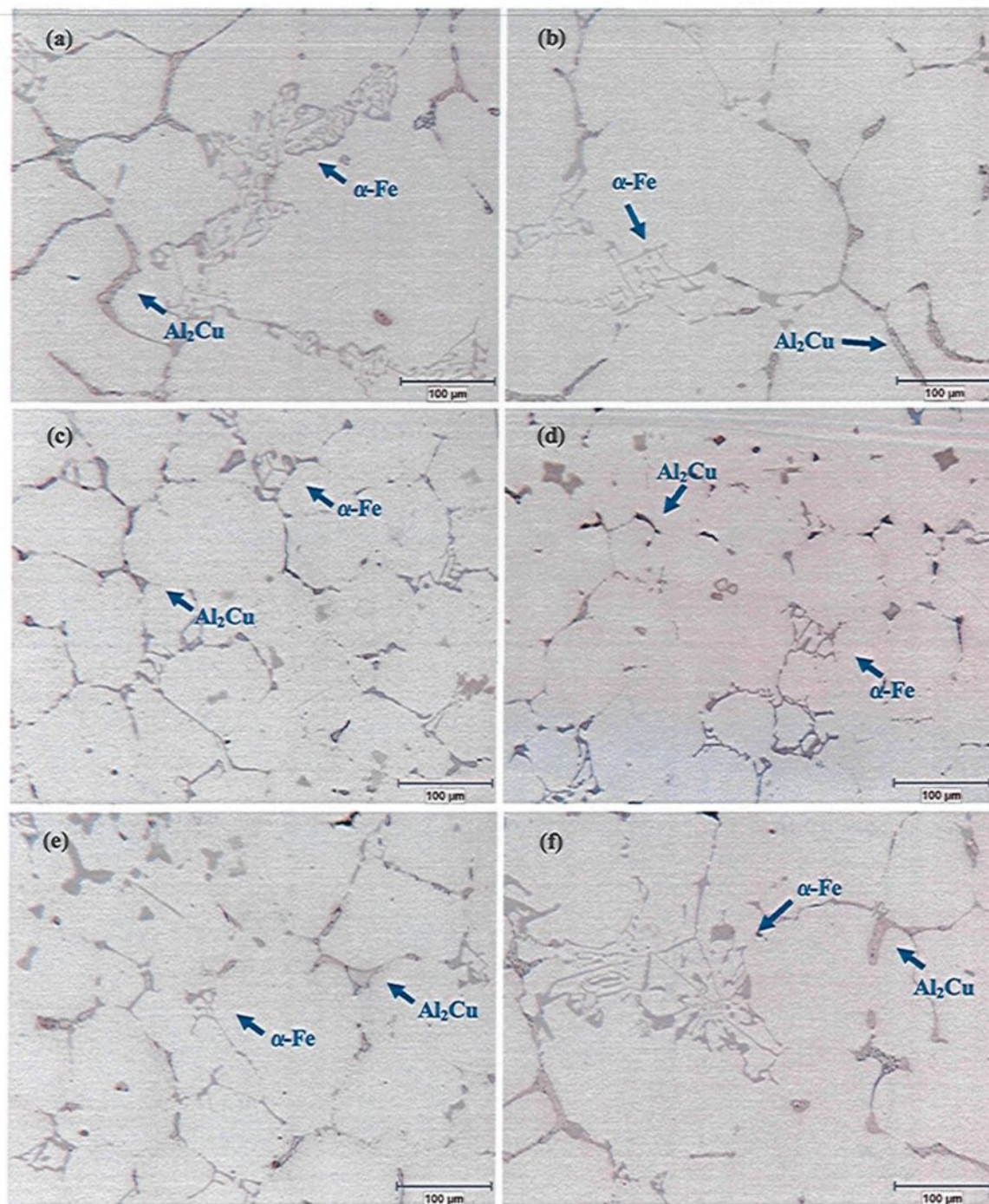


Figure 4.21 Microstructure of a number of alloys investigated; (a) base alloy, (b) Z-alloy (0.5Zr), (c) SZ-alloy (0.5wt%Sc-0.5wt%Zr), (d) GSZ-alloy (0.2wtTi-0.5wtSc-0.5wtZr), (e) GSZA-alloy (0.2wtTi-0.5wtSc-0.5wtZr-0.5wtAg), and (f) S-alloy (0.5wtSc)

The refining effect which the addition of transition elements are observed to have on the surface area and morphology of the Al_2Cu and $\alpha\text{-Fe}$ intermetallic particles may be

attributed to the role of such elements in producing refined non-dendritic structure of α -Al. The fine non-dendritic structure of α -Al contributes to distributing liquid metal, enriched with Fe and Cu, in a homogeneous manner during solidification as small dispersed pools. As the solidification proceeds, these pools solidify into fine intermetallic particles distributed throughout the α -Al grains. The coarse morphology of the intermetallic particles observable in the S-alloy, however, is a result of the coarse grain structure and the dendritic morphology of the α -Al in this alloy. This type of morphology, in the case of the S-alloy, causes the liquid metal to be distributed in a non-homogeneous and extended form producing coarse and elongated intermetallic particles of Al_2Cu and α -Fe.

The beneficial role played by a refined non-dendritic structure in the production of fine globular particles of Al_2Cu and α -Fe intermetallic phases can be illustrated by charting the average surface area of both phases against the grain size for a number of alloys, as shown in Figures 4.22 and 4.23. The relationship between the average surface area of Al_2Cu and the α -Fe particles can be represented by linear trend lines having linear equations with R^2 values tending towards one, *i.e.* 0.89 for Al_2Cu and 0.94 for α -Fe.

Based on the above data, it is expected that the refined non-dendritic grain structure will improve the tensile properties by producing fine globular intermetallic particles of Al_2Cu and α -Fe. Aspects pertaining to this improvement will be discussed in the chapter on tensile properties.

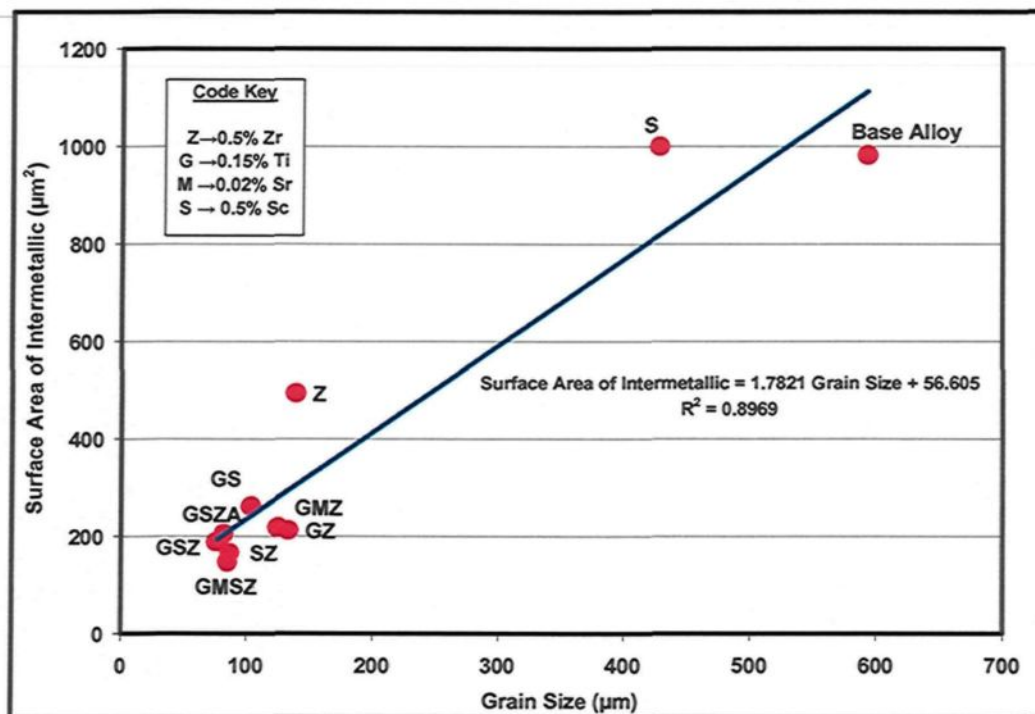


Figure 4.22 Average surface area of Al_2Cu particles vs. grain size in several of the alloys investigated

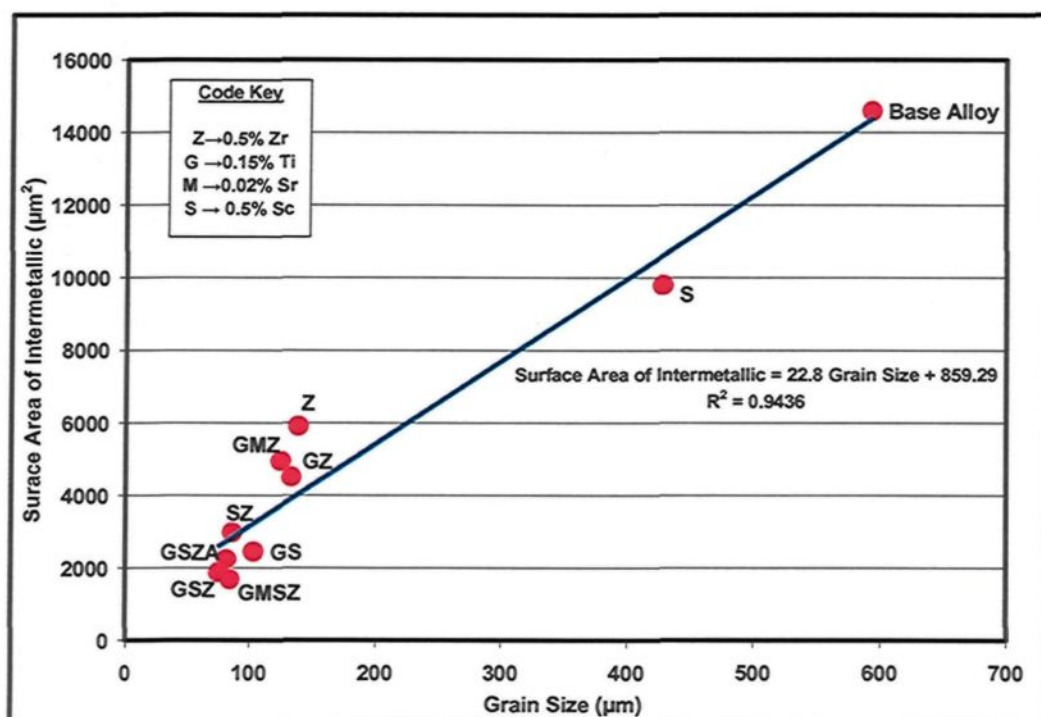


Figure 4.23 Average surface area of $\text{Al}_{15}(\text{Mn,Fe,Cu})_3\text{Si}_2$ particles vs. grain size in several alloys investigated

It is worth noting that the Zr-rich intermetallic phases may appear as large localized coarse particles in Zr-containing alloys from which Sc is absent; as Sc is added to the Zr alloys, the Zr intermetallic phase particles become observably finer and more uniformly distributed throughout the matrix. The influence of Sc-addition on the size and the manner of distribution of Zr-rich intermetallic phases may be identified by comparing the intermetallic features in the Z, GZ, and GMZ alloys shown in Figure 4.24 with the intermetallic features of SZ, GSZ, and GMSZ indicated in Figure 4.25.

The explanation of this variation in the features of Zr-rich intermetallic phases as a result of the presence of Sc is that the Zr element is normally segregated near the boundaries of the dendrites or grains during solidification, whereas by contrast, the element Sc is segregated at the center of the dendrites or grains. The combined additions of Sc and Zr will thus lead to the formation of more uniformly distributed intermetallic phases than may occur with the addition of each element in its individual form. Based on observation, the author believes that, in the presence of Sc in Zr-containing alloys, the star-like phase, $\text{Al}_3(\text{Sc}_{1-x}\text{Zr}_x)$, is more likely to form than are the ternary (AlZrSi) and quaternary (AlZrTiSi) phases having a coarse morphology.

This study did not discern any evidence that additions of Sr and Ag make any difference to the transition elements intermetallic phase reactions or that they form any intermetallic compounds at all except for $\text{Al}_2\text{Si}_2\text{Sr}$ which was detected in the Sr-containing alloys.

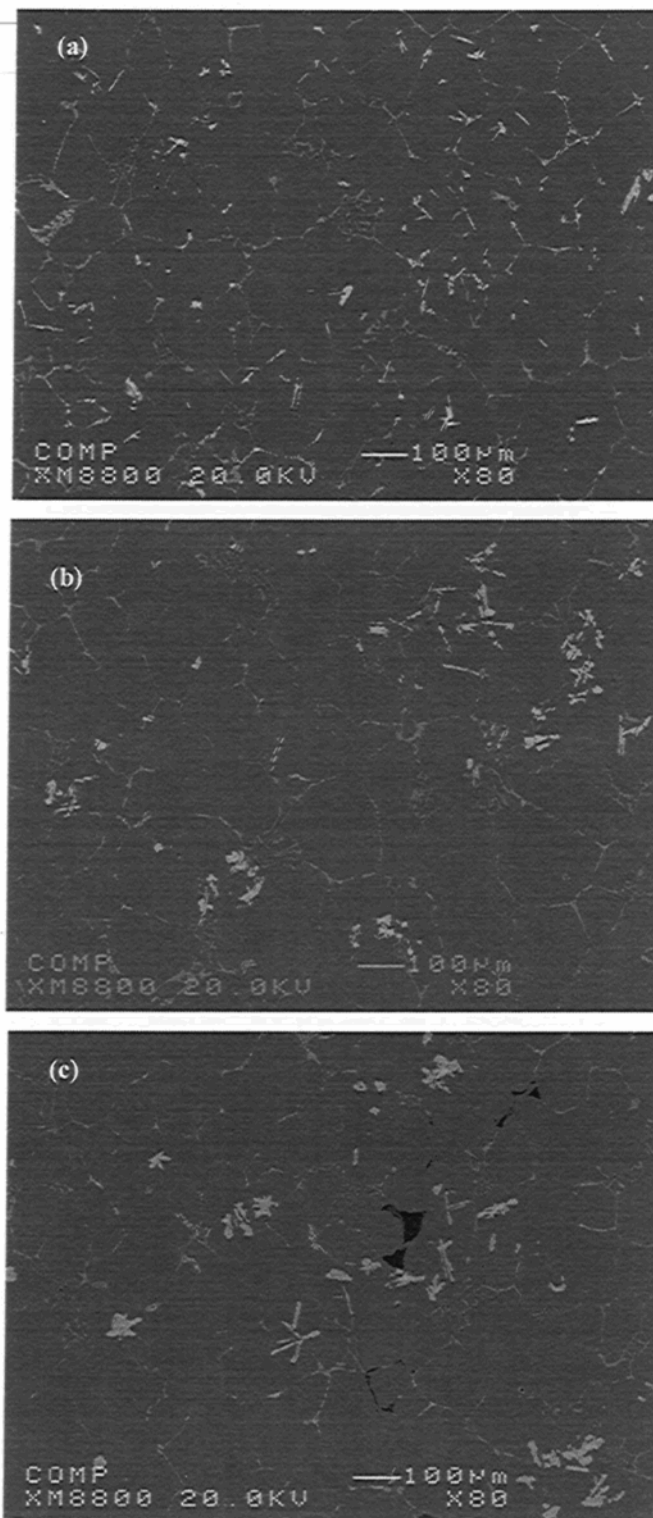


Figure 4.24 Backscattered images of microstructure of number of Zr-alloys: a) Z-alloy (0.5wt%Zr), b) GZ-alloy (0.2wt%Ti-0.5wt%Zr), and c) GMZ-alloy (0.2wt%Ti-0.02wt%Sr-0.5wt%Zr)

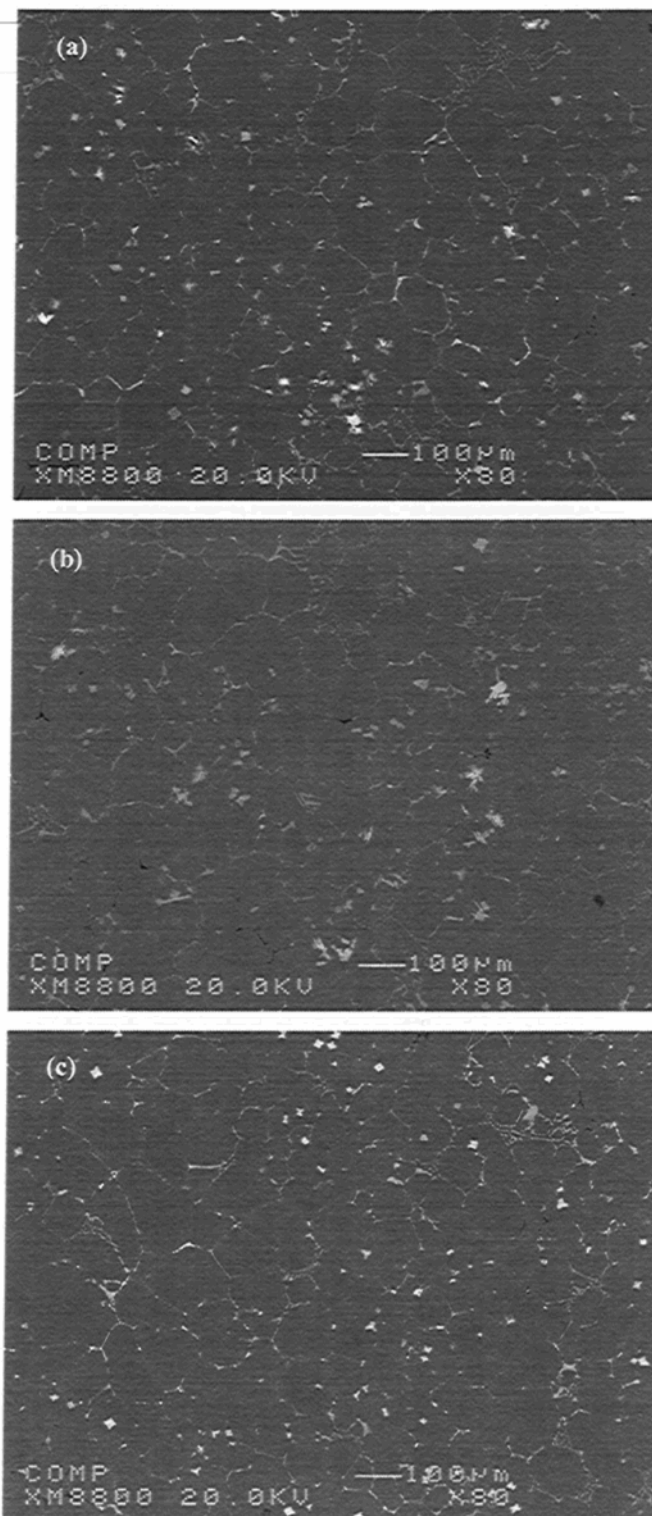


Figure 4.25 Backscattered images of the microstructure of a number of Sc-Zr alloys: a) SZ-alloy (0.5wt%Sc-0.5wt%Zr), (b) GSZ-alloy (0.2wt%Ti-0.5wt%Sc-0.5wt%Zr), and c) GMSZ-alloy (0.2wt%Ti-0.02wt%Sr-0.5wt%Sc-0.5wt%Zr)

4.4 Conclusions

In this chapter the main phase reactions and the precipitation of Zr- and Sc-containing intermetallics were investigated with regard to Al-2wt%Cu base alloys containing relatively high levels of Zr (0.5 wt%) and Sc (0.5 wt%), under low cooling rate conditions (0.3°C/s); the effects of these reactions and intermetallics on the alloy microstructure were also discussed. Based on the results obtained, the following conclusions may be drawn.

1. Three main reactions are detected during the solidification of the Al-2wt%Cu base alloy: the formation of an α -Al dendritic network at 640°C; followed by the precipitation of α -Al₁₅(Mn,Fe,Cu)₃Si₂ phase at 619°C, and thereafter precipitation of Al₂Cu and Al₅Mg₈Cu₂Si₆ phases simultaneously at 495°C.
2. Al₃Zr crystals act as nuclei for the star-like phase, Al₃(Sc_{1-x}Zr_x), which grows through the precipitation of layers of Al₃Sc on these nuclei, with the successive substitution of Sc by Zr atoms, resulting in particles comprised of different layers having different brightness levels.
3. Growth of the star-like primary phase continues in the solid state during solution heat treatment, as evidenced by the precipitation of the Al₃Sc phase in the form of a new rim around the edges of the star-like phase particle.
4. The different levels of transition elements in the alloy determine the final composition of the star-like phase.

5. Observations made in this study of the occurrence of the V-phase (AlSc_2Si_2) in conjunction with other intermetallics, such as the $\text{Al}_{2.73}(\text{Sc}_{0.79}\text{Ti}_{0.21})$, Al_2Cu , and Q-phases, support the suggestion that the V-phase tends to precipitate in two reactions, peritectic and eutectic, as reported in the literature.
6. Two Zr-containing intermetallic phases were detected in the present study: (a) a ternary AlZrSi intermetallic phase, the particles of which are rose-shaped, and (b) a quaternary AlZrTiSi intermetallic phase displaying a starfish-like morphology.
7. Combined Zr-Sc additions reduce the grain size of the Al_2Cu base alloy from $593 \mu\text{m}$ to grain sizes ranging from 139 to $77 \mu\text{m}$; they also transform the morphology of the alloy matrix from dendritic to non-dendritic. This latter morphology is attributed to the dense formation of the star-like $\text{Al}_3(\text{Sc}_{1-x}\text{Zr}_x)$ phase and to the expected high level of the growth-restriction factor (GRF).
8. Adding $0.5 \text{ wt}\%$ Sc alone to the base alloy does not alter the grain size or the morphology of the alloy matrix, since the Al_3Sc phase does not form at Sc levels of less than the eutectic composition of $0.55 \text{ wt}\%$ Sc.
9. In the alloys investigated, the grain size decreases in a linear fashion as the volume fraction of intermetallics increases with the combined addition of Zr and Sc which promote the profuse formation of star-like phase.
10. The beneficial effects of the transition elements Zr, Sc, and Ti in refining the $\alpha\text{-Al}$ grain size and transforming the morphology from a dendritic to a non-dendritic type

leads, indirectly, to a noticeable reduction in the size of the intermetallic compounds such as the Al_2Cu and $\alpha\text{-Fe}$ phases.

11. In general, the Zr-containing intermetallic compounds appear to be refined and more uniformly distributed in the matrix when Sc is present in the alloy.

CHAPTER 5
TENSILE PROPERTIES

CHAPTER 5

TENSILE POROPERTIES

Seventeen alloys were prepared and investigated under different aging conditions in order to determine the optimum age-hardening treatments with the appropriate chemical compositions which would provide the maximum tensile properties. These seventeen alloys may be divided into four sub-groups as follows: (a) the Zr-Ti alloy group involving the G1Z-, G3Z-, G5Z-, G7Z-, 7Z-, and G-alloys; (b) the Zr-Sr alloy group involving the M-, GM-, M7Z-, GM7Z-, and AGM7Z-alloys; (c) the Zr-Sc alloy group involving the GS, GS1Z, and AGS1Z alloys; and (d) the Si alloy group which include the B1Si-, and the B2Si-alloys. The microstructures of these alloys were also examined using an optical microscope in conjunction with a Clemex image analyzer.

The discussion of the results obtained will be presented in this chapter in the following order.

- Microstructure
- Tensile Properties
 - As-Cast and As-Solutionized Conditions
 - Age-Hardening Conditions
 - Zr-Ti Alloy Group
 - Zr-Sr Alloy Group

- Zr-Sc Alloy Group
- Si Alloy Group
- Fracture Mechanism
- Conclusions

5.1 Microstructure

The general effect of chemical additives on the microstructure of base alloys will be discussed in the light of a number of aspects including grain size, grain morphology, porosity (%), and surface fraction of the Al_2Cu phase. The subject of zirconium and scandium intermetallics will not be addressed in this section since they were covered under the heading of Phase Identification and Quantification in the preceding chapter.

It will be observed that the grain size for the base alloy illustrated in Figure 5.1 has undergone refinement to a noticeable degree through the addition of Zr, Sc, and Ti. The grain size value for these additions is thus reduced from 219 μm to a range of 104-46 μm for the base alloy under study. This degree of grain refining does not appear in the case of the M-, B1Si-, and B2Si-alloys where the grain size for the base alloy remains constant as it does for the M-alloy, or it is otherwise decreased by only 20 μm , as may be observed in Si-containing alloys. These Sc-containing alloys attain the smallest grain size measurements in the presence of Zr or Ti, as follows: 54 μm for the GS-alloy, 48 μm for the GS1Z, and 52 μm for the AGS1Z-alloy. The high refining capacity of Zr, whether for a high or low Zr content, is found to be improved in the presence of Ti. Also, it has been noted that a high Zr content of 0.7%, such as in the case of the 7Z-alloy, refines the α -Al to a lower degree than is the case for combined additions of Zr-Ti. It will also be observed from Figure 5.1 that the high grain refining efficiency of Zr reappears in the presence of Sr, as displayed by the

M7Z-alloy with a grain size of 57 μm . The presence of Ti in the form of a single addition refines the grain size of the base alloy significantly, from 219 μm to 57 μm in the G-alloy. It is worth noting here that the poisoning effect which Sr has on the grain refining ability of Ti-B additions does not appear with this particular combination of Sr-Ti, as displayed by the MG-alloy.

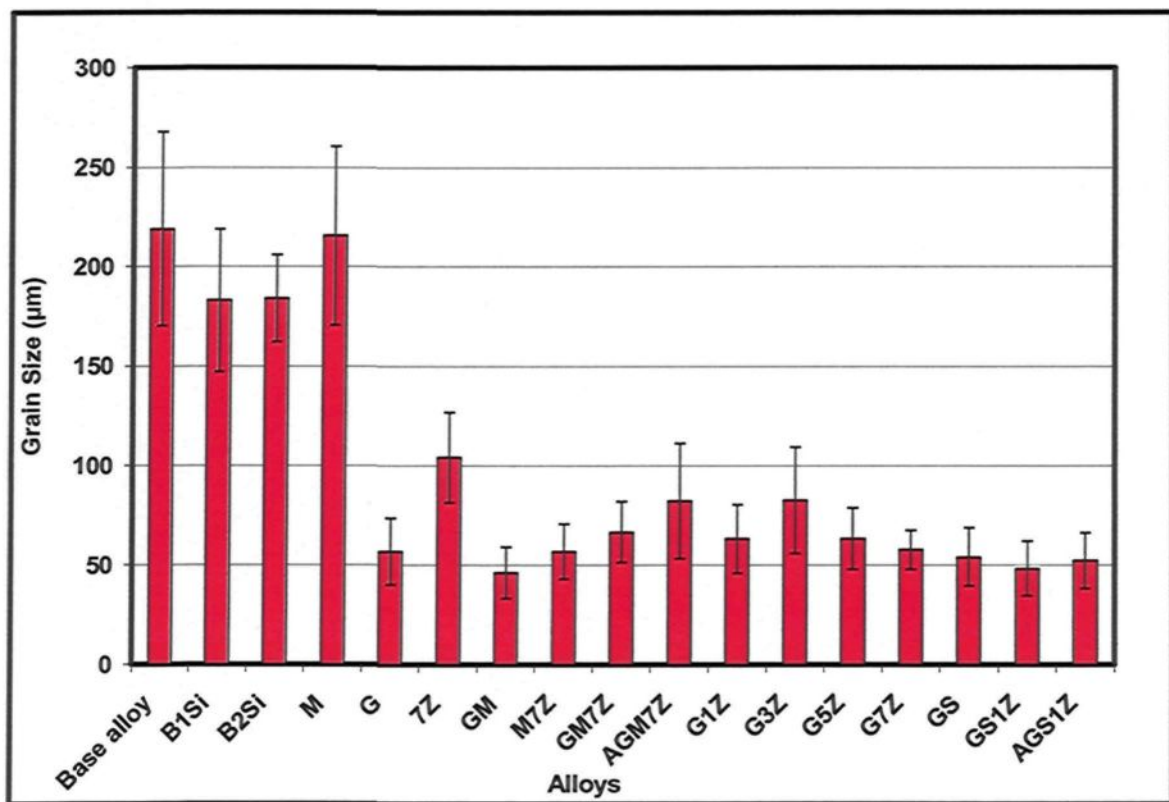


Figure 5.1 Average grain size of the alloys investigated

The smallest grain size measurements which may be obtained through the combined additions of Sc-Zr and Sc-Zr-Ti are ascribed to the profuse formation of the star-like phases $\text{Al}_3(\text{Sc}_{1-x}\text{Zr}_x)$, and $\text{Al}_3(\text{Sc}_{1-x-y}\text{Zr}_x\text{Ti}_y)$ as reported in Chapter 4. The development of the grain refining effect of Zr on α -Al grains in the base alloy can be described as follows: when the

Zr content exceeds 0.11wt%, primary Al_3Zr phase particles form in a peritectic reaction providing potent heterogeneous nucleation sites for $\alpha\text{-Al}$ during solidification.^{75,78} The improving influence brought about by Ti on the refining efficiency of Zr additions may be attributed to the fact that the Zirconium atoms in Al_3Zr phase particles may be replaced by Ti atoms in combined Zr-Ti additions, thus producing $\text{Al}_3(\text{Zr}_{1-x}\text{Ti}_x)$ phase particles with a lattice structure displaying a low mismatch with $\alpha\text{-Al}$ and consequently possessed of a higher refining efficiency. The $\text{Al}_3(\text{Zr}_{1-x}\text{Ti}_x)$ may form on the surface of Al_3Zr particles providing a greater nucleation capacity of Al_3Zr for $\alpha\text{-Al}$ grains during solidification, as already reported in the preceding chapter. It should also be noted that such a refining effect from combined additions of Zr-Ti may arise due to high growth-restriction factors, GRF as was also discussed in the previous chapter.^{153,154,155} The intermediate refining efficiency of high Zr addition levels of 0.7wt% may be explained by the fact that, at a specified cooling rate and in the absence of Ti, a further increase in the Zr content may produce coarse Al_3Zr particles. Also, the coarse Al_3Zr particles deriving from the master alloy are observed to remain undissolved. These coarse Al_3Zr particles may have low grain refining ability since they are few in number and coarse in size.

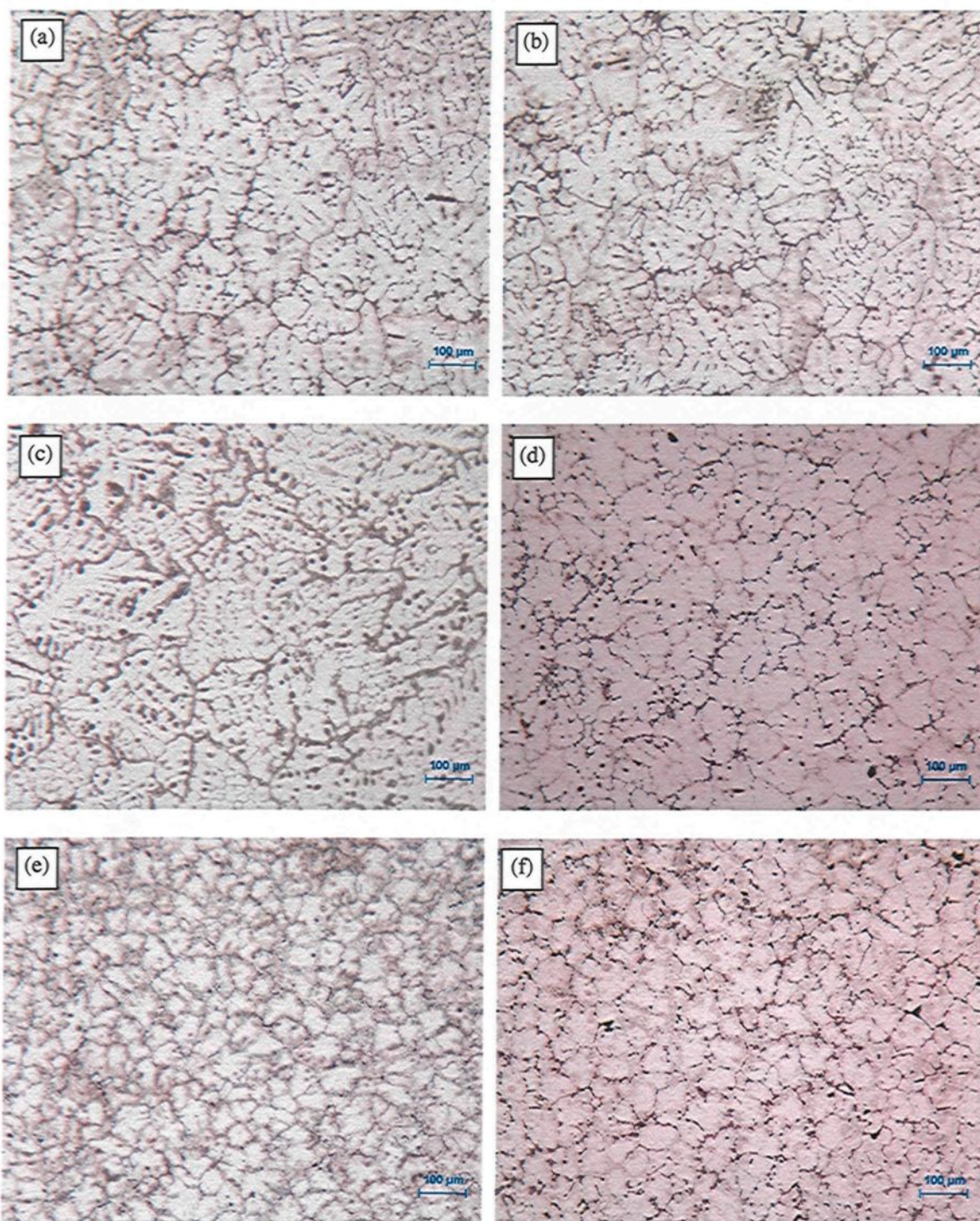
The beneficial effects of Sr addition on the refining capacity of Zr are relatively ambiguous because Sr as a sole addition does not have any considerable effect on grain size, as shown in Figure 5.1. A number of studies^{157,158,159} have pointed to the intensified affinity of strontium for forming oxides in the melt. These oxides, such as SrO and Al_2SrO_3 , have a higher negative free energy, making it possible for their formation to take place easily during the melting process. Based on the preceding fact, this study has revealed

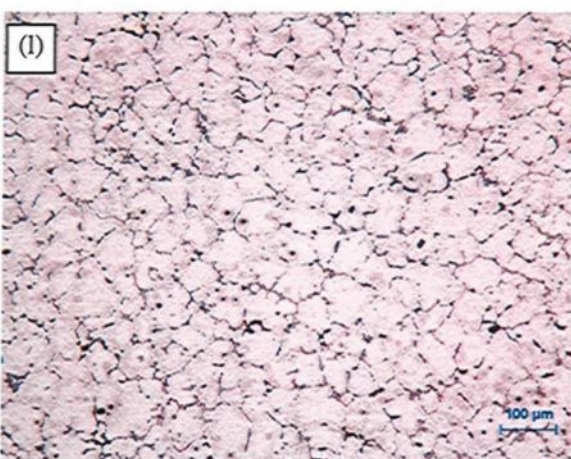
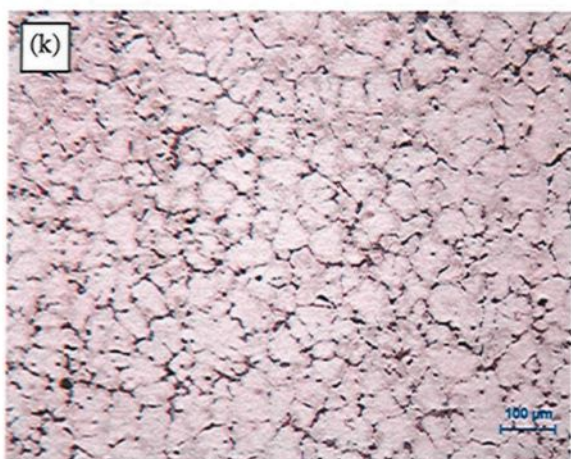
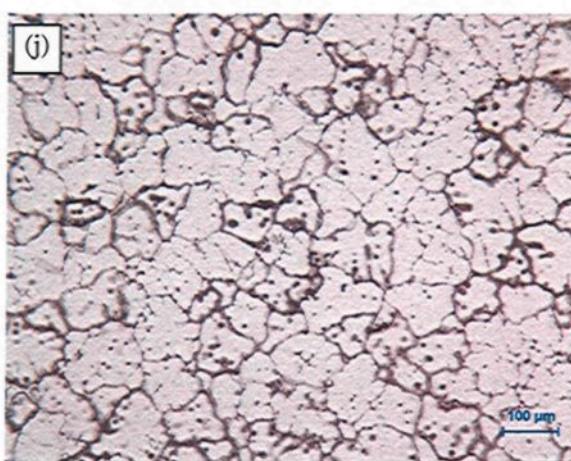
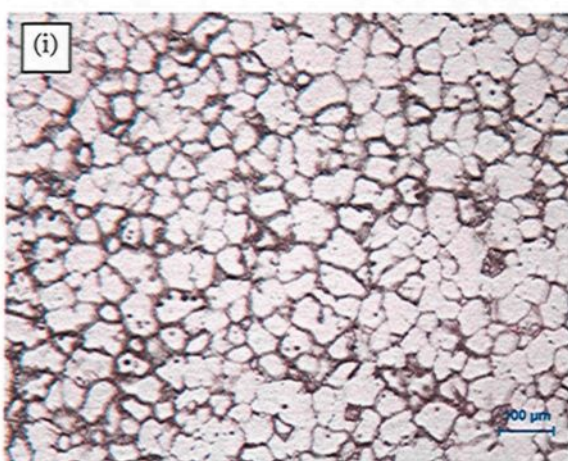
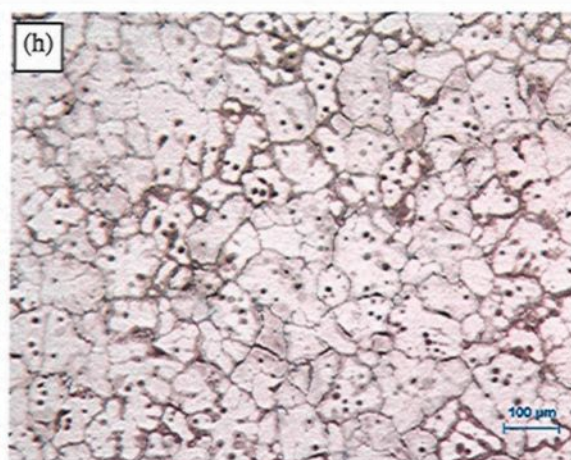
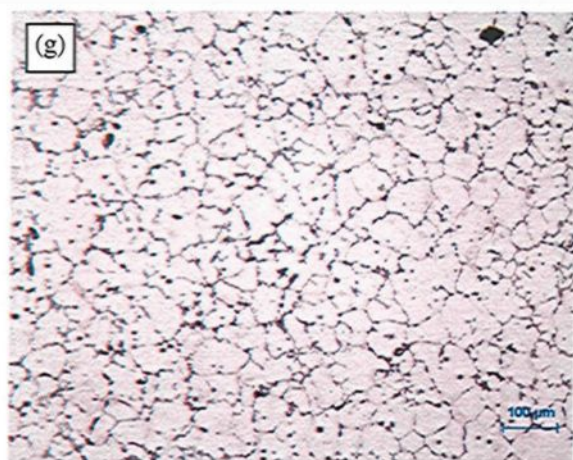
that the tiny oxide particles which form during melting may act as nucleation sites for the Zr trialuminide particles, Al_3Zr , producing a dense profusion of these particles. Such an abundant formation of Al_3Zr particles may thus be deemed responsible for obtaining the high refining efficiency elicited by the addition of 0.7wt% Zr, in the case of the presence of Sr.

Titanium, in this study, was added in the form of the Al-5Ti-1B master alloy which is characterized by a high grain refining capacity. The grain refining action of this type of master alloy has received much attention in a number of recent studies^{160,161,162,163} which attribute the grain refining capacity of this master alloy to the duplex morphology of Al_3Ti particles whose surface is covered with small boride particles of TiB_2 or $(\text{Ti,Al})\text{B}_2$; it is also attributed to the 5Ti/1B ratio as well as to the prolonged fading time.

Although a number of researchers^{164,165} have reported the poisoning effect which Sr has on the grain refining efficiency of Ti-B additions in which Sr interacts with B forming a (Sr,B) compound, this effect does not emerge in the results obtained, as displayed in Figure 5.1. The absence of this poisoning effect in the Al-2wt%Cu base alloy may be attributed to the low Si content of this alloy which contains only 1%Si, compared to previous studies where the Si content was never less than 10%.^{164,165}

A further beneficial effect of the addition of transition elements may be observed in Figure 5.2. The dendritic morphology of the base alloy becomes non-dendritic through the addition of transition elements, as shown in Figure 5.2. The alloys containing Zr-Sc produce the finest non-dendritic structures, followed by those containing Zr-Ti.





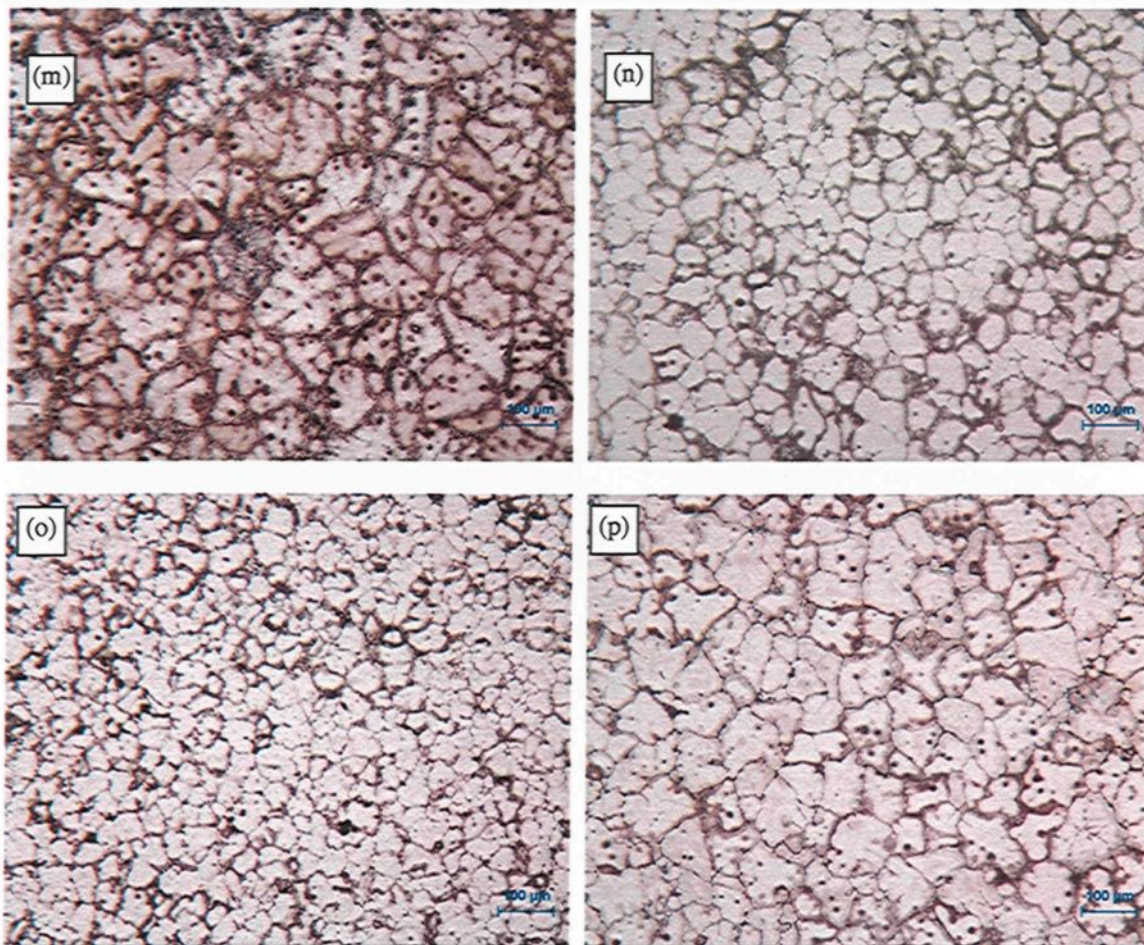


Figure 5.2 Morphology of primary α -Al observed in Al-2wt%Cu alloy containing various additions: (a) base alloy, (b) B2Si-alloy, (c) M-alloy, (d) G-alloy, (e) GM-alloy, (f) MZ-alloy, (g) GM7Z-alloy, (h) AGM7Z, (i) G1Z-alloy, (j) G3Z-alloy, (k) G5Z-alloy, (l) G7Z-alloy, (m) 7Z-alloy, (n) GS-alloy, (o) GS1Z-alloy, and (p) AGS1Z-alloy.

Although the addition of Ti refines the base alloy grain structure, fine dendritic branches can still be identified in G-alloy, as shown in Figure 5.2 (d). Globular dendritic morphology may also be detected with the addition of 0.7wt%Zr as a sole addition, in the 7Z-alloy. Silicon and strontium as individual additions do not cause any observable alteration in the dendritic morphology of the base alloy, as represented by the B2Si-alloy and the M-alloy shown in Figures 5.2 (b) and (c), respectively.

The transforming action which occurs within the base alloy, going from a dendritic to a non-dendritic morphology, and which is obtained through the addition of transition elements, was reported upon in chapter 4 on grain structure although in connection with a slower cooling rate of 0.3°C/s. The transformation in morphology may be interpreted in terms of the dense formation of active nucleants for α -Al grains and/or the high GRF value. Thus the number of α -Al grains will increase and will thus impinge upon each other early on during growth, thereby reducing the chances of dendrite branching. As shown in the last chapter, the potent nucleating particles are those of the star-like phases $\text{Al}_3(\text{Sc}_{1-x}\text{Zr}_x)$ and $\text{Al}_3(\text{Sc}_{1-x-y}\text{Zr}_x\text{Ti}_y)$ in alloys containing Zr-Sc and Zr-Sc-Ti; or the Al_3Zr and the $\text{Al}_3(\text{Zr}_{1-x}\text{Ti}_x)$ in alloys containing Zr-Ti; or the Al_3Ti and the $(\text{Ti},\text{Al})\text{B}_2$ in Ti-containing alloys. Adding either Si or Sr as a sole addition does not have any effect on the dendritic morphology since these additions have no refining action on the α -Al grains.

Figure 5.3 shows the measurements of the surface fraction of Al_2Cu in a number of alloys, in the as-cast and as-solutionized conditions. From this figure, it will be observed that the surface fraction, whether before or after the solution heat treatment, is decreased by the addition of transition elements from 1.22% to a range of 0.37-0.5% for the as-cast condition and from 0.65% to a range of 0.17-0.29% for the as-solutionized condition, illustrated by the G1Z-, G3Z-, G7Z-, 7Z-, M7Z-, and GS1Z-alloys. The same reduction level in the surface fraction of Al_2Cu will also be observed for additions of 2wt% Si as follows: 0.5% and 0.39% for the as-cast and as-solutionized conditions, respectively. In contrast, the surface fraction of Al_2Cu is increased up to 1.39% and 0.99% for the as-cast and as-solutionized conditions, respectively, when Sr alone is added to the base alloy.

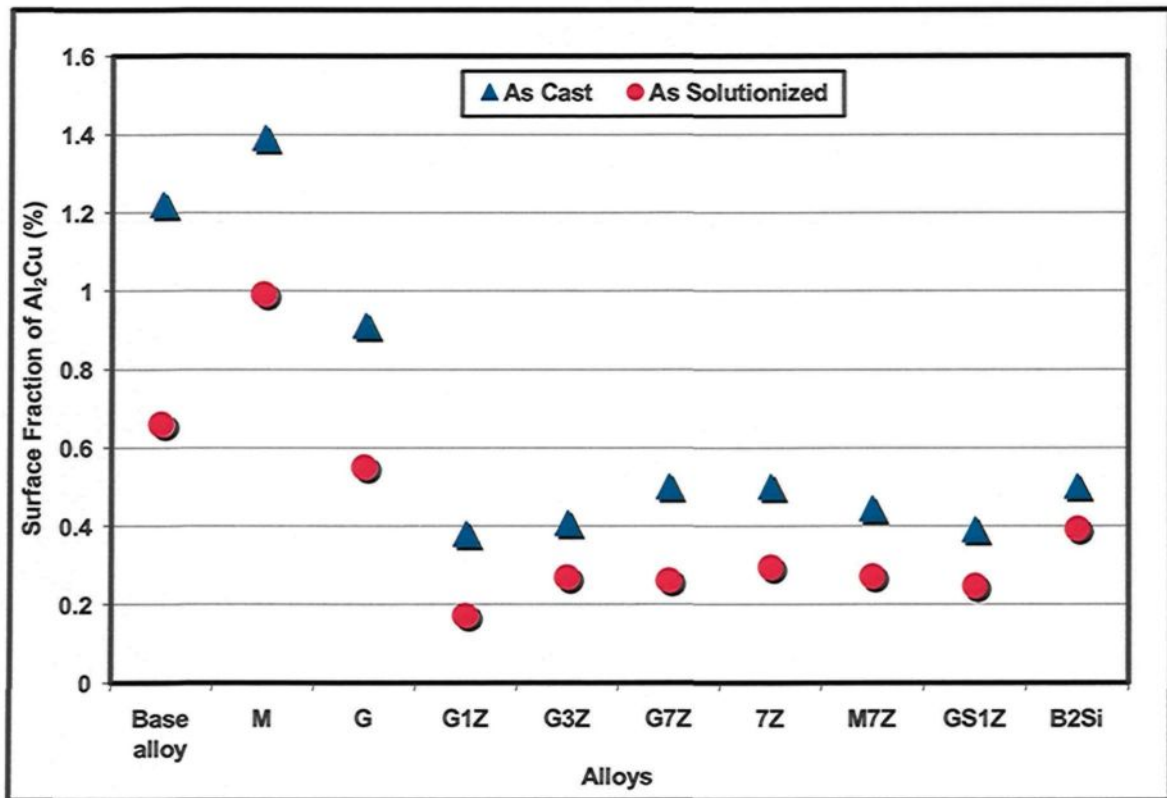


Figure 5.3 Surface fraction of Al_2Cu (%) in various alloys investigated in the as-cast and as-solutionized conditions.

Although Ti as a sole addition provides a high surface fraction for Al_2Cu , namely, 0.91% and 0.54%, this level is still lower when compared to the case of Sr-containing alloy. It should be noted that the decrease in the surface fraction of Al_2Cu in the base alloy through the addition of transition elements implies that the amount of Al_2Cu in the base alloy decreases as a result of these additions. This decrease in the surface fraction of Al_2Cu through the addition of transition elements may be explained by the transition in morphology of the matrix from a dendritic to a fine non-dendritic structure. As discussed in chapter 4 on grain structure, the fine non-dendritic morphology contributes to distributing liquid metal, enriched with Cu, in a homogeneous manner as small dispersed pools during

solidification. These pools then solidify as fine intermetallic particles of Al_2Cu distributed homogeneously throughout the matrix. These fine particles of Al_2Cu are expected to dissolve faster and more easily than the coarse particles since the active surface area of the particle for the small-size particles will be larger, thereby leading to a high rate of diffusion.

Earlier studies^{166,167,168} have concluded that, as the Si content increases, the α -Al fraction decreases, and also that a Cu-rich liquid pool then disperses uniformly throughout the intricate network of interdendritic channels. As solidification proceeds, these pools will continue to solidify as fine particles of Al_2Cu . This reasoning would tend to explain why the surface fraction of Al_2Cu decreases upon the addition of 2wt%Si.

An increase in the surface fraction of Al_2Cu through the addition of Sr may be attributed to the fact that the Sr increases the segregation level of Cu in the form of blocklike Al_2Cu particles during solidification.^{169,170,171,172} These particles, having a coarse structure, are difficult to dissolve during solution heat treatment leading to a high volume fraction of undissolved Al_2Cu .

The effects of the various chemical additions on the porosity levels of the base alloy are shown in Figure 5.4. The porosity (%) is found to be reduced by the addition of transition elements from 0.46% for the base alloy to a range of 0.22-0.13% for alloys containing Zr, Sc, or Ti, as shown in Figure 5.4. When Sr is the sole addition, it does not increase the porosity level in the base alloy as may be observed in the M-alloy which shows a porosity level of 0.21%. The addition of 2wt% Si, obtaining the B2Si-alloy, decreases the porosity of the base alloy to 0.2%, as shown in Figure 5.4.

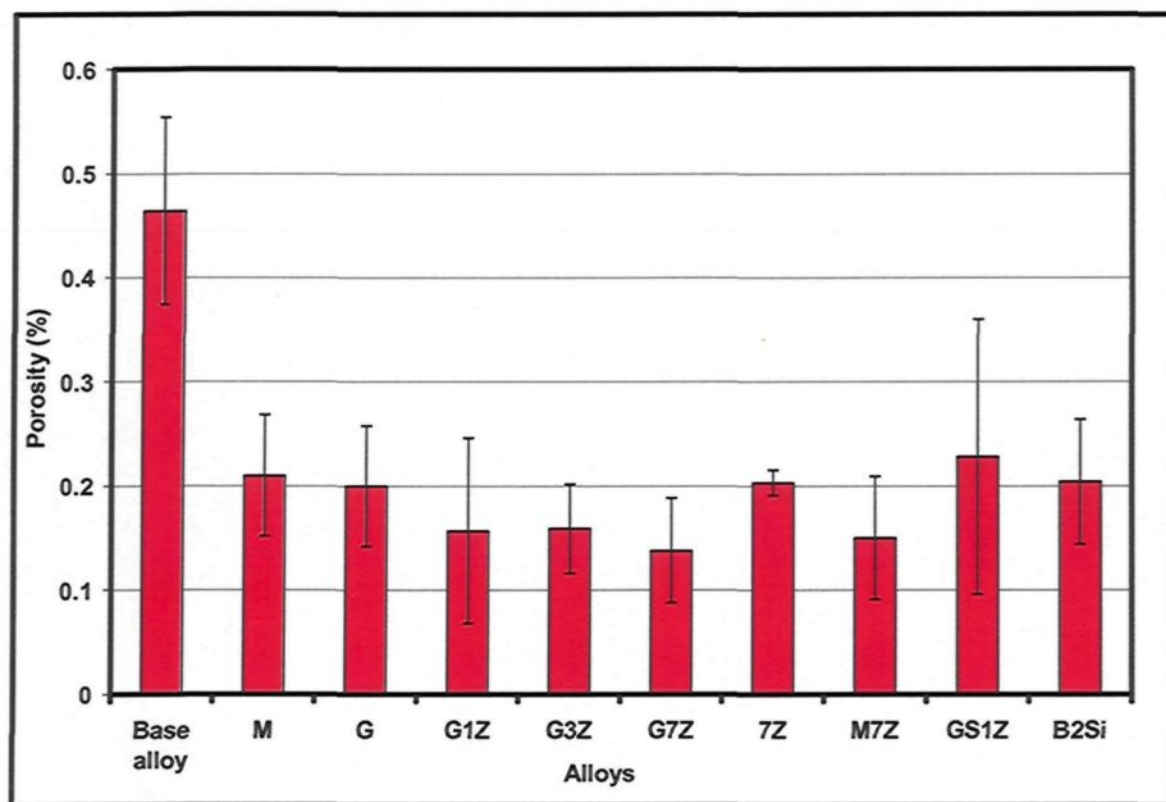


Figure 5.4 Surface fraction of porosity (%) in a number of alloys investigated

Diminishing the porosity content in the base alloy by more than 50% with the addition of transition elements, indicates once again the beneficial effects of these elements in obtaining the refined non-dendritic structure of the α -Al, which in turn enhances the feedability aspect. The long dendritic branches as well as the greater DAS make the feeding ability of the liquid metal more difficult by increasing the long feeding distance and by closing the interdendritic liquid channel, thereby intensifying the tendency of pores to form between the dendrites.^{17,173} Accordingly, a refined non-dendritic structure would be more favorable to feedability and would thus result in less porosity formation.

In the case of alloys containing high Si levels, it was observed that there is a direct crystallographic orientation relationship between the eutectic Si and the adjacent primary

aluminum dendrites; this relationship disappears in the presence of Sr in such a way that the eutectic Si can nucleate and grow independently of these primary dendrites.^{174,175,176} The independent nucleation and growth decreases the permeability and feeding efficiency of the dendritic structure as a result of the obstruction of the feeding paths which increases the tendency towards porosity formation. Accordingly, the amount of the eutectic will be too low at low levels of Si content, and thus any difference in the crystallographic orientation relationship between the eutectic Si and the adjacent primary aluminum dendrites will be non-significant. Strontium addition will thus have no preferential effect on the formation of pores in any Al-2wt%Cu base alloy containing 1wt% Si; this observation is also in agreement with what was reported in an earlier study.¹⁷⁷ The drop observed in the porosity of the base alloy from 0.46% to 0.2% with the addition of 2wt% Si may be attributed mainly to the contribution of an increased amount of eutectic Si which consistently improves the liquid fluidity and feedability during solidification.^{178,179}

Figure 5.5 highlights the significant effects of adding transition elements on the production of refined non-dendritic morphology which in its own turn reduces the surface fraction of Al_2Cu and the level of porosity (%). In this figure, the porosity (%) and the surface fraction of Al_2Cu observed in alloy samples containing various transition elements/additions are plotted against the grain size. It may be seen that both the porosity and the surface fraction of Al_2Cu decrease as the grain size decreases in a linear fashion, as represented by the linear trend lines and equations with R^2 values of 0.91 for Al_2Cu (%) and 0.8 for porosity, for the two parameters. These results further confirm the beneficial

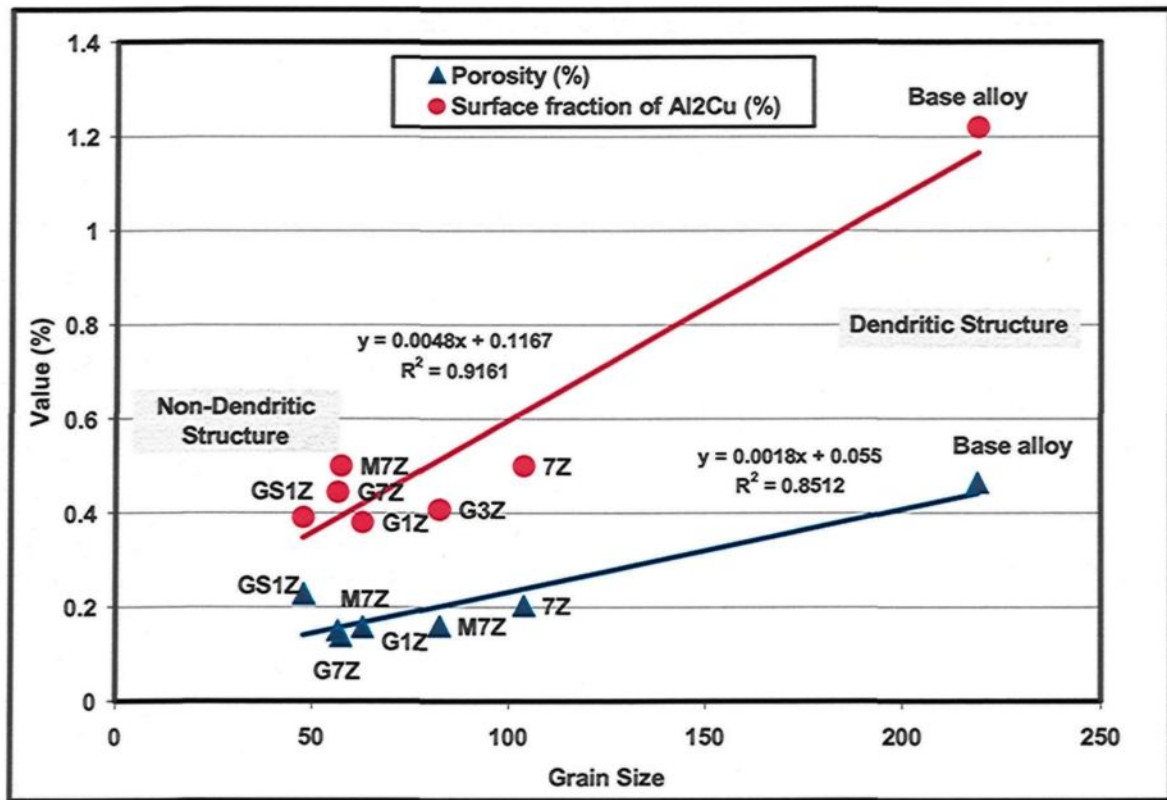


Figure 5.5 Porosity (%) and surface fraction of Al₂Cu versus grain size in Al-2wt%Cu alloys containing various additions of transition elements

effects of the refined non-dendritic structure obtained through the addition of transition elements.

The modifying effects of Sr addition on α -Fe intermetallic compounds were observed in this study. Figure 5.6 represents the morphology of α -Fe particles in the base alloy and in two of the Sr-containing alloys, namely, the M-alloy and the GM-alloy. In the base alloy, the α -Fe particles may be observed in the form of elongated and branched particles. In the case of the M-alloy, in which Sr alone was added to the base alloy, it is clear that the small sizes of the α -Fe intermetallic compound particles have started to fragment and spheroidize, as shown in Figure 5.6(b). It will be found that the addition of Ti

to M-alloy, yielding GM-alloy, enhances the modifying effect of Sr in terms of the formation of fine-rounded α -Fe particles. This observation may be due to the production of a fine non-dendritic morphology of the α -Al matrix; therefore it becomes much easier for these fine α -Fe particles to fragment and spheroidize.

It may be suggested that the modifying effect of Sr on α -Fe intermetallic compounds occurs during solidification and at the formation temperature of the α -Fe intermetallic phase, approximately 619°C, the Sr is absorbed throughout the α -Fe phase leading to its destabilization. The destabilization of α -Fe particles occurs through two subsequent stages of fragmentation and spheroidization where the thin arms of α -Fe particles break down into small segments and, in turn, themselves undergo spheroidization. The modifying action of Sr on the α -Fe particles where the Sr leads to fragmentation of the α -Fe particles and the rejection of Si was reported in other studies^{180,194}.

The Same modifying effect of Sr on iron intermetallics was observed in pure Al (99.78wt%Al containing 0.16wt% Fe and 0.05wt% Si),¹⁸¹ where it was found that the Sr is absorbed throughout the β -iron and α -iron intermetallic particles, causing fragmentation and spheroidization of these intermetallics, as shown in Figure 5.7. It should be mentioned that, the combination of Sr with grain refiner additions such as Zr and Ti is believed to minimize the segregation effects of Sr on Cu and also maximizes the modifying effect of Sr in producing small rounded α -Fe particles, which is believed to contribute to the tensile properties of the base alloys to a considerable degree. As will be observed further on, next

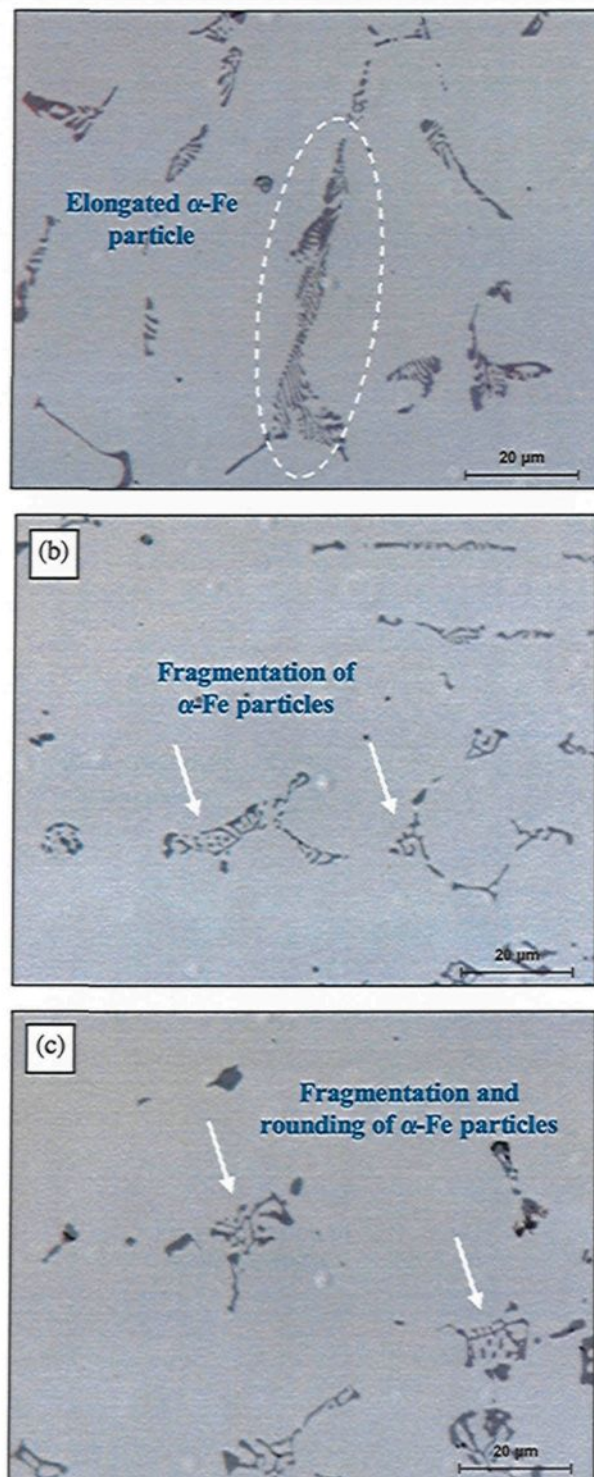


Figure 5.6 Morphology of α -Fe intermetallic particles in as-solutionized condition for (a) the base alloy, (b) the M-alloy, and (c) the GM-alloy.

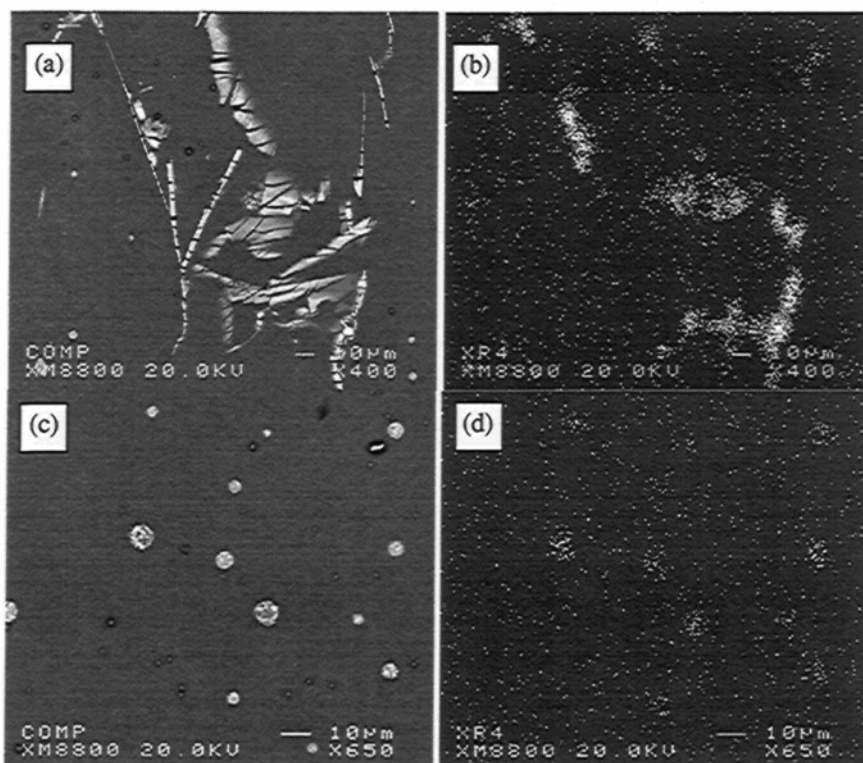


Figure 5.7 (a) Backscattered image of β -iron particles; (b) corresponding X-ray image of Sr; (c) backscattered image of α -Fe; and (d) corresponding X-ray image of Sr.¹⁸¹

section, the combined additions of Sr grain-refiners produce the best results for tensile properties.

5.2 Tensile Properties

5.2.1 As-Cast and As-Solutionized Conditions

The ultimate tensile strength values for all of alloys investigated whether in as-cast or in as-solutionized conditions will be displayed in Figure 5.8. It will be observed that the ultimate tensile strength for alloys in the as-cast condition increases by about 30% to 47% after applying solution heat treatment; for example, the ultimate tensile strength of the base

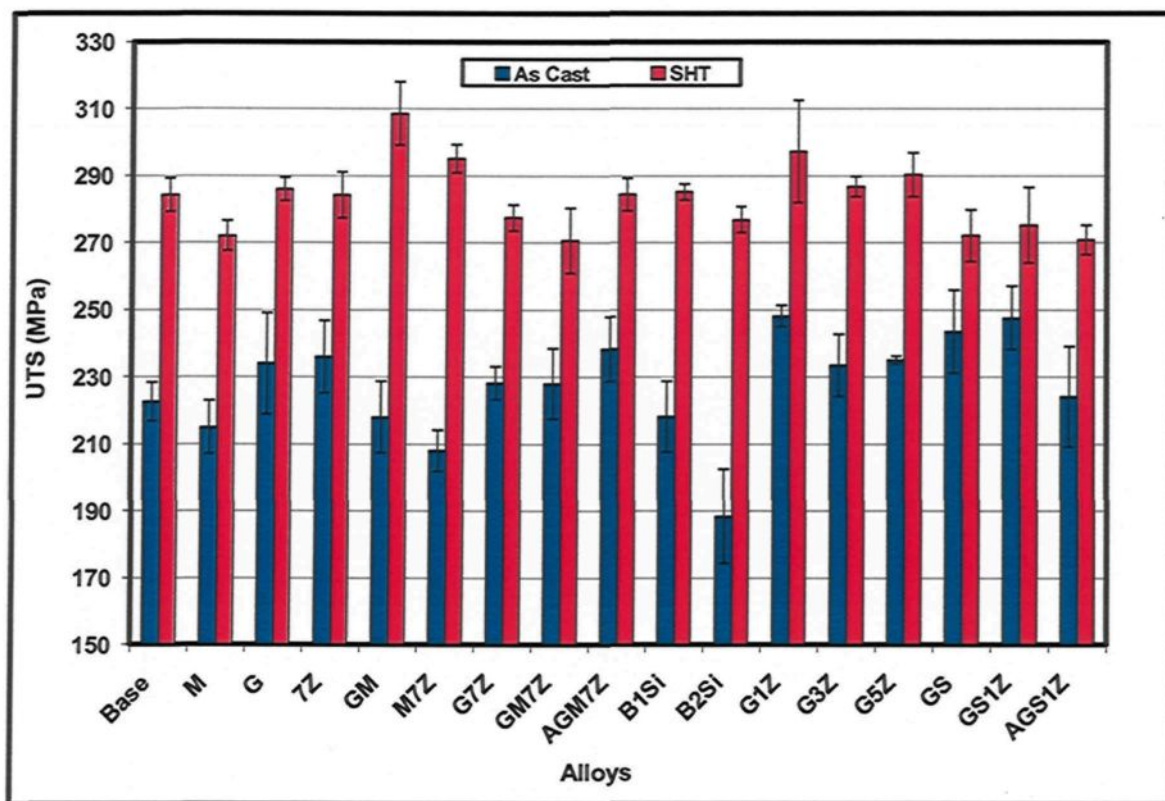


Figure 5.8 Ultimate tensile strength for as-cast and as-solutionized conditions

alloy and the M7Z-alloy increases from 223 and 208 MPa in the as-cast condition to 284 and 309 MPa, respectively, after solution heat treatment.

Microstructure and soundness of casting are the main controlling factors which influence ultimate tensile strength. In the as-cast condition, the microstructure of the alloy investigated may contain mainly coarse particles of the solidified intermetallics or phases such as Al_2Cu , $\text{Al}_5\text{Mg}_8\text{Cu}_2\text{Si}_6$, $\text{Al}_{15}(\text{Mn},\text{Fe},\text{Cu})_3\text{Si}_2$, and Si. These particles have a deleterious effect on the ultimate tensile strength and ductility of the alloy because of their sharp edges which act as crack initiators. During tensile testing, the cracking phenomenon

is usually instigated by the breaking up of these intermetallics or by the decohesion of the intermetallic particles from the surrounding matrix, as will be discussed further on in the text on the subject of fractography.^{182,183} As the solution heat treatment is applied, these intermetallics will break down and dissolve by losing their elements which then return to the matrix producing a supersaturated solid solution of α -Al; this solid solution strengthens the matrix by increasing the resistance of the dislocation movement during the deformation of tensile testing.^{20, 184}

Figure 5.9 represents the yield strength results for as-cast and as-solutionized conditions. From this figure, it will be noted that, in the as-cast condition, the addition of the transition elements of Zr and Sc increase the yield strength of the base alloy from 153 MPa to a range of 171-190 MPa, as displayed by Zr- and Sc-containing alloys. For these alloys, the yield strength is higher in the as-cast condition than it is in the as-solutionized condition; this implies that the yield strength of the as-cast condition decreases as a result of the application of a solution heat treatment. For example, in the G1Z-, G3Z-, GS1Z-, and 7Z-alloys, the yield strengths decrease from 188, 188, 190, and 181 MPa in the as-cast condition to 166, 164, 176, and 159 MPa, respectively, after solution heat treatment. This is not the case, however, for the base alloy where the yield strength in the as-cast condition increases from 153 MPa to 159 MPa after solution heat treatment. As reported previously,^{70,71,81,82} Zr and Sc as transition elements form dispersoid precipitates of Al_3Zr , Al_3Sc , $\text{Al}_3(\text{Zr}_{1-x}\text{Sc}_x)$, and $\text{Al}_3(\text{Sc}_{1-x}\text{Zr}_x)$ throughout the α -Al matrix displaying an intensified hardening effect. The author suggested that these dispersoids may form during the cooling of the solidified alloy from the melting temperature to room temperature when passing

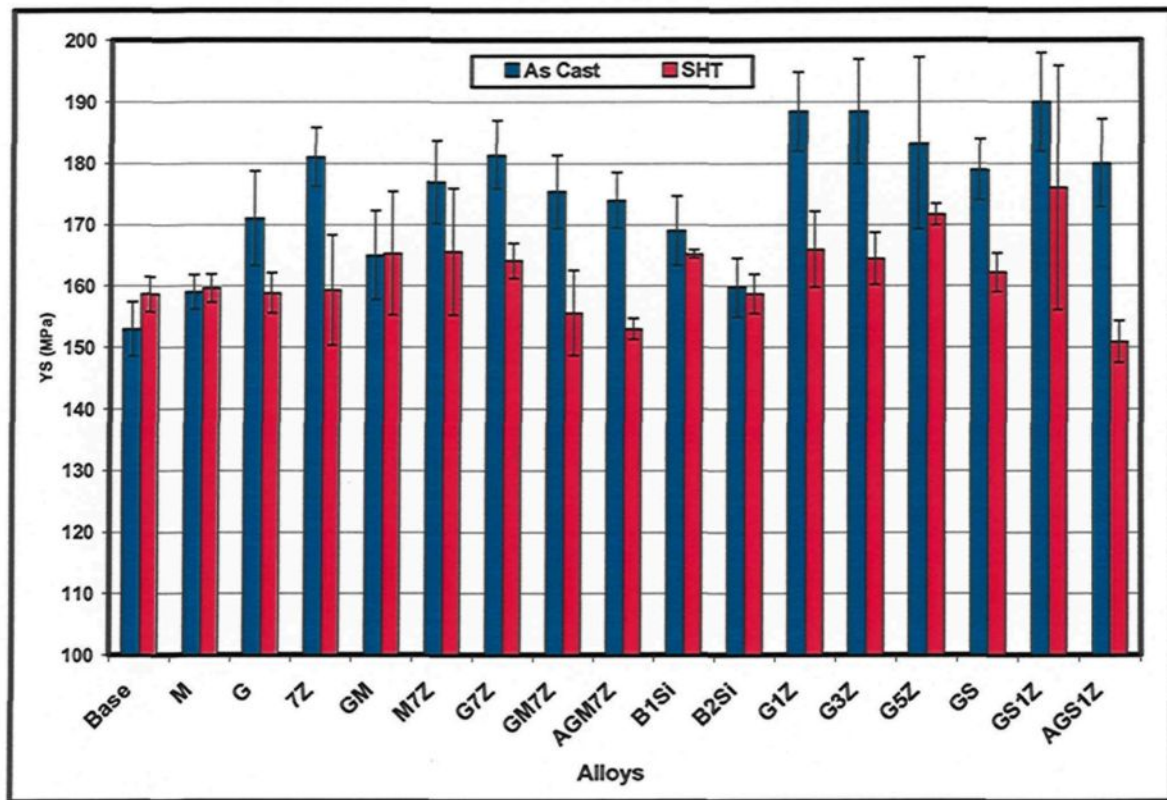


Figure 5.9 Yield strength for as-cast and as-solutionized conditions

through the temperature formation range of these dispersoids. Thus the formation of dispersoids during solidification would explain why the yield strengths of Zr- and Sc-containing alloys are higher than the yield strengths of other alloys in the as-cast condition. On the other hand, it has been reported that the highest precipitation kinetics and growth rate occur at a temperature of 495°C for 0.13 wt% Zr.⁷⁴ Accordingly, at high Zr contents of 0.15 to 0.7 wt% in the alloys under investigation and at a solution temperature of 490°C, a high coarsening rate in the dispersoids is to be expected; this may be the reason for the reduction obtained in the yield strength of the alloys containing transition elements after the application of the solution heat treatment.

As will be seen in Figure 5.10, the elongation of the alloys investigated in the as-cast condition has been improved upon by applying a solution heat treatment. For example, elongation (%) of the base alloy, and the G-, B2Si-, M7Z-, and G1Z-alloys increase from 2.8, 1.8, 1, and 2.4 % in the as-cast condition, respectively, to 5.6, 7.6, 5.7, and 5.8 % after undergoing solution heat treatment. It will also be observed that the GM-alloy reached the highest level of elongation, specifically 7.6 %, after solution heat treatment with an improvement of about 300%.

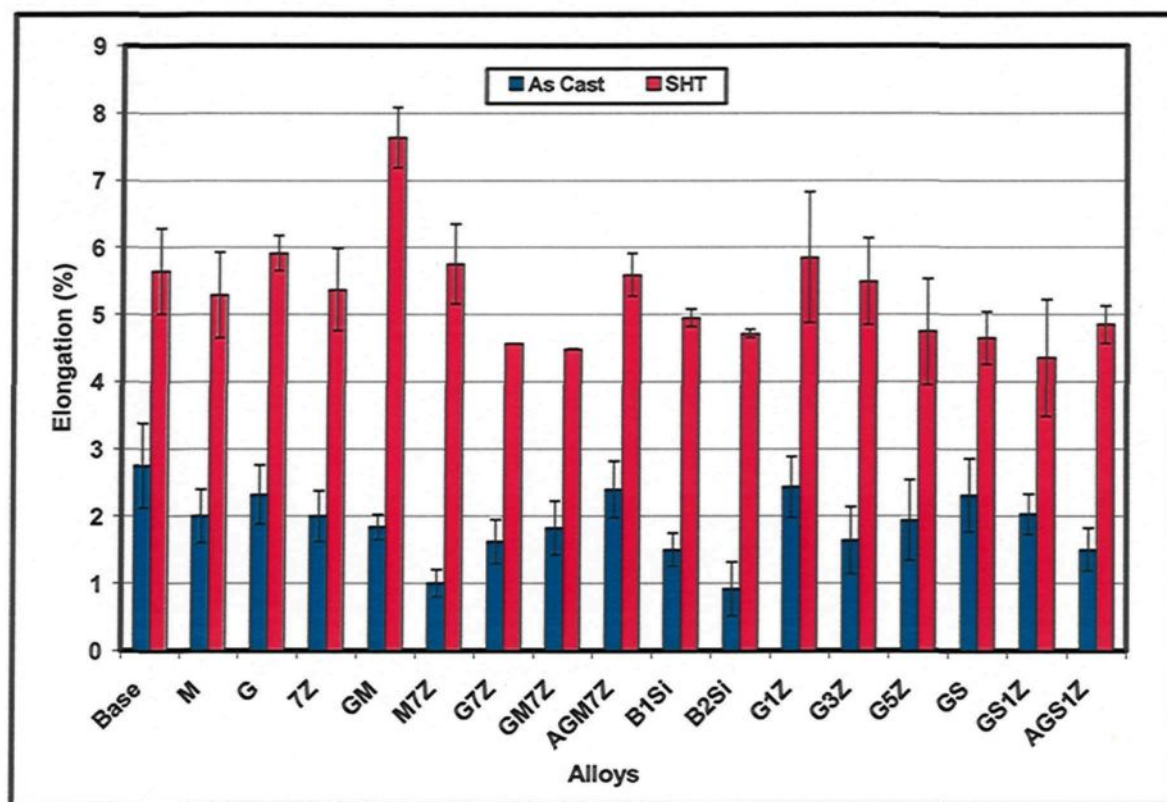


Figure 5.10 Elongation (%) for as-cast and as-solutionized conditions

During solidification of the alloy, the alloying elements tend to segregate as localized clusters producing intermetallic particles in coarse shapes. As mentioned above,

the solution heat treatment dissolves and refines the brittle intermetallic particles such as Al_2Cu and $\text{Al}_5\text{Mg}_8\text{Cu}_2\text{Si}_6$ existing in the as-cast condition and identifiable by their coarse morphology. This refining retards the cracking action and provides uniform plastic deformation during the tensile testing and hence high elongation (%) may be obtained. The observable improvement in elongation of the GM-alloy is attributed to the combined addition of Sr-Ti. The addition of Ti-B refines the morphology of the alloy and may treat the segregating effect which Sr has on Cu, and which causes it to precipitate as blocklike Al_2Cu in the presence of Sr; this is in addition to the modifying effect of Sr on the α -Fe intermetallic which was reported upon in the section on microstructure. All of these beneficial effects explain the improvement in elongation obtained by the combined addition of Sr-Ti as represented by the GM-alloy.

5.2.2 Age-Hardening Conditions

In this section, age-hardening results will be illustrated and discussed through the following four alloy groups: the Zr-Ti alloy group, the Zr-Sr alloy group, the Zr-Sc alloy group, and the Si alloy group. The results of age-hardening treatment obtained for each group may be divided into two sub-groups based on the aging temperature, as follows: (i) at 180°C (T6 peak-aged condition) for 2, 4, 6, 10, 16, 24, and 48h aging periods, and (ii) at 220°C (T7 overaged condition) for 0.5, 1, 1.5, 2, 4, 6, 10, 16, 24, and 48h aging periods

5.2.2.1 Zr-Ti Alloy Group

Figures 5.11 through 5.13 present the tensile properties composed of ultimate tensile strength, yield strength, and elongation (%), respectively, for the Zr-Ti alloy group

at 180°C aging temperature. It will be seen from Figures 5.11 and 5.12, that the tensile and yield strengths of the base alloy have been improved by the combined addition of Zr-Ti in the amount of about 20 MPa. The base alloy displays two main age-hardening peaks, obtained after 10h and 24h of aging, and which increased as a result of Zr-Ti additions, as shown in Figures 5.11 and 5.12.

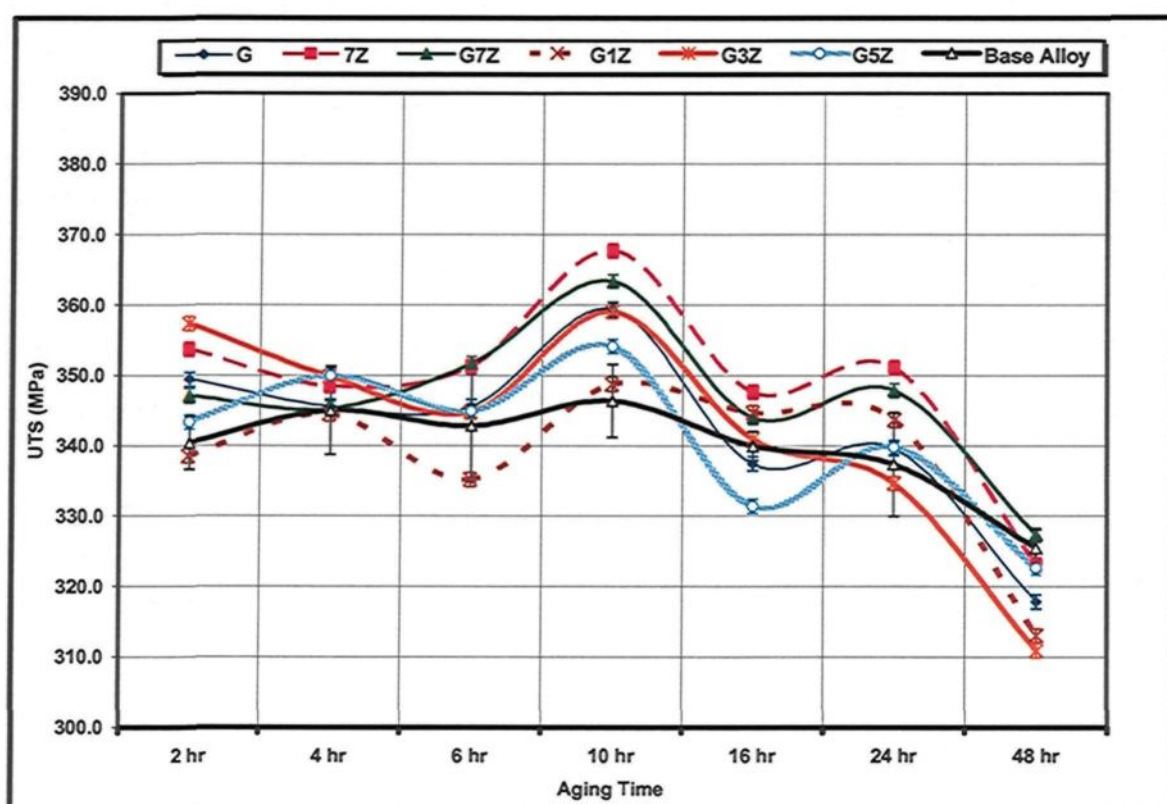


Figure 5.11 Effects of aging time on the ultimate tensile strength of the Zr-Ti alloy group at 180°C

It will also be observed that increasing the Zr content has a beneficial effect on the strength values, as may be seen in the following case. The ultimate tensile strength and the yield strength of the G1Z-alloy containing 0.15wt% Zr increase from 349 and 305 MPa to 364 and 323 MPa, respectively, as displayed by the G7Z-alloy containing 0.7wt% Zr,

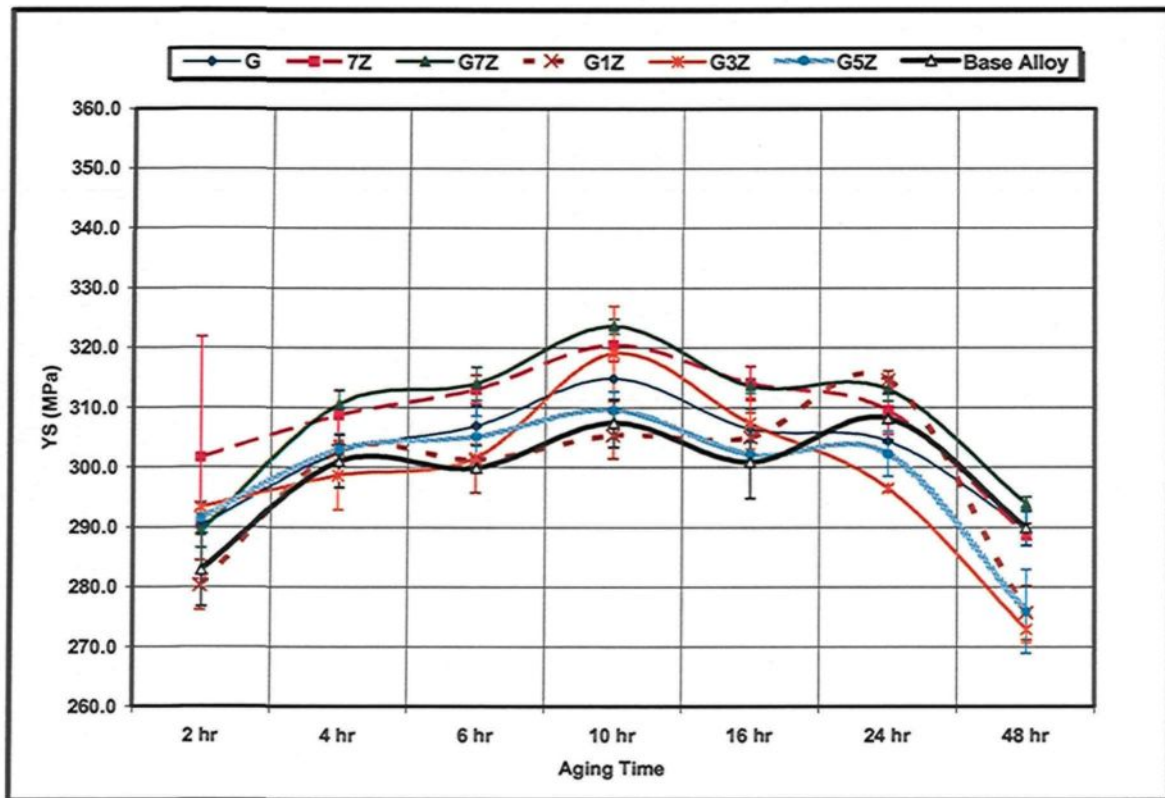


Figure 5.12 Effects of aging time on the yield strength of the Zr-Ti alloy group at 180°C

shown in Figures 5.11 and 5.12.

Titanium-boron as a sole addition to the base alloy, yielding the G-alloy, provides an intermediate level of improvement in the tensile properties of the alloy. At an aging temperature of 180°C, the highest values of ultimate tensile and yield strength are obtained after 10h. The 7Z-alloy displays the best ultimate tensile strength values of almost all the aging periods, as shown in Figure 5.11; at the same time, the G7Z-alloy provides the best yield strength values, as shown in Figure 5.12.

After 48h of aging, the strength of the alloys decreases to the lowest strength levels from 327 to 310 MPa for ultimate strength and from 294 to 273 MPa for yield strength. The

elongation values of the base alloy, however, were not enhanced to any considerable degree by the combined addition of Zr-Ti. The elongation values remain almost constant at approximately 1.5% during the aging periods except for 2h and 48h when it reaches values of around 2.6%, as shown in Figure 5.13.

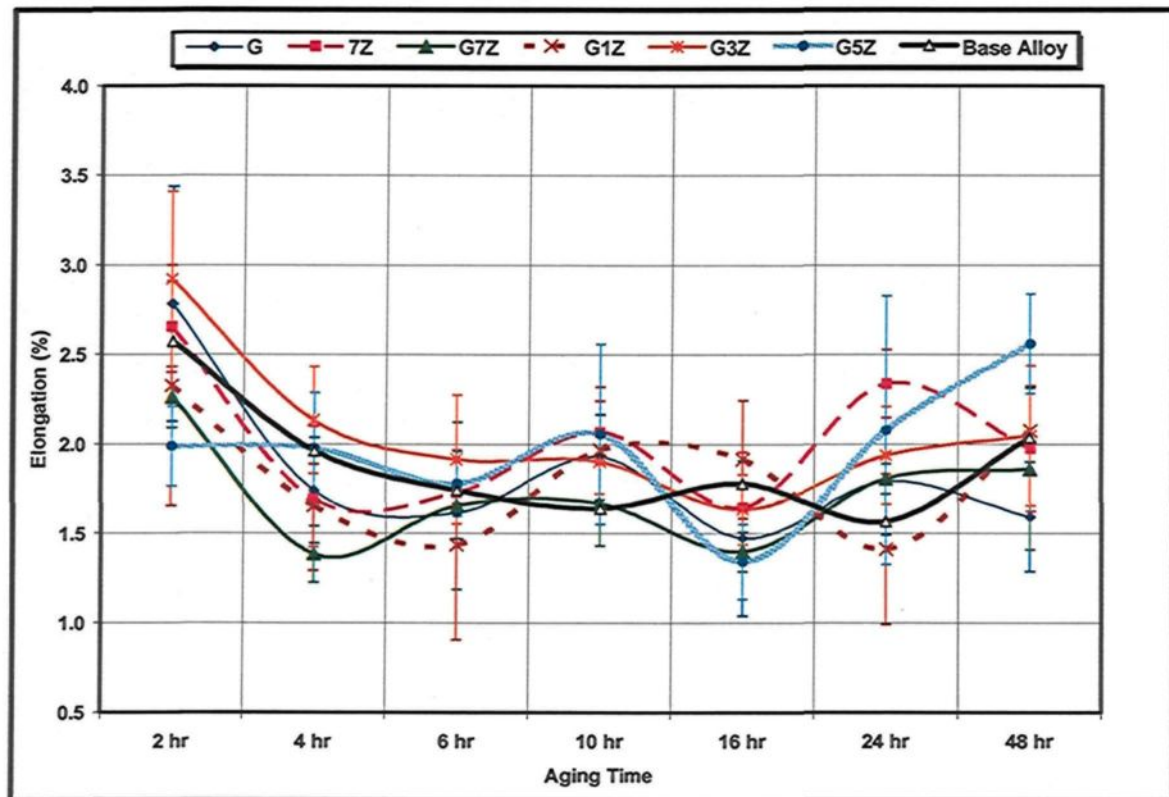


Figure 5.13 Effects of aging time on the elongation (%) of the Zr-Ti alloy group at 180°C

In the Al-Cu-Mg-Si system, the main hardening phases expected to occur are θ' (Al_2Cu), β'' (Mg_2Si), Q' (AlMgSiCu), S'' (Al_2CuMg), and the Si phases.^{46,47} Thus, the phases predicted for the alloy under investigation here, having the composition Al-2Cu-1Si-0.4Mg-0.42Fe-0.6Mn, are connected to the four phases mentioned above. Also, it has been postulated that both the Mg:Si ratio and the copper content

determine the main hardening phases in the aging process.^{46,58} Again, with regard to the alloy under investigation, which has a Mg:Si ratio of 0.4 and a Cu content of 2wt%, the hardening phases expected are θ' (Al₂Cu), β'' (Mg₂Si), the Si phase, and possibly S'(Al₂CuMg). It is suggested that these phases may also be responsible for the two age-hardening peaks observed in Figures 5.11 and 5.12.

The improvement in strength of the base alloy as a result of combined additions of Zr-Ti may be attributed to a number of factors, as discussed below. The section on microstructure shows that the addition of Zr-Ti produces a refined non-dendritic structure which in turn decreases the porosity level and increases the amount of dissolved Al₂Cu after solution heat treatment, as shown in Figure 5.3. This increase makes it possible to obtain an elevated level of Cu-rich supersaturated solid solution of α -Al, thus creating an intensified driving force for precipitation reactions, and thereby leading to a high degree of strength.²⁰

It is assumed that the dispersoid precipitates of Al₃Zr and/or Al₃(Zr_{1-x}Ti) may act as nucleation sites for the age-hardening phases during the aging process, ultimately leading to further improvement in strength.^{139,185,186} According to a different study,¹⁸⁷ there is also a possibility that Zr modifies the S'-phase precipitates due to the high binding energy (0.24±0.02 eV) between Zr atoms and vacancies in aluminum. As the Zr content increases, it is expected that the degree of improvement will also increase with it. It is worth mentioning that additions of Zr-Ti lead to the formation of primary intermetallic particles of Al₃Zr and Al₃(Zr_{1-x}Ti), as reported in the preceding chapter, and that these intermetallics may have a deleterious effect on the ductility of alloys since they have the potential for

acting as crack initiators. Figures 5.14 and 5.15 and present the effects of combined additions of Zr-Ti on the tensile strength and yield strength, respectively, at 220°C aging temperature. The tensile strength of the alloys investigated in the as-solutionized condition increases by about 40 MPa after 0.5h of aging at 220°C; the yield strength of these alloys in the as-solutionized condition, however, increases by about 130 MPa after the same aging period.

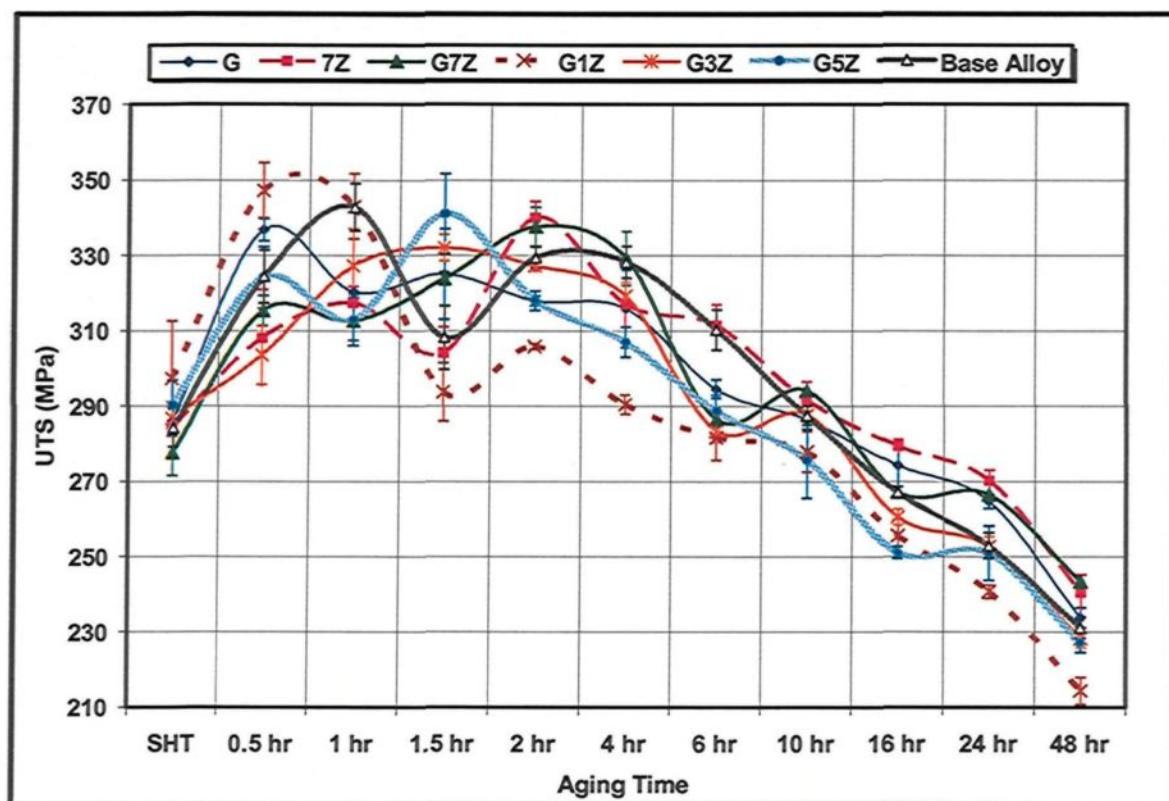


Figure 5.14 Effects of aging time on the ultimate tensile strength of the Zr-Ti alloy group at 220°C

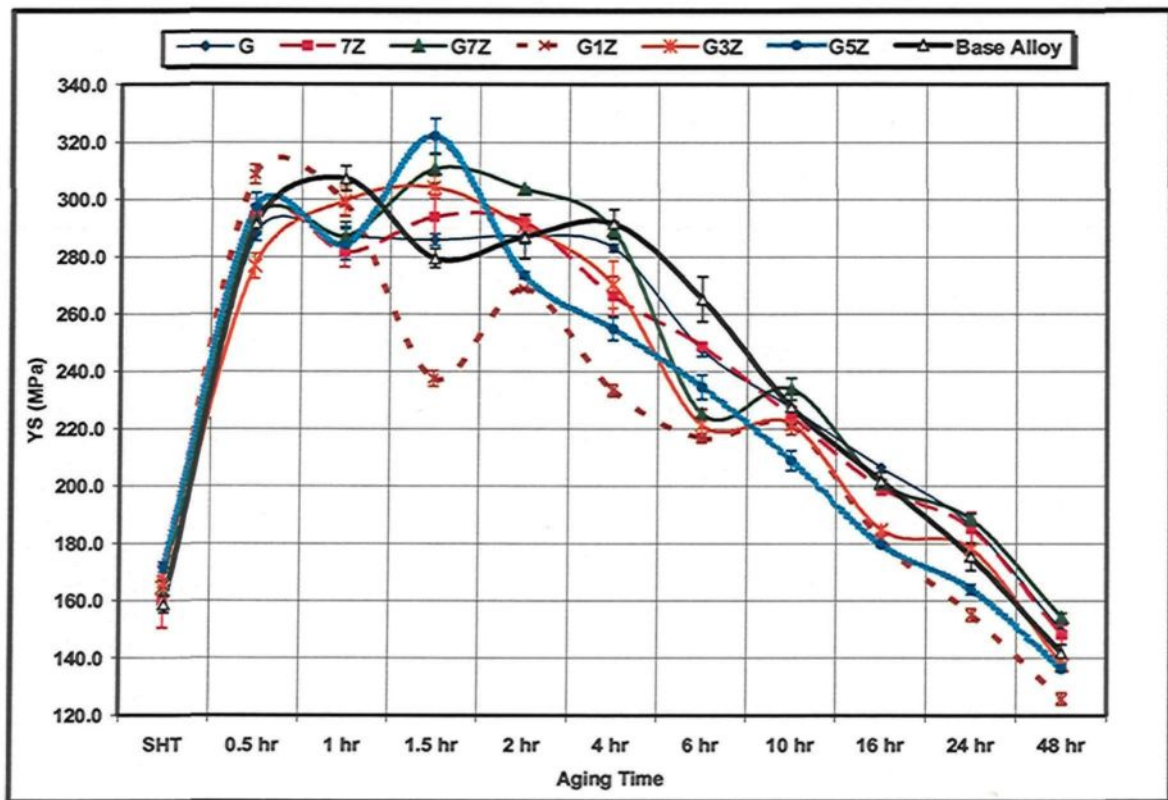


Figure 5.15 Effects of aging time on the yield strength of the Zr-Ti alloy group at 220°C

At the earlier aging periods of 0.5h to 2h, the alloy strength may be varied by obtaining several distinct age-hardening peaks. At these aging times of 0.5h to 2h, both the G3Z-alloy and the G-alloy display the most stable age-hardening behavior of all the alloys investigated whether it be for tensile strength or for yield strength.

After 2h of aging, the softening begins to be more observable where all of the alloys investigated lose their strength in a linear fashion attaining the lowest level of 243-214MPa for tensile strength and 154-125MPa for yield strength after 48h of aging. The elongation of the alloys investigated is improved by an increase in the aging time period reaching its highest level (4-5%) after 48h of aging, as shown in Figure 5.16.

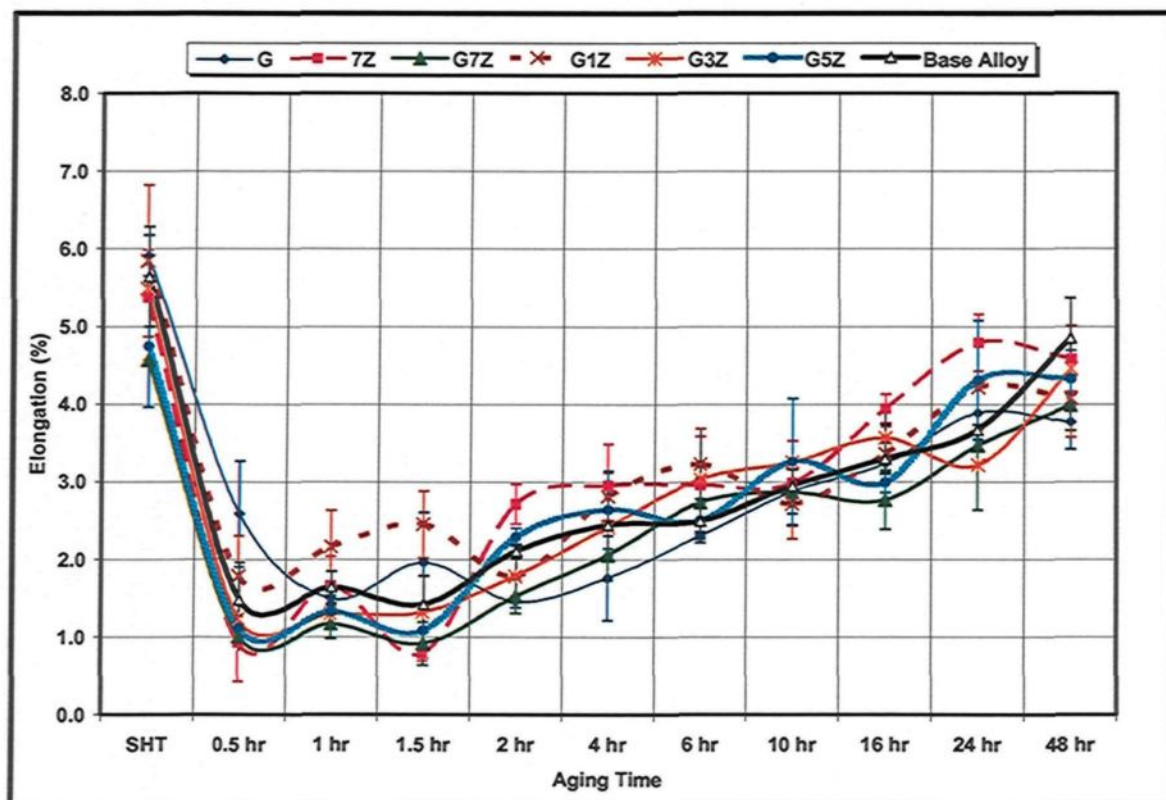


Figure 5.16 Effects of aging time on the elongation (%) of the Zr-Ti alloy group at 220°C

A temperature of 220°C is considered to be an elevated aging temperature at which precipitation would not occur in the normal sequences; in the case of Al-Cu systems at a high aging temperature of 220°C, the GP zones cannot be expected to form because such an aging temperature would be above their solvus line although, instead, the θ'' will nucleate directly.^{188,189} At high aging temperatures of 220°C, the kinetics of the aging process are high as a result of the higher solute diffusivity,^{188,190} leading to peak strength in a short time, thus explaining the increase in the strength values after only 0.5h of aging.

From the point of view of precipitation reactions, the Al-2wt%Cu base alloy, having the chemical composition of Al-2wt%Cu-1wt%Si-0.4wt%Mg-0.42wt%Fe-0.6wt%Mn, is considered to be a complicated system as a result of the wide variety of the age-hardening

phases which are expected to form during the age-hardening treatment. As mentioned previously, the age-hardening phases under discussion are θ' (Al_2Cu), β'' (Mg_2Si), the Si phase, and possibly S' (Al_2CuMg); these phases have different precipitation sequences which may occur either simultaneously or independently.⁵⁸ As was indicated in the discussion on the effects of 180°C aging temperature, Zr content has an observable effect on the precipitation process from a number of aspects; the Al_3Zr dispersoids provide heterogeneous nucleation sites for age-hardening phases, while the Zr modifies the S' metastable phase.^{185,186,187} The Zr additions produce a refined non-dendritic structure, which in turn reduces the porosity level and the amount of the undissolved Al_2Cu , thus improving alloy strength.

The variations in strength for the earlier aging periods of 0.5 to 2h may occur in different manners as a result of the rapid formation and coarsening of the various age-hardening phases. In the case of the base alloy, the first peak at 0.5h may be attributed to the formation of θ'' succeeded by rapid coarsening leading to a drop in strength followed by the precipitation of other types of age-hardening phases such as β' resulting in further peak strength, and so forth. The effects of Zr content on the precipitation behavior of the alloys investigated can be confirmed by the variations detected in the age-hardening peaks. Also, it is believed that there is an optimum Zr content providing stability of the precipitation behavior, as displayed by G3Z.

As the aging time exceeds 2h, the age-hardening metastable phases begin to lose coherency while the dislocation accommodates the interface misfit between the precipitates and the matrix leading to the formation of the equilibrium precipitate θ - Al_2Cu .^{20,39} This

would explain the decrease in strength and the increase in the elongation as the aging time exceeds 2h, reaching a maximum level after 48h.

5.2.2.2 Zr-Sr Alloy Group

Adding Zr-Sr combined to the base alloy will affect both the tensile strength and the yield strength through the application of different aging times at an aging temperature of 180°C, as shown in Figures 5.17 and 5.18, respectively. It will be noted that additions of Zr-Sr in combination obtain the highest strength levels for all the alloys under investigation.

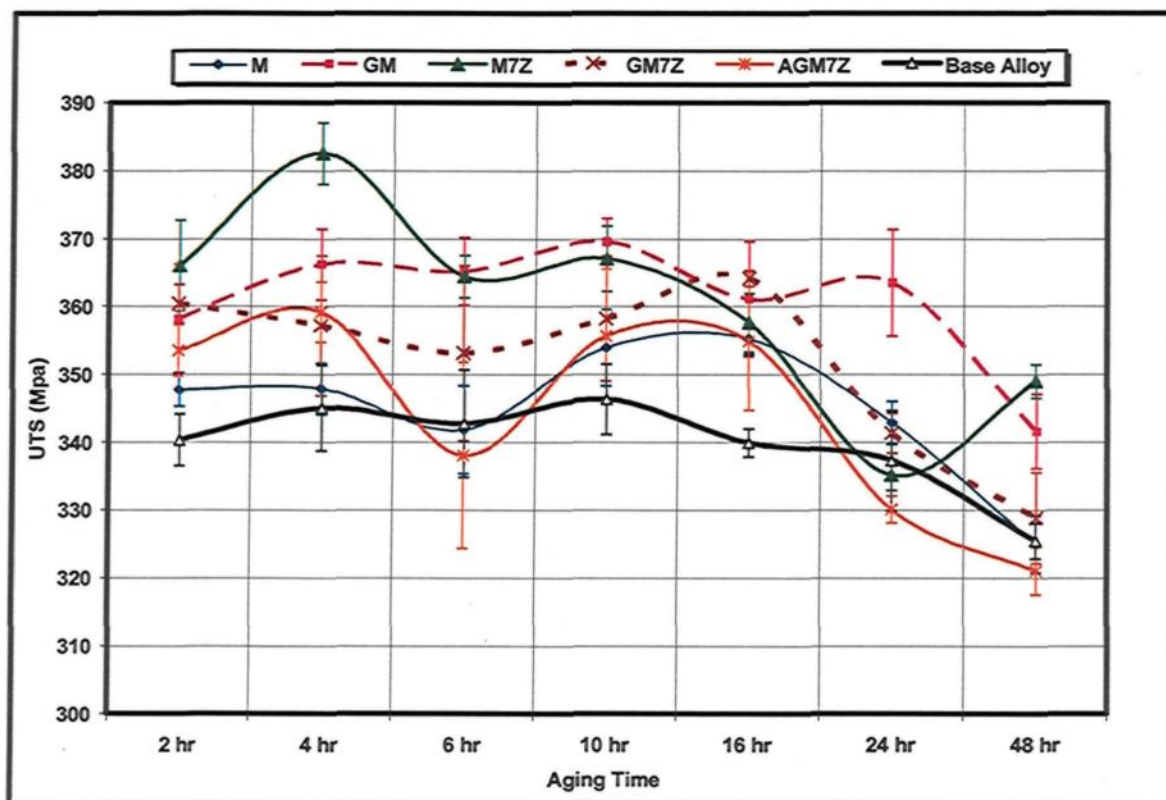


Figure 5.17 Effects of aging time on the ultimate tensile strength of the Zr-Sr alloy group at 180°C

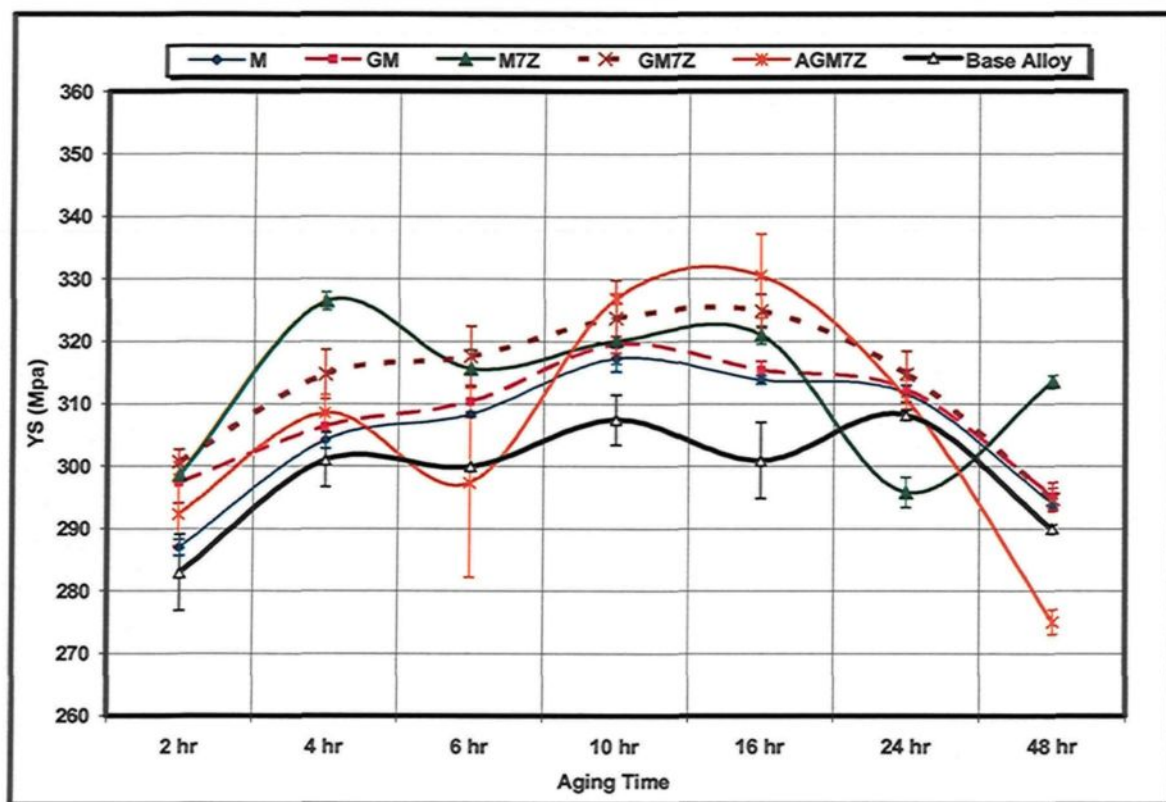


Figure 5.18 Effects of aging time on the yield strength of the Zr-Sr alloy group at 180°C

The improvement in the tensile and yield strengths thus obtained reach 40 MPa for the tensile properties and 30 MPa for the yield strength, as displayed by the M7Z-alloy. This alloy reached the highest strength levels of 383 MPa and 326 MPa for the tensile and yield strengths, respectively.

It will also be observed that the age-hardening peak shifts so as to occur after only 4h of aging through the addition of Sr to the 7Z-alloy, thus producing the M7Z-alloy. It may be observed that the improvement in tensile strength brought about by the combined additions of Zr-Sr and displayed by the M7Z-alloy, may be decreased slightly by means of additions of Ti, as observed in the GM7Z-alloy. The addition of Sr-Ti without any added Zr also reveals an improvement in the strength of the base alloy, as represented by the

GM-alloy. As silver is added to GM7Z, producing the AGM7Z-alloy, this alloy displays the highest yield strengths at 10h and 16h of aging time. Figure 5.19 reveals the effects of combined additions of Zr-Sr on the elongation values of the base alloy at 180°C aging temperature for various aging time periods. In this figure, it will be seen that the combined addition of Sr-Ti obtains the highest elongation level for all the alloys under investigation, as shown by the GM-alloy. The M7Z-alloy occupies the second level in the order of ductility improvement. Although the combined additions of Zr-Sr and Sr-Ti alter the tensile properties of the base alloy, adding Sr as a sole addition does not.

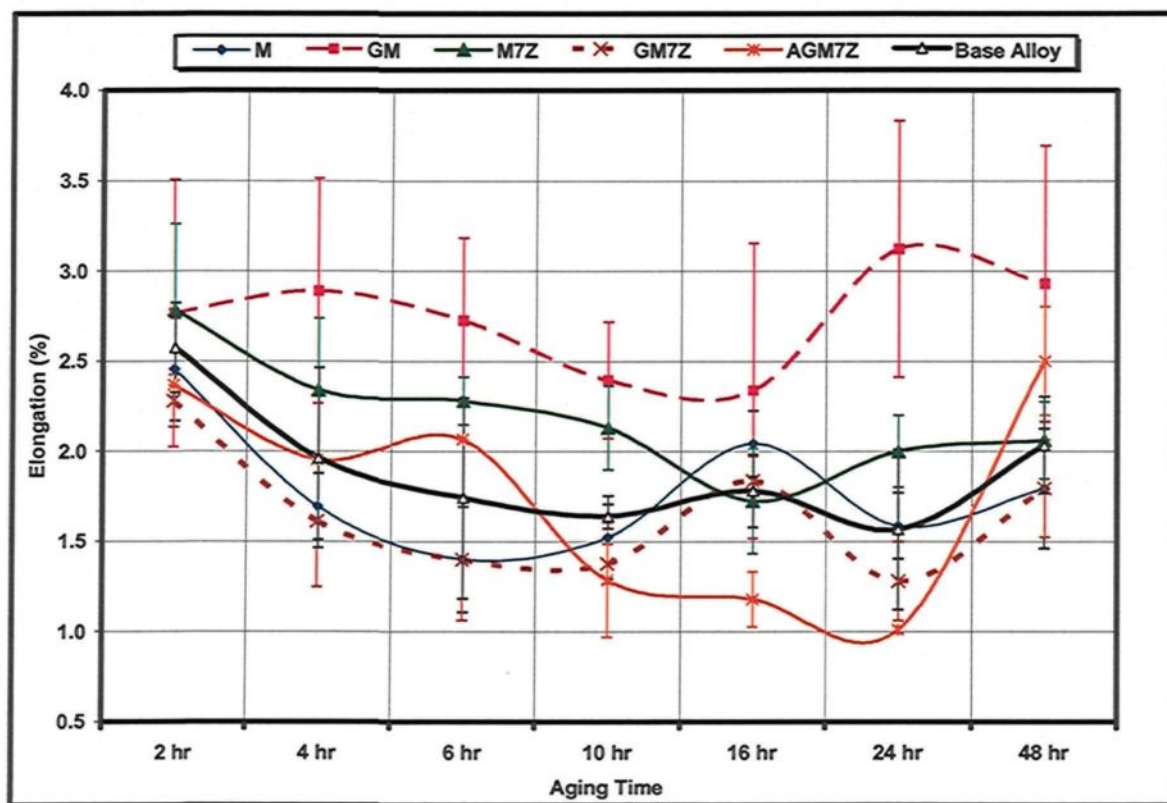


Figure 5.19 Effects of aging time on the elongation (%) of the Zr-Sr alloy group at 180°C

Strontium is known as a surface-active element used as a modifier for eutectic silicon,^{191,192,193} as well as for the intermetallic phases which form during the solidification process, thus leading to many of the improvements occurring in the tensile properties.^{180,194} Strontium is also found to have an indirect yet favorable effect on the age-hardening process, where it promotes the formation of β'' -Mg₂Si precipitation as a result of an increase in the excess-silicon content of the Al solid solution, thereby providing further nucleation sites for the β'' phase during artificial aging.¹⁹⁵ Also, the Sr retards the growth of the β' metastable phase and prevents its transformation into equilibrium Mg₂Si.¹⁹⁵ All of the data presented here is in conformity with the results from tensile testing obtained for Zr-Sr alloys. The shift of the age-hardening peak, occurring after 4 h, indicates that the manner in which Sr accelerates the precipitation kinetics is by providing nucleation sites for β'' precipitates through the increase in excess silicon. Also the increment in strength obtained when using combined additions of Zr-Sr is a result of maximizing the heterogeneous nucleation sites for different age-hardening phases. The addition of Ti to the M7Z-alloy yields the GM7Z-alloy with a slightly lower level of tensile strength. As a result of the addition of Ti in the form of the Al-5Ti-1B master alloy, the reduced level may be attributed to the interaction of Zr and Sr with B, thereby forming (Zr,B) and (Sr,B) compounds.^{79,164,165}

The enhancement obtained in the yield strength of the GM7Z-alloy through the addition of Ag may be ascribed to its solid-solution hardening effect and its supportive effect in the formation of the Ω -phase.^{62,63,64} The combined addition of Zr-Ti and Sr causes an intensified improvement in elongation values since the Zr-Ti produces a fine non-

dendritic morphology associated with the production of fine solidified intermetallics; the Sr, on the other hand, refines and modifies the α -iron intermetallics and Mg_2Si phases. The effects of combined additions of Zr-Sr on both tensile and yield strength at an aging temperature of 220°C through a range of different aging times will be shown in Figures 5.20 and 5.21, respectively. The variation in the strength values at the earlier aging times of 0.5h-2h, as observed in the Zr-Ti alloy group, is now observed to be eliminated to a large extent in the Zr-Sr alloy group. The highest level of strength at 220°C aging temperature was obtained by the GM-alloy.

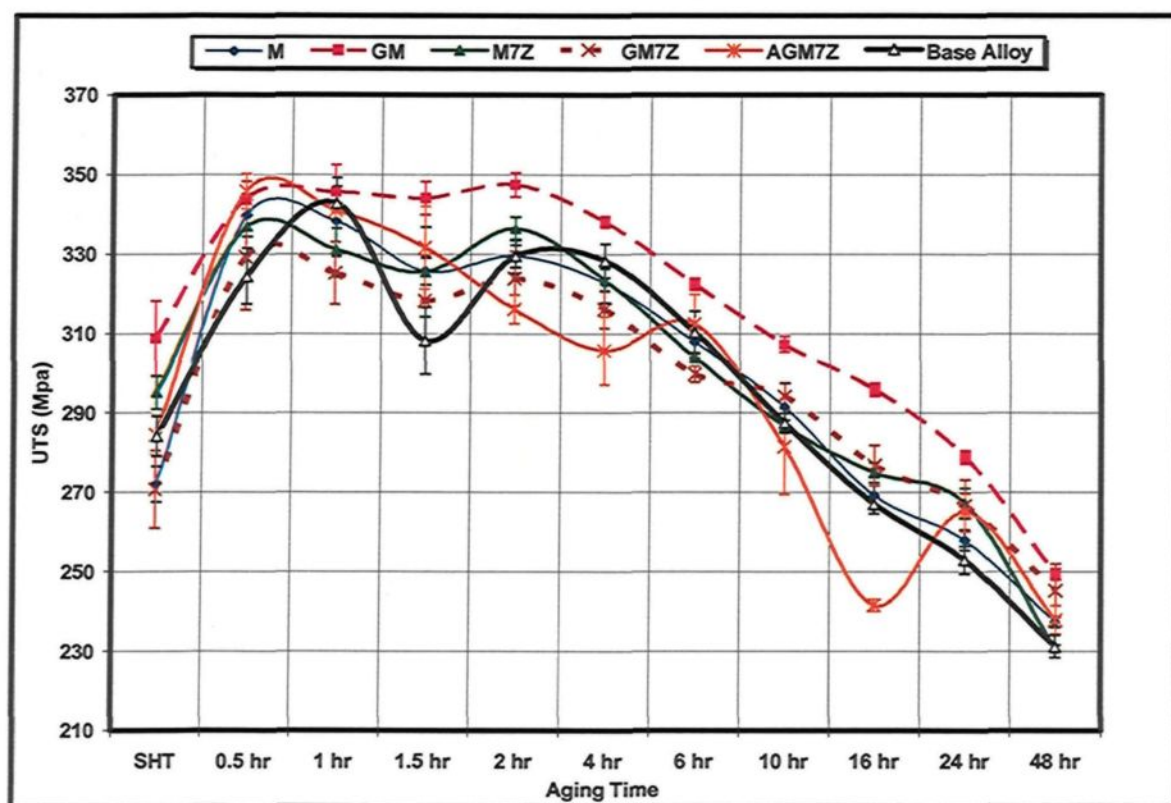


Figure 5.20 Effects of aging time on the ultimate tensile strength of the Zr-Sr alloy group at 220°C

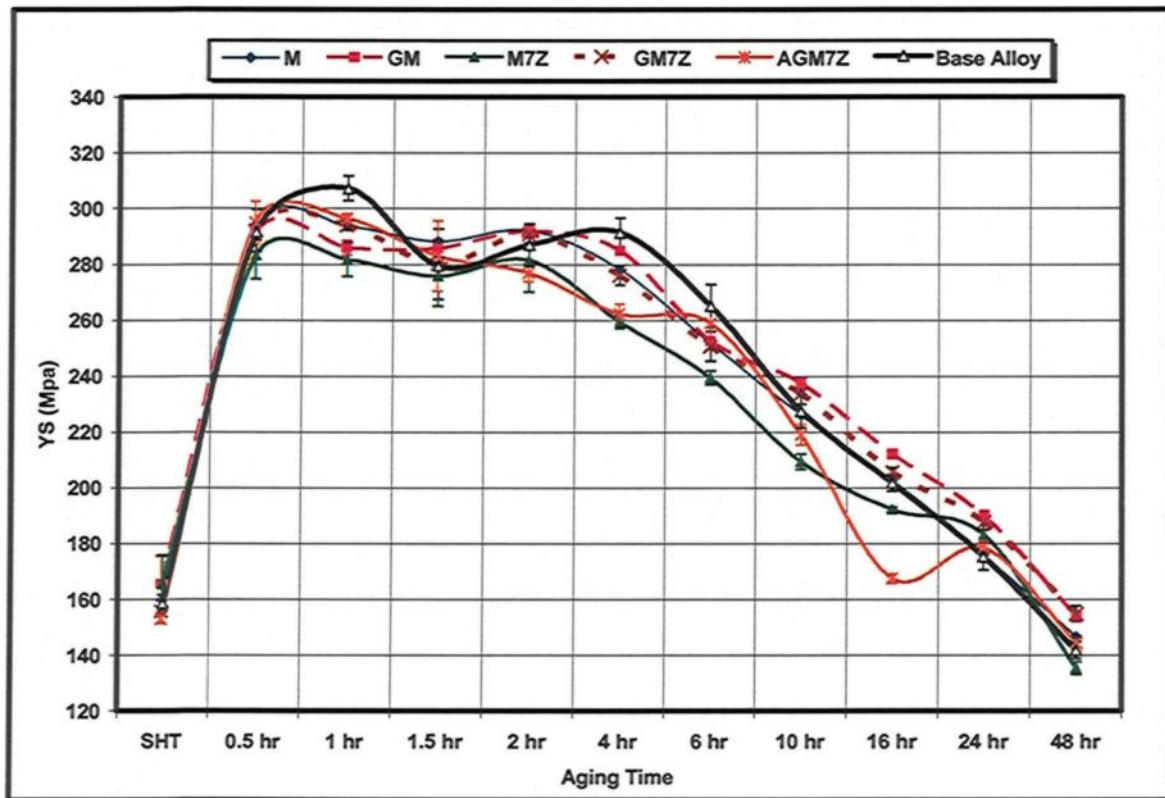


Figure 5.21 Effects of aging time on the yield strength of the Zr-Sr alloy group at 220°C

The elongation results for the Zr-Sr alloy group at an aging temperature of 220°C for various aging times are provided in Figure 5.22. The best elongation results obtained at the aging temperature of 220°C were observed for the Zr-Sr alloys, as shown in Figure 5.22. From this figure, it will also be observed that the GM-alloy obtains the highest elongation level, followed by the M7Z-alloy. The GM7Z-alloy, however, reaches the lowest elongation level of all in the Zr-Sr alloy group, as shown in Figure 5.22.

It will be observed that, as the aging time exceeds 2h at 220°C aging temperature, the softening behavior becomes more evident in the Zr-Sr alloy group and the strength decreases in a linear fashion as aging time increases, although the elongation values do indeed improve with this increase. The highest degree of softening was reached after 48h of

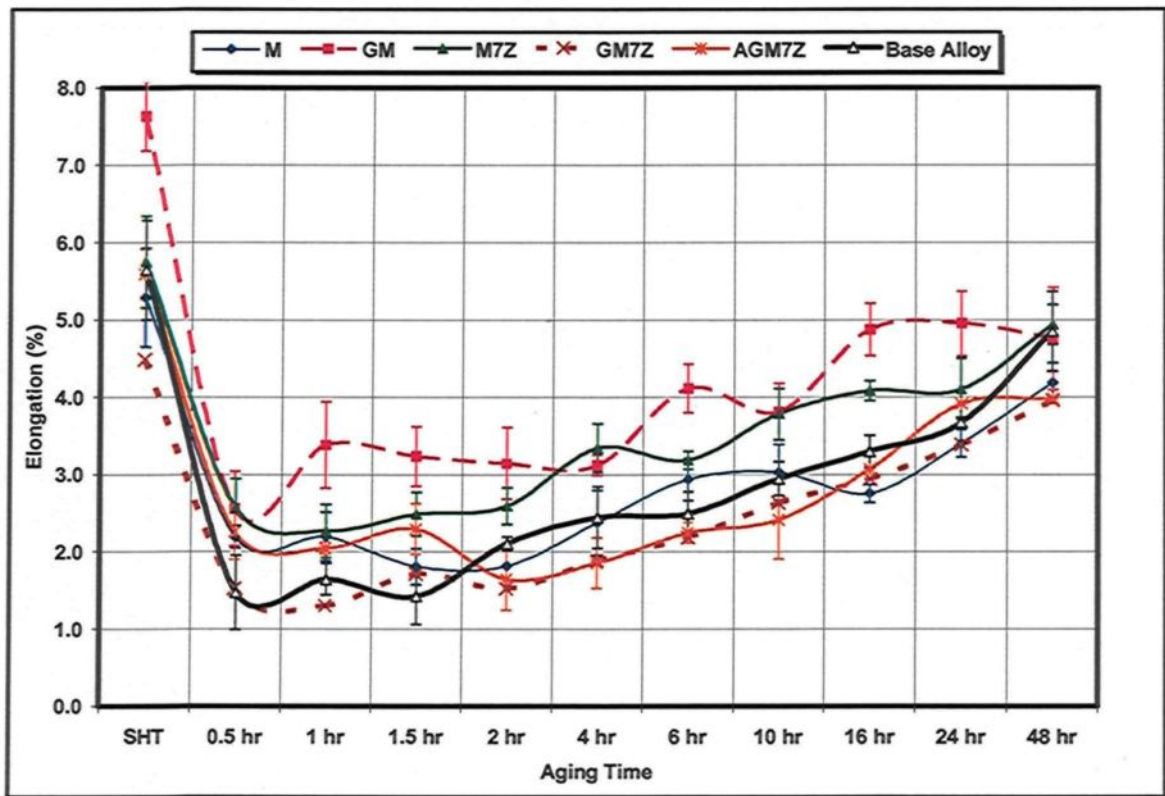


Figure 5.22 Effects of aging time on the elongation (%) of the Zr-Sr alloy group at 220°C

aging at which point the strength values reach the lowest range of 250-230MPa for tensile strength and 160-140MPa for yield strength. The elongation values also attain the highest percentage range of 4-5% after 48h of aging.

The stability observed in the results obtained for strength values in the Zr-Sr alloy group at the earlier aging times of 0.5 to 2h, can be explained by the presence of similar type of stability in the precipitation behaviour brought about by Sr. As discussed earlier, the variation in strength values in the earlier aging times is related to the competitive action occurring between the rapid precipitation and coarsening of the different age-hardening phases at 220°C. As result of the presence of these phases, which may form simultaneously or independently, the variation in strength becomes more apparent. The role of Sr in

controlling or eliminating this variation in strength may be attributed to the effect it produces in promoting the formation of β'' -Mg₂Si precipitates; this may also be attributed to the retarding effect of Sr on the growth of β' , thereby preventing its transformation into equilibrium Mg₂Si.¹⁹⁵ Also, the effects of Sr in increasing the excess-silicon content of the Al solid solution contribute to the stabilization of strength values at the earlier stages of aging; it was also reported in an earlier study¹⁹⁵ that the excess silicon may serve as heterogeneous nucleation sites for a number of age-hardening phases and may also help in the uniform distribution of these same phases.

The improvements obtained in the strength and elongation values of the GM-alloy and the M7Z-alloy are attributed to the modifying and refining effects of Sr on the iron intermetallics and the Mg₂Si phases; this is in addition to the beneficial refining effect of Zr and Ti on the α -Al structure and precipitation behaviour, as observed previously. The reduction in the tensile properties of the M7Z-alloy, caused by adding Ti to produce the GM7Z-alloy, may be attributed to the probability of the interactions between Zr and Sr with B to form (Zr,B) and (Sr,B) compounds.^{164,165}

As the aging time exceeds 2h, the overaging becomes more effective, the age-hardening metastable phases lose their coherency with the matrix, and also the equilibrium state of such phases as θ -Al₂Cu and β -Mg₂Si are then formed, leading to a reduction in strength and an increase in ductility. These changes describe the softening action of the aging treatment beyond 2h, which will reach the maximum value after 48h.

5.2.2.3 Zr-Sc Alloy Group

The results obtained for tensile and yield strength in the Zr-Sc alloy group at 180°C for different aging times may be seen in Figures 5.23 and 5.24, respectively. It will be observed from these figures that the combined additions of Zr-Sc have not produced any noticeable improvement in the base alloy strength values. The GS-alloy recorded the best ultimate tensile strength values of 360 MPa in the Zr-Sc alloy group after 10h of aging. Also, the AGS1Z-alloy obtained the highest yield strength of 323 MPa in the Zr-Sc alloy group after 10h of aging.

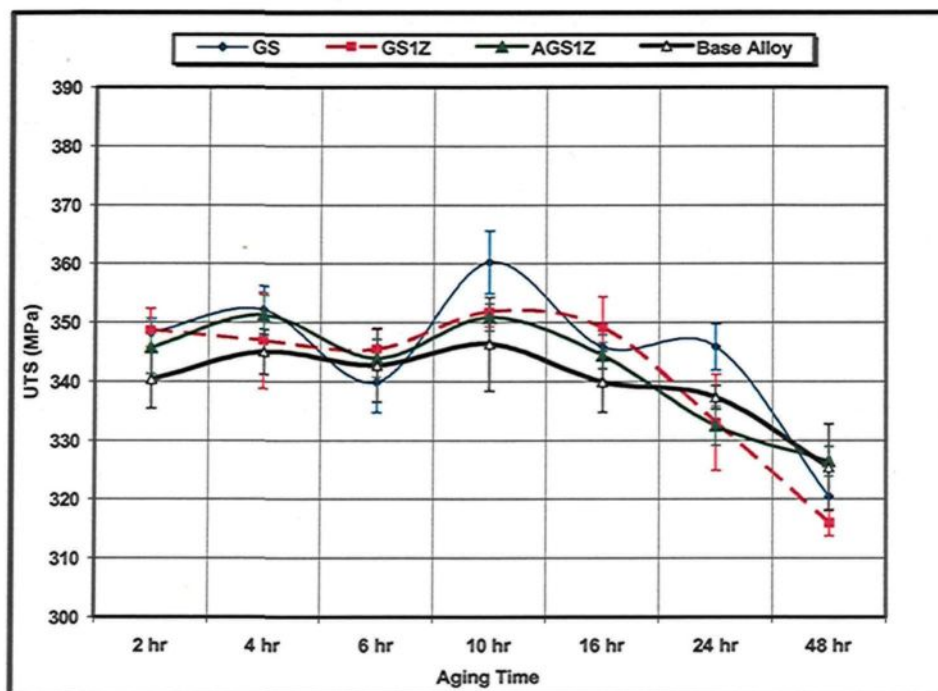


Figure 5.23 Effects of aging time on the ultimate tensile strength of the Zr-Sc alloy group at 180°C

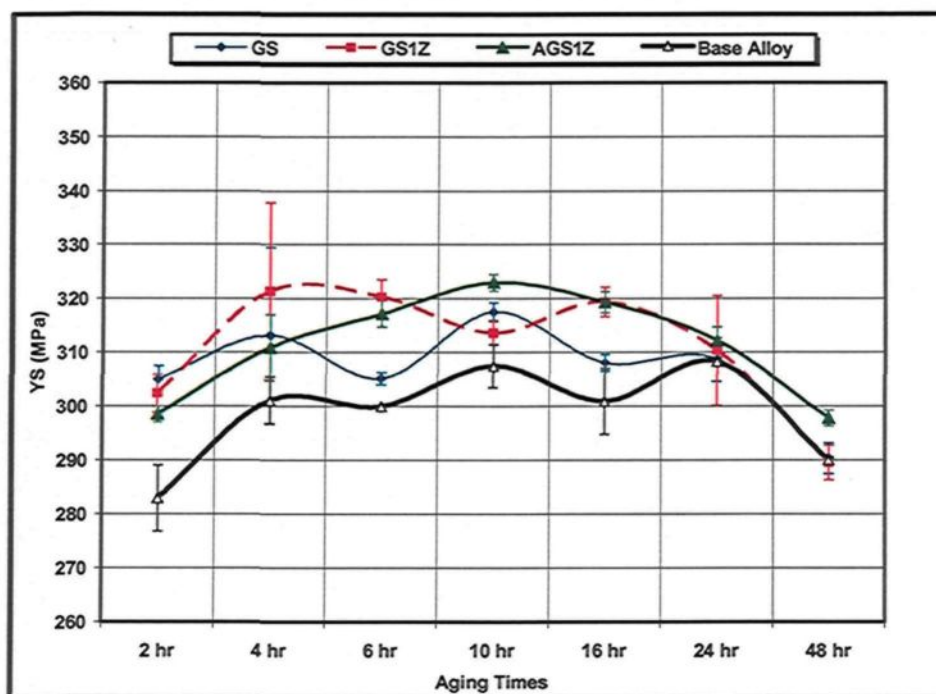


Figure 5.24 Effects of aging time on the yield strength of the Zr-Sc alloy group at 180°C

Figure 5.25 shows the elongation results for the Zr-Sc alloy group at an aging temperature of 180°C for various aging times. It will be observed that adding a combined addition of Zr-Sc to the base alloy does not cause any improvement in the elongation values.

Although it was reported previously that Zr and Sc form dispersoids producing a significant hardening effect,^{70,81} no hardening effect was displayed after the combined additions of Zr-Sc. This absence of any hardening effect can be explained based on the high growth rate of the dispersoids at 495°C solution temperature as was reported in previous studies,⁷⁴ Also, this observation is in agreement with the reduction detected in the yield strength results for the as-cast condition after the application of solution heat treatment. The Sc has the potential for interacting with Si and Cu thereby producing two harmful

intermetallics of the AlSc_2Si_2 , or V-phase and the $\text{Al}_{5.8}\text{Cu}_{7.4}\text{Sc}$, or W-phase, respectively;^{75,76} these are brittle intermetallics deteriorate the tensile properties by acting as crack initiators and by reducing the homogeneity of the structure. It should be mentioned here that the V-phase was detected in this study in the last chapter. The solubility of Si and Cu in the Al-matrix can be reduced by Sc additions;⁷⁴ as a result the age-hardening effects of Cu and Si may be diminished, thus leading to low strength levels in Sc-containing alloys. This interaction between Sc and Cu, and Si individually can be used to explain the absence of any beneficial effects from the combined Zr-Sc additions.

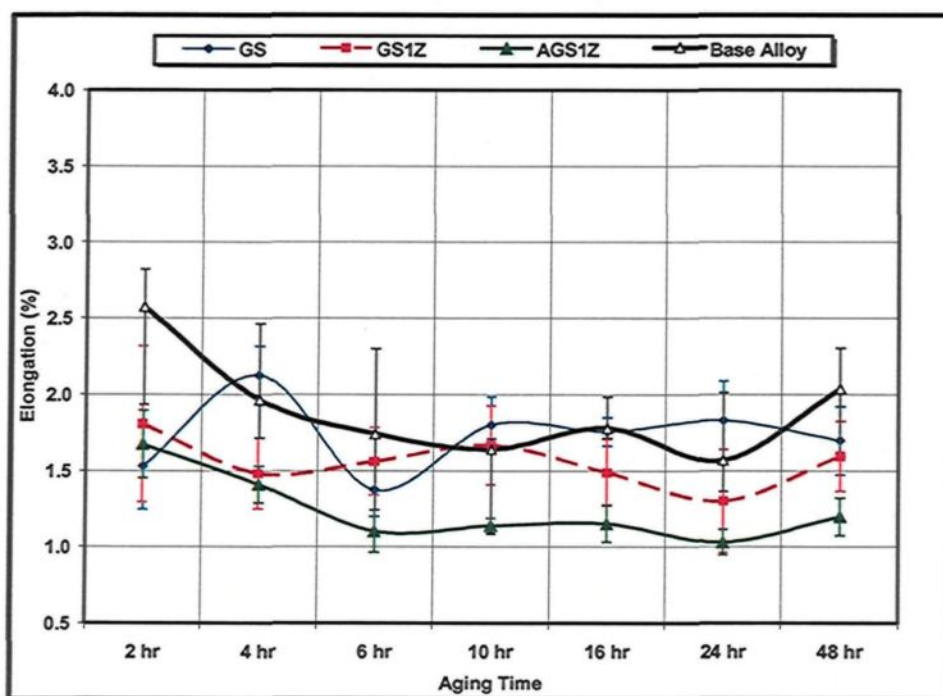


Figure 5.25 Effects of aging time on the elongation (%) of the Zr-Sc alloy group at 180°C

The ultimate tensile and yield strength results of the Zr-Sc alloy group at 220°C for different aging times are shown in Figures 5.26 and 5.27. At 220°C aging temperature, the strength results of the Zr-Sc alloy group follows almost the same trend displayed by the

strength results of the Zr-Ti alloy group. The variation in strength at the earlier aging times of 0.5h-2h was also observed in the Zr-Sc alloy group. The AGS1Z-alloy has reached the highest yield strength level of all the alloys investigated in this study, particularly at the earlier aging times of 0.5h-2h.

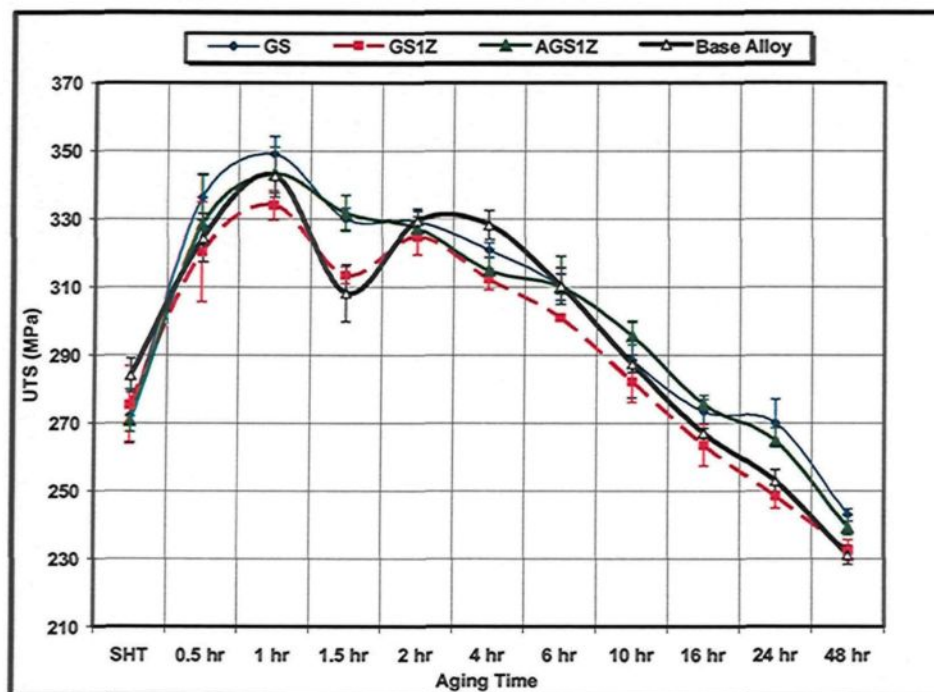


Figure 5.26 Effects of aging time on the ultimate tensile strength of the Zr-Sc alloy group at 220°C

After 2h of aging, all of the alloys exhibit an observable strength reduction in a linear fashion as aging time increases; this reduction reaches the maximum level after 48h. The elongation results of the Zr-Sc alloy group at 220°C may be seen in Figure 5.28. It will be observed that the combined additions of Zr-Sc do not produce any improvement in the elongation values, as shown in Figure 5.28.

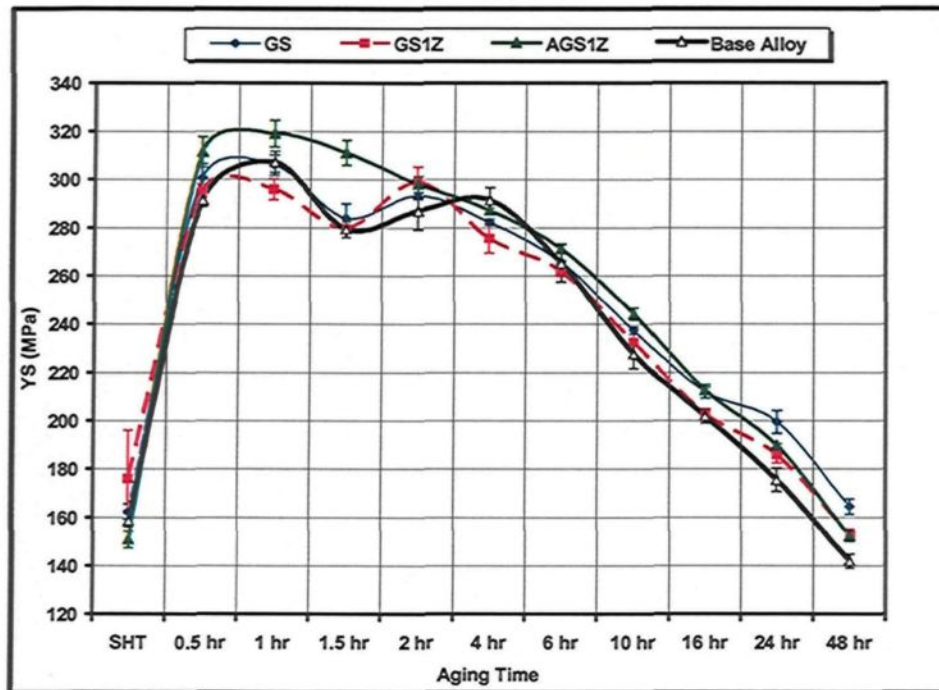


Figure 5.27 Effects of aging time on the yield strength of the Zr-Sc alloy group at 220°C

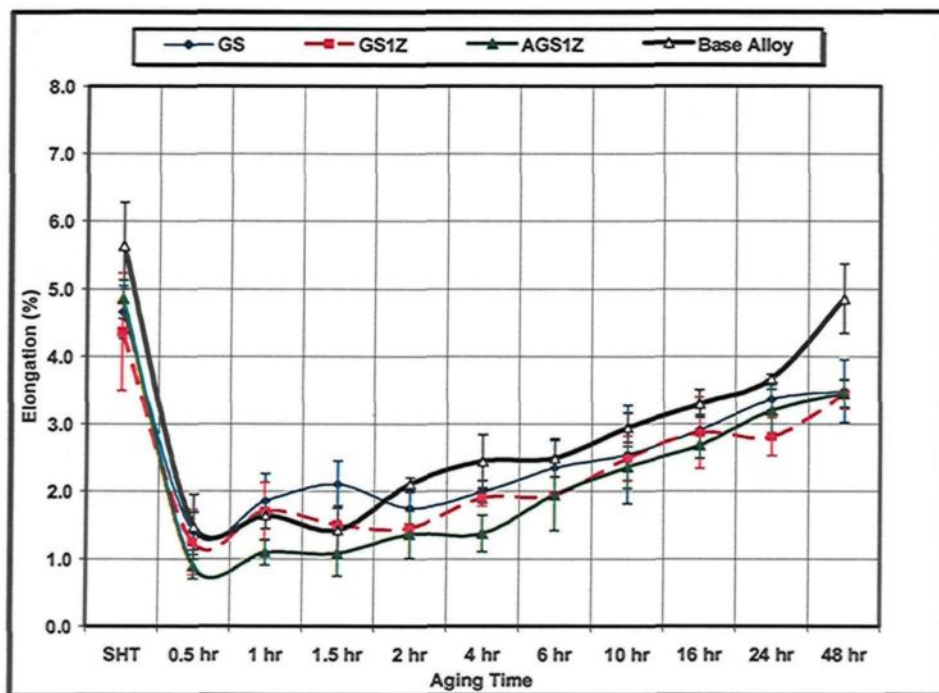


Figure 5.28 Effects of aging time on the elongation (%) of the Zr-Sc alloy group at 220°C

The variations in the ultimate tensile and yield strength of the Zr-Sc alloy group for the earlier aging times may be explained in the same way as for the Zr-Ti alloy group. The variations in strength at the earlier aging times occur because of the competition arising between the nucleation of the newest age-hardening precipitates, which enhance strength, and the coarsening of the oldest age-hardening precipitates, which cause strength reduction. The highest levels of yield strength and strength stability, as exhibited by the AGS1Z-alloy at the earlier aging times, are attributed to the addition of Ag. The hardening effect of Ag additions may be ascribed to two hardening actions. The first is that the silver may interact with magnesium and form clusters along $\{111\}_\alpha$ which in turn are combined with Cu and act as precursors of the Ω phase during aged hardening.^{64,65} The second factor is that Ag itself is considered to be a hardener in that it is able to harden the α -Al matrix through a solid solution strengthening mechanism.⁶³ As aging time exceeds 2h, softening occurs and the equilibrium states of the age-hardening phases form, causing a reduction in strength. The absence of improvement in the elongation values of the Zr-Sc alloy group may be attributed to the formation of harmful Sc intermetallic phases of the V-phase and the W-phase.

5.2.2.4 Si Alloy Group

The ultimate tensile and yield strength values obtained for the Si alloy group at 180°C for various aging times may be seen in Figures 5.29 and 5.30, respectively. It will be observed that the additions of Si have not altered the base alloy strength to any great degree. The addition of 2% Si obtained the best results for the tensile and yield strength in the Si alloy group. Also the age-hardening peaks at 10h and 24h which were detected in

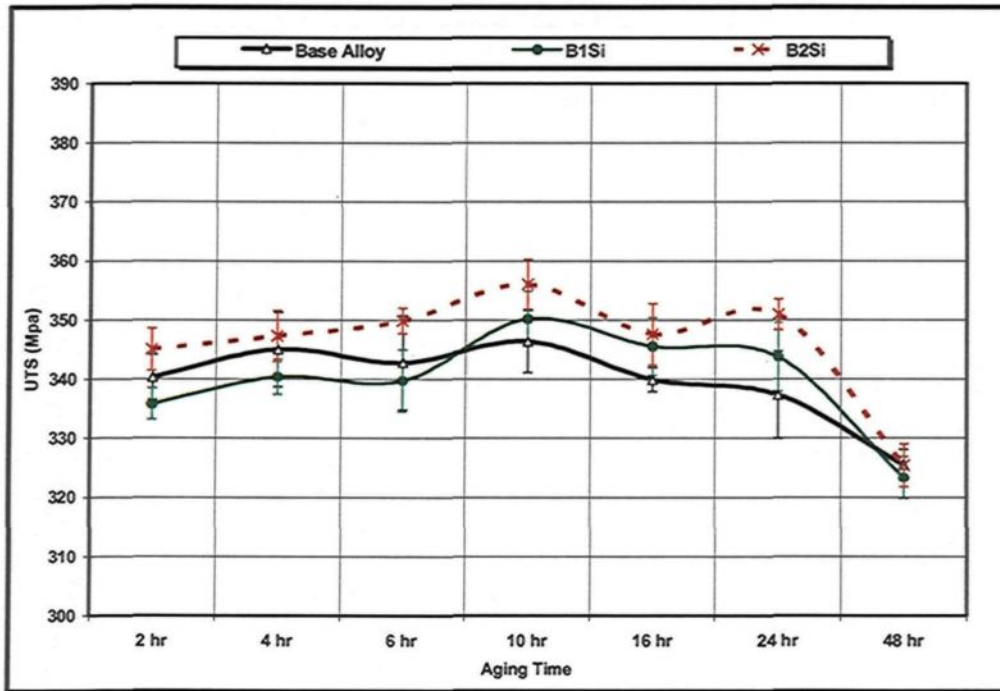


Figure 5.29 Effects of aging time on the ultimate tensile strength of the Si alloy group at 180°C

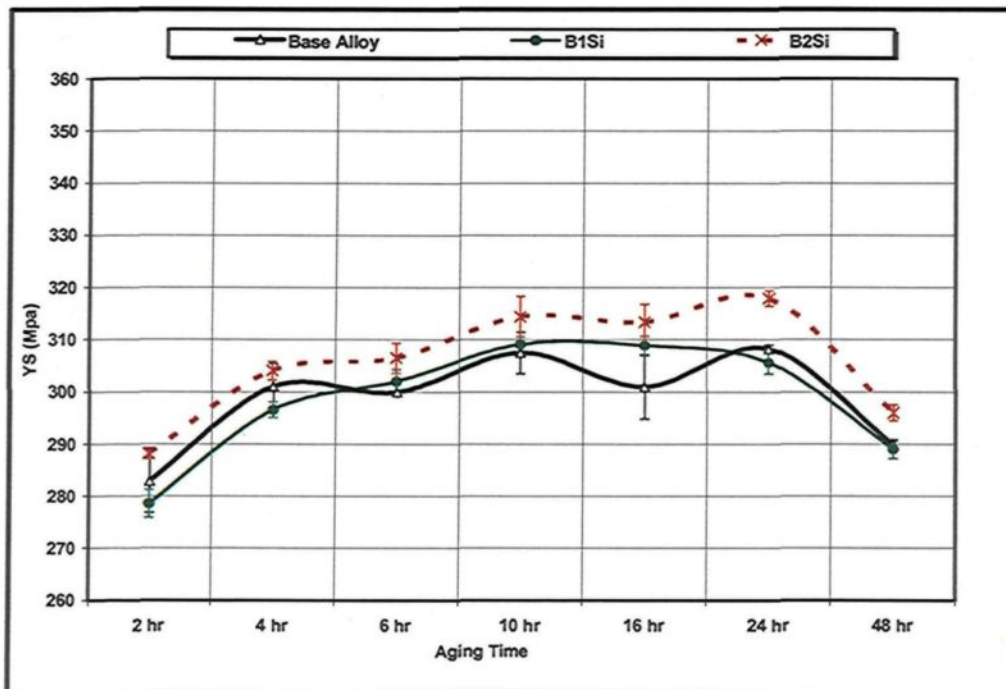


Figure 5.30 Effects of aging time on the yield strength of the Si alloy group at 180°C

previous alloy groups were also detected in the Si alloy group. Figure 5.31 represents the effects of Si addition on the elongation of the base alloy at 180°C for different aging times. It will be observed from Figure 5.31 that the Si additions cause a deterioration in the elongation values of the base alloy. The B2Si-alloy obtained the lowest elongation levels of the Si-alloy group.

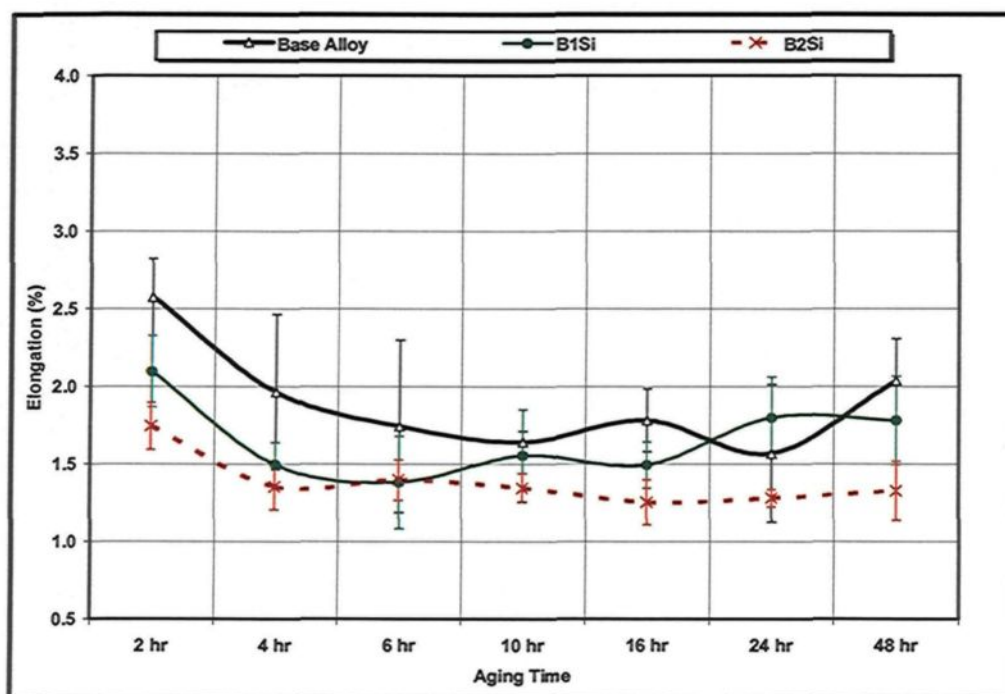


Figure 5.31 Effects of aging time on the elongation (%) of the Si alloy group at 180°C

It will be observed from the recent figures that the strength values improve slightly as Si-content increases from 1% represented by the base alloy to 2% or to 3% represented by the B1Si- and B2Si-alloys, respectively. As shown previously in Figure 5.3 in the section on microstructure, the high silicon content contributes to lowering the amount of undissolved Al_2Cu in the as-cast condition as well as to lowering the amount of undissolved Al_2Cu remaining after the application of solution heat treatment. The

beneficial effects of a high silicon content on Al_2Cu can also be explained by the fact that, as Si-content increases, the $\alpha\text{-Al}$ fraction decreases and Cu-rich liquid pools disperse uniformly throughout the intricate network of interdendritic channels.^{168 167}

The uniform distribution of the Cu-rich liquid pools will reduce Cu segregation and produce fine dispersed particles of Al_2Cu which easily dissolve during solution heat treatment. Thus, it is possible to declare that the high Si-content will accelerate the driving force for precipitation by producing a high degree of supersaturated solid solution of the Cu-rich $\alpha\text{-Al}$, thereby leading to an intensification in strength.

It was found that the elongation levels in the base alloy decrease as the Si-content increases. The decrease in elongation may be attributed to the fact that, as the Si-content increases, the eutectic Si particles start to form in abundance thereby leading to a reduction in elongation values of the base alloy; this is a result of the fact that the Si particles reduce the uniformity of plastic deformation and act as crack initiators, as will be seen in the section on fractography.

Figures 5.32 and 5.33, respectively, present the results obtained for the tensile and yield strength of Si alloys at 220°C for different aging times. The strength variation at the earlier aging times of 0.5h-2h will also be observed in the Si alloy group. After 2h of aging, the alloy strength values begin by decreasing in a linear fashion with aging time. After 48h of aging, the softening level reaches the highest degree for all of the Si alloys investigated.

Figure 5.34 shows the effects of 220°C aging temperature on the elongation of the Si alloy group for different aging times. Although the elongation increases in general as

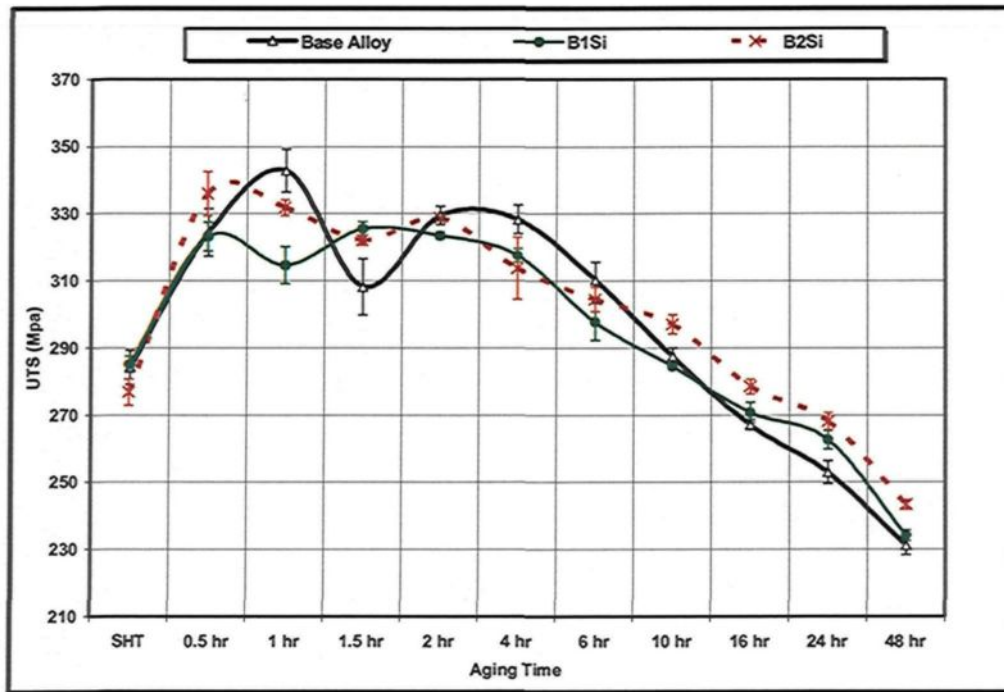


Figure 5.32 Effects of aging time on the ultimate tensile strength of the Si alloy group at 220°C

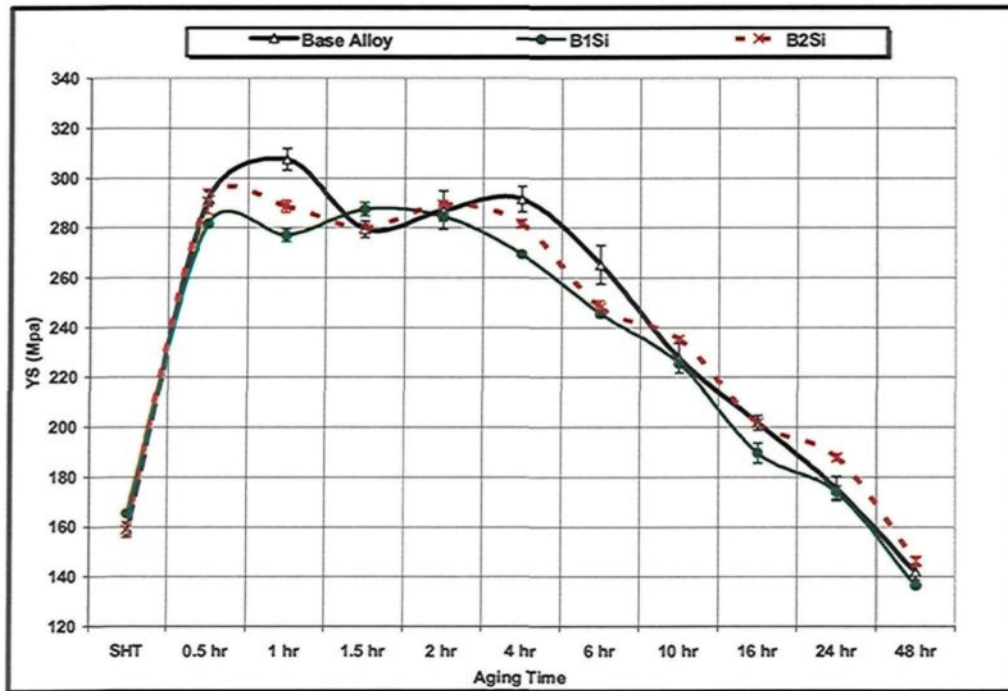


Figure 5.33 Effects of aging time on the yield strength of the Si alloy group at 220°C

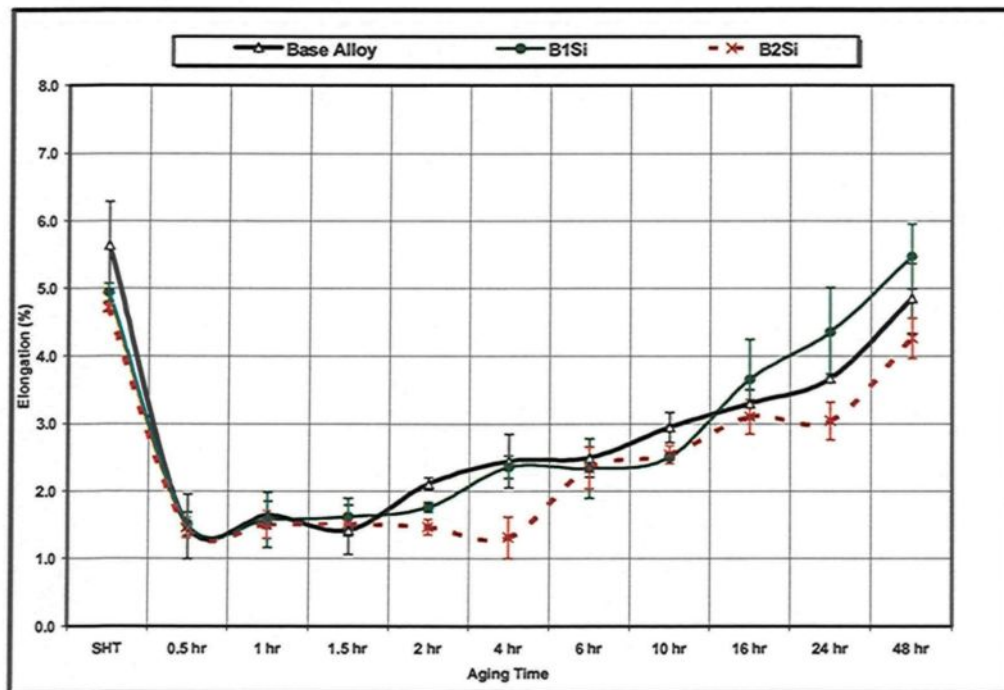


Figure 5.34 Effects of aging time on the elongation (%) of the Si alloy group at 220°C

aging time increases, the additions of Si do not appear to have any improving effect on elongation. The highest level of elongation was obtained after 48h of aging, as shown in Figure 5.34.

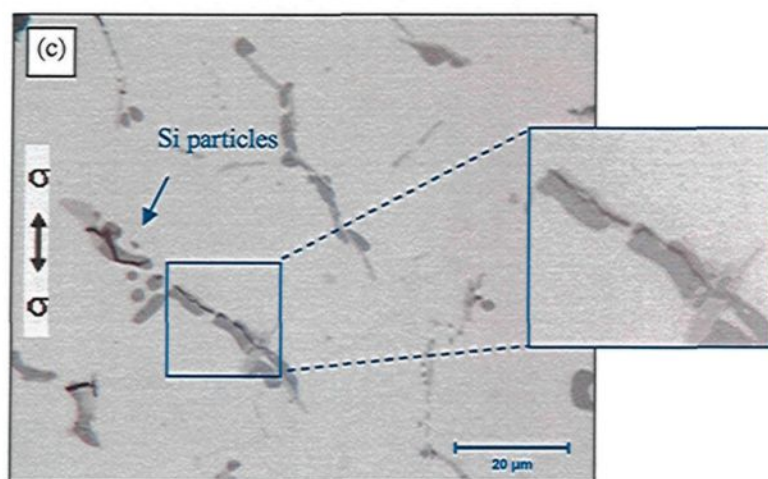
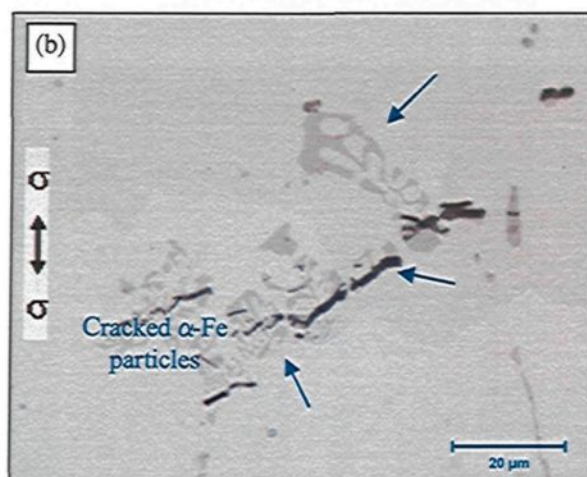
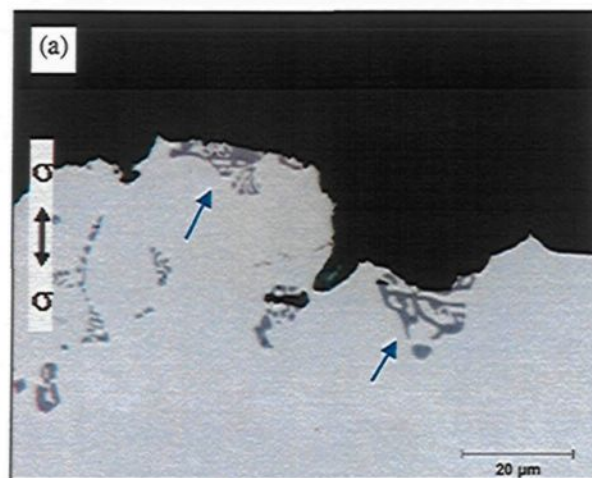
No major improving effect was detected as a result of Si additions with regard to the strength of the base alloy since Si is not a hardener. The variations in strength observed for the earlier aging times with regard to Si alloys may be attributed to the emergence of the same competing behavior between the nucleation of the most recent age-hardening metastable phases and the formation of an equilibrium state of the precipitates formed earlier. After 2h of aging, the strength decreases gradually as the age-hardening metastable phases lose their coherency with the matrix and their equilibrium phases begin to form. The

Si-containing alloys display low levels of elongation as a result of the formation of eutectic silicon.

5.3 Fracture Mechanism

Figure 5.35 shows optical micrographs of the microstructure taken close to the tensile fracture surface in longitudinal sections for a number of the alloys investigated in the peak-aged condition. It will be seen, from Figure 0.34(a), that the fracture surface edge in the base alloy is covered mainly by broken solidified intermetallic particles, especially α -Fe particles. In the base alloy, cracks seem to be generated from within the α -Fe intermetallic instead of from the α -Fe/matrix interface, as shown in Figure 5.35(b). By contrast, in the B2Si-alloy which contains 3wt% Si, the cracks generate either at the eutectic-Si/ $\text{Al}_5\text{Mg}_8\text{Cu}_2\text{Si}_6$ -phase interface or within from the eutectic Si particles themselves, as shown in Figure 5.35(c). The Si particles act as nucleation sites for many of intermetallic phases such as the $\text{Al}_5\text{Mg}_8\text{Cu}_2\text{Si}_6$ -phase (Q-phase) Under the tensile loading, the interface between the eutectic-Si and Q-phase particles may act as crack initiation sites, as displayed in the magnified image as shown in Figure 5.35(c).

It will be seen from Figure 5.35 that the elongated α -Fe intermetallic particles contain more cracks than they do in the case of the more rounded particles of α -Fe. In Zr-containing alloys, the cracking may be generated within from coarse Al_3Zr as well as from α -Fe intermetallic particles, as shown in Figure 5.35(e). The cracks in the intermetallic particles are usually formed perpendicular to the loading axis, as shown in Figure 5.35. From this figure, it will be observed that the intraparticle cracks, which follow the same



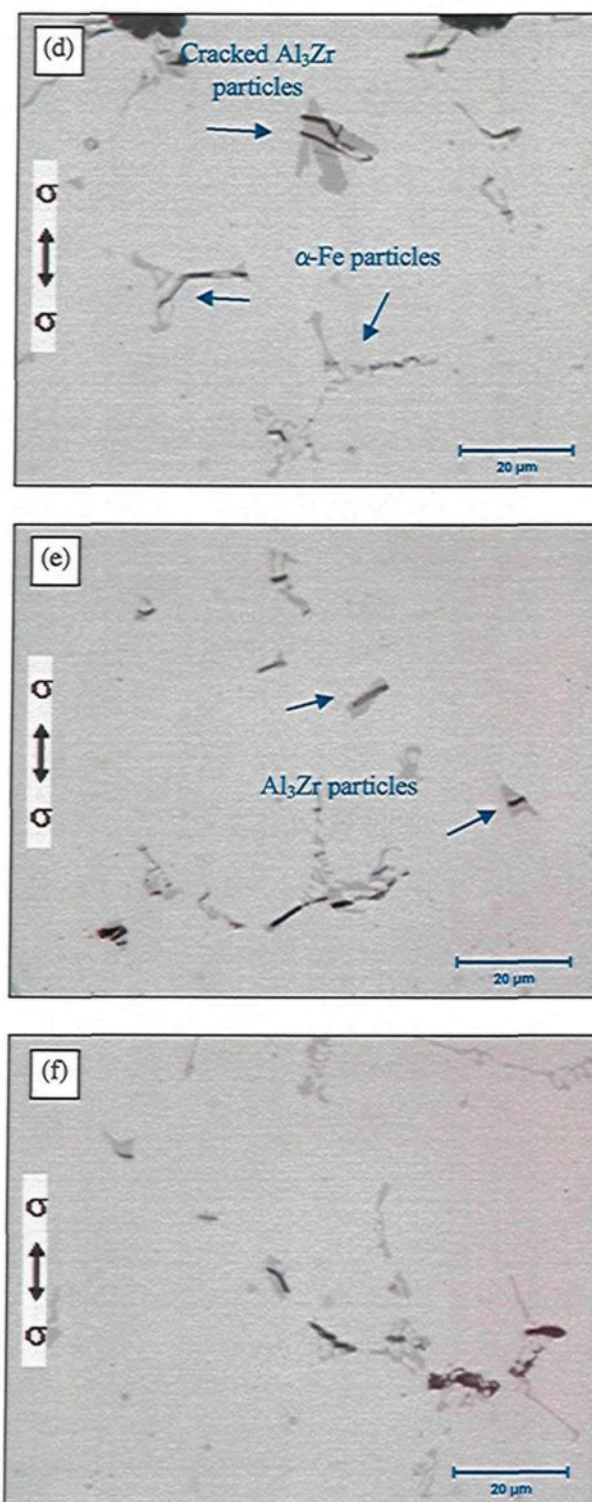


Figure 5.35 Optical microstructure near tensile fracture surface in a longitudinal section: (a), (b) base alloy, (c) B2Si-alloy, (d) M7Z-alloy, (e) G7Z-alloy, and (f) GS1Z-alloy.

orientation as that of crack propagation, have heightened possibility of connecting with each other under the applied stress, thereby forming one long crack. Based on the abovementioned observations, the fracture damage process in Al-2wt%Cu alloys is believed to occur in three stages as follows: intermetallic particle cracking, microcrack formation and growth, and the localized interlinkage of microcracks.

Upon the application of tensile stress, the stresses are imposed by the matrix on the intermetallic particles; in this case the dislocations accumulate at the particle/matrix interface leading to concentrations of high stress which in turn cause particle/matrix decohesion or particle cracking.^{14,182,183} In the case of α -Fe intermetallic particles, the cracks do not form on the α -Fe/matrix interface but within the particles themselves; this is an indication of a strong coherency between the intermetallic particles and the matrix, which is in agreement with what has been revealed by other studies.^{182,196,197} In Si-containing alloys, it appears that the coherency between the matrix and eutectic Si is high, the cracks may thus occur within the particles themselves or on the interface between the eutectic-Si and the Q-phase. Also, it was reported elsewhere that^{182,197,198} the large particle size increases the density of the possible defects existing in the particle, which in turn tends to reduce the fracture stress of the particle.¹⁹⁹

Additionally, the elongated particles received higher levels of imposed stress from the matrix than they did in the case of the rounded particles, thereby causing the formation of multiple cracks, as displayed by the α -Fe particles. As the intermetallic particles crack, the voids, or microcracks, form and grow under the continually applied stress. The formation of microcracks and the crack growth process are expected to continue

accompanied by further particle cracking and the initiation of intraparticle cracks in a stable strain region.¹⁸² As the critical volume fraction of the cracked particles is attained and the inter-cracked-particle spacing is less than the critical value, the matrix between the cracked particles becomes unstable leading to the rapid linking between a number of microcracks existing in the same orientation. When the linking process starts, it is believed that the final fracture process occurs too.^{182,199,200}

Accordingly, the cracking process in Al-2wt%Cu base alloys is controlled by certain factors such as particle size, whether small or large, particle aspect ratio, whether elongated or rounded, the extended clustering of particles such as particle distribution, particle fracture strength, and matrix properties. These controlling factors indicate the importance of Zr-Ti and Zr-Sr additions in improving the elongation levels of the base alloy by producing a refined non-dendritic structure which, in turn, causes a reduction in size and the homogeneous distribution of solidified intermetallic particles. The homogenous distribution of refined intermetallic particles increases the resistance of the particle to cracking and delays the crack linkage process, thereby reducing the crack propagation rate.

The beneficial effects of producing the refined non-dendritic structure through combined additions of Zr-Ti and Zr-Sr will be counteracted, however, by the formation of coarse Al₃Zr intermetallics which act as nucleation sites for cracks. In order to avoid the formation of this kind of coarse Al₃Zr intermetallic compound, the application of low levels of Zr additions and high cooling rates are recommended.

5.4 Conclusions

The effects of the chemical additives Zr, Sc, Ti, Sr, Ag, and Si on the microstructure, tensile properties, and fracture mechanism of the base alloy were studied for samples aged at temperatures of 180°C and 220°C for aging times of 2, 4, 6, 10, 16, 24, and 48h, and 0.5, 1, 1.5, 2, 4, 6, 10, 16, 24, and 48h, respectively. Based on the results obtained the following may be concluded.

1. Combined additions of Zr-Ti, Zr-Sr, or Zr-Sc refine the grain size of the base alloy considerably, from 219 μm to grain sizes in the range of 104-46 μm since these elements form primary trialuminide intermetallics including $\text{Al}_3(\text{Sc}_{1-x}\text{Zr}_x)$, $\text{Al}_3(\text{Sc}_{1-x-y}\text{Zr}_x\text{Ti}_y)$, and Al_3Zr which act as nucleation sites for α -Al grains, thereby producing a fine non-dendritic structure.
2. The poisoning effect which Sr is known to have on the grain refining capacity of Ti-B additions was not in evidence in this study; this may be attributed to the low Si-content (1 wt%) of the base alloy, compared to the high Si-alloys in which this poisoning effect has been reported.
3. The refined non-dendritic morphology produced by the combined additions of Zr-Ti, Zr-Sr, or Zr-Sc causes a reduction by about 65% in the amount of Al_2Cu phase in the base alloy, and to a reduction in the porosity by about 50%. The addition of 2 wt% Si

also produces the same results, brought about by the increase in the Al-Si eutectic content.

4. Strontium as a sole addition increases the surface fraction of Al_2Cu phase in the base alloy by about 40%. This increase may be attributed to the fact that the Sr leads to segregation of the Cu-phase causing it to appear in the form of blocklike Al_2Cu particles during solidification.
5. Strontium addition leads to the fragmentation and spheroidization of the α -Fe intermetallic compounds. This effect is intensified in the presence of Zr and Ti grain-refining additions.
6. A combined addition of Zr and Sc increases the yield strength of the as-cast base alloy by about 35 MPa, which subsequently decreases after solution heat treatment, the increase and decrease in yield strength are attributed respectively to the formation of transition-elements dispersoids, followed by their rapid coarsening during solution heat treatment.
7. The strength of the base alloy increases in the Zr-Ti alloy group with the increase in Zr content from 0.15wt% to 0.7wt% after aging at 180°C for 10h. This increase may be variously attributed to Al_3Zr and $Al_3(Zr_{1-x}Ti_x)$ dispersoids acting as heterogeneous nucleation sites for age-hardening phases; to the modifying action of Zr on the S'

(Al₂CuMg) phase; and to the action of Zr-Ti in producing a refined non-dendritic grain structure, and facilitating dissolution of Cu in the matrix to a greater extent.

8. Combined additions of Zr-Sr bring about significant improvements in the tensile properties, for which the highest strength value of 383 MPa is obtained in the M7Z-alloy after only 4 h of aging at 180°C. This shift in peak hardening towards a lower aging time is related to the beneficial effects which Sr and Zr have on the microstructure and on precipitation hardening.
9. Combined additions of Zr-Sr and Sr-Ti provide the best elongation levels of all the alloys investigated, as witnessed by the M7Z and GM alloys. These improved levels may be the result of the modifying effects of Sr on α -Fe particles, as well as of the roles of Zr and Ti in producing a fine non-dendritic α -Al structure.
10. The addition of Ag improves the yield strength as evidenced by the AGM7Z-alloy which displays the highest yield strength value of about 330 MPa between 10h and 16h of aging at 180°C. The enhancing effect of Ag on the yield strength may be attributed to precipitation of the Ω (Al₂Cu) phase, and to the solid-solution strengthening effect of Ag itself.
11. Softening is observed in all the alloy groups after 2h of aging at 220°C. The 0.02wt%Sr-0.15wt%Ti containing GM alloy displays the highest level of resistance to

softening because of the respective modifying and refining effects of Sr and Ti on the microstructure.

12. The fracture damage process in Al-2wt%Cu based alloys starts with the cracking of intermetallic particles or the decohesion of two phases (one nucleated on the other) under the application of tensile stress; the α -Fe intermetallic particles are most susceptible to cracking, as are the eutectic Si particles in the Si-containing alloys. Rounded or compact α -Fe intermetallic particles have a higher resistance to cracking than elongated ones.

13. While the refined non-dendritic structure obtained through combined Zr-Ti or Zr-Sr additions may improve the elongation, the formation of coarse Al_3Zr intermetallics which act as crack initiators may counteract the beneficial effect of such additions. In such cases, low levels of Zr and at a high cooling rate are recommended to eliminate the problem.

CHAPTER 6
HOT-TEARING SUSCEPTIBILITY

CHAPTER 6

HOT-TEARING SUSCEPTIBILITY

This chapter will discuss the susceptibility of Al-2wt%Cu base alloys to hot tearing or HTS; this susceptibility was tested using the constrained rod casting mold, also known as the CRC mold. The effects of chemical composition on this susceptibility were studied using six alloys selected from among those which were previously prepared for tensile testing. These alloys included the base alloy, M-alloy (0.02wt%Sr), G-alloy (0.15wt%Ti), G1Z-alloy (0.15wt%Ti-0.15wt%Zr), G3Z (0.15wt%Ti-0.3wt%Zr), and B1Si-alloy (1wt%Si). On the basis of the chemical composition of these alloys, listed above, it becomes possible to investigate the effects of (i) Sr-modification, (ii) grain refining, (iii) changes in α -Al morphology, and (iv) Si content on hot-tearing susceptibility. The different mold temperatures of 450°C, 400°C, 350°C, 300°C, and 250°C were used in order to investigate the effects of mold temperature on the HTS of the alloys investigated. A number of hot-tearing trials with the G3Z-alloy were conducted using various types of mold coatings such as graphite and/or boron nitride lubricoat-Zv, different dwell times of 2, 4, and 8 min, as well as alternate mold slope angles of 0°, and 17°, in order to select the optimum hot-tearing test conditions. The boron nitride lubricoat-Zv coating, 4min dwell time, and 0° mold slope angle were ultimately selected as fixed conditions for carrying out

the hot-tearing tests. The 206-type alloy was tested using the CRC mold in the same testing conditions with the same chemical additions, in order to compare the HTS results obtained with Al-2wt%Cu base alloys for which the 206 alloy was taken as a commercial reference alloy.

In this chapter, HTS results will be discussed in the following subsections:

- Hot-Tearing Susceptibility (HTS)
- Effects of Mold Temperature
- Effects of Grain Structure
- Effects of Silicon Content
- Effects of Strontium Addition
- Effects of α -Iron Intermetallic Phase
- Proposed Hot-Tearing Criteria
- Conclusions

6.1 Hot-Tearing Susceptibility (HTS)

The HTS results obtained for the G3Z-alloy using the different dwell times 2 min, 4 min, and 8 min at the two mold slope angles of 0° and 17° are presented in Figure 6.1 and Figure 6.2. From the preceding figures, it will be observed that the 4 min dwell time is the most suitable period for obtaining the lowest HTS values whether at the 0° or at the 17° mold slope angles. It will also be noted that the difference between the HTS values for the two slope angles of the mold is fairly slight; this indicates the weak effect which the mold slope angle has on the hot tearing susceptibility of the G3Z-alloy. The short dwell time of 2 min may lead to an increase in the HTS values because in this short period the CRC mold

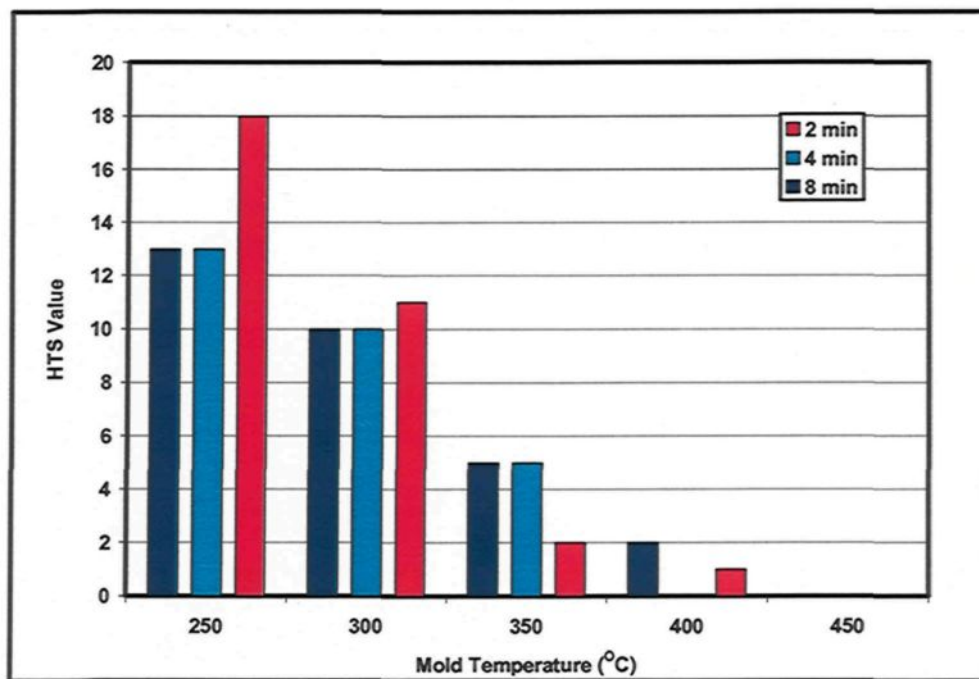


Figure 6.1 Effects of dwell time on the hot-tearing susceptibility of G3Z-alloy at 0° mold slope angle.

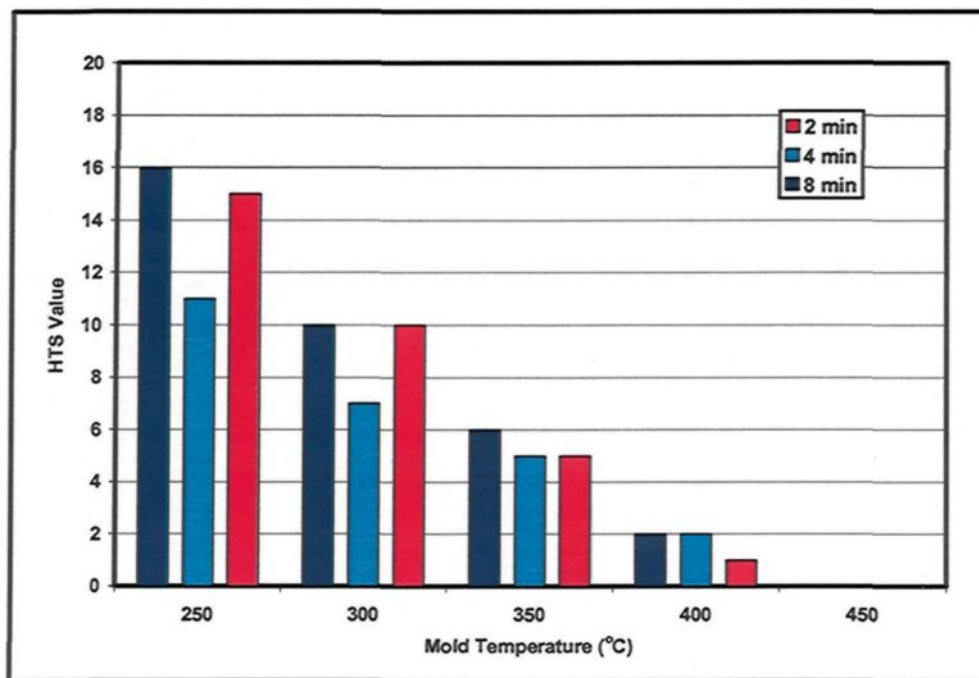


Figure 6.2 Effects of dwell time on the hot-tearing susceptibility of G3Z-alloy at 17° mold slope angle.

casts are still incompletely solidified and thus they may tear easily when being released from the mold or, at the very least, the severity of the hot-tearing might be doubled. Also, the long dwell time of 8 min may cause an increase in the HTS values as result of extending the period of time in which thermal contraction occur.

It should be mentioned that the coating type used for the CRC mold has an appreciable effect on hot-tearing test results, for which it was found that, when the graphite coating type was used in the earlier trials, it was difficult to remove the castings from the mold; also that the severity of the cracking observed was intensified. As the type of the graphite coating was replaced by boron nitride lubricoat-Zv, the releasing process of the castings became easier and the resulting severity of the cracking was lower. The difference observed between these two coatings may be attributed to the difference between the degree of surface roughness as obtained by each coating. The constrained contraction level of the CRC mold during solidification may depend, to a certain extent, on the friction level between the mold and the casting sample. It is believed that the boron-nitride lubricoat-Zv coating provides a lower degree of surface roughness than does the graphite coating, thereby reducing the friction between the mold and the cast sample and leading to a reduction in the HTS level and easily released castings. This explanation is in agreement with finding reported by Parkin and Cowan,¹²⁰ who found that mold friction is capable of exerting sufficient restraint to cause tearing.

The significant effects of mold temperature and chemical composition on the hot-tearing susceptibility (HTS) of Al-2wt%Cu and 206 alloys will be shown in Figures 6.3 and 6.4, respectively. The HTS results obtained indicate the beneficial effects of an

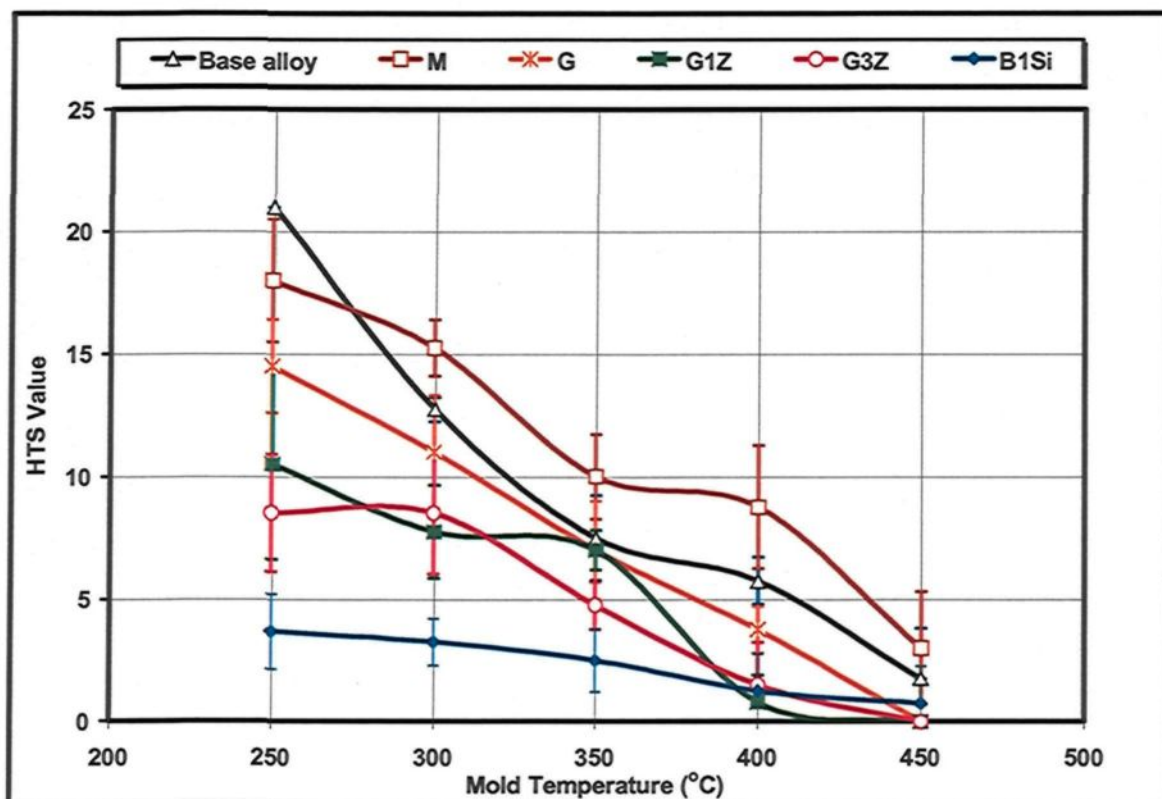


Figure 6.3 HTS vs. composition of Al-2wt%Cu base alloy at different mold temperatures.

elevated mold temperature on the reduction of HTS levels, where the HTS values of the alloys investigated decrease in a linear fashion as the mold temperature increases.

In Al-2wt%Cu alloys, the highest HTS value of 21 obtained at 250°C decreases to 3 as the mold temperature increases to 450°C. The highest value obtained for HTS in 206 alloys also decreases from 21 to 9 as the mold temperature increases from 250°C to 450°C. It will be observed that the hot-tearing susceptibility (HTS) levels, as obtained by 206 alloys, are higher than the ones obtained by Al-2wt%Cu alloys. The effects of mold temperature on HTS level is found to vary from one alloy to another. In the Si-containing

alloys such as the B1Si-alloy and 206-B2Si alloy, the role of the mold temperature in HTS is low. For the grain-refined alloys such the G1Z-, G3Z-, 206-G1Z, and 206-G3Z alloys, the mold temperature has more significant effect than it does in the case of Si-containing alloys. The most noticeable effect of mold temperature on HTS values was observed in the Al-2wt%Cu alloy, the 206 alloy, and the Sr-containing alloys.

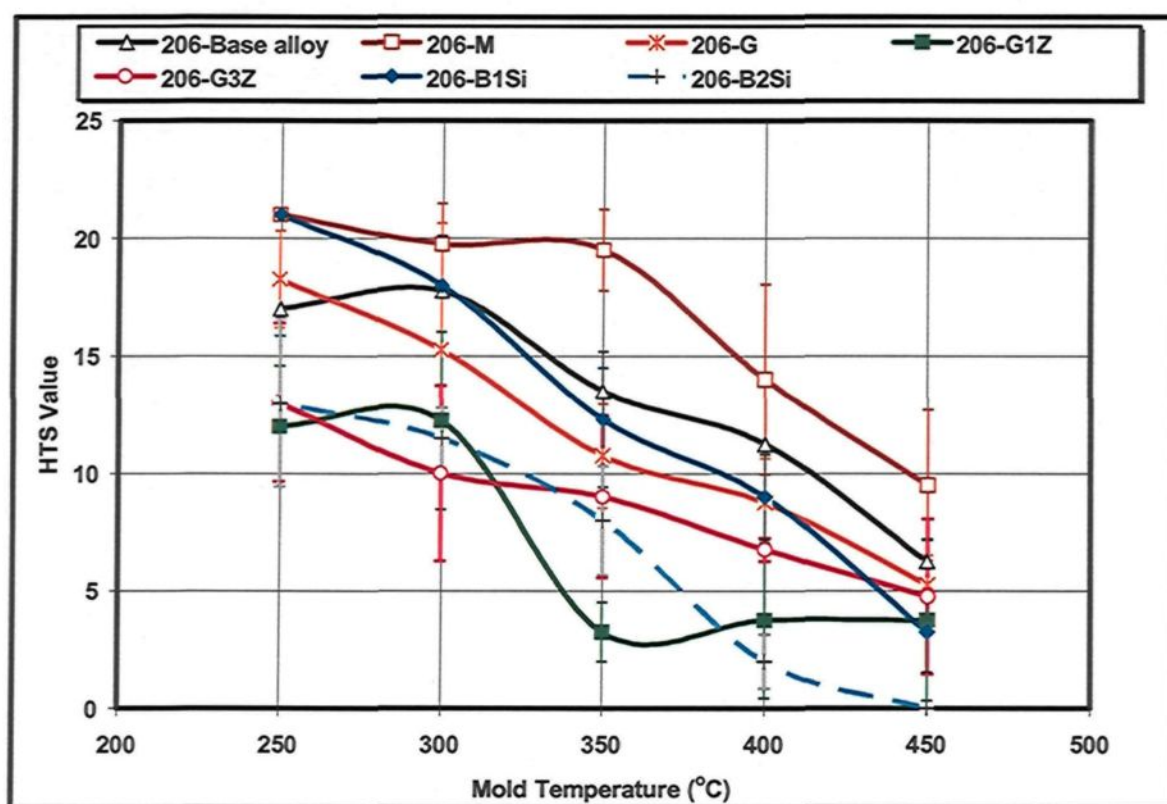


Figure 6.4 HTS vs. composition of 206 alloy at different mold temperatures

The preceding figures show the effects of chemical additions on the values obtained for HTS, as follows. The addition of Sr causes a deterioration in the resistance of the base alloys to hot-tearing, and it also reduces the HTS values of these alloys to lower levels, as displayed by the M-alloys and the 206M alloys. Combined additions of Zr-Ti reinforce the

resistance of the base alloys to hot tearing as displayed by the G1Z-, G3Z, 206-G1Z, and 206-G3Z alloys. The addition of Ti-B produces an intermediate effect in the improvement of the hot-tearing susceptibility of the base alloy. Additions of Si have provided the lowest HTS values of all the alloys investigated especially with regard to the Al-2wt%Cu alloy.

In order to represent the effects of mold temperatures (MT) and chemical compositions on the HTS of the Al-2wt%Cu and 206 alloys in linear mathematical relationships, Figures 6.3 and 6.4 have been redrawn and presented in Figures 6.5 and 6.6, respectively. The mathematical equations for each alloy of the Al-2wt%Cu alloys and for the 206 alloys are represented in Table 6.1 and Table 6.2, respectively. These equations have R^2 values tending towards one. Each equation consists of a constant and one variable which, in this case, is the mold temperature (MT) associated by a particular coefficient. Such constants and MT coefficients represent the degree of resistance of each alloy to hot tearing, as well as the extent to which the mold temperature affects the HTS of the alloy. For example, the Al-2wt%Cu base alloy represents the highest constant of 41.6 and the highest MT coefficient of 0.091 implying that this alloy has minimal resistance to hot-tearing and that the mold temperature may control the HTS values to a significant degree. By contrast, the B1Si-alloy with a high Si content provides the lowest constant of 7.7 and the lowest MT coefficient of 0.0157 indicating the heightened resistance of this alloy to hot tearing and the nominal effect of the mold temperature on the HTS values obtained for the alloy.

Based on these constants and the MT coefficients, the Al-2wt%Cu alloys may be classified into three groups as follows: (i) the alloys providing high HTS values, namely the

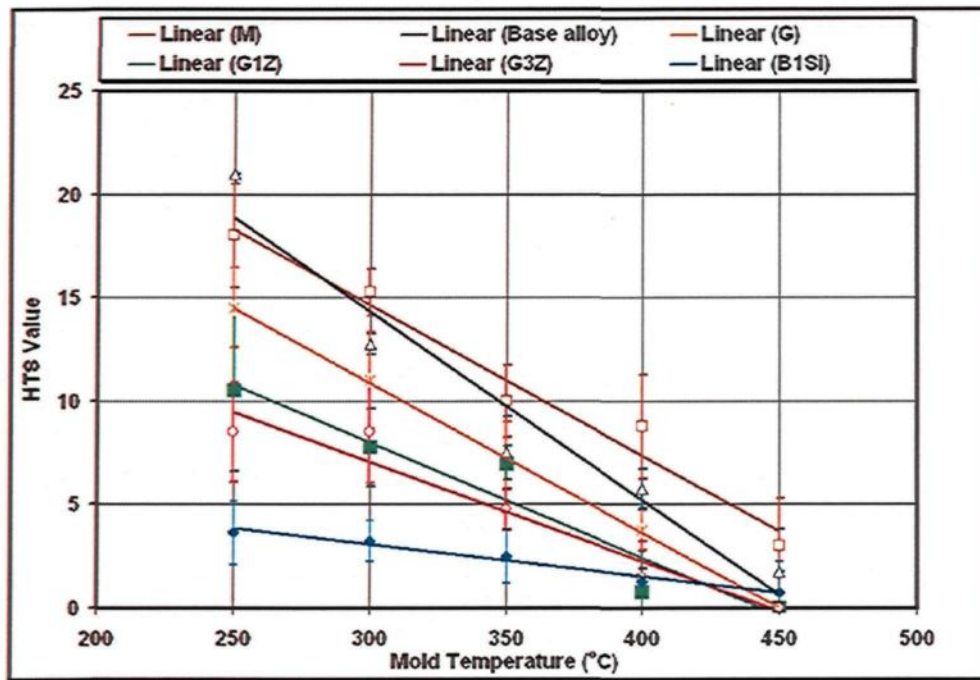


Figure 6.5 The linear relationship between HTS values and mold temperature for Al-2wt%Cu base alloys.

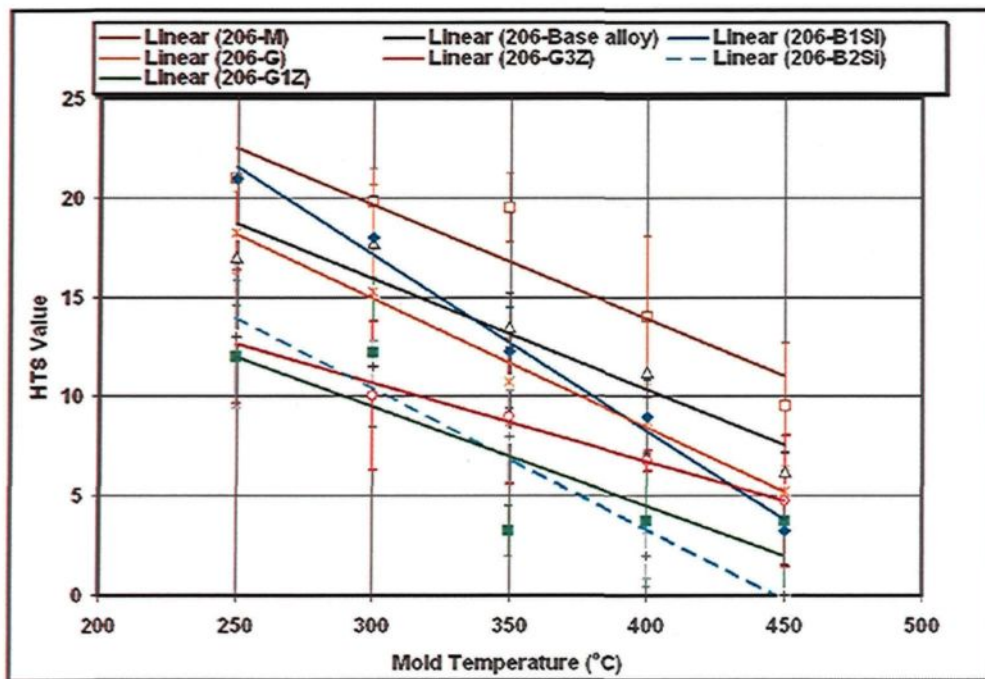


Figure 6.6 The linear relationship between HTS values and mold temperature for 206 alloys.

Table 6.1 The linear representative Equation between HTS Values and MT in Al-2wt%Cu Base Alloys

<i>Alloys</i>	<i>The linear relationship between Hot-Tearing Susceptibility (HTS) Values and Mold Temperature (MT)</i>	<i>R-Squared Value</i>
Base Alloy	$HTS = -0.091*(MT) + 41.6$	0.9384
M-Alloy	$HTS = -0.073*(MT) + 36.55$	0.9716
G-Alloy	$HTS = -0.0725*(MT) + 32.625$	0.9993
G1Z-Alloy	$HTS = -0.0559*(MT) + 24.775$	0.9274
G3Z-Alloy	$HTS = -0.048*(MT) + 21.45$	0.9412
B1Si-Alloy	$HTS = -0.0157*(MT) + 7.7667$	0.9718

Table 6.2 The linear representative Equation between HTS Values and MT in 206 Alloys

<i>Alloys</i>	<i>The linear relation between Hot-Tearing Susceptibility (HTS) Values and Mold Temperature (MT)</i>	<i>R-Squared Value</i>
206-Base Alloy	$HTS = -0.056*(MT) + 32.75$	0.8978
206-M Alloy	$HTS = -0.0575*(MT) + 36.875$	0.9716
206-G Alloy	$HTS = -0.065*(MT) + 34.4$	0.9899
206-G1Z Alloy	$HTS = -0.05*(MT) + 24.5$	0.7123
206-G3Z Alloy	$HTS = -0.0395*(MT) + 22.525$	0.9831
206-B1Si Alloy	$HTS = -0.089*(MT) + 43.86$	0.9895
206-B2Si Alloy	$HTS = -0.071*(MT) + 31.75$	0.9606

base alloy, the M-alloy, and the G-alloys; (ii) the alloys providing intermediate HTS levels, namely the G1Z-, and G3Z-alloys; and (iii) the alloy providing low HTS levels, namely the B1Si-alloy. The 206 alloys display the same behavior as the Al-2wt%Cu base alloy with

one major difference which is that the 206-B1Si alloy displays a high level of HTS. This high level of HTS in 206-B1Si alloys is reduced even further by an increase in the Si content of up to 2wt%, as may be seen in 206-B2Si alloy.

6.2 Effects of Mold Temperature

Mold temperature is considered to be one of the metallurgical factors which has a major effect on hot-tearing susceptibility. As mentioned above, the HTS values of Al-2wt%Cu base alloys and 206 alloys decrease in a linear fashion with an increase in the mold temperature, as shown in Figures 6.3 and 6.4, respectively, indicating the significance of the effects of mold temperature on HTS. For example, the HTS values at 450°C mold temperature may not exceed 3 value for Al-2wt%Cu base alloys and 9 value for 206 alloys, however at 250°C mold temperature the HTS values exceed 20 value for Al-2wt%Cu base alloys and also for 206 alloys. The intermediate mold temperatures also provide intermediate levels of HTS values.

Based on the strain theory formulated by Pellini,^{121,122} the occurrence of hot tearing in the metal depends on the amount and the rate of strain developed in the liquid film regions. There is a critical strain rate at which the metal undergoes hot tearing. Accordingly, the beneficial effects of the elevated mold temperature on the HTS values may be attributed to the lessening of the contraction strain rate; this reduction in the strain rate provides an opportunity for the casting sample to adapt and compensate for such a strain through microscopic movements of the dendrite cells, grains, or liquid metal. It is believed that this kind of compensation may not be possible at such a high strain rate. This explanation is in

good agreement with what was reported in a previous study¹¹⁶ in which it was reported that the development of the load/load rate drops from 185 N/s at a mold temperature of 200°C to 70N/s for a higher mold temperature of 380°C. The increase in the mold temperature not only lessens the contraction strain rate but also improves the feedability (i.e., ability to feed liquid to compensate shrinkage) and the occurrence of crack healing.

The beneficial effect of elevated mold temperature on the feedability of the liquid metal during solidification can be monitored by observing the level of shrinkage porosity in the castings. Based on the alloy microstructure shown in Figure 6.7, it will be observed that the severity of shrinkage porosity and hot cracking may be reduced significantly upon increasing the mold temperature from 250°C to 350°C. At a mold temperature of 350°C, the occurrence of the crack healing process is clearly in evidence through the presence of the eutectic intermetallics all along the crack path, as shown in Figure 6.7(b). The occurrence of this process at the higher mold temperature of 350°C provides a partial explanation for the improving effect of such a temperature on the HTS of the alloys under investigation.

The porosity measurements displayed by Al-2wt%Cu base alloys at 250°C and 350°C mold temperatures are provided in Figure 6.8. From this figure, it will be noticed that the porosity (%) of the Al-2wt%Cu base alloy decreases from 1.33 % to 0.134 % as the mold temperature increases from 250°C to 350°C, respectively. It will thus be observed here that the porosity levels decrease as do the HTS values with an increase in the mold temperature. This parallelism between the results obtained from HTS and porosity can be explained by considering the role of porosity in the crack initiation process; it is believed that

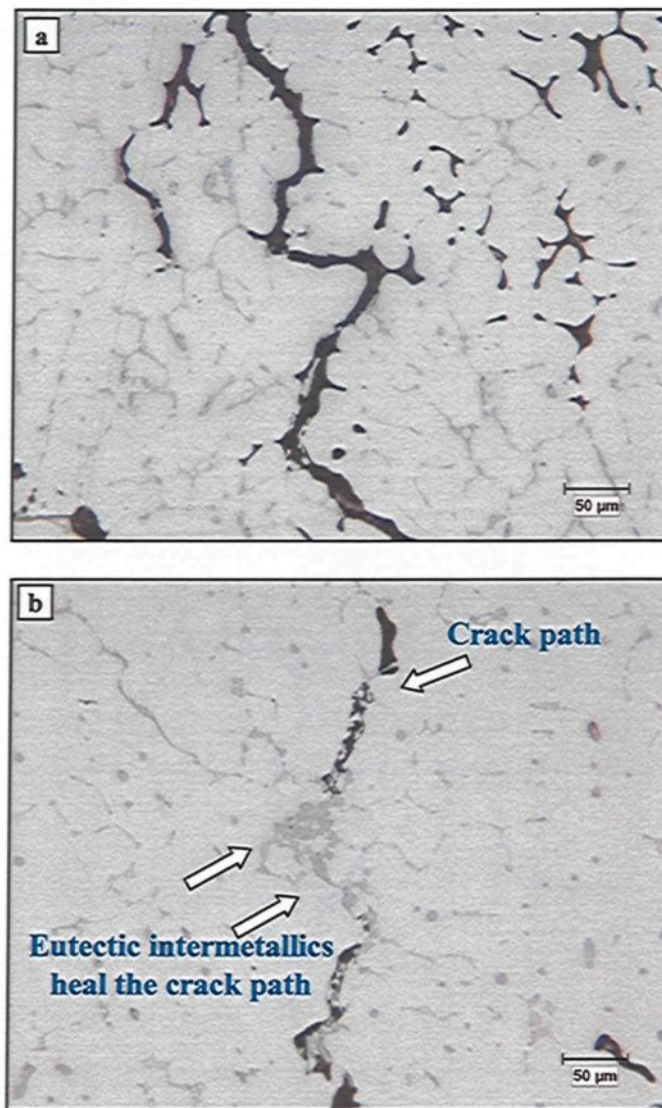


Figure 6.7 Microstructure of base alloy at two mold temperatures; (a) 250°C, and (b) 350°C.

the hot-tearing crack initiates from a pore or a series of pores in conditions of non-uniform thermal contraction of the coherent dendrites.⁹⁴ Such parallelism may also be explained by the deteriorating effect caused by the limited feedability and the diminished permeability of the mushy zone leading to the formation of high levels of porosity and to the difficulties

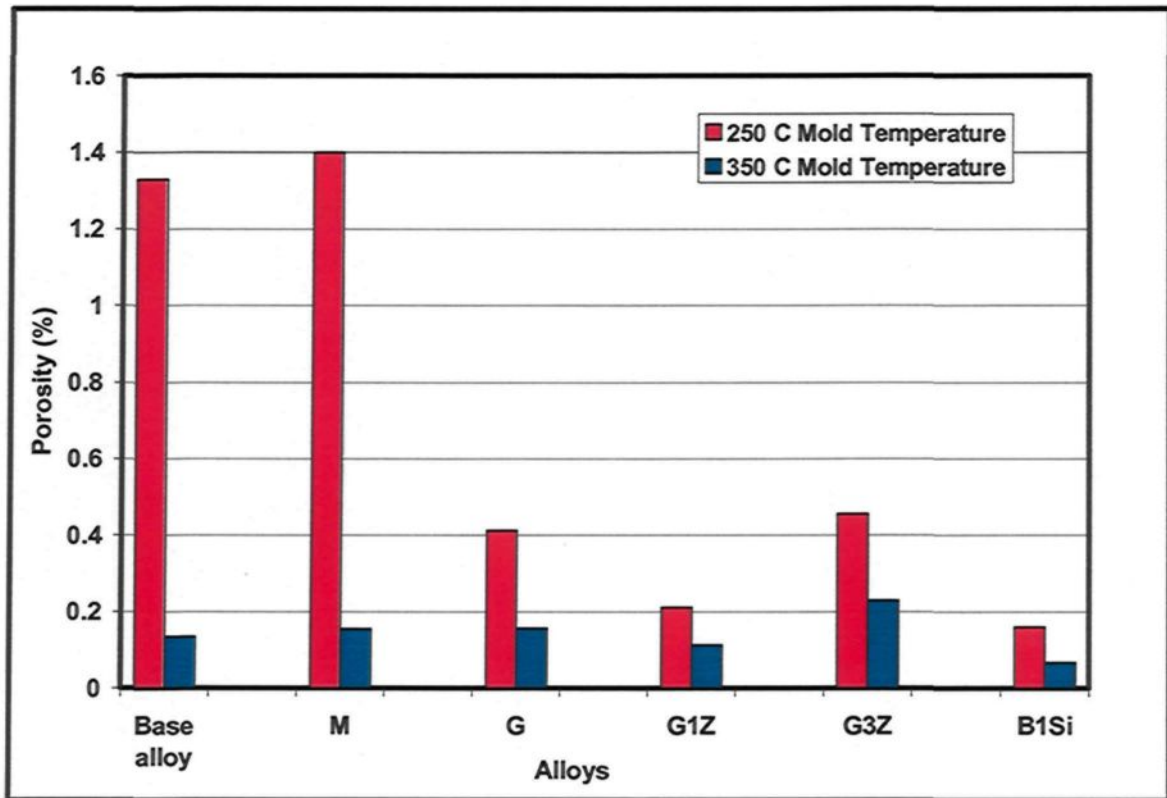


Figure 6.8 Measurement of porosity (%) in Al-2wt%Cu base alloys

involved in crack healing with liquid metal. This deteriorating effect can be alleviated by the application of high mold temperatures. From Figure 6.8, it will also be noted that the chemical composition may affect the porosity (%), as is the case with the grain-refining additions of Ti-B, Zr-Ti, as well as the addition of Si, all of which reduce the porosity level to a noticeable degree. It is also believed that the elevated mold temperature tends to widen the hot spot region leading to a reduction in the extension per unit volume of the hot spot, thereby diminishing the severity of the hot-tearing.

6.3 Effects of Grain Structure

Grain structure is a further metallurgical factor controlling the hot-tearing susceptibility (HTS) of base alloy; grain refinement may thus, in numerous cases, reduce the severity of hot-tearing. The grain-size measurements of the Al-2wt%Cu base alloys at 250°C mold temperature are provided in Figure 6.9. From this figure, it will be noted that the Zr-Ti and Ti additions reduce the grain size of the base alloy from 230 μm to a range of 94-55 μm . The finest grain sizes of 70 μm and 55 μm may be obtained from G1Z- and G3Z-alloys. The addition of Si produces a moderate reduction in the grain size, as displayed by the B1Si-alloy with a grain size of 184 μm . The Sr addition does not alter the grain size of the base alloy to any considerable degree, as may be seen in Figure 6.9.

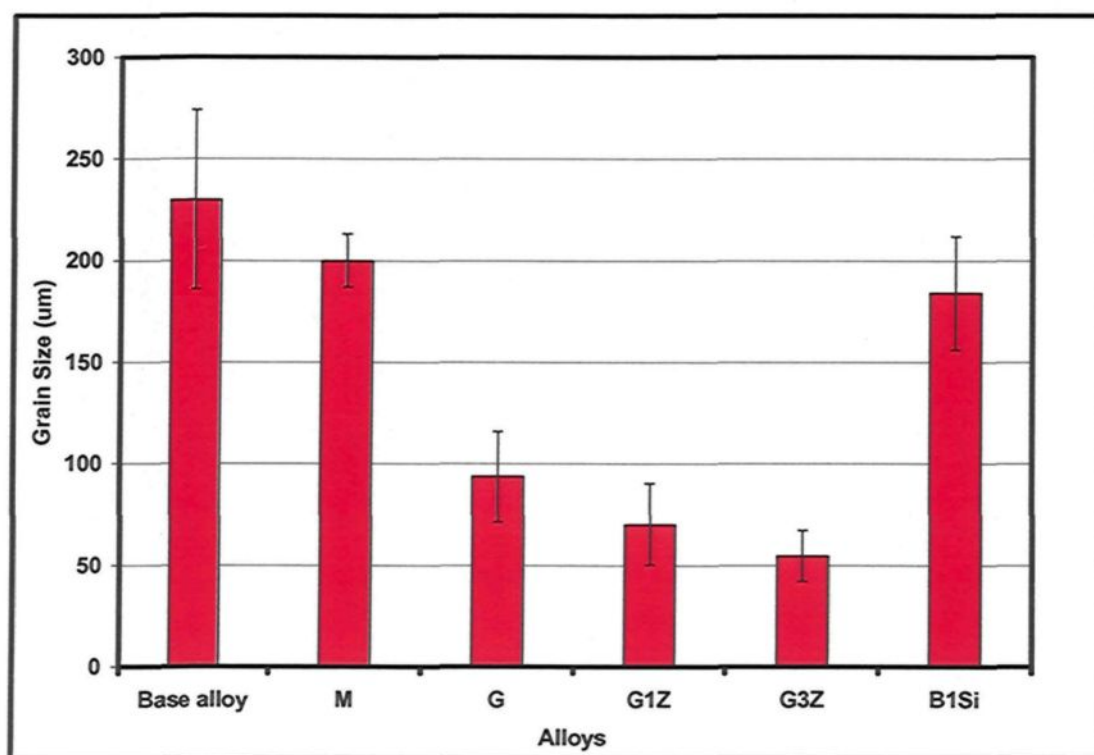


Figure 6.9 Average grain size of alloys investigated using hot-tearing test at 250°C mold temperature.

Figure 6.10 displays the grain structure obtained at the hot tear surface of the alloys investigated. The high degree of refinement obtained through additions of Zr-Ti and Ti leads to the transformation of the coarse elongated dendritic morphology of the base alloy into a fine globular non-dendritic structure, as shown in Figure 6.10. This morphological transformation is present at different levels in the alloys investigated and depends mainly on the refining efficiency of the additions. The optimum degree of transformation takes place in Zr-Ti containing alloys, namely, G1Z-, and G3Z-alloys. From the same figure as above, it is clear that the hot tearing occurs along the grain boundaries or the dendrite cell boundaries and hence it can be classified as an intergranular fracture. This type of fracture implies that the hot tearing takes place in the intergranular liquid films before the completion of solidification.

The grain size measurements of the Al-2wt%Cu alloys were replotted against the hot-tearing susceptibility of the same alloys, as illustrated in Figure 6.11. It was found that the hot-tearing susceptibility of the alloys decreases with a decrease in the grain sizes in linear fashion. This linear relationship between the HTS values and the grain sizes of the alloys investigated may be represented using the following equation:

$$\text{HTS} = 0.0623(\text{Grain Size}) + 6.4203, \text{ with } R^2 (0.93).$$

It should be mentioned that the B1Si-alloy is not covered by this equation. These results which were illustrated in the preceding three figures may help to explain the beneficial role of the grain refining additions, namely Zr-Ti and Ti, in reducing the hot-tearing susceptibility of the Al-2wt%Cu base alloy. Based on a study carried out by Kim and Loper,¹⁰⁷ it may be possible to state that the small grain structure, which was obtained

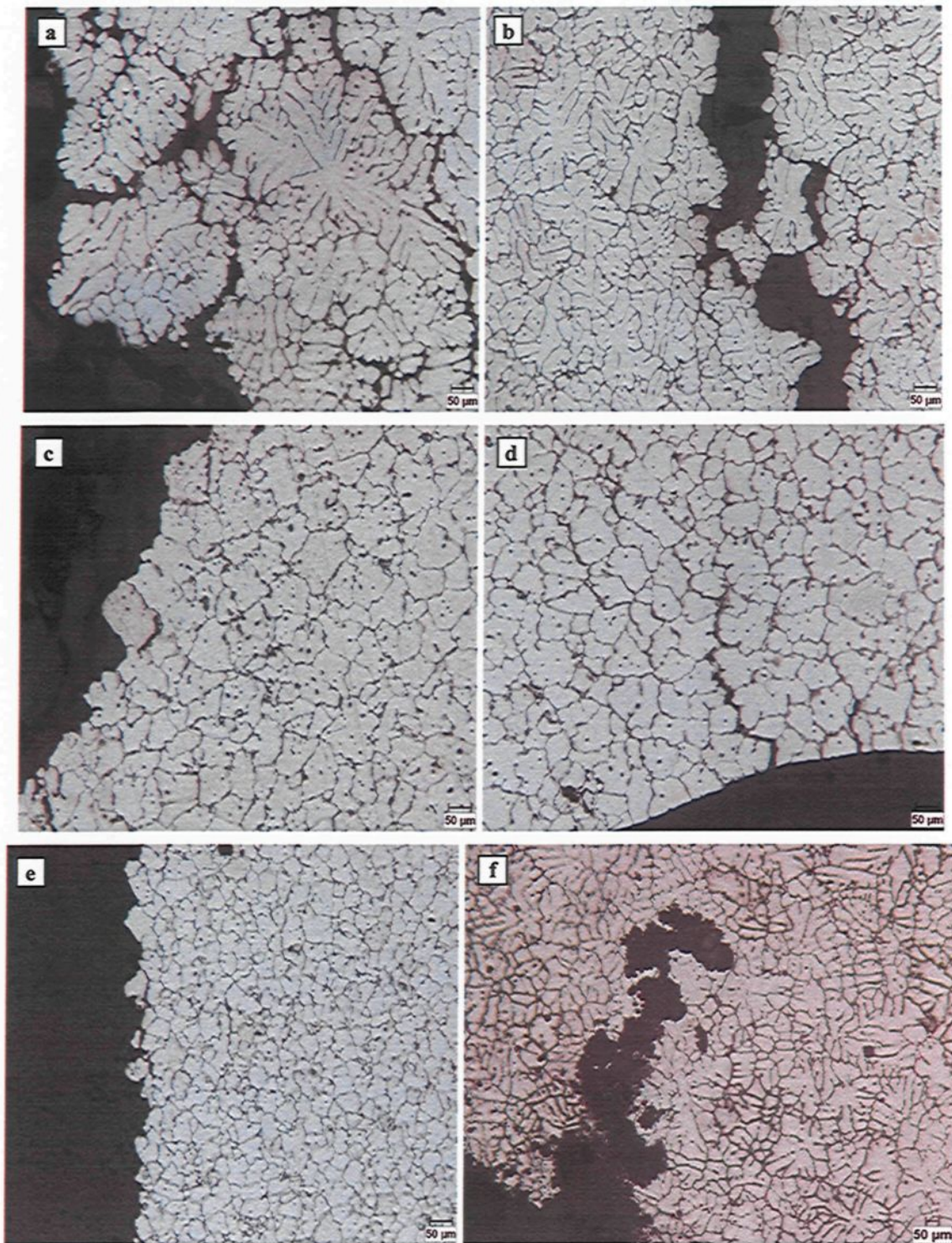


Figure 6.10 Grain structure obtained for the different Al-2wt%Cu alloy compositions: (a) base alloy, (b) M-alloy, (c) G-alloy, (d) G1Z-alloy, (e) G3Z-alloy, and (f) B1Si-alloy.

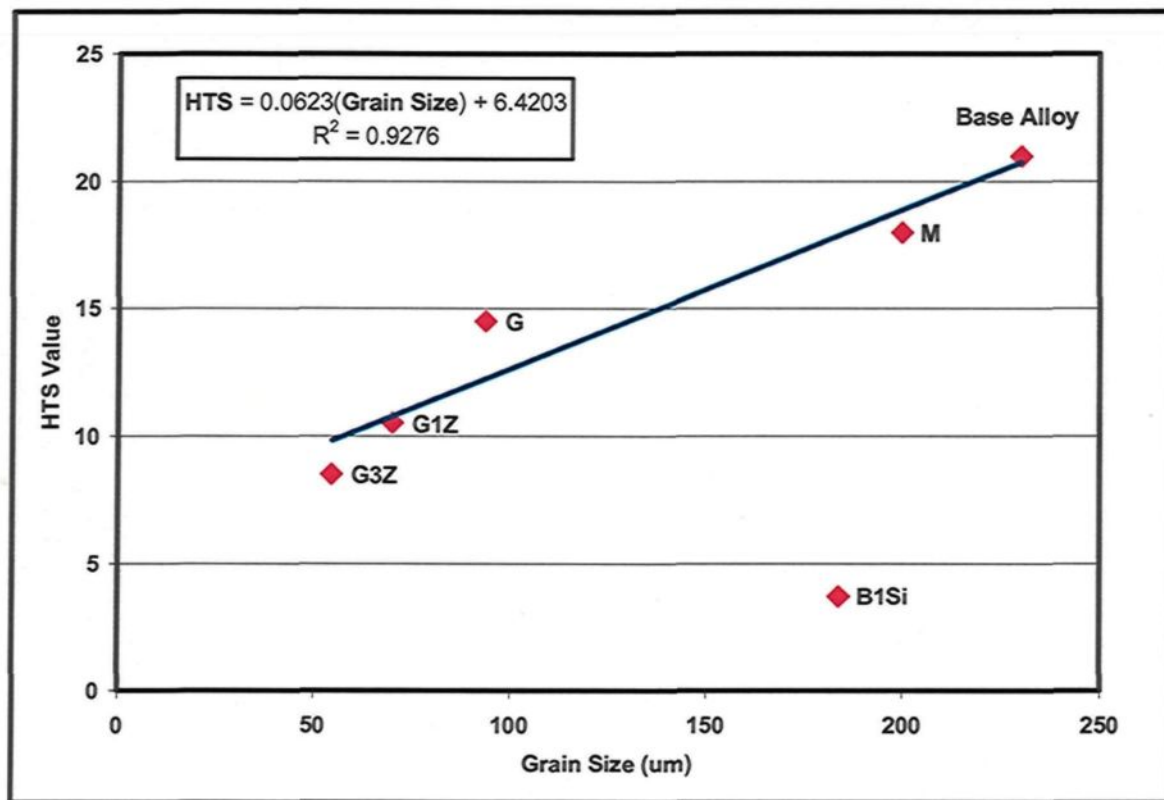


Figure 6.11 HTS vs. average grain size of the alloys investigated at 250°C mold temperature.

for G1Z- and G3Z-alloys, increases the number of the intergranular liquid films per one unit volume leading to a dispersal of the contraction stress and thus to an all-over reduction of hot-tearing susceptibility (HTS). By contrast, the coarse elongated dendritic structure of the Al-2wt%Cu base alloy will allow the contraction stress to concentrate in a small number of grain boundary films per unit volume, leading to high HTS.

It is believed that the coarse dendritic structure of the base alloy reduces the period of time in which the grains remain isolated from each other to a much shorter time than occurs with G1Z and G3Z-alloys having a fine globular non-dendritic structure. This difference leads to the observation that the resulting flow stress during solidification may be higher in

the coarse dendritic structure than in the fine non-dendritic one; such a fact is in agreement with the investigation results reported by Metz and Fleming.¹⁰⁸

The grain refining effect on the Al-2wt%Cu base alloy, of additions of Zr-Ti, improve structural permeability and the feedability (i.e., ability to feed liquid to compensate shrinkage) of the alloy, thereby enhancing crack healing and hot-tearing resistance. The improvements in permeability and feedability may be monitored by observing the porosity (%); these porosity values for the alloys investigated at 250°C mold temperature were thus replotted against the grain size values for the same alloys, as shown in Figure 6.12. It will be observed that the porosity (%) values decrease in linear fashion as grain sizes decrease; for example, as the grain size of the base alloy decreases from 230 μm to 70 μm as obtained by G1Z-alloy, the porosity, in turn decreases from 1.33 % to 0.211 %, respectively. The linear relation between the porosity and grain size may be represented by the following equation:

$$\text{Porosity (\%)} = 0.0067(\text{Grain Size}) - 0.1051 \text{ with } R^2 = 0.910.$$

Based on Figure 6.12, the effect of Zr-Ti additions on the reduction of HTS levels in the base alloy can also be explained by the improvement of the permeability and feedability of the alloy during solidification. The reduction of the porosity level has a direct effect on the decrease in the hot-tearing susceptibility of the alloy since porosity may promote the initiation of hot-tearing cracks.

The beneficial effects of grain refinement in lowering the HTS may be attributed to the fact that grain refinement tends to retard the coherency point to a lower temperature, thereby enhancing the liquid interdendritic feeding and healing the cracks.¹⁰⁹ This delaying

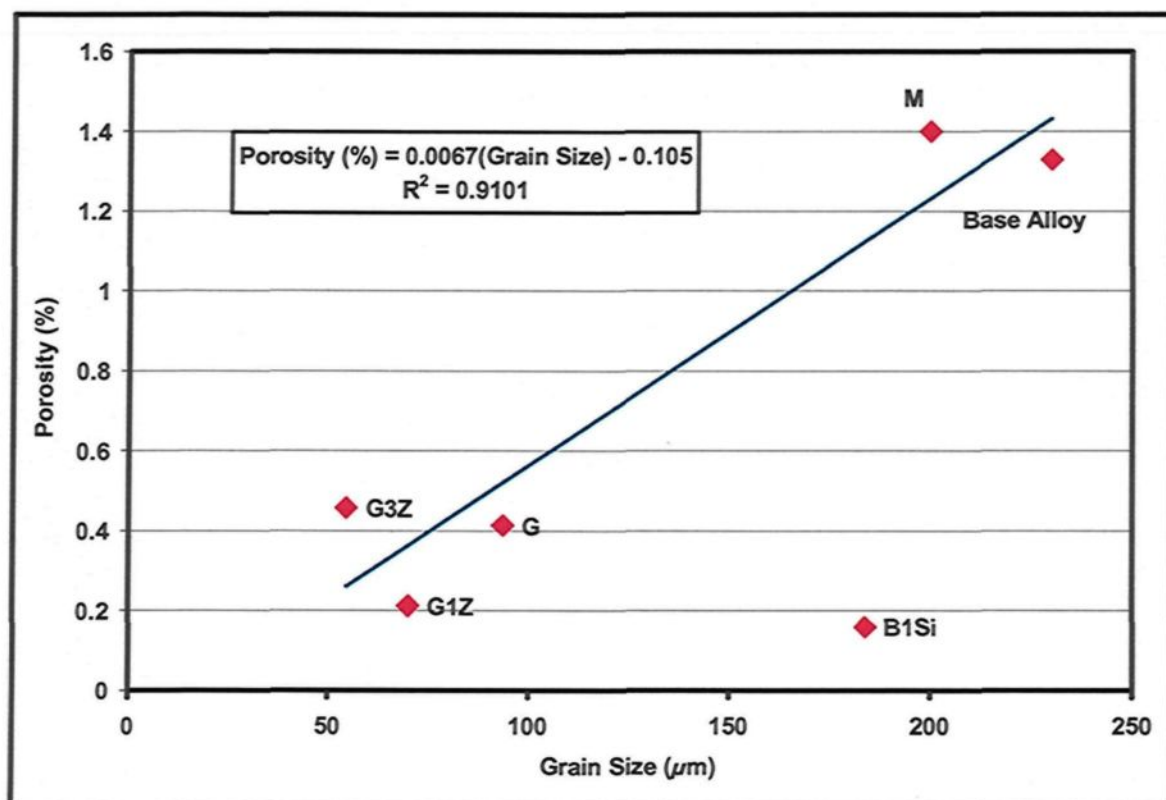


Figure 6.12 Average grain size vs. porosity (%) of alloys investigated at 250°C mold temperature

effect observed with the addition of Zr-Ti, or grain refinement addition, with regard to coherency was detected in this study using thermal analysis techniques under two different graphite mold temperatures of 200°C and 600°C. The delaying coherency point is determined by measuring the time difference between the formation reactions of dendrites at the boundary and at the center of the graphite mold using two thermocouples, one at the center of the mold, and the other 5 mm from the boundary.

The cooling curves and the first derivative curves of the base alloy and G3Z-alloy, at both mold temperatures of 200°C and 600°C, will be shown in Figures 6.13 and 6.14, respectively. In base alloy, the first derivative curves related to the two thermocouples

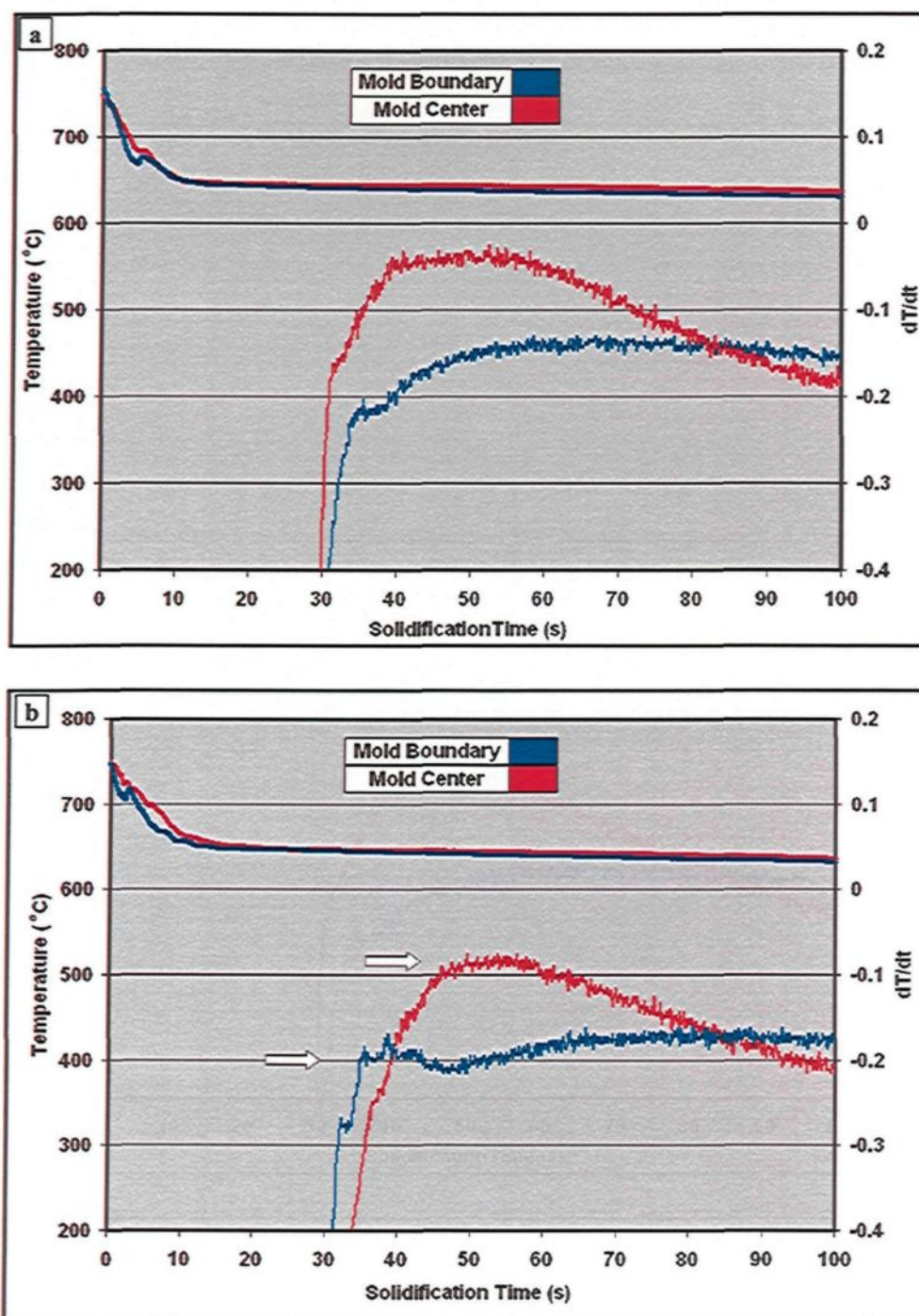


Figure 6.13 Cooling curves and first derivatives of Al-2wt%Cu base alloy (a), and G3Z-alloy (b) obtained at the center and the boundary of 200°C preheated mold

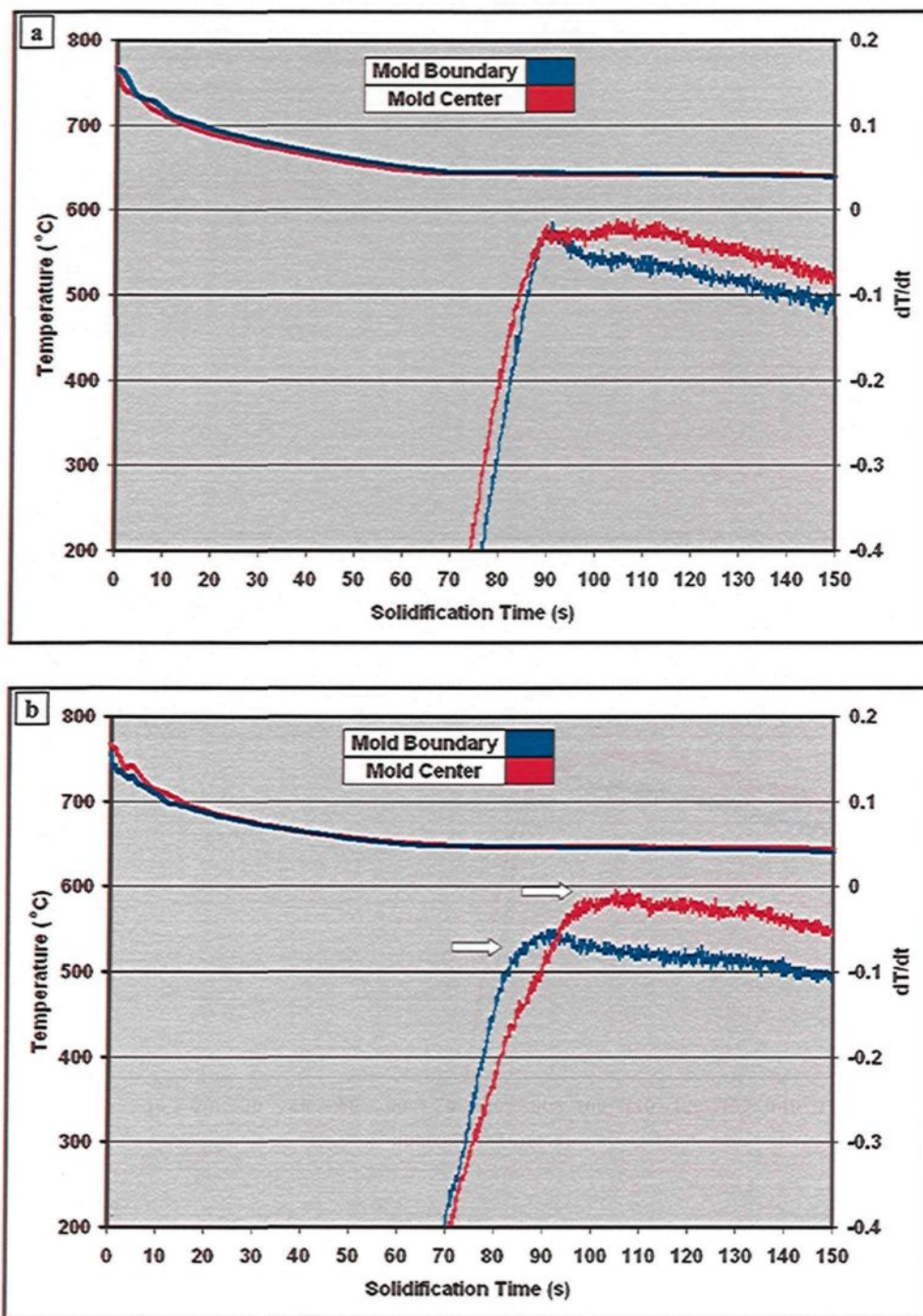


Figure 6.14 Cooling curves and first derivatives of Al-2wt%Cu base alloy (a), and G3Z-alloy (b) obtained at the center and the boundary of 600°C preheated mold

located at the center and at the boundary of the graphite mold are identical and do not display any time difference for dendritic formation reactions. In the case of G3Z-alloy, the first derivative curves display a time difference of 15 s between the first dendritic formation reaction at the boundary of the graphite mold and the second one at the center of the graphite mold. This time difference indicates that the addition of Zr-Ti to the base alloy may delay the coherency point to a certain degree, namely by 15s, as determined under the current experimental conditions. As mentioned previously, the delaying of the coherency point improves the feeding and crack-healing mechanisms; it also increases the stress and strain accommodation ability of the alloy, thereby causing the hot-tearing resistance of the alloy to become heightened.

Also, it is expected that the grain refinement using combined additions of Zr-Ti may reduce the hot-tearing susceptibility of the alloy by decreasing the degree of contraction of the alloy during solidification. Eskin *et al.*¹⁰² reported that the addition of an appropriate grain refiner to the 6061 alloy diminishes the solidification contraction by 2 to 3 times.

6.4 Effects of Silicon Content

As shown in Figure 6.3, the hot-tearing susceptibility of the Al-2wt%Cu base alloy decreases sharply upon increasing the Si-content by 1wt%, as displayed by the B1Si-alloy. The improvement effects of the Si content on the hot-tearing resistance may also be represented in the following equation, which describes the hot-tearing susceptibility behavior of the B1Si-alloy:

$$\text{HTS} = -0.0157*(\text{MT}) + 7.7667, \text{ (see Table 6.1)}$$

As mentioned previously in section 6.1, the small constant and MT coefficient values in the preceding equation indicate the elevated hot tearing resistance of the B1Si-alloy and the diminished effect of the mold temperature on the HTS of this alloy. The increased hot-tearing resistance displayed by the B1Si-alloy may be attributed to an increase in the eutectic fraction resulting from the increase in Si content which in turn activates the crack healing mechanism. Such an improvement caused by the high eutectic liquid fraction, is illustrated in Figure 6.15. This figure reveals that the crack paths are healed either completely or partially by eutectic silicon particles, as well as by other eutectic intermetallic compounds such as Al_2Cu and $\text{Al}_5\text{Mg}_8\text{Cu}_2\text{Si}_6$.

The high volume fraction of the eutectic Si improves the interdendritic liquid flow which, in turn promotes crack healing. Such an effect, as produced by the addition of Si, concords with work carried out by Jennings and Singer¹⁰⁵ who found that an increase in Si content beyond the solid solubility limit leads to an improvement in hot-tearing resistance deriving from an increase in the eutectic fraction which, in turn, enhances the crack healing mechanism. Also Lu *et al.*,¹¹⁰ suggested that the occurrence of tearing causes a local pressure differential in the liquid leading to an influx of liquid which, in turn, heals the crack and thus the HTS decreases.

The long freezing range of the Al-2wt%Cu base alloy, up to 145°C, is considered to be one of the main reasons for the high susceptibility of this alloy to hot tearing. This long freezing range extends the liquid film stage, that is to say, the critical range for hot tearing, and also maximizes the degree of solidification shrinkage whereby intensified hot-tearing susceptibility is obtained.^{93,105,201} The addition of Si is liable to play an important role in

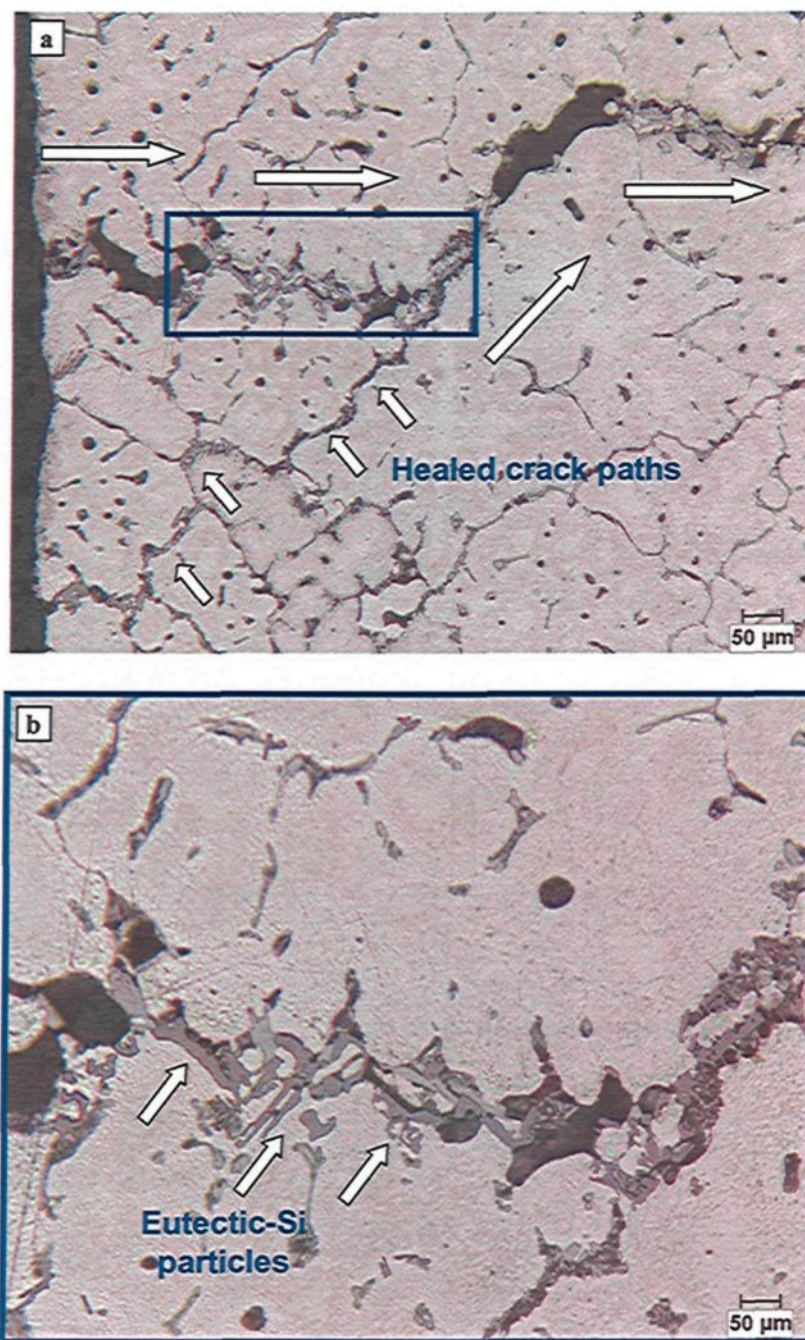


Figure 6.15 (a) Crack-path healed with eutectic Si, (b) higher magnification of region, blue-framed rectangle

reducing or shortening the freezing range of the base alloy by lowering the liquidus temperature. Using thermal analysis techniques, the cooling curve of the base alloy was determined and then compared with the cooling curves of the B1Si- and B2Si-alloys in order to identify the effects Si on the freezing range. Figure 6.16 shows the cooling curves obtained. It was found that the liquidus temperature of the base alloy containing 1wt% Si decreases by 10°C and 16°C as the Si content increases to 2wt%, as displayed by the B1Si-alloy, and to 3%, as displayed by the B2Si-alloy, respectively. It will also be observed in Figure 6.17 that the liquidus temperature decreases linearly with increasing Si content; this linear relation may be represented using the following equation:

$$\text{Liquidus Temperature} = -7.85 * (\text{wt\%Si}) + 647.84, R^2 = 0.9865$$

These findings indicate a further beneficial effect of Si addition on the reduction of the hot tearing susceptibility of the base alloy; this is accomplished by shortening the freezing range as a result of lowering the liquidus temperature. Similar effects on the liquidus temperature and freezing range have been reported by Jennings and Singer¹⁰⁵ with regard to Si content; they found that the addition of this element to the Al-Cu system reduces the liquidus temperature, and consequently the freezing range as well, thereby diminishing hot-tearing susceptibility.

Figure 6.4 shows that the 1% Si addition does not reduce the hot-tearing susceptibility of the 206 alloy to any significant degree, as illustrated by the 206-B1Si alloy. Such a situation arises as a result of the fact that the 206 alloy contains 0.11wt% Si; the addition of 1wt%Si to this alloy will thus increase the Si content causing it to approach the solid solubility limit which has already been described by a number of researchers^{104,128}

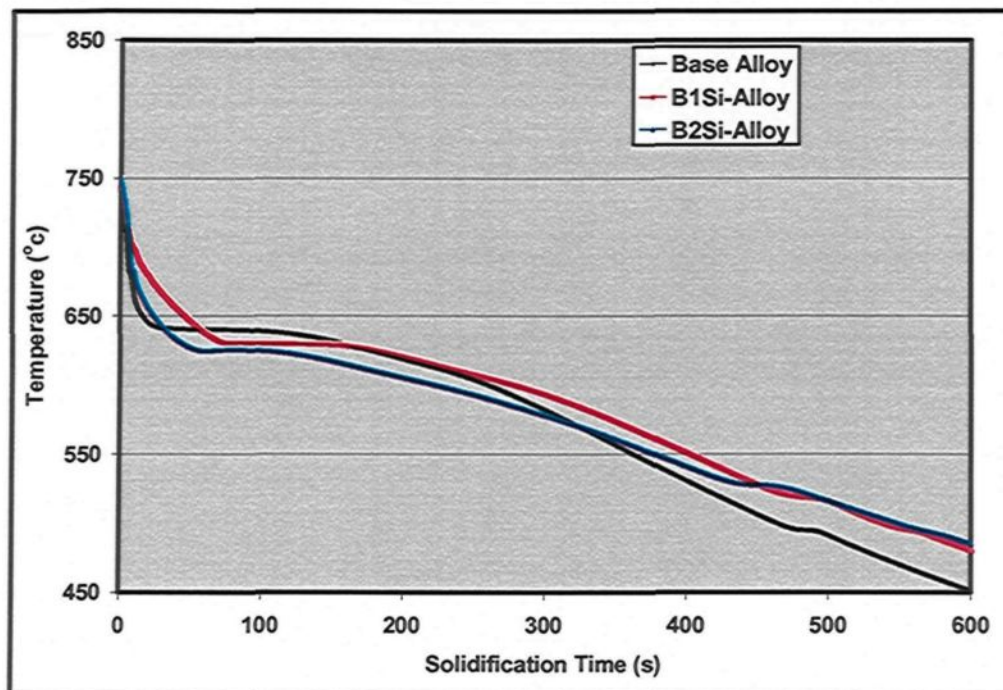


Figure 6.16 Effect of Si content on the cooling curve of the Al-2wt%Cu base alloy.

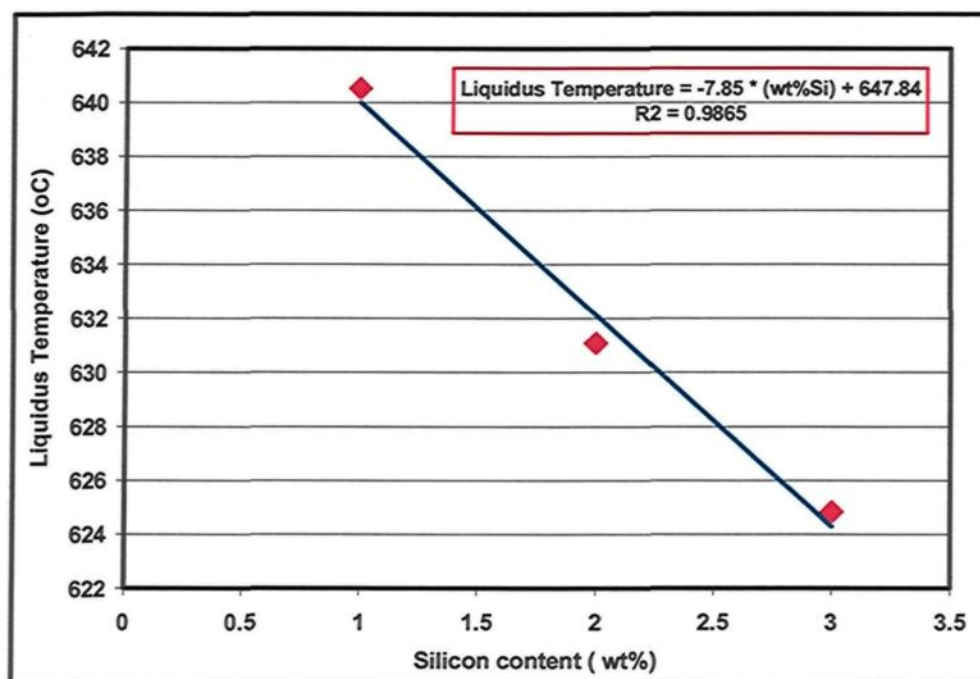


Figure 6.17 The liquidus temperature against Si content

as the composition which is most susceptible to hot tearing. As the Si content increases beyond the solubility limit of Si reaching 2wt%, as displayed by the 206-B2Si alloy, the susceptibility to hot tearing decreases, thereby corroborating the above explanation.

6.5 Effects of Strontium Addition

The addition of Sr to the Al-2wt%Cu or 206 base alloys reduces their resistance to hot tearing and also results in obtaining high HTS values, as shown in Figures 6.3 and 6.4, respectively. The deleterious effects of Sr on hot tearing resistance may be identified from the following equations representing M- and 206-M alloys:

$$\text{HTS} = -0.073*(\text{MT}) + 36.55, \text{ with } R^2 = 0.9716$$

$$\text{HTS} = -0.0575*(\text{MT}) + 36.875, \text{ with } R^2 = 0.8724$$

As mentioned earlier in subsection 6.2, entitled Effects of Grain Structure, the high constant values 36.5 and 36.8 in the preceding equations indicate the low hot-tearing resistance of these alloys which contain Sr. Also the deteriorating effects of Sr, as a sole addition, on the tensile properties were recorded in the preceding chapter, entitled Tensile Properties. Arnberg *et al.*²⁰¹ deduced that the harmful effects of Sr include (i) the formation of an oxide bifilm, (ii) a reduction in the surface tension of the liquid, (iii) an increase in the volumetric shrinkage, (iv) a reduction in interdendritic feeding, (v) extending of the freezing range, and (vi) porosity formation. Figure 6.18 shows examples of the Sr-oxide particles detected in the M-alloy. It will be observed in Figure 6.18 (a) that the Sr-oxide particle was trapped between the dendrite boundaries during solidification; this is attributed to the fact that the advancing solidification front can not grow through the oxides and they are thus rejected and pushed by the advancing dendrites.²⁰² From the

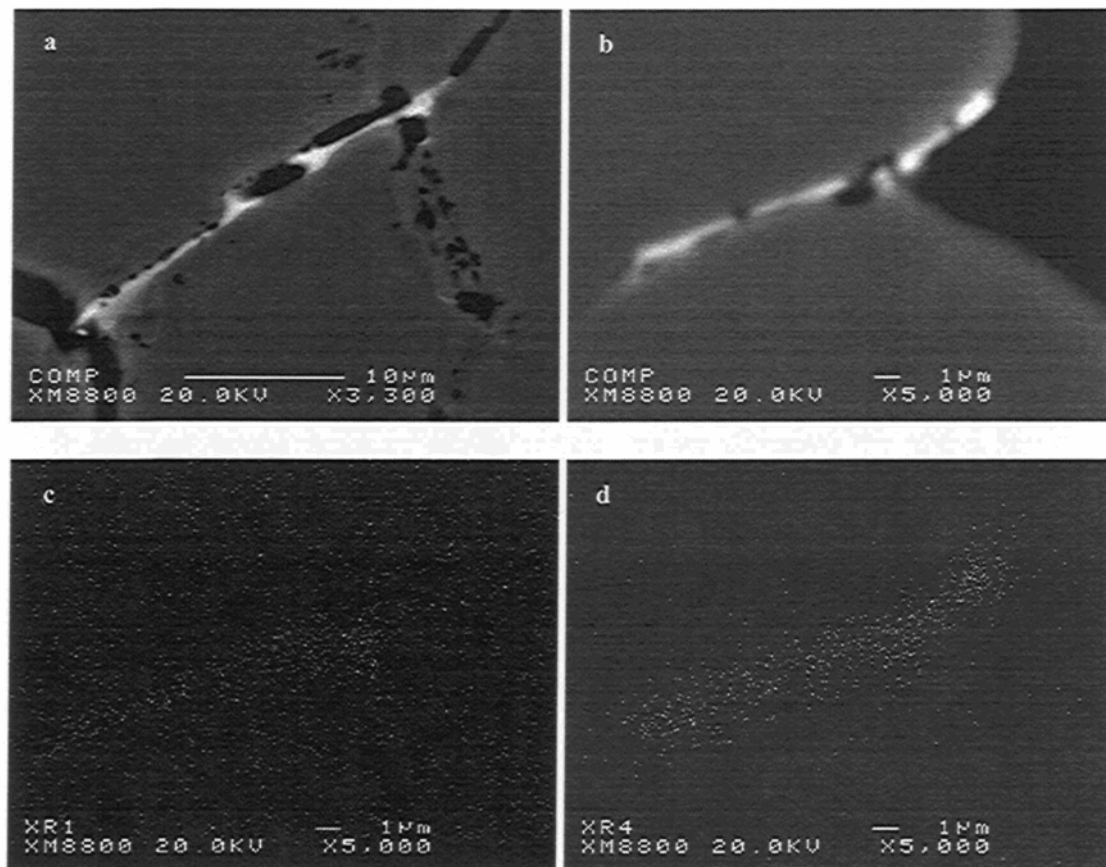


Figure 6.18 Sr-oxide particles detected in M-alloy: (a) backscattered image of Sr-oxide particle trapped between dendrites; (b) backscattered image of Sr-oxide particle on the crack surface, (c) corresponding oxygen X-ray image for (b); and (d) corresponding Sr X-ray image for (b).

preceding figure it may also be observed that the Sr bifilm is associated with the formation of pores or cavities located along the bifilm surface. The oxide particles act as heterogeneous nucleation sites for pores since these oxides grow independently without any bonding relationship with the liquid metal as a result of the presence of the separating layer of entrained gas on their surface.²⁰² This type of oxide thus heightens the porosity level which reduces the hot tearing resistance of the alloy, as discussed in a previous subsection. It is worth noting that the Sr addition itself may lead to an increase in the gas porosity by increasing the solubility of hydrogen in the liquid metal or decreasing the solubility of

hydrogen in the solid.²⁰¹ The maximizing effect which the addition of Sr has on the porosity level is already illustrated by the M-alloy in Figure 6.8.

Figure 6.18 (b) provides an example of a hot tearing crack which is opened up by the decohesion of the oxide particles from the matrix under the effects of solidification shrinkage and thermal contraction. This decohesion takes place because of the minimum driving force, since there is neither atomic relationship nor bonding between these oxides and the matrix. Accordingly, the presence of these particles will, in turn, increase the hot-tearing susceptibility of the alloy. Figures 6.18 (c) and (d) display the corresponding X-ray images of Sr and oxygen, respectively, and indicate the way in which these elements are distributed through the Sr-oxide particles, thereby also confirming the manner of their formation. The same type of Sr oxide particle is detected in the 206-M alloy, as may be seen in Figure 6.19.

The effects of Sr on the freezing range were also investigated using thermal analysis techniques. The relevant data obtained were used to draw the cooling curves of the base alloy and the M-alloy, as displayed in Figure 6.20. From this figure it will be observed that the addition of Sr prolongs the freezing range of the base alloy by 7°C. This extension was obtained not by lowering the solidus temperature but by raising the liquidus temperature by the 7°C already mentioned. As discussed in section 6.4, extending the freezing range leads to intensified hot-tearing susceptibility as a result of maximizing the degree of solidification shrinkage and lengthening the liquid film stage.^{93,105,202}

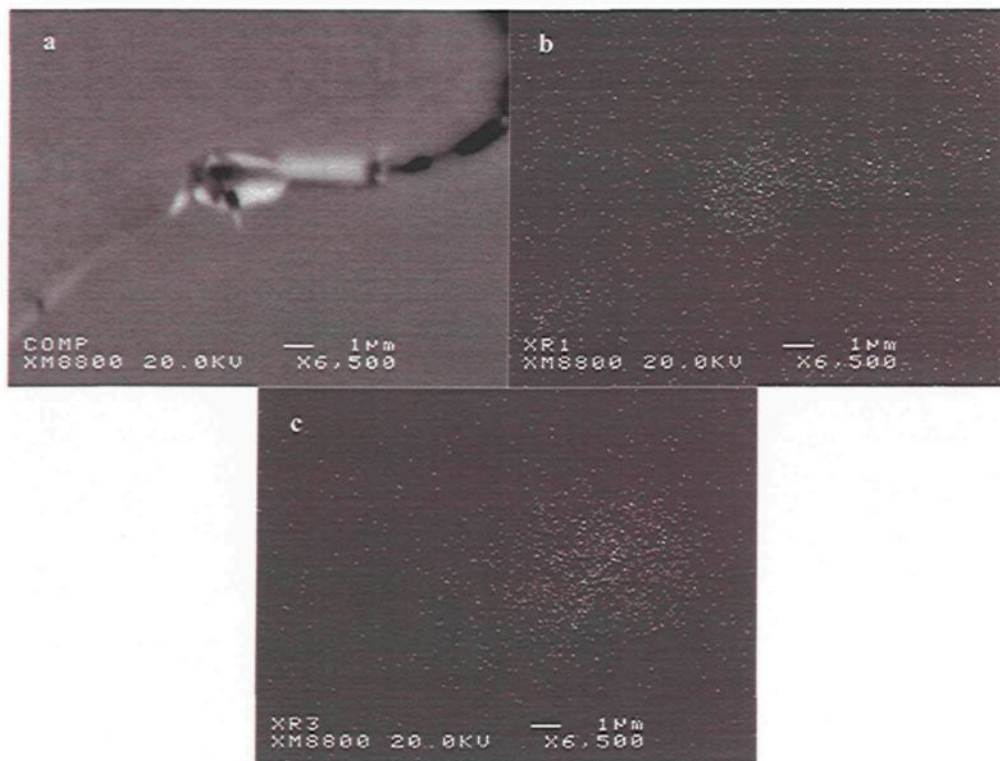


Figure 6.19 (a) Backscattered image taken from 206-M alloy showing the presence of Sr-oxide particle on crack surface, and (b) and (c) corresponding X-ray images of Oxygen and Sr, respectively.

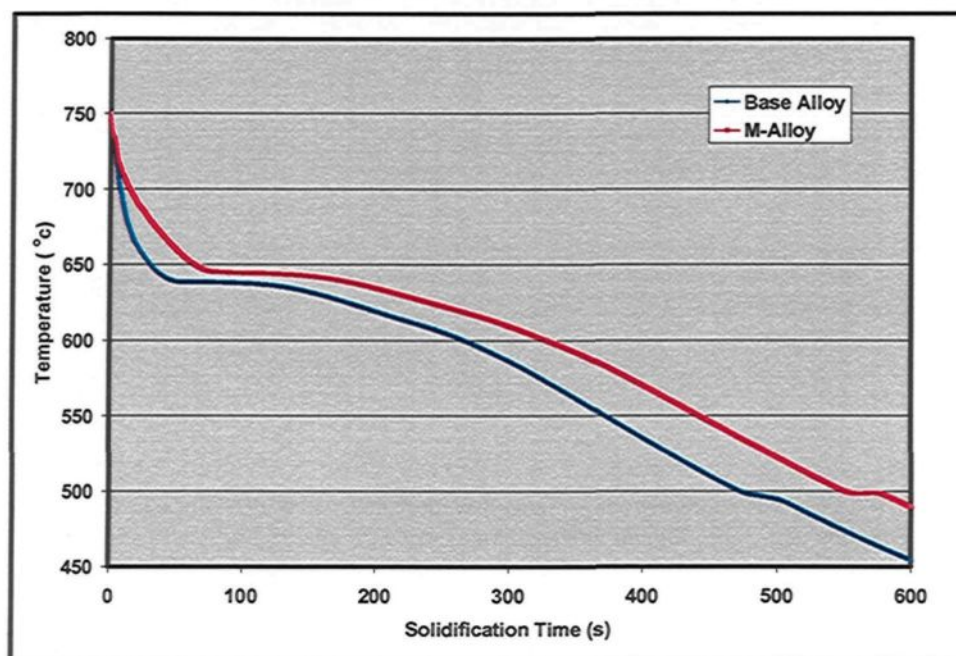


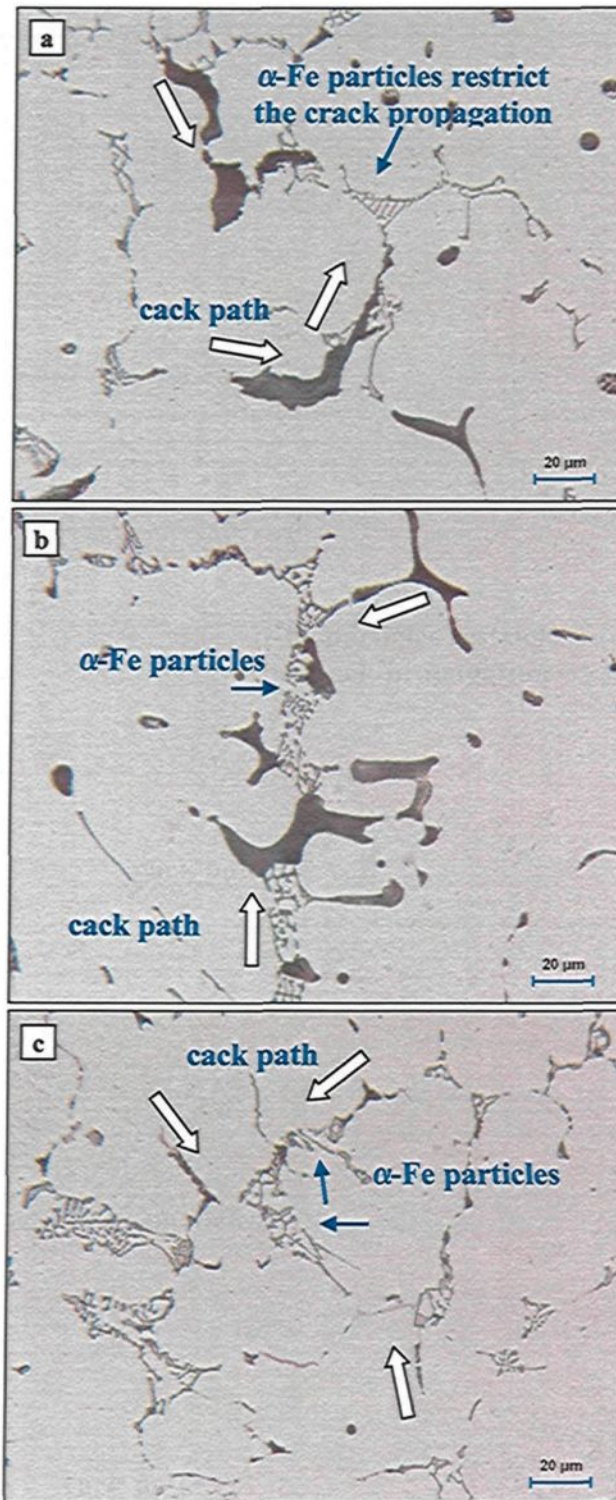
Figure 6.20 Effects of Sr addition (200 ppm) on the cooling curve of the Al-2wt%Cu base alloy.

The effects of the addition of Sr on the reduction of the surface tension of liquid and on the increase in solidification contraction are not included in this study although they are found in the literature and have already been reported upon in a number of studies.^{203,204} The reduction of the surface tension of the liquid will lead to a decrease in the dihedral angle tending towards zero thereby making it easy to create liquid cracks from an energy point of view.¹³¹ Increasing of the volumetric shrinkage will also maximize the amount of strain during solidification causing an intensified tendency towards hot-tearing.

6.6 Effects of α -Iron Intermetallic Phase

During the investigation of the microstructures of the hot-tearing test samples, it was observed that the α -iron intermetallic particles may act as obstacles to prevent the propagation of the hot-tearing crack through the liquid film. From Figure 6.21, it may be noted that the α -Fe intermetallic particles obstruct the crack paths and prevent their linking. It is also seen that the widths of the crack paths in grain-refined alloys G1Z and G3Z are smaller than those appearing in the unrefined base, and M alloys, indicating the beneficial effects of Zr and Ti as grain refining agents.

A schematic sketch of the obstructing effect of the α -Fe intermetallic particles on hot-tear crack propagation is displayed in Figure 6.22. In the base Al-2wt%Cu alloy, the α -Al dendrites form first, at 640°C, followed by the α -Fe intermetallic phase at 619°C, in the form of compact script-like particles. As growth of these phases proceeds during solidification, the α -Fe particles become trapped between the dendrites such that they appear joined or bonded to the dendrites. In this way the α -Fe particles may enhance the



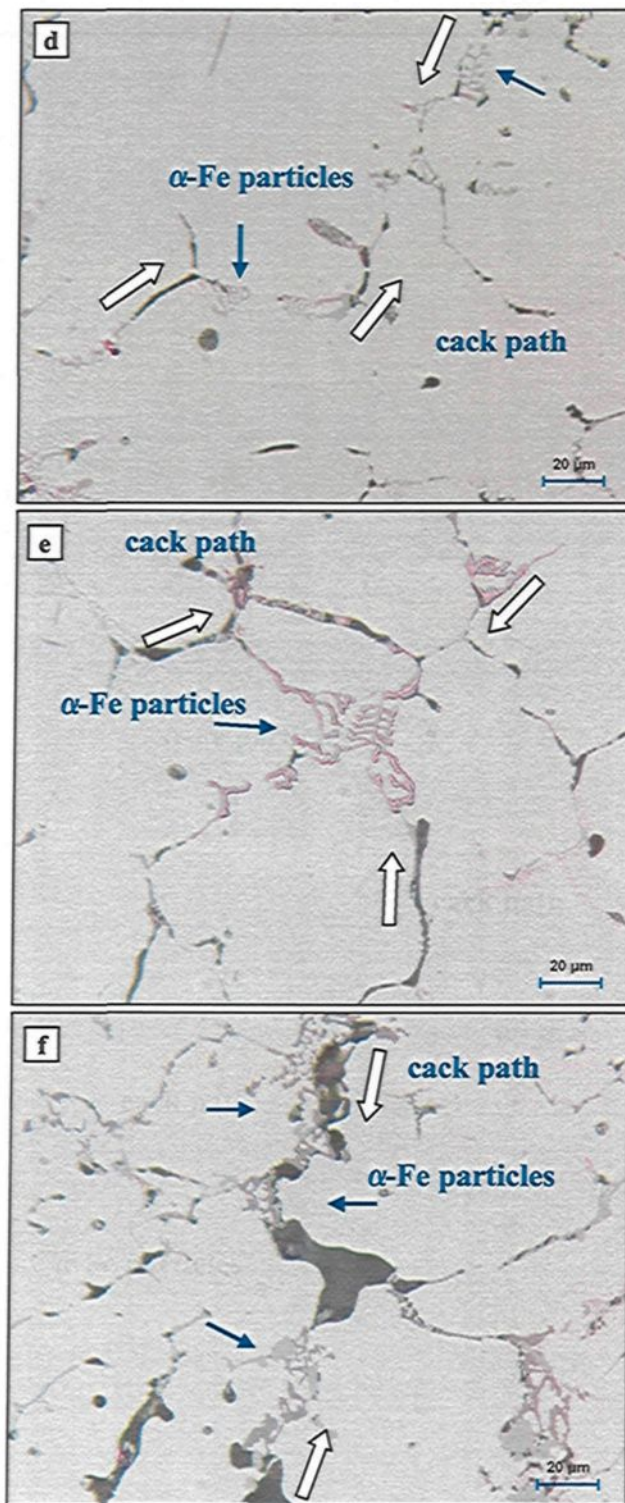


Figure 6.21 Optical micrographs demonstrating the role of α -Fe particles in preventing the propagation of hot-tear cracks in: (a) base alloy, (b) M-alloy, (c) G-alloy, (d) G1Z-alloy, (e) G3Z-alloy, and (f) B1Si-alloy.

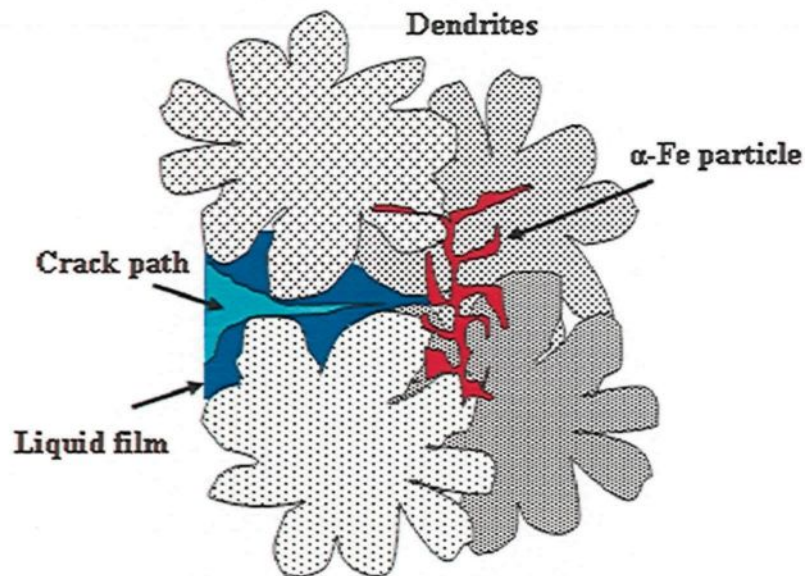


Figure 6.22 Schematic sketch showing how the α -Fe particles obstruct crack propagation in the alloy.

strength of the alloy during solidification, allowing it to withstand the liquid-to-solid contraction and so reducing the occurrence of hot tearing. Moreover, the α -Fe particles also obstruct the propagation of the hot-tear crack initiated in the liquid metal between the dendrite cells. The branched morphology and the high hardness of the α -Fe particles ($\sim 11\text{GPa}$)²⁰⁵ also assist in enhancing their capacity for reducing the hot-tearing susceptibility of the alloy. As discussed in the two preceding chapters, the refined non-dendritic structure of the alloys with Zr and Ti additions also results in a refinement or reduction in size of the α -Fe particles, improving their efficiency in reducing the hot-tearing the hot-tearing susceptibility of said alloys.

6.7 Proposed Hot-Tearing Criteria

Based on the discussion presented in the preceding sections and in the light of the literature, it is possible to define five main factors controlling the hot-tearing phenomenon in Al-2%Cu-based alloys as follows:

1. The strength of the alloy in the vulnerable temperature range for hot-tearing.
2. The contraction strain rate.
3. The presence of non-wetted inclusions which decrease the necessary driving force for hot-tearing crack initiation.
4. Capacity of the alloy for crack healing.
5. The freezing range based upon which the level of the accumulated contraction strains and the extent of the liquid film stage will be determined.

These factors are, in turn, controlled or limited by other parameters as displayed in the flow chart shown in Figure 6.23. In the light of the experimental conditions of the current study and the resulting observations, these parameters may be reduced to four main parameters as follows:

- (i) the contraction strain rate – which is controlled by the mold temperature *viz.*, the cooling rate;
- (ii) the eutectic fraction-which is controlled by the amount of alloying elements such as Cu and Si present in the alloy;
- (iii) the grain size and morphology - controlled by grain refining additions such as Zr-Ti or Ti; and
- (iv) the level of non-wetted inclusions such as Sr-oxides – which is controlled by the Sr content and melt cleanliness.

Accordingly, the expected level of hot-tearing susceptibility (HTS) may be expressed in terms of the above four parameters in the form of a mathematical relationship as follows:

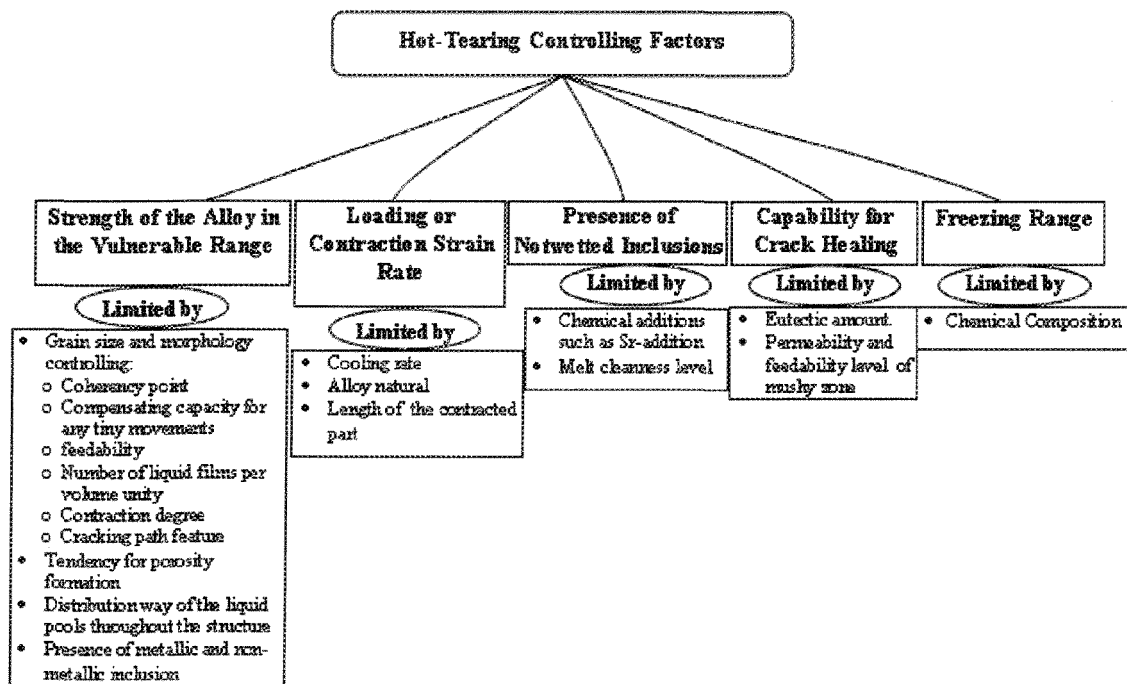


Figure 6.23 Flow chart of the suggested factors and corresponding parameters controlling hot-tearing.

$$HTS = [\pm C_1 * (CSR) \pm C_2 * (EF) \pm C_3 * (GS) \pm C_4 (size \text{ and vol. fraction of non-wetted inclusions)}] \quad (1)$$

where

- HTS: Hot-tearing susceptibility;
- CSR: Contraction strain rate;
- EF: Eutectic fraction;
- GS: Grain Size;
- C_1 , C_2 , C_3 , and C_4 are mathematical coefficients representing the effectiveness of each parameter, depending on the testing method and the way by which hot-tearing is estimated.

According to the observations that the Si content and the elevated mold temperature were the most effective parameters controlling HTS, as shown in Figure 6.3, it appears that the effectiveness of the terms in equation (1) are likely to follow the order $C_2 * (EF) > C_1 *$

(CSR) > C₄ (size and vol. fraction of non-wetted inclusions) > C₃* (GS) based on the observation A constant may also be added to the equation in order to balance it.

Based on the results shown in Figure 6.3, it may be suggested that depending on the cooling rate and eutectic fraction in question, Equation (1) may be reduced to a simpler form as

$$HTS = [\pm C_1 * (CSR) \pm C_2 * (EF)] \quad (2)$$

With respect to Equation (2) it is suggested that the terms associated with each coefficient may be further specified as follows:

$$HTS = [Cof._1 (ACSR - HCRNT) + Cof._2 (LEFNT - AEFNT)] \quad (3)$$

where

- ACSR: Actual contraction strain rate.
- HCRNT: The highest contraction strain rate with no tearing.
- LEFNT: The lowest eutectic fraction with no tearing.
- AEFNT: Actual eutectic fraction.

If the value obtained from the above equation has a positive sign, the probability that hot-tearing will occur will be determined by this value. If the value is negative, the probability that hot-tearing will not occur will be determined by the corresponding value. It ought to be mentioned here that the above equations have been proposed as a theoretical means to provide a mathematical formulation for the hot-tearing susceptibility. However, much experimental work is still required to correctly estimate each of the terms in the above equations.

6.8 Conclusions

The hot-tearing susceptibility (HTS) of six different compositions of the Al-2wt%Cu base alloy, namely the base alloy, M-alloy (0.2wt%Sr), G-alloy (0.15wt%Ti), G1Z-alloy (0.15wt%Ti-0.15wt%Zr), G3Z (0.15wt%Ti-0.3wt%Zr), and B1Si-alloy (1wt%Si), were tested using the constrained rod casting (CRC) mold, at various mold temperatures of 450°, 400°, 350°, 300°, and 250°C. The HTS results obtained from the Al-2wt%Cu-based alloys were compared with seven alloys prepared from the commercial 206 alloy with the same levels of additions. From the analysis of the results obtained, the following may be concluded:

1. An elevated mold temperature is beneficial in reducing the hot-tearing susceptibility of the Al-2wt%Cu and 206 alloys in that the HTS value decreases from 21 for the two alloys to 3 and 9, respectively, as the mold temperature is increased from 250°C to 450°C.
2. The beneficial role of the elevated mold temperature in decreasing the HTS level is attributed to:
 - i) a lowering of the contraction strain rate;
 - ii) an improvement in the feedability of the molten alloy (i.e., ability to feed liquid to compensate shrinkage);
 - iii) a reduction in the porosity level; and
 - iv) a widening of the hot spot region.

3. Grain refining additions of Zr-Ti or Ti reduce the grain size of the Al-2wt%Cu base alloy from 230 μm to grain sizes in the a range of 94-55 μm , changing the matrix structure morphology from an elongated, coarse dendritic type to a globular, non-dendritic structure. The G1Z and G3Z alloys display the finest grain sizes, i.e., 70 μm and 55 μm , respectively.

4. The refinement of the grain structure obtained with the Zr-Ti or Ti additions decreases the hot-tearing severity as a result of:
 - i) an increase in the number of intergranular liquid films per unit volume;
 - ii) a delay in reaching the coherency point;
 - iii) an improvement in the permeability and feedability mushy zone;
 - iv) a lowering of the porosity level;
 - v) a reduction in the contraction level obtained during solidification; and
 - vi) an increase in the capacity of the alloy to accommodate the stress and strain resulting with the progress of solidification.

5. The hot tearing cracks occur along the grain boundaries or along the dendrite cell boundaries and hence may be classified as an intergranular type of fracture, which would indicate that the hot tearing takes place in the intergranular liquid films before the completion of solidification.

6. Increasing the Si content reduces the hot-tearing susceptibility of the Al-2wt%Cu alloy considerably. This reduction is attributed to:
 - i) an increase in the volume fraction of eutectic which, in turn, enhances the fluidity and feedability of the liquid metal, and improves the capacity for crack healing in the alloy; and
 - ii) a decrease in the freezing range of the alloy caused by a depression in the liquidus temperature.

7. Strontium addition increases the hot-tearing susceptibility of the Al-2wt%Cu base alloy as result of:
 - i) the formation of Sr-oxide particles which may act as hot-tearing crack initiators;
 - ii) an augmentation of the porosity level; and
 - iii) an extension of the freezing range of the alloy.

8. The α -Fe intermetallic particles may act as obstacles to hot-tearing crack propagation through the liquid film during solidification, thus helping to enhance the resistance of the alloy to hot-tearing.

9. The parameters which determine the hot-tearing susceptibility (HTS) behavior of the Al-2wt%Cu base alloys are:
 - i) the contraction strain rate which is controlled by the mold temperature i.e., the cooling rate;

- ii) the eutectic fraction which is controlled by alloying elements such as Si and Cu;
- iii) the grain size and morphology, controlled by grain refining additions such as Zr-Ti or Ti; and
- iv) the presence of non-wetted inclusions which decrease the necessary driving force for hot-tearing crack initiation.

10. Based on theoretical considerations, the HTS value for the Al-2wt%Cu alloys may be expressed by the following mathematical relationship:

$$\text{HTS} = [\pm C_1 * (\text{CSR}) \pm C_2 * (\text{EF}) \pm C_3 * (\text{GS}) \pm C_4 (\text{size and vol. fraction of non-wetted inclusions})]$$

RECOMMENDATIONS FOR FUTURE WORK

1. The results of this study were obtained under controlled conditions using standard metallic molds in order to understand the parameters controlling the performance of this series of alloys. It is proposed that some castings should be carried out under industrial conditions, for example, the casting of cylinder heads by automotive castings suppliers. Such a process would assist in adapting the results obtained under laboratory conditions in the present study to real industrial settings, thereby enabling a proper transfer of technology.
2. One of the main criteria which control the alloy application is the role played by the alloying elements in preserving the tensile properties under high temperature service conditions. Therefore, it is suggested that a study should be undertaken to investigate this aspect in detail.
3. Another possible line of investigation could be to carry out transmission electron microscopic examination of the Zr- and Sc-containing Al-2%Cu alloys to understand the role of Al_3Zr and Al_3Sc on the precipitation hardening behavior and stability of GP zones.

REFERENCES

- 1 D. Jing-Zhi, H. Yu-Feng, C. Jun, "Effect of Sc and Zr on Microstructures and Mechanical Properties of As-Cast Al-Mg-Si-Mn Alloys," *Transactions of Nonferrous Metals Society of China*, 2009, Vol. 19, pp. 540-544.
- 2 Y. Yi-Cong, H. Liang-Ju, L. Pei-Jie, "Differences of Grain-Refining Effect of Sc and Ti additions in Aluminum by Empirical Electron Theory Analysis," *Transactions of Nonferrous Metals Society of China*, 2010, Vol. 20, pp. 465-470.
- 3 P. N. Raju, K. S. Rao, G. M. Reddy, M. Kamaraj, K. P. Rao, "Microstructure and High Temperature Stability of Age Hardenable AA2219 Aluminum Alloy Modified By Sc, Mg, and Zr Additions," *Materials Science and Engineering A*, 2007, Vol. 464, pp. 192-201.
- 4 A. K. Lohar, B. Mondal, D. Rafaja, V. Klemm, S. C. Panigrahi, "Microstructural Investigations on As-Cast and Annealed Al-Sc and Al-Sc-Zr Alloys," *Materials Characterization*, 2009, Vol. 60, pp.1387-1394.
- 5 L. Bäckerud, Guocai, J. Tamminen, *Solidification Characteristics of Aluminum Alloys*, Vol. 2, AFS/SKANALUMINUM, USA, 1990, p. 255.
- 6 N. Han, X. F. Bian, Z. K. Li, T. Muo, C. D. Wung, "Effect of Si on the Microstructure and Mechanical Properties of the Al-4.5%Cu Alloys," *Acta Metallurgica Sinica*, 2006, Vol. 19, pp. 405-410.
- 7 G. G. Garcia, J. E. Cuadra, H. M. Molinar, "Copper Content and Cooling Rate Effects over Effects Second Phase Particles Behavior in Industrial Aluminum-Silicon Alloy 319," *Materials and Design*, 2007, Vol. 28, pp. 428-433.
- 8 E. Rincon, H. F. Lopez, M. M. Cisneros, H. Mancha, M. A. Cisneros, "Effect of Temperature on the Tensile Properties of an As-Cast Aluminum Alloy A319," *Materials Science and Engineering A*, 2007, Vol. 452-453, pp. 682-687.
- 9 Z. Ma, A. M. Samuel, F. H. Samuel, H. W. Doty, S. Valtierra, "A Study of Tensile Properties in Al-Si-Cu and Al-Si-Mg Alloys: Effect of β -Iron Intermetallics and Porosity," *Materials Science and Engineering A*, 2008, Vol. 490, pp. 36-51.
- 10 P. N. Crepeau, "Effect of Iron in Al-Si Casting Alloys: A Critical Review," *AFS Transactions*, 1995, Vol. 110, pp. 361-366.

-
11. L. Lu, A. K. Dahle, "Iron-Rich Intermetallic Phases and Their Role in Casting Defect Formation in Hypoeutectic Al-Si Alloys," *Metallurgical and Materials Transactions A*, 2005, Vol. 36A, pp. 819-835.
 12. J. Y. Hwang, H. W. Doty, M. J. Kaufman, "The Effects of Mn Additions on the Microstructure and Mechanical Properties of Al-Si-Cu Casting Alloys," *Materials Science and Engineering A*, 2008, Vol. 488A, pp. 496-504.
 13. S. G. Shabestari, H. Momeni, "Effect of Copper and Solidification Conditions on the Microstructure and Mechanical Properties of Al-Si-Mg Alloys", *Journal of Materials Processing Technology*, 2004, Vol. 153-154, pp. 193-198.
 14. L. Ceschini, I. Boromei, A. Morri, S. Seifeddine, I. L. Svensson, "Microstructure, Tensile and Fatigue Properties of Al-10%Si-2%Cu Alloy with Different Fe and Mn Content Cast under Controlled Conditions," *Journal of Materials Processing Technology*, 2009, Vol. 209, pp. 5669-5679.
 15. D. Eskin, Q. Du, D. Ruvalcaba, L. Katgerman, "Experimental Study of Structure Formation in Binary Al-Cu Alloys at Different Cooling Rates," *Materials Science and Engineering A*, 2005, Vol. 405A, pp. 1-10.
 16. L. Y. Zhang, Y. H. Jiang, and W. K. Wang, "Effect of Cooling Rate on Solidified Microstructure and Mechanical Properties of Aluminum-A356 Alloy," *Journal of Materials Processing Technology*, 2008, Vol. 207, pp. 107-111.
 17. D. Argo, J. E. Gruzleski, "Porosity in Modified Aluminum Alloy Castings", *AFS Transactions*, 1988, Vol. 16, pp. 65-74.
 18. D. Emadi, J. E. Gruzleski, "Effects of Casting and Melt Variables on Porosity in Directionally-Solidified Al-Si Alloys," *AFS Transactions*, 1994, Vol. 95, pp. 307-312.
 19. ASM Handbook, *Properties and Selection: Nonferrous Alloys and Special-Purpose Materials*, L. A. Abel, R. T. Kieppura, P. Thomas, H. F. Lampman, N. D. Wheaton (Eds.), The Materials Information Society, 1990, Vol. 2, p. 1328
 20. J. E. Hatch, *Aluminum: Properties and Physical Metallurgy*, American Society for Metals, Materials Park, OH, 1984, p.135.
 21. A. M. Samuel, J. Gauthier, F. H. Samuel, "Microstructural Aspects of the Dissolution and Melting of Al₂Cu Phase in Al-Si Alloys during Heat Treatment," *Metallurgical and Materials Transactions A*, 1996, Vol. 27A, pp. 1785-1798.

-
22. F. H. Samuel, "Incipient melting of $\text{Al}_5\text{Mg}_8\text{Si}_6\text{Cu}_2$ and Al_2Cu intermetallics in unmodified and strontium-modified Al-Si-Cu-Mg (319) alloys during solution heat treatment," *Journal of Materials Science*, 1998, Vol. 33, pp. 2283 – 2297.
 23. O. Reiso, H.G. Øverlie, N. Ryum, "Dissolution and Melting of Secondary Al_2Cu Phase Particles in an Al-Cu Alloy," *Metallurgical Transactions A*, 1990, Vol. 21A, pp.1689-1695.
 24. D. O. Northwood, X. Sun, G. Byczynski, J. H. Sokolowski, "The development of A two-Stage Solution treatment for Cast Al-Si-Cu Alloys," *IMMA ADCA Conference Proceedings*, 1995, Vol. 4, pp.15-19.
 25. J. H. Sokolowski, X-C. Sun, A. Esseltine, "The Removal of Copper-Phase Segregation and the Subsequent Improvement in Mechanical Properties of Cast 319 Aluminum Alloys by a Two-Stage Solution Heat Treatment," *Journal of Materials Processing Technology*, 1995, Vol. 53, pp. 385-392.
 26. P. Shiang Wang, S. L. Lee, M. T. Jahn, "Effects of Solution Temperature on Mechanical Properties of 319.0 Aluminum Casting Alloys Containing Trace Beryllium," *Journal of Materials Research*, 2000, Vol. 15, pp. 2027-2035.
 27. D. Apelian, S. Shivkumar, G. Sigworth, "Fundamental Aspect of Heat Treatment of Cast Al-Si-Mg Alloys," *AFS Transactions*, Vol. 137, 1989, pp. 727-742.
 28. E. Tillova, M. Panuskova, "Effect of Solution Treatment on Intermetallic Phases Morphology in AlSi9Cu3 Cast Alloy," *Metallurgija*, 2008, Vol. 47, pp. 207-210.
 29. H. J. Li, S. ShivKumar, X. J. Luo, D. Apelian, "Influence of Modification on the Solution Heat-Treatment Response of Cast Al-Si-Mg Alloys," *Cast Metals*, 1989, Vol. 1, pp. 227-234.
 30. M. Tash, F. H. Samuel, F. Mucciardi, H. W. Doty, "Effect of Metallurgical Parameters on the Hardness and Microstructural Characterization of As-Cast and Heat-Treated 356 and 319 Aluminum Alloys," *Materials Science and Engineering A*, 2007, Vol. 443A, pp. 185-201.
 31. Z. Ma, A. M. Samuel, F. H. Samuel, H. W. Doty, and S. Valtierra, "A Study of Tensile Properties in Al-Si-Cu and Al-Si-Mg Alloys: Effect of β -iron Intermetallics and Porosity", *Materials Science and Engineering A*, 2008, Vol. 490, pp. 36-51.

-
32. T. O. Mbuya, B. O. Odera, "Influence of Iron on Castability and Properties of Aluminum Silicon Alloys: Literature Review," *International Journal of Cast Metals Research*, 2003, Vol. 16, pp. 451-465.
 33. J. G. Kaufman, E. L. Rooy, *Aluminum Alloy Castings: Properties, Processes and Applications*, ASM International, Materials Park, OH, 2004, p. 340.
 34. D. L. Zalenskas (Ed.), *Aluminum Casting Technology*, American Foundrymen's Society, Inc., Des Plaines, IL, 1993, p. 356.
 35. D. Steele, D. Evans, P. Nolan, D. J. Lloyd, "Quantification of Grain Boundary Precipitation and the Influence of Quench Rate in 6xxx Aluminum Alloys," *Materials Characterization*, 2007, Vol. 58, pp. 40-45.
 36. D. S. Mackenzie, "Design of Quench Systems for Aluminum Heat Treating: Part I-Quenchant Selection," *Industrial Heating*, 2006, Vol. 73, pp. 53-57.
 37. G. E. Byczynski, W. Kierkus, D. O. Northwood, D. Penrod, J. H. Sokolowski, R. Thomas, "The Effect of Quench Rate on Mechanical Properties of 319 Aluminum Alloy Castings," *Materials Science Forum*, 1996, Vol. 217, pp. 783-788.
 38. T. Gladman, "Precipitation Hardening in Metals," *Materials Science and Technology*, 1999, Vol. 15, pp. 1421-1426.
 39. J. W. Martin, *Precipitation Hardening*, Butterworth-Heinemann, Oxford, England, 1998, p. 215.
 40. A. Kelly, R. B. Nicholson, "Precipitation Hardening," *Progress in Materials Science*, 1963, Vol. 10, pp. 149-173.
 41. R. E. Smallman, A. H. W. Ngan, *Physical Metallurgy and Advanced Materials*, Butterworth-Heinemann, Oxford, England, 2007, p. 650.
 42. S. P. Ringer, B. T. Sofyan, K. S. Prasad, G. C. Quan, "Precipitation Reactions in Al-4Cu-0.3Mg (wt.%) Alloy," *Acta Materialia*, 2008, Vol. 56, pp. 2147-2160.
 43. G. E. Totten, and D. S. Mackenzie (Eds), *Handbook of Aluminum*, Marcel Dekker, Inc., New York, Basel, 2003, p. 1296.
 44. H. Sehitoglu, T. Foglesong, H.J. Maier, "Precipitation Effects on the Mechanical Behaviour of Aluminum Copper Alloys: Part I. Experiments," *Metallurgical and Materials Transactions A*, 2005, Vol. 36A, pp. 749-761.

45. R. N. Lumley, J. Buha, I.J. Polmear, A.J. Morton, A.G. Crosky, "Secondary Precipitation in Aluminum Alloys & Its Role in Modern Heat Treatment," *Materials Science Forum*, 2006, Vol. 519, pp. 283-290.
46. J. Y. Yao, Geoffrey A., Edwards, Daniel A. Graham, "Precipitation and Age-Hardening in Al-Si-Cu-Mg-Fe Casting Alloys," *Materials Science Forum*, 1996, Vol. 217-222, pp. 777-782.
47. W. Reif, S. Yu, I. Dutkiewicz, R. Ciach, I. Krol, "Pre-aging of AlSiCuMg Alloys in Relation to Structure and Mechanical Properties," *Materials & Design*, 1997, Vol. 18, pp. 253-256.
48. J. Buha, R. N. Lumley, A. G. Crosky, "Microstructural Development and Mechanical Properties of Interrupted Aged Al-Mg-Si-Cu Alloy," *Metallurgical and Materials Transactions A*, 2006, Vol. 37A, pp. 3119-3129.
49. G. A. Edwards, K. Stiller, G. L., Dunlop, and M. J. Couper, "The precipitation Sequence in Al-Mg-Si Alloys", *Acta Mater.*, 1998, Vol. 46, pp. 3893-3904.
50. S. Abis, M. Massazza, P. Mengucci, G. Riontino, "Early Aging Mechanisms in a High-Copper AlCuMg Alloy," *Scripta Materialia*, 2001, Vol. 45, pp. 685-691.
51. P. Ratchev, B. Verlinden, P. Van Houtte, "S' Phase Precipitation in Al-4wt.%Mg-1 wt% Cu Alloy," *Scripta Metallurgica et Materialia*, 1994, Vol. 30, pp. 599-604.
52. C. R. Hutchinson, S. P. Ringer, "Precipitation Processes in Al-Cu-Mg Alloys Microalloyed with Si," *Metallurgical and Materials Transactions A*, 2000, Vol. 31A, pp. 2721-2733.
53. C. Cayron, P. A. Buffat, "Transmission Electron Microscopy Study of The β' Phase (Al-Mg-Si Alloys): Ordering Mechanism and Crystallographic Structure," *Acta Materialia.*, 2000, Vol. 48, pp. 2639-2653.
54. K. Matsuda, D. Teguri, T. Sato, S. Ikeno, "EFTEM Observation of Q' Phase in Al-Mg-Si-Cu Alloy," *Materials Science Forum*, 2002, Vol. 396-402, pp. 947-952.
55. J. Y. Hwang, R. Banerjee, H. W. Doty, M. J. Kaufman, "The Effect of Mg on the Structure and Properties of Type 319 Aluminum Casting Alloys," *Acta Materialia*, 2009, Vol. 57, pp. 1308-1317.
56. G. Wang, Q. Sun, L. Feng, L. Hui, C. Jing, "Influence of Cu Content on Aging Behavior of AlSiMgCu Cast Alloys," *Materials and Design*, 2007, Vol. 28, pp. 1001-1005.

-
57. Y. J. Li, S. Brusethaug, A. Oslen, "Influence of Cu on the Mechanical Properties and Precipitation Behavior of AlSi7Mg0.5 Alloy During Aging Treatment," *Scripta Materialia*, 2006, Vol. 54, pp. 99-103.
 58. D. G. Eskin, "Decomposition of Supersaturated Solid Solution in Al-Cu-Mg-Si Alloys," *Journal of Materials Science*, 2003, Vol. 38, pp. 279-290.
 59. G. K. Sigworth, J. F. Major, "Factors Influencing the Mechanical Properties of B206 Alloy Castings," *Light Metals 2006*, T. J. Galloway (Ed.), The Minerals, Metals & Materials Society, 2006, Vol. 4, pp. 795-799.
 60. J. Gauthier, P. R. Louchez, F. H. Samuel, "Heat Treatment of 319.2 Aluminum Automotive Alloy: Part 2, Aging Behaviour," *Cast Metals*, 1995, Vol. 8, pp. 107-114.
 61. M. Zeren, "Effect of Copper and Silicon Content on Mechanical Properties in Al-Cu-Si-Mg Alloy," *Journal of Materials Processing Technology*, 2005, Vol. 169, pp.292-298.
 62. D. H. Xiao, J. Wang, D. Y. Ding, S. P. Chen, "Effect of Cu Content on the Mechanical Properties of an Al-Cu-Mg-Ag Alloys," *Journal of Alloys and Compounds*, 2002, Vol. 343, pp. 77-81.
 63. Y. S. Kuo, B. C. Wang, E. Chang, "The Influence of Ag on the Mechanical Properties of A201 Aluminum Alloy," *AFS Transactions*, 1988, Vol. 154, pp. 725-726.
 64. L. Reich, M. Murayama, K. Hono, "Evolution of Ω Phase in an Al-Cu-Mg-Ag Alloy-A Three-Dimensional Atom Probe Study," *Acta Materialia*, 1998, Vol. 46, pp. 6053-6062.
 65. B. M. Gable, G. J. Shiflet, E. A. Starke, "Alloy Development for the Enhanced Stability of Ω Precipitates in AL-Cu-Mg-Ag Alloys," *Metallurgical and Materials Transactions A*, 2006, Vol. 37A, pp. 1091-1105.
 66. A. K. Mukhopadhyay, G. Eggeler, B. Skrotzki, "Nucleation of Ω Phase in an Al-Cu-Mg-Mn-Ag Alloy Aged at Temperatures Below 200°C," *Scripta Materialia*, 2001, Vol. 44, pp. 545-551.
 67. N. A. Belov, A. N. Alabin, D. G. Eskin, V. V. Istomin-Kastrovskii, "Optimization of Hardening of Al-Zr-Sc Cast Alloys," *Journal of Matierals Science*, 2006, Vol. 41, pp. 5890-5899.

-
68. D. Srinivasan, K. Chattopadhyay, "Non-equilibrium Transformations Involving L₁₂-Al₃Zr in Ternary Al-X-Zr Alloys," *Metallurgical and Materials Transactions A*, 2005, Vol. 36A, pp. 311-320.
 69. P. Cavaliere, "Effect of Friction Stir Processing on the Fatigue Properties of a Zr-Modified 2014 Aluminum Alloy," *Materials Characterization*, 2006, Vol. 57, pp. 100-104.
 70. B. Forbord, H. Hallem, K. Marthinsen, "The Effect of Alloying Elements on Precipitation and Recrystallisation in Al-Zr Alloys," *Proceedings of the 9th International Conference on Aluminum Alloys*, Brisbane Australia, 2004, pp 1179-1185.
 71. Z. Jia, G. Hu, "Effect of Homogenization and Alloying Elements on Resistance of Al-Zr-Mn Alloys," *Materials Science and Engineering A*, 2007, Vol. 444A, pp.284-290.
 72. P. Sepehrband, R. Mahmudi, F. Khomamizadeh, "Effect of Zr Addition on the Aging Behavior of A319 Aluminum Cast Alloy," *Scripta Materialia*, 2005, Vol. 52, pp. 253-257.
 73. J. D. Robson P. B. Prangnell, "Dispersoid Precipitation and Process Modelling in Zirconium Containing Commercial Aluminum Alloys," *Acta Materialia*, 2001, Vol. 49, pp. 599-613.
 74. J. D. Robson, "Optimizing the Homogenization of Zirconium Containing Commercial Aluminum Alloys Using a Novel Process Model," *Materials Science and Engineering A*, 2002, Vol. 338A, pp. 219-229.
 75. N. A. Belov, D. G. Eskin, A. A. Aksenov, *Multicomponent Phase Diagrams: Application for Commercial Aluminum Alloys*, Elsevier, Boston, 2005, p. 413.
 76. L. S. Toropova, D. G. Eskin, M. L. Kharaktrova T. V. Dobakina, *Advanced Aluminum Alloys Containing Scandium: Structure and Properties*, Gordon and Breach Science Publishers, Canada, 1998, p. 175.
 77. J. Royset, N. Ryum, "Scandium in Aluminum Alloys," *International Materials Reviews*, 2005, Vol. 50, pp. 19-44.
 78. A. F. Norman, P. B. Prangnell, R. S. McEwen, "The Solidification Behaviour of Dilute Aluminum-Scandium Alloys," *Acta Materialia*, 1998, Vol. 46, pp. 5715-5732.

-
79. A. A. Rao, B. S. Murty, M. Chakraborty, "Role of Zirconium and Impurities in Grain Refinement of Aluminum with Al-Ti-B", *Materials Science and Technology*, 1997, Vol. 13, pp. 769-777.
 80. D. N. Seidman, E. A. Marquis, D. C. Dunand, "Precipitation Strengthening at Ambient and Elevated Temperatures of Heat-Treatable Al(Sc) Alloys," *Acta Materialia*, 2002, Vol. 50, pp. 4021-4035.
 81. V. G. Davydov, T. D. Rostova, V. I. Yelagin, "Scientific Principles of Making an Alloying Addition of Scandium to Aluminum Alloys," *Materials Science and Engineering A*, 2000, Vol. 280A, pp. 30-36.
 82. S. Iwamura, Y. Miura, "Loss in Coherency and Coarsening Behaviour of Al₃Sc Precipitates," *Acta Materialia*, Vol. 52, 2004, pp. 591-600.
 83. E. A. Marquis, and D. N. Seidman, "Nanoscale Structural Evolution of Al₃Sc Precipitates in Al(Sc) Alloys," *Acta Materialia*, 2001, Vol. 49, pp. 1909-1919.
 84. V. V. Zakharov, "Effect of Scandium on the Structure and Properties of Aluminum Alloys," *Metal Science and Heat Treatment*, 2003, Vol. 45, pp. 246-253.
 85. K. B. Hyde, A. F. Norman, P. B. Prangnell, "The Effect of Cooling Rate on the Morphology of Primary Al₃Sc Intermetallic Particles in Al-Sc Alloy," *Acta Materialia*, Vol. 49, pp. 1327-1337.
 86. O. N. Senkov, M. R. Shagiev, S. V. Senkova, D. B. Miracle, "Precipitation of Al₃(Sc,Zr) Particles in an Al-Zn-Mg-Cu-Sc-Zr Alloy during Conventional Heat Treatment and its Effect on Tensile Properties," *Acta Materialia*, 2008, Vol. 56, pp. 3723-3738.
 87. C. B. Fuller, J. L. Murray, D. N. Seidman, "Temporal Evolution of the Nanostructure of Al(Sc,Zr) Alloys: Part I-Chemical Compositions of Al₃(Sc_{1-x}Zr_x) Precipitates," *Acta Materialia*, 2005, Vol. 53, pp. 5401-5413.
 88. E. Clouet, M. Nastar, A. Barbu, C. Sigli, G. Martin, "Precipitation in Al-Zr-Sc Alloys: a Comparison between Kinetic Monte Carlo, Cluster Dynamics and Classical Nucleation Theory," *In Solid-Solid Phase Transformations in Inorganic Materials*, The Minerals, Metals & Materials Society, Warrendale, PA, 2005, pp. 1-21.
 89. B. Forbord, W. Lefebvre, F. Danoix, H. Hallem, K. Marthinsen, "Three Dimensional Atom Probe Investigation on the Formation of Al₃(Sc,Zr)-Dispersoids in Aluminum Alloys," *Acta Materialia*, 2004, Vol. 51, pp. 333-337.

-
90. M. S. Kaiser, M. K. Banerjee, "Effect of Ternary Scandium and Quaternary Zirconium and Titanium Additions on the Tensile and Precipitation Properties of Binary Cast Al-6Mg Alloys," *Jordan Journal of Mechanical and Industrial Engineering*, 2008, Vol. 2, pp. 93-99.
 91. Y. Li, Z. Liu, Q. Xia, Y. Liu, "Grain Refinement of the Al-Cu-Mg-Ag Alloy with Er and Sc Additions," *Metallurgical and Materials Transactions A*, 2007, Vol. 38A, pp. 2853-2858.
 92. J. Campbell, *The New Metallurgy of Cast Metals: Castings*, Butterworth-Heinemann, Second Edition, Oxford, 2003, pp. 232-258.
 93. Briggs, *The Metallurgy of Steel Casting*, McGraw-Hill Book Company, New York, 1956, p.317.
 94. D.G. Eskin L. Katgerman, "A Quest for a New Hot Tearing Criterion," *Metallurgical and Materials Transactions A*, 2007, Vol. 38A, pp. 1511-1519.
 95. D. G. Eskin, Suyitno, L. Katgerman, in *Aluminum Cast, House Technology 2005*, Proc. 9th Australasian Conf., J. Taylor, I. Bainbridge, and J. Granfield (Eds.), CSIRO Publishing, Collingwood, 2005, pp. 77-84.
 96. T. W. Clyne, G. J. Davies, "Comparison between Experimental Data and Theoretical Predictions Relating to Dependence of Solidification Cracking on Composition," *Solidification and Casting of Metals*, Proc. Int. Conf., University of Sheffield, 1977, pp. 275-278.
 97. X. Yan, J. C. Lin, "Prediction of Hot Tearing Tendency for Multicomponent Aluminum Alloys," *Metallurgical and Materials Transactions B*, 2006, Vol. 37B, pp. 913-918.
 98. Suyitno, D.G. Eskin, V.I. Savran, L. Katgerman, "Effects of Alloy Composition and Casting Speed on Structure Formation and Hot Tearing During Direct Chill Casting of Al-Cu Alloys," *Metallurgical and Materials Transactions A*, 2004, Vol. 35A, pp. 3551-3561.
 99. D. Viano, D. StJohn, J. Grandfield, C. Cáceres, "Hot Tearing in Aluminum-Copper Alloys," *Light Metals: Proceedings of the Technical Sessions Presented by TMS Aluminum Committee at 134th Annual Meeting*, 2005, pp. 1069-1073.
 100. Y. F. Guven, J. D. Hunt, "Hot Tearing in Aluminum Copper Alloys," *Cast Metals*, 1988, Vol. 1, pp. 104-111.

-
101. A. Chojecki, I. Telejko, T. Bogacz, "Influence of Chemical Composition on the Hot Tearing Formation of Cast Steel," *Theoretical and Applied Fracture Mechanics*, 1997, Vol. 27, pp. 99-105.
 102. D. G. Eskin, Suyitno, J. F. Mooney, L. Katgerman, "Contraction of Aluminum Alloys During and After Solidification", *Metallurgical and Materials Transactions A*, 2004, Vol. 35A, pp. 1325-1335.
 103. J. A. Spittle, A. A. Cushway, "Influences of Superheat and Grain Structure on Hot Tearing Susceptibilities of Al-Cu Alloy Castings," *Metals Technology*, 1983, Vol. 10, pp. 6-13.
 104. A. R. E. Singer, P. H. Jennings, "Hot Shortness of the Aluminum Silicon Alloys of Commercial Purity," *Journal of the Institute of Metals*, 1947, Vol. 73, pp. 197-212.
 105. P. H. Jennings, A. R. E. Singer, "Hot Shortness of Some High Purity Alloys in the Systems Aluminum-Magnesium-Silicon," *Journal of the Institute of Metals*, 1947, Vol. 74, pp. 227-748.
 106. K. T. Kim, J. M. Kim, K. D. Sung, "Effect of Alloying Elements on the Strength and Casting Characteristics of High Strength Al-Zn-Mg-Cu Alloys." *Materials Science Forum*, 2005, Vols. 475-479, pp. 2539-2542.
 107. W. B. Kim, C. R. Loper, "Effect of Casting Conditions and Grain Refinement on Hot Tearing Behavior in A356 Al Alloy," *AFS Transactions*, 2000, Vol. 108, pp. 541-546.
 108. S. A. Metz, M. C. Flemings, "A Fundamental Study of Hot Tearing," *AFS Transactions*, 1970, Vol. 78, pp. 453-460.
 109. S. Lin, C. Aliravci, M. O. Pekguleryuz, "Hot Tear Susceptibility of Aluminum Wrought Alloys and the Effect of Grain Refining," *Metallurgical and Materials Transactions A*, 2007, Vol. 38A, pp. 1056-1068.
 110. L. Lu, A. K. Dahle, D. StJohn, "Hot Tearing of Al-Si Alloys," *Light Metals: Proceedings of the Technical Sessions Presented by TMS Aluminum Committee at 136th Annual Meeting*, The Minerals, Metals and Materials Society, Warrendale, PA 2007, pp. 721-726.
 111. D. C. G. Lees, "The Hot Tearing Tendencies of Aluminum Casting Alloys," *Journal of the Institute of Metals*, 1946, Vol. 72, pp. 343-364.

-
112. D. Warrington D. G. McCartney, "Hot Cracking in Aluminum Alloys 7050 and 7010 a Comparative Study," *Cast Metals*, 1991, Vol. 3, pp.202-208.
 113. T. Sumitomo, D. H. StJohn, T. Steinberg, "The Shear Behavior of Partially Solidified Al-Si-Cu Alloys," *Materials Science and Engineering A*, 2000, Vol. 289A, pp. 18-29.
 114. T. W. Clyne, G. J. Davies, "A Quantitative Solidification Test for Casting and an Evaluation of Cracking in Aluminum-Magnesium Alloys," *The British Foundryman*, 1975, Vol. 68, pp. 238-249.
 115. D. G. Eskin, V. I Savran, L. Katgerman, "Effects of Melt Temperature and Casting Speed on the Structure and Defect Formation during Direct-Chill Casting of an Al-Cu Alloy," *Metallurgical and Materials Transactions A*, 2005, Vol. 36A, pp. 1965-1976.
 116. S. Li, D. Apelian, "Hot Tearing in Cast Al Alloys: Measures and Effect of Process Variables," CANMET Materials Technology Laboratory, May 20th, 2008, Report No. 08-01, pp. 1-40.
 117. C. Limmaneevichitr, A. Saisiang, S. Chanpum, "The Role of Grain Refinement on Hot Crack Susceptibility of Aluminum Alloy Permanent Mold Castings," *Proceedings of the 65th World Foundry Congress*, Gyeongju, Korea 2002, pp.220-227
 118. D. C. G. Lees, "Note on the Effect of Dissolved Gas on the Hot-Tearing of Aluminum Casting Alloys," *Journal of the Institute of Metals*, 1947, Vol. 14, pp. 537-540.
 119. J. H. Andrew, H. T. Protheroe, "Investigation of the Influence of Mould Friction on Tearing in Castings," *Journal of Iron and Steel Institute*, 1942, Vol. 145, pp. 101-109.
 120. R. N. Parkins, A. Cowan, "Effects of Mold Resistance on Internal Stress in Sand Castings," *Foundry Trade Journal*, 1953, Vol. 95, pp. 105-111.
 121. W. S. Pellini, "Strain Theory of Hot Tearing," *Foundry*, 1952, Vol. 80, pp. 125-199.
 122. W. S. Pellini, H. F. Bishop, C. G. Ackerlind, "Metallurgy and Mechanics of Hot Tearing," *Transactions of the American Foundrymen's Society*, 1952, Vol. 60, pp. 818-833.
 123. D. G. Eskin, Suyitno, L. Katgerman, "Mechanical properties in the semi-solid state and hot tearing of aluminum alloys," *Progress in Materials Science*, 2004, Vol. 49, pp. 629-711.

-
124. J. C. Borland, "Generalized Theory of Super-Solidus Cracking in Welds and Casting," *British Welding Journal*, 1960, Vol. 7, pp. 508-512.
 125. A. Norton, "Hot Shortness Testing Machine for Aluminum Alloys," *Transactions of the American Society of Mechanical Engineers.*, 1914, Vol. 8, p. 124
 126. Archbutt, Grogan, Jenkin, "Properties and Production of Aluminum Alloy Die Castings," *Journal of the Institute of Metals*, 1928, Vol. 40, P. 219.
 127. J. Vero, "The Hot shortness of Aluminum Alloys," *The Metal Industry*, 1936, Vol. 48, pp. 431-442.
 128. A. R. E. Singer S. A. Cottrell, "Properties of the Al-Si Alloys at Temperatures in the Region of the Solidus," *Journal of the Institute of Metals*, 1946, Vol. 73, pp. 33-54.
 129. C. S. Smith, "Grains, Phases and Interfaces: An Interpretation of Microstructure," *Transactions. TMS-AIME*, 1948, Vol. 175, pp. 15-51.
 130. H. Fredriksson B. Lehtinen, "Continuous Observation of Hot Crack Formation During Deformation and Heating in SEM," *Solidification and Casting of Metals*; Proc. Int. Conference, University of Sheffield, 1977, pp. 260-267.
 131. M. J. Kelly N. S. Stoloff, "Analysis of Liquid Metal Embrittlement from a Bond Energy Viewpoint," *Metallurgical and Materials Transactions A*, 1975, Vol. 6A, pp. 159-166
 132. R. G. Roth, G. C. Weatherly, W. A. Miller, "The Temperature Dependence of the Mechanical Properties of Aluminum Alloys Containing Low Melting Point Inclusions," *Acta Materialia.*, 1980, Vol. 26, pp. 841-853.
 133. G. Cao, and S. Kou, "Hot Cracking of Binary Mg-Al Alloy Castings", *Materials Science and Engineering A*, 2006, Vol. 417, pp. 230-238.
 134. C. H. Cáceres, B. Johannesson, J. A. Taylor, A. Canales-Nuñez, M. Cardoso, J. Talamantes, "The Effect of Si Content on the Size and Morphology of Fe-Rich and Cu-Rich Intermetallics in Al-Si-Cu-Mg Alloys," P. N. Crepeau, M. Tiryakioğlu, and J. Campbell (Eds.), *Shape Casting: 2nd International Symposium*, The Minerals, Metals & Materials Society, 2007, pp.1-7.
 135. J. A. Taylor, "The Effect of Iron in Al-Si Casting Alloys," <http://www.aomevents.com/conferences/afi/papers/Taylor.pdf>.

-
136. A. Couture, "Iron in Aluminum Casting Alloys - A Literature Survey," *AFS International Cast Metals Journal*, 1981, Vol. 67, pp. 9-17.
137. S. Seifeddine, "The Influence of Iron and Mn Content on the Microstructure and Tensile Properties of Cast Al-Si-Mg-Alloys," *Vikteffektiva lättmetallstrukturer*, Report 23, [http://www.simr.se/hemsida/PROJEKT/Vikteffektiva.nsf/28eca27ed1db5bb6c1256a2500292c45/8f053b177edf460fc12573c4004297b9/\\$FILE/Vilmer%20Rapport%2023.pdf](http://www.simr.se/hemsida/PROJEKT/Vikteffektiva.nsf/28eca27ed1db5bb6c1256a2500292c45/8f053b177edf460fc12573c4004297b9/$FILE/Vilmer%20Rapport%2023.pdf), pp. 1-13.
138. F. Zeng, C. Xia, Y. Gu, "The 430°C Isothermal Section of the Al-4Mg-Sc-Zr Quaternary System in the Al-rich Range," *Journal of Alloys and Compounds*, 2004, Vol. 363, pp. 175-181.
139. K. Yu, W. Li, S. Li, J. Zhao, "Mechanical Properties and Microstructure of Aluminum Alloy 2618 with Al₃(Sc,Zr) Phases," *Materials Science and Engineering A*, 2004, Vol. 368, pp. 88-93.
140. Z. Liu, Z. Li, M. Wang, Y. Weng, "Effect of Complex Alloying of Sc, Zr and Ti on the Microstructure and Mechanical Properties of Al-5Mg Alloys," *Materials Science and Engineering A*, 2008, Vol. 483A, pp. 120-122.
141. Z. Yin, Q. Pan, "Effect of Minor Sc and Zr Additions on the Microstructure and Mechanical Properties of Al-Mg Based Alloys," *Materials Science and Engineering A*, Vol. 280A, 2000, pp. 151-155.
142. Y. Li, Z. Liu, "Grain Refinement of the Al-Cu-Mg-Ag Alloy with Er and Sc Additions," *Metallurgical and Materials Transactions A*, Vol. 38A, 2007, pp. 2853-2858.
143. L. L. Rokhlin, T. V. Dobatkina, "Structure of the Phase Equilibrium Diagrams of Aluminum Alloys with Scandium," *Powder Metallurgy of Metal Ceramics*, Vol. 36, 2007, pp. 128-132.
144. O. N. Senkov, R. B. Bhat, S. V. Senkova, J. D. Schiloz, "Microstructure and Properties of Cast Ingots of Al-Zn-Mg-Cu Alloys Modified with Sc and Zr," *Metallurgical and Materials Transactions A*, 2005, Vol. 36A, pp. 2115-2126.
145. V.V. Zakharov, "Effect of Scandium on the Structure and Properties of Aluminum Alloys," *Metal Science and Heat Treatment*, Vol. 45, 2003, pp. 246-253.

-
146. K. B. Hyde, A. F. Norman, "The Effect of Cooling Rate on the Morphology of Primary Al_3Sc Intermetallic Particles in Al-Sc Alloy," *Acta Materialia*, Vol. 49, 2001, pp. 1327-1337.
 147. H. Yong-dong, Z. Xin-ming, "Effect of Minor Sc and Zr on Microstructure and Mechanical Properties of Al-Zn-Mg-Cu Alloy," *Transactions of Nonferrous Metals Society of China*, Vol. 16, 2006, pp. 1228-1235.
 148. Røyset, N. Ryum, "Scandium in Aluminum Alloys," *International Materials Reviews*, Vol. 50, 2005, pp. 19-44.
 149. M. L. Kharakterova, D. G. Eskin, "Precipitation Hardening in Ternary Alloys of the Al-Sc-Cu and Al-Sc-Si Systems," *Acta Metallurgica Materialia*, Vol. 42, 1994, pp. 2285-2290.
 150. M. L. Kharakterova, D. G. Eskin, "Effect of Scandium and Zirconium on Structure and Age Hardening of the Al-Mg-Si Alloys," *Russian Metallurgy (Metally)*, No. 1, 1997, pp. 104-109.
 151. H. G. Paris, T. H. Sanders, "Assessment of Scandium Additions in Aluminum Alloy Design," *Proceedings of ICAA-6: Aluminum Alloys*, Vol. 1, Georgia Institute of Technology, Atlanta 1998, pp. 489-504.
 152. D. Srinivasan, K. Chattopadhyay, "Non-equilibrium Transformations Involving $L1_2$ - Al_3Zr in Ternary Al-X-Zr Alloys," *Metallurgical and Materials Transactions A*, 2005, Vol. 36A, pp. 311-320.
 153. M. Easton, D. StJohn, "Grain Refinement of Aluminum Alloys: Part I. The Nucleant and Solute Paradigms - a Review of the Literature," *Metallurgical and Materials Transactions A*, 1999, Vol. 30A, pp. 1613-1623.
 154. K. T. Kashyap, T. Chandrashekar, "Effects and Mechanisms of Grain Refinement in Aluminum Alloys," *Bulletin of Materials Science*, Indian Academy of Sciences, 2001, Vol. 24, pp.345-353.
 155. M. Johnsson, "Grain Refinement of Aluminum Studied by Use of a Thermal Analytical Technique," *Thermochimica Acta*, 1995, pp. 107-121.
 156. A. F. Norman, P. B. Prangell, R. S. McEwen, "The Solidification Behaviour of Dilute Aluminum-Scandium Alloys," *Acta Materialia*, 1998, Vol. 46, pp. 5715-5732.

-
157. S. M. Miresnaeil, J. Campbell, S. G. Shabestari, S. M. A. Boutorabi, "Precipitation of Sr-Rich Intermetallic Particles and their Influence on Pore Formation in Sr-Modified A356 Alloy," *Metallurgical and Materials Transactions A*, 2005, Vol. 36A, pp. 2341-2349.
 158. L. Liu, A. M. Samuel, F. H. Samuel, H. W. Doty, S. Valtierra, "Influence of Oxides on Porosity Formation in Sr-Treated Al-Si Casting Alloys," *Journal of Materials Science*, 2003, Vol. 38, pp. 1255-1267.
 159. R. Raiszadeh, W. D. Griffiths, "A Method to Study the History of a Double Oxide Film Defect in Liquid Aluminum Alloys," *Metallurgical and Materials Transactions B*, 2006, Vol. 37B, pp. 865-871.
 160. P. S. Mohanty, J. E. Gruzleski, "Grain Refinement Mechanisms of Hypoeutectic Al-Si Alloys," *Acta Materialia*, 1995, Vol. 44, pp. 3749-3760.
 161. G. K. Sigworth, "Grain Refining of Aluminum Casting Alloys," *AFS Transactions*, 2001, Vol. 109, pp. 1-12.
 162. T. Sritharan, H. Li, "Influence of Titanium to Boron Ratio on the Ability to Grain Refine Aluminum-Silicon Alloys," *Journal of Materials Processing Technology*, 1997, Vol. 63, pp. 585-589.
 163. C. Limmaneevichitr, W. Eidhed, "Fading Mechanism of Grain Refinement of Aluminum-Silicon Alloy with Al-Ti-B Grain Refiners," *Materials Science and Engineering A*, 2003, Vol. 349A, pp. 197-206.
 164. H. Liao, G. Sun, "Mutual Poisoning Effect between Sr and B in Al-Si Casting Alloys," *Scripta Materialia*, 2003, Vol. 48, pp. 1035-1039.
 165. L. Lu, A. K. Dahle, "Effects of Combined Additions of Sr and AlTiB Grain Refiners in Hypoeutectic Al-Si Foundry Alloys," *Materials Science and Engineering A*, 2006, Vol. 435-436A, pp. 288-296.
 166. J. Hutt, M. Easton, L. Hogan, D. H. StJohn, "The effect of nucleant particles and alloy chemistry on the grain structure of aluminium castings," *Solidification Processing*, 1997, Sheffield, England, pp. 268-272.
 167. C. H. Cáceres, I. L. Svensson, J. A. Taylor, "Strength-Ductility Behaviour of Al-Si-Cu-Mg Casting Alloys in T6 Temper," *International Journal of Cast Metals Research*, 2003, Vol. 15, no. 5, pp. 531-543

-
168. C. H. Cáceres , J. A. Taylor (2005). "Enhanced ductility in Al-Si-Cu-Mg casting alloys with high Si content,". *Shape Casting: The John Campbell Symposium (134th TMS Annual Meeting & Exhibition)*, TMS, 13-17 Feb 2005, San Francisco (USA), pp. 245-25.
 169. F. H. Samuel, P. Ouellet, A. M. Samuel, H. W. Doty, "Effect of Mg and Sr Additions on the Formation of Intermetallics in Al-6 Wt Pct Si-3.5 Wt Pct Cu-(0.45) to (0.8) Wt Pct Fe 319-Type Alloys," *Metallurgical and Materials Transactions A*, 1998, Vol. 29A, pp. 2871-2884.
 170. M. Djurdjevic, T. Stockwell, J. Sokolowski, "Effect of Strontium on Microstructure of Al-Si and Al-Cu Eutectics in 319 Aluminum Alloy," *International Journal of Cast Metals Research*, 1999, Vol. 12, pp. 67-73.
 171. S. D. McDonald, "Eutectic Solidification and Porosity Formation in Unmodified Hypoeutectic Al-Si Alloys," Ph.D. Thesis, University of Queensland, Brisbane, Australia, 2002.
 172. G. K. Sigworth, "The Modification of Al-Si Casting Alloys: Important Practical and Theoretical Aspects," *International Journal of Metalcasting*, 2008, Vol. 2, pp. 19-40.
 173. R. Nadella, D. G. Eskin, Q. Du, L. Katgerman, "Macrosegregation in Direct-Chill Casting of Aluminum Alloys," *Progress in Materials Science*, 2008, Vol. 53, pp. 421-480.
 174. A. K. Dahle, "Eutectic nucleation and growth in hypoeutectic Al-Si alloys at different strontium levels", *Metallurgical and Materials Transactions A*, 2001, Vol. 32A, pp. 949-960.
 175. K. Dahle, J. Hjelen, L. Arnberg, "Formation of Eutectic in Hypoeutectic Al-Si Alloys," *Proc. 4th Decennial Int. Conf. on Solidification Processing*, 1997, University of Sheffield, Sheffield ,uk, pp. 527-530.
 176. L. Liu, A. M. Samuel, F. H. Samuel, H. W. Doty, S. Valtierra, "Role of Strontium Oxide on Porosity Formation in Al-Si Casting Alloys," *AFS Transactions*, 2002, Vol. 139, pp. 449-462.
 177. C. M. Dinnis, M. O. Oti. A. K. Dahle, J. A. Taylor, "The Influence of Strontium on Porosity Formation in Al-Si Alloys," *Metallurgical and Materials Transactions A*, 2004, Vol. 35, pp. 3531-3541.

-
- 178 W. Li, S Cui, J. Han, C. Xu, "Effect of Silicon on the Casting Properties of Al-5.0%Cu Alloy," *Rare Metals*, 2006, Vol. 25, pp. 133-135.
- 179 K. R. Ravi, R. M. Pillai, K. R. Amaranathan, B. C. Pai, M. Chakraborty, "Fluidity of Aluminum Alloys and Composites: A Review," *Journal of Alloys and Compounds*, 2008, Vol. 456, pp. 201-210.
180. F. H. Samuel, A. M. Samuel, H.W. Doty, S. Valtierra, "Decomposition of Fe-Intermetallics in Sr-Modified Cast 6xxx type Aluminum Alloys for Automotive Skin," *Metallurgical and Materials Transactions A*, 2001, Vol. 32A, pp. 2061-2075.
- 181 J. Guo, "Use of the Ultrasonic Technique in Measuring Inclusions in Al-Si Alloy Melts," M. Eng. Thesis, UQAC, 2007, p.106.
182. Q. G. Wang, "Microstructural Effects on the Tensile and Fracture Behavior of Aluminum Casting Alloys A356/357," *Metallurgical and Materials Transactions A*, 2003, Vol. 34A, pp. 2887-2891.
183. K. Lee, Y. N. Kwon, S. Lee, "Effects of Eutectic Silicon Particles on Tensile Properties and Fracture Toughness of A356 Aluminum Alloys Fabricated by Low-Pressure-Casting, Casting-Forging, and Squeeze-Casting Processes," *Journal of Alloys and Compounds*, 2008, Vol. 461, pp. 532-541.
- 184 G. E. Dieter, *Mechanical Metallurgy*, Third Ed., McGraw-Hill, Boston, 1986, p.751.
185. M. H. Tosten, P. R. Howell, "The Early Stages of Aging in an Al-3%Cu-2%Li-0.12% Zr Alloy," in *Aluminum Alloys - Physical and Tensile Properties, EMAS*, 1986, Vol. 2, pp. 727-741.
186. C. N. J. Tite, P. J. Gregson, "Further Precipitation Reactions Associated with β' in Al-Li-Cu-Mg-Zr Alloys," *Scripta Metallurgica*, 1988, Vol. 22, pp. 1005-1010.
187. S. Özbilen, H.M. Flower, " Zirconium-Vacancy Binding and Its Influence on S'-Precipitation in an Al-Cu-Mg Alloy," *Acta Metallurgica*, 1989, Vol. 37, pp. 2993-3000.
188. S. P. Ringer, K. Hono, "Microstructural Evolution and Age Hardening in Aluminum Alloys: Atom Probe Field-Ion Microscopy and Transmission Electron Microscopy Studies," *Materials Characterization*, 2000, Vol. 44, pp. 101-131.
189. T. Abe, K. Miyazaki, K. Hirano, "Imaging of Pure Al and Aged Al-4wt.% Cu Alloys by Field ion Microscopy," *Acta Metallurgica*, 1982, Vol. 30, pp. 357-366.

-
190. J. M. Silcock, T. J. Heal, H. K. Hardy, "Structural Ageing Characteristics of Binary Aluminum-Copper Alloys," *Journal of the Institute of Metals*, 1953, Vol. 82, pp. 239-228.
 191. A. K. Dahle, K. Nogita, "Eutectic Modification and Microstructure Development in Al-Si Alloys," *Materials Science and Engineering A*, 2005, Vol. 413-414A, pp. 243-248.
 192. S. D. McDonald, N. Kazahiro, "Eutectic Grain Size and Strontium Concentration in Hypoeutectic Aluminum-Silicon Alloys," *Journal of Alloys and Compounds*, 2006, Vol. 422, pp. 184-191.
 193. S. D. McDonald, N. Kazahiro, "Eutectic Nucleation in Al-Si Alloys," *Acta Materialia*, 2004, Vol. 52, pp. 4273-4280.
 194. M. H. Mulazimoglu, F. Paray, "Modification of Intermetallic Phases by Strontium in Aluminum Wrought Alloy," *Light Metals*, TMS Warrendale, 1994, pp. 1047-1056.
 195. M. H. Mulazimoglu, A. Zaluska, F. Paray, J.E. Gruzleski, "The Effect of Strontium on the Mg₂Si Precipitation Process in 6201 Aluminum Alloy," *Metallurgical and Materials Transactions A*, 1997, Vol. 28A, pp. 1289-1295.
 196. S. F. Frederick, W.A. Bailey, "Relation of ductility to dendrite cell size in a cast aluminum-silicon-magnesium alloy," *Transactions of TMS-AIME*, 1968, Vol. 242, pp. 2063-2067.
 197. C. H. Cáceres, J. R. Griffiths, P. Reiner, "The influence of microstructure on the Bauschinger effect in an Al-Si-Mg casting alloy," *Acta Materialia*, 1996, Vol. 44, pp. 15-23.
 198. G. Ran, J. E. Zhou, Q.G. Wang, "Precipitation and Tensile Fracture Mechanism in a Sand Cast A356 Aluminum Alloy," *Journal of Materials Processing Technology*, 2008, Vol. 207, pp. 46-52.
 199. W. H. Hunt, J. R. Brockenbrough, P. E. Magnusen, "An Al-Si-Mg Composite Model System: Microstructural effects on deformation and damage evolution," *Scripta Metallurgica et Materialia*, 1991, Vol. 25, pp. 15-20.
 200. P. E. Magnusen, D. J. Srolovitz, D. A. Koss, "A Simulation of Void Linking during Ductile Microvoid Fracture," *Acta Materialia*, 1990, Vol. 38, pp. 1013-1022.

-
201. L. Arnberg, L. Bäckerud, A. Dahle, "Castability of Aluminum Foundry Alloys: Final Report," AFS Research Report, American Foundrymen's Society, Des Plaines, IL, 1999, p. 111.
 202. J. Campbell, "Entrainment Defects," *Materials Science and Technology*, 2006, Vol. 22, pp. 127-145.
 203. J. Kim, J. Choi, C. Lee, E. Yoon, "A Study on the Variation of A356 Aluminum Alloy with Sr Addition," *Journal of Materials Science Letters*, 2000, Vol. 19, pp. 1395-1398.
 204. J. P. Anson, R. A. L. Drew, J. E. Gruzleski, "The Surface Tension of Molten Aluminum and Al-Si-Mg Alloy Under Vacuum and Hydrogen Atmospheres," *Metallurgical and Materials Transactions B*, 1999, Vol. 30B, pp. 1027-1032.
 205. C. L. Chen, A. Richter, R. C. Thomson, "Mechanical Properties of Intermetallic Phases in Multi-Component Al-Si Alloys Using Nanoindentation," *Intermetallics*, 2009, Vol. 17, pp. 634-641.